Reflection, Refraction and Transmission of Light in Grosseteste's Physics

ScuDo
Scuola di Dottorato ~ Doctoral School
WHAT YOU ARE, TAKES YOU FAR

Doctoral Dissertation
Doctoral Program in Materials Science and Technology
(XXX Cycle)

Graphene-based Supercapacitors

By
Arnaud Gigot

Supervisors:
Prof. Candido Fabrizio Pirri
Dr. Paola Rivolo

Doctoral Examination Committee:

Prof. Elisabetta Comini, Referee, Università degli Studi di Brescia
Dr. Vittorio Morandi, Referee, C.N.R. di Bologna
Prof. Luca Ottaviano, Referee, University degli Studi dell'aquila
Dr. Hugh Sutherland, Referee, ZapGo Ltd
Prof. Elena Tresso, Referee, Politecnico di Torino

Politecnico di Torino
2018

Declaration

I hereby declare that, the contents and organization of this dissertation constitute my own original work and does not compromise in any way the rights of third parties, including those relating to the security of personal data.

Arnaud Gigot
2018

* This dissertation is presented in partial fulfilment of the requirements for **Ph.D. degree** in the Graduate School of Politecnico di Torino (ScuDo).

To my lovely parents

The Science of today is the Technology of tomorrow
Edward Teller (1908-2003)

Stones in the road?
I save every single one, and,
one day, I'll build a castle
Fernando Pessoa (1888-1935)

ACKNOWLEDGMENTS

This Ph.D. thesis is the fruitful result of three years of multidisciplinary activity which merges into a single framework Chemistry, Physics, Electronics, and Materials Science of course. Naturally, this work would not have been possible without the contributions of colleagues and friends.

First of all, I would like to thank Prof. Candido F. Pirri for giving me the opportunity to join the Istituto Italiano di Tecnologia, but also for his support and research freedom, which allowed me to grow from both the scientific and the personal point of view. My deep gratitude goes to Dr. Paola Rivolo who perfectly played the co-supervisor role. In these three years, she advised, supported me and, more importantly, gave me feedbacks and suggestions, thus helping me to organize responsibly the scientific research work.

In addition, I would like to thank my team-mates (or colleagues) who gave a scientific contribution. The randomly sorted list of contributors is: Dr. Stefano Bianco, Dr. Andrea Lamberti, Dr. Mara Serrapede, Dr. Marco Fontana, Dr. Micaela Castellino, Dr. Marco Armandi, Prof. Barbara Bonelli, Dr. Simone Marasso, Prof. Elena Tresso, Dr. Rossella Giardi, Dr. Matteo Cocuzza, and Mr. Pietro Zaccagnini who is now Ph.D. student in our research group giving new inputs with his electronic knowledge and infinite curiosity.

Moreover, I would like to thank Prof. Robert A.W. Dryfe and his research group from the University of Manchester. This “more abroad” experience gave me the opportunity to learn new practical skills and to discuss supercapacitors with another approach.

This academic journey started actually before my Ph.D. thanks to Dr. Etienne Gicquel who was my lecturer during my Master in Belgium. Indeed, his inestimable mentorship provided me enough energy to overcome the activation energy required to take my start far from home (this sentence is voluntarily "nerd"). However, the Italian part of my life would not have been possible without Prof. Marco Sangermano who hosted me in his laboratories and gave the opportunity and confidence to work freely during my Master thesis and on "side-projects" during these three years. The "Ex-Polymer" group is full of good people making the day life easier: Dr. Annalisa Chiappone, Dr. Alessandra Vitale, Dr. Erika Fantino, Dr. Giovanna Colucci, Dr. Sofie Marchi, Dr. Florence Vivier, Dr. Julia Amici, and, last but not least, Dr. Ignazio Roppolo who has been like a big brother, during these years, due to his advices, suggestions, and supports within Politecnico or outside.

Life would be probably more boring without sports and party. I have to acknowledge my team-mates from "*Durex*" and the guys from the "*Ph.D. Drink day*" for the unforgettable moments.

Then, I have to thanks my friends (actually more than friends) from Belgium who gave me supports, good time, and patience: Quentin, Isabelle, your baby-boy who is close to start his journey at the moment I am writing these line, Kâline, and Lorenzo.

I would like to thank separately Federica with whom I shared all the good and bad moments during this journey. You helped me to stay on the track when I overwhelmed, and you have my deep gratitude for that.

Lastly, but more importantly, I am forever indebted to my family, who raised, supported, taught, and love me.

PREFACE

In Chapter I, the current worldwide energy scenario is thoroughly presented, along with the recent development in renewable technologies. The crucial need of energy storage devices is presented. Electrical storage technologies, with a focus on electrochemical storage, are reviewed.

Chapter II deals with the fundamentals of Supercapacitors such as operating principles and cell architectures. Moreover, the history of Graphene is reported with the recent development on its synthesis and production. Materials used to enhance the performance of Graphene-based Supercapacitors are presented.

Chapter III is focused on the electrochemical characterization of Graphene-based Supercapacitors with the different measurements available for the performance evaluation and the key parameters.

In Chapter IV, a comparison study was performed among several graphene composites containing metal oxides or metal dichalcogenides. However, this chapter was aimed to *in-situ* synthesize a hybrid 1T-2H-molybdenum disulphide together with the reduction of graphene oxide by one-pot hydrothermal synthesis. The supercapacitor resulting from this innovative hybrid demonstrates outstanding electrochemical performance with a stability up to 50.000 cycles.

Chapter V deals with the hydrothermal synthesis of reduced graphene oxide aerogel decorated with molybdenum oxide particles. This work was carried out to demonstrate the feasibility of the concomitant hydrothermal processes using the L-ascorbic acid (Vitamin C) as reducing agent. The addition of this green reducing agent induces a better reduction of graphene oxide and a higher reproducibility of the desired chemical reduction yield. The presence of molybdenum oxide particles permits to increase the specific capacitance using Faradaic processes.

As-synthesized materials are tested in micro-supercapacitors in Chapter VI. PDMS-based micro-supercapacitors were fabricated through a simple photolithographic process. Moreover, the use of a conductive binder, PEDOT:PSS, is investigated. The binder induces the formation of a spring-like rod configuration with the embedded active material. This spatial conformation is determined by the filling of the interdigitated channels by capillarity. As-fabricated micro-supercapacitors show high flexibility and good cycling stability.

Finally, Chapter VII presents the integration of supercapacitor devices to textiles fabrics. Two different works are presented: synthesis and characterization of an *in-situ* reduced graphene oxide aerogels onto a copper wire; and fabrication of exfoliated graphene-based wearable supercapacitors. The first part shows a peculiar morphology of the aerogel wadded around the current collector. The fabricated device demonstrates outstanding electrochemical properties in comparison with state-of-the-art works. Moreover, flexibility tests are performed and results are encouraging. In the second part, high performance exfoliated graphene-based wearable supercapacitors are studied. The padding method allows to produce 100 meters of textile fabrics coated with electrochemical exfoliated graphene. Obtained results are promising but, more importantly, the approach used is scalable and cost-effective.

The experimental part of this thesis has been carried out in the Center for Sustainable Future Technologies (Istituto Italiano di Tecnologia, Torino), in the Department of Applied Science and Technology (Politecnico di Torino), in the School of Chemistry and the National Graphene Institute (The University of Manchester, UK). The work was mainly focused on the synthesis and development of active materials prior to be tested for electrode in supercapacitor applications.

Table of Contents

Chapter 1

Energy: Demand and Storage Technologies

The current worldwide energy demand and consumptions are thoroughly presented, along with the recent development in renewable technologies necessary to address the growing energy demands. Then, the crucial need of energy storage devices is highlighted. Electrical storage technologies are reviewed. Moreover, the maturity of these technologies is discussed. Finally, electrochemical energy storage devices are presented alongside their reciprocal correlations.

1.1. Worldwide Energy Demand

Energy is used all the time and everywhere. Humankind does not even think about its continuous daily use. The worldwide consumption of marketed energy was 549.10^{15} British Thermal Units (BTU) in 2012 and is expected to expand to 629.10^{15} BTU in 2020, and even 815.10^{15} BTU in 2040. This increase corresponds to a value of 48% from 2012 to 2040.[1] Something even more worrying is the worldwide consumption level against the production as reported in Figure 1.1 and Figure 1.2, respectively. Indeed, the consumption of primary energy is higher than the production for several countries around the world. If we look globally, the worldwide total primary energy consumed for 2016 was 13,903 Mtoe (Million Tonnes of Oil Equivalent) and the production was 13,910 Mtoe, which means that globally we produce more energy than that we consumed. Nevertheless, the trend from 2015 to 2016 displays an increase of 1% of the

primary energy consumed worldwide while the production decreased of -0.4% for the same period, which reinforces the need of developing new efficient technologies.[2]

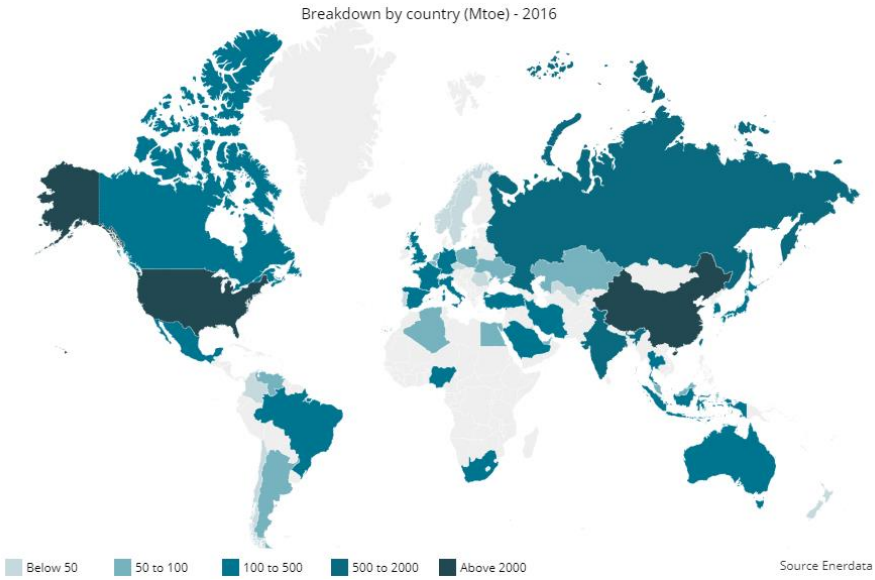

Figure 1. 1 primary energy consumption for 2016[2]

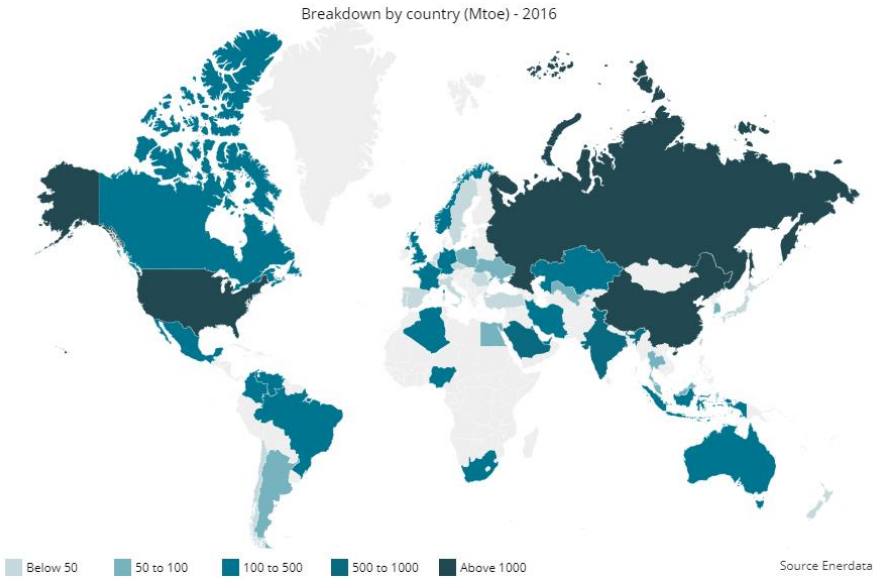

Figure 1. 2 primary worldwide energy production for 2016[2]

Undeniably, the actual situation is patently unsustainable whether in a social, environmental, or even economic point of view. Indeed, the current trends on carbon dioxide (CO_2) emissions related to the energy consumption will more than double by 2050 if the current trends will be not suitably substituted.[3] The CO_2 is produced using mainly fossil energy. The main energy sources, which lead the total world energy consumption, are liquid fuels, coal and natural gas as reported in Figure 1.3. Renewables technologies are projected to take a bigger part of the market in the next decade hopefully for a "greener" future.

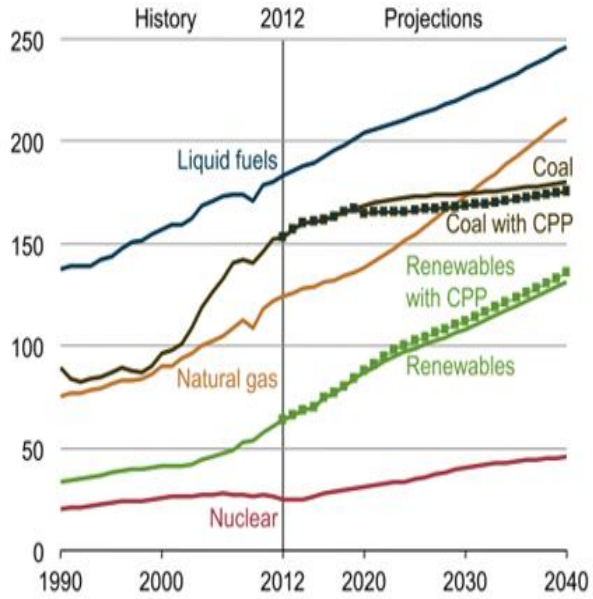

Figure 1. 3. Total world energy consumption by energy source, 1990-2040 (quadrillion Btu). Dotted lines for coal and renewables show projected effects of the U.S. Clean Power Plan.[3]

However, most of the renewables technologies cannot be suitably exploited in comparison with the fossil fuels because the energy cannot be stored or transported to the final-use place. To overcome this issue, the energy produced by means of renewable technologies, such as solar and wind turbine, should be converted to electricity.[4] Electricity is the world's fasted-growing form of end-use energy consumption and the

prediction reveals a doubling of the worldwide electricity demand by 2050 and tripling by the end of the century.[1,5]

Electricity is easily transportable in an efficient way. Consequently, its production is highly centralized and, often, a long distance away from the end-user. This centralized production must be taken account some drawbacks of using renewable technologies. Indeed, these technologies have a complete dependence of the metrological variables such as the wind force and the illumination for example. These variables directly influence the amount of energy that can be produced which makes difficult the stabilization of the power network.[6] Moreover, it is well known that the demand in electricity fluctuates importantly during the day. To overcome this problem, engineers have the choice between two solutions: (i) over-dimensioning of the production and transmission equipment or (ii) use energy storage technologies to store energy when the production is higher than the user's demand and release it when the demand increases.[5,6] The two solutions are illustrated in Figure 1.4.

Without electrical energy storage, the ratio between the end-user demand peak and the average of power generated level can reach a value of 10, which means that the equipment for production and transmission must be designed to release the energy requested by the end-user for the peak period.[6] In this case, the production equipment becomes bulky and, more importantly, expensive. This increase of costs will be, of course, added to the bill of the final user. Then, low-cost energy storage technologies become necessary. These storage devices can store the energy when the end-user demand is low (during the night-time) and will release it when the end-user demand increases (during peak time). Furthermore, the capacity of the energy storage technologies depends of the grid asset's response. So, a conventional turbine unit with an important capacity size (MW) could be substituted by a fast-responding energy storage device with less capacity.[5]

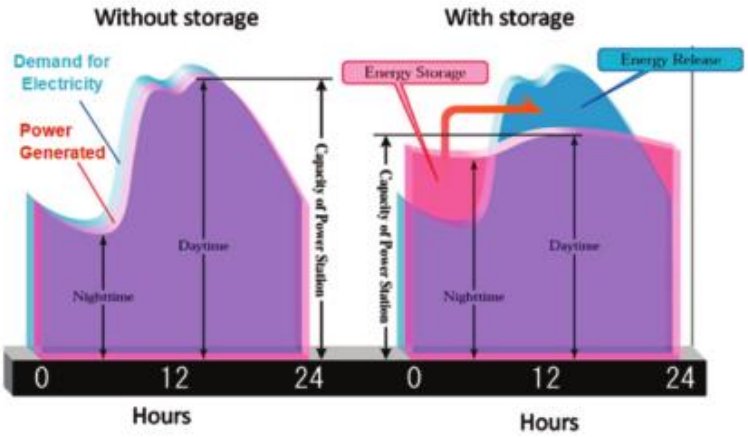

Figure 1. 4. Schematic representation of the balancing generation and demand via load levelling.[5]

1.2. Electricity Storage Technologies

Energy storage technologies are a crucial tool for the integration of renewable energy into the grid. Indeed, as described earlier, these technologies allow to stabilize the energy production level, which is one of the main concern for wind turbine and solar plant. Despite the important cost, which can be prohibitive for regions without developed technologies, support of the government, and/or low-cost financing; energy storage systems are expected to increase significantly their deployments in emerging markets in the next decade.[7]

Storage technologies are using for a plenty of applications such as seasonal storage, frequency regulation, demand shifting for examples. They can absorb energy and store it until its release become necessary, which means that they can bridge a temporal gap between energy supply and demand. If these technologies are coupled with adequate energy infrastructures, they can also be a geographical bridge between the energy supply and demand.[3] Demand for storage is, of course, different in function of the geographical topology or situation. Indeed, non-interconnected island systems must have larger storage capability than country with large hydro capacity reservoir such as Sweden for example.[8]

Electrical storage devices can be defined using two factors: the amount of energy that can be stored and the rate of charging/discharging of the energy storage devices.[9] The ideal energy storage device would be able to combine both factors. In addition to these typical characteristics, storage devices must be reliable and have a long-life expectancy with minimal maintenance cost. However, no energy storage technologies currently available can meet all these requirements simultaneously.[5,10,11] The main concern for a complete integration of energy storage devices is the cost of the apparatus. Indeed, the improvement of the overall performance is not as high as expected and, then, does not motivate the industry to integrate costly equipment if the return on investment does not reach a valuable level.[12]

To overcome this issue, development of new energy storage technologies and/or advance in existing technologies are necessary. In Figure 1.5, the maturity of the energy storage technologies currently investigated is reported.[13]

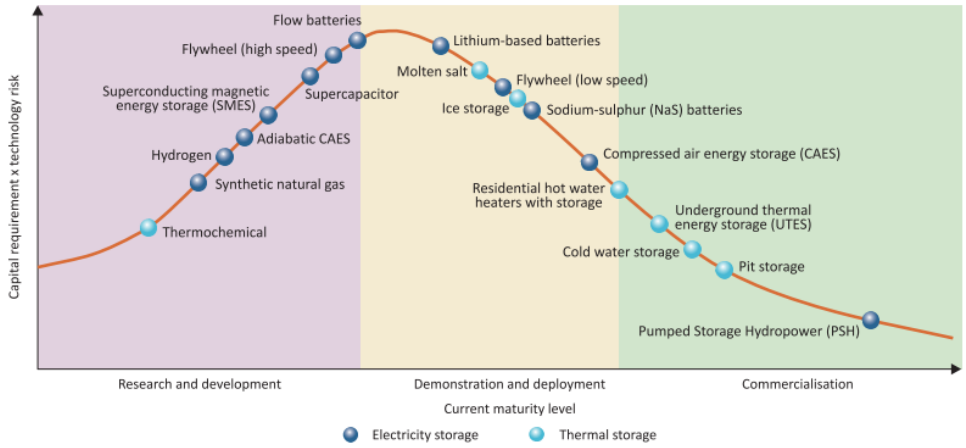

Figure 1. 5. Representation of the maturity for both electricity and thermal storage technologies.[13]

The graph reports the capital investment required multiplied by the technology risk in function of the current maturity level. Higher the technology is in the figure, higher is the capital required for the technology and/or higher is the risk took for the investigation of the feasibility. Three current maturity levels are defined: R&D, Demonstration and

Deployment, and Commercialisation. Looking in details on electricity storage technologies, Pumped Storage Hydropower (PSH) is the only one that reached a commercialisation level. Close to the commercialisation, Compressed Air Energy Storage (CAES), Flywheel, and Batteries technologies can be found. In the R&D phase, Flow batteries, and Supercapacitors are currently under investigation and required large investment to reach the proof of concept level.

The electricity grids worldwide currently use large-scale energy storage devices for 140 gigawatts (GW).[3] Of course, PSH technologies took the almost majority of the market with 99% due to its proved maturity. The remaining 1% is divided between CAES, Flywheel, and Electrochemical devices such as batteries, redox-flow and supercapacitors technologies as reported in Figure 1.6.[14]

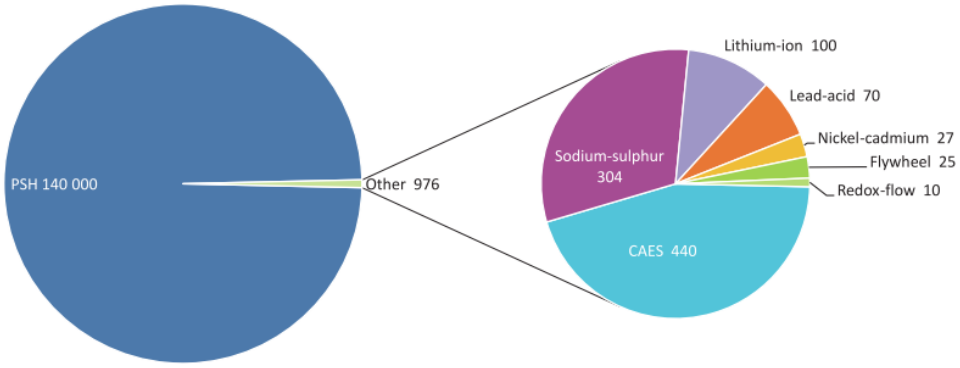

Figure 1. 6. Composition of the electricity grids worldwide in megawatts [14]

Even if the PSH technology is the most mature technology and almost exclusively used to date, it is important to note that the performance requirements depend of the application and expectations regarding the power and energy ratings, the ratio of power to energy, the charging time, the discharging time, the cycling life, etc. are different.[5] In the following sections, PSH, CAES, Flywheel and electrochemical storage technologies will be shortly described.

1.2.1. Pumped Storage Hydropower (PSH)[15–21]

Pumped Storage Hydropower (PSH) is the most mature technology for electricity storage technology as already reported above. It is also the larger energy storage system in operation. This technology represents approximatively 3% of the world's total installed power capacity, and 97% of the total storage capacity. In some countries, hydroelectricity is the majority source. Norway (98,9%) uses almost completely this production method. Other countries such as Brazil (83.7%) and Venezuela (73.9%) can be cited as example of these countries using hydroelectricity as the primary source. This storage technology stores potential energy using height differences between two reservoirs as reported in Figure 1.7.

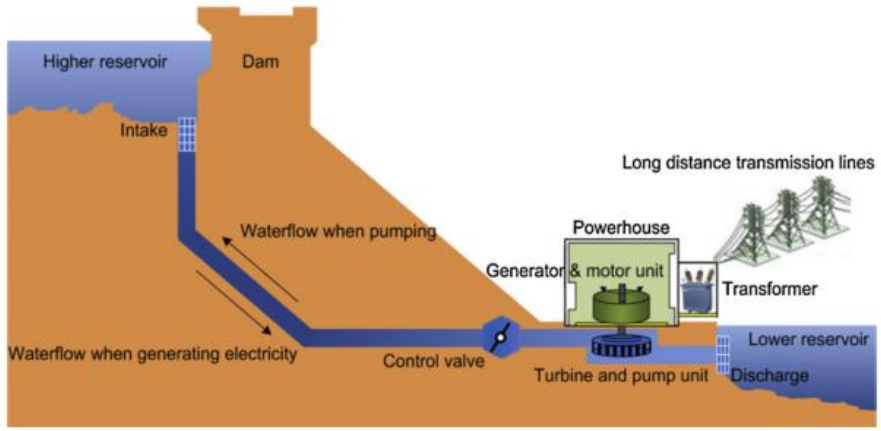

Figure 1. 7. a pumped storage hydropower plan layout[21]

As it can be seen in Figure 1.7, a PSH system can be described with three key units: (1) two reservoirs located at different elevation. Larger is the height difference between the two reservoirs, higher will be the amount of energy stored by the system because the stored energy is proportional to the elevation difference. The amount of the stored energy is also proportional to the water volume of the upper reservoir; (2) a pomp unit used to pump water from the lower reservoir to the higher reservoir during the off-peak period; and (3) a powerhouse unit which uses a turbine for the generation of electricity allowing the conversion of the potential energy to

electricity during the peak hours. This pump unit represents the difference from ordinary hydroelectric power system because it allows the PSH to pump water from the lower reservoir to the upper reservoir, acting as an electromotor.

The efficiency of PHS systems are evaluated around 65-85% depending on the evaporation and the conversion losses. Its relatively high efficiency is an advantage which can be summed to the other characteristics of PHS, which are large power capacity (typically 100-1000 MW), large storage capacity, and a long life (30-60 years), at a lowest energy cost ($0.1-1.4/kWh/cycle). Furthermore, despite the large power volumes and energy management in this installation, the system can react with a response time lower than 1 minute enabling the use of this technology for the control electrical network frequency and in provision of reserve generation.

The above characteristics are a testament of the affordability, robustness, and scalability of this energy system technology. However, this system has also huge drawbacks. Certainly, the most important drawback is the lack of available sites for building two large reservoirs and one (or two) irrigation dam(s). The construction of this plant lies to serious environmental issues such as removing trees and vegetations in a surface typically around 10-20 km² of land before to the reservoir being flooded. Of course, all the construction is expensive, which is also one of the main concern. The capital cost varies from $100 million to $3 billion US, which is of course prohibitive for a lot of countries/regions. The last major constraint is the lead time which is typically around 10 years.

To reduce the cost and the environmental issues, improvements of PSH technology were investigated and will be constructed. Indeed, some PSH plants will use flooded mine shafts, underground caves, and/or oceans as reservoirs. The best example is in Okinawa Yanbaru island in Japan with a 30 MW seawater project, which was completed in 1999.[21,22] A picture of the site is shown in Figure 1.8.

Figure 1. 8. Okinawa Yanbaru (Japan), the first seawater Pumped Storage Hydropower[22]

1.2.2. Compressed Air Energy Storage (CAES)[15–17,19–21,23,24]

CAES is, with PHS system, one of the two electrical storage technologies currently suitable for large-scale power and/or high energy storage applications. To date, it exists only two CAES sites in the world. The first is in Huntorf (Germany) and was installed in 1978. It has a capacity of 290 MW for 2 hours. The second is in McIntosh (AL, USA), with a capacity of 110 MW for 26 hours. The site located in the US can switch from full generation to full compression in only 5 minutes, and back to full generation in less than 15 minutes. Even if it exists only two sites opened worldwide, both have demonstrated economic feasibility and high reliability.

As described for the McIntosh plant, CAES system must be able to compress and to expanse air. Indeed, this technology stores energy by compressing air, with a pressure typically around 4.0 – 8.0 MPa, when the demand is low. To extract the stored energy from its topological confinement, compressed air is drawn from the storage vessel, heated, and then expanded through a high-pressure turbine.

Typically, a CAES plant consists in five key units as shown in Figure 1.9. The first key unit is a motor/generator which can switch engagement to the compressor or turbine trains. The second is obviously the air compressor with two or more stages to achieve economic viability. The plant contains also: (3) a turbine train which contains both high- and low-pressure turbines; (4) a topological confinement for the

compressed air, typically underground rock caverns, salt caverns, porous-media reservoirs; (5) equipment controls.

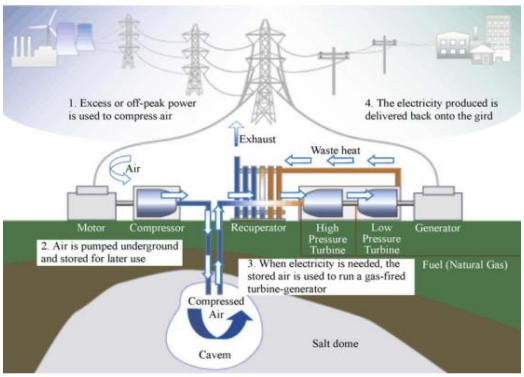

Figure 1. 9. a compressed air energy storage plan layout[15]

CAES have attractive qualities close to PHS systems such as high-power capacity (50 – 300 MW), long storage period (over a year), relatively long life (approximately 40 years), and a high efficiency typically between 60 and 80 %. Moreover, CAES is more attractive than PHS because the capital cost is significantly lower ($400-800/kW) and the environmental issue is limited since the storage is underground.

However, CAES plants suffer of the same major barrier than PHS with the research of the appropriate geographical site to build the plant. Moreover, in the research of "greener" solution for energy production/consumption, CAES lies with the requirement of combusting fossil fuels for the expansion cycle, which means that this technology is not carbon neutral. Last but not least, system design is difficult due to the heat transfer during the cycling. Indeed, the air compression is an exothermic process while the expansion is endothermic. To overcome this issue, advanced research is focusing on three modifications: isothermal storage, adiabatic system, or diabatic storage systems.

To conclude, CAES plants cannot solve alone the problems of excess electricity production. However, this technology is attractive, feasible, and can save investments in power plant capacities.

1.2.3. Flywheel[15–18,20,23,25,26]

Flywheel technology is simpler than PHS and CAES as it can be seen in Figure 1.10.

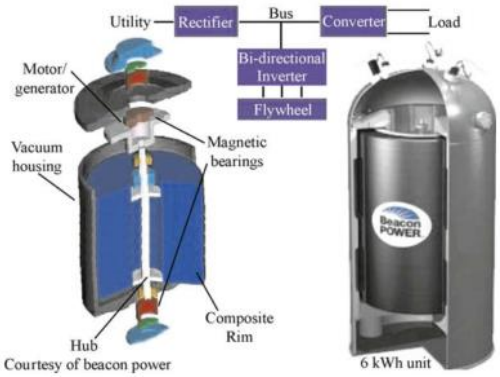

Figure 1. 10. A Flywheel technology layout (left) and a flywheel storage system of 6 kWh unit from beacon power, courtesy of Beacon power (right).[27]

The storage is in this device is driven by the angular momentum of a spinning mass. The electromotor rotates at high speed where electrical energy is converted to kinetic energy; when the speed decreases, kinetic energy is converted into electrical energy to release the stored energy. The total energy of a flywheel system is dependent on the size and speed of the rotor while the power rating is dependent on the motor-generator.

Interestingly, the input/output power is limited only by the power converter that means that flywheels can provide very high peak power. Devices are relatively small and light, which allow the technology to find its market when batteries would be too large or heavy. The systems can be fully charged/discharged for several hundreds of thousands of times. Its efficiency is in the range of 90 – 95 %. The life of the device is not function of the depth of discharge.

However, the capital cost for flywheel is high with a value in the range of $1000 – 5000 kWh and devices suffer of self-discharging rate typically around 55% and 100%/day.

To conclude, flywheels become interesting for market applications when long-term storage is not required such as

frequency smoothing. For example, the most common application is to act as a power quality device to bridge temporal gap between the shift from one power source to another. This system can supply highly reliable electric power for seconds to minutes at a time.

1.2.4. Electrochemical Energy Storage

Portable energy storage technologies are required for several applications from miniaturized dimensions (phones, laptops, etc.) to large scale such as transport. Of course, storage systems described previously are not portable (PHS, CAES) or only for some size-restricted devices in the case of Flywheels. To overcome this issue, electrochemical energy storage devices were developed and currently under investigation to improve their performances.

It is difficult to have a correct overview of the energy storage devices performances using only table with number. To compare easily storage systems, D. Ragone has developed in the 60's a diagram which represents performance in terms of the ratio of mass to energy and power. This diagram is called after him as "Ragone's plot" or "Ragone's diagram", see Figure 1.11.[28]

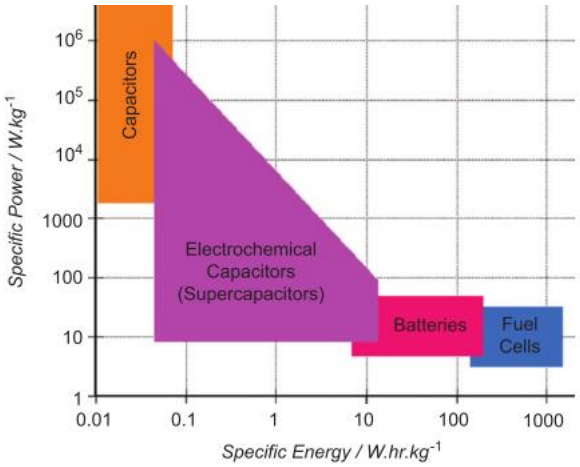

Figure 1. 11. Energy-storage Ragone Plot[11]

The Ragone plot displays Specific Power (W/kg) in function of Specific Energy (W/h.kg) using the mass to rationalize

Power and Energy. Indeed, device's mass is a critical aspect for portable energy storage units. For stationary units such as PHS and CAES, it is completely useless to compare using the mass as the critical criteria. In these cases, it is more important to look at the life expectancy, and the total costs.[6]

Looking at Figure 1.11, four different technologies can be seen: Capacitors, Supercapacitors, Batteries, and Fuel Cells. Four different technologies and four completely different Specific Power and Specific Energy. Capacitors, and Supercapacitors (also called "Electrochemical Capacitors") have Specific Power with several orders of magnitude higher than Batteries and Fuel Cells. However, their Specific Energies are significantly lower than the two other devices. So, depending on the applications, engineers will choose one system or another. Although the energy storage and the conversion mechanisms are different, there are "electrochemical similarities" of these four systems.[29]

Electrochemical energy storage devices which can also be used as alternative power sources are considered as the principal actor to overthrow a worldwide issue: the vehicle fuel economy. Indeed, the fuel consumption rate will consume all the global petroleum resources within 50 years according to the scientific estimations. During the same period, the global number of vehicles will increase from 700 million to 2.5 billion. To reduce the fuel consumption, electrical vehicles are developed, such as all-electrical range (AER) or hybrid electrical vehicles (HEVs). The efficiency of both technologies is depending on their energy storage systems. Due to their performances, portability, and scalability, Batteries and Supercapacitors are considered as the most viable applications for transport applications because they can supply the output of the engine during the acceleration and cruise and for energy recovering during braking.[23,30,31]

1.2.4.1. Batteries[9,18,29,32–41]

Batteries are one of the most cost-effective technologies available and they are the most common on the market. They generate electrical energy using redox reaction to convert chemical energy. The first commercial battery was introduced by Sony Corporation in the early 1990's. It was a Lithium-ion battery. The principle of operation of this battery is reported in Figure 1.12. In this figure, the anode, Li_yC, will intercalate Lithium-ions, Li^+, during the charging cycles. During the discharge, the cathode, Li_xCoO_2, will intercalate the Lithium-ions removed from the anode. The electrons migrate in the same direction flow than the Lithium ions through an outer electrical circuit.

The insertion of Lithium ions that enables the redox reaction is controlled by the diffusion through bulk electrodes materials. This diffusion-controlled mechanism is the reason for the low power density of batteries technology. The intercalation/deintercalation of ions through bulk-materials will also have an impact on the electrode volumes during the charge/discharge cycles. Sometimes, this change of volume can produced short-circuit with terrible consequences such as fires and explosions. The safety is probably one of the main concern for Li-ion battery and a lot of efforts are made in this direction.[42–44] To date, battery manufacturers can produce high-quality lithium-ion cells with less than one reported safety incident for every one million lithium-ion cells produced.

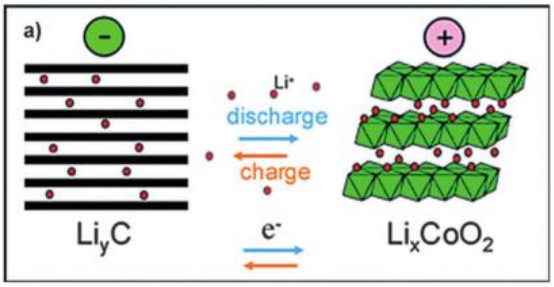

Figure 1. 12. Lithium ions migrate back and forth between the anode and cathode through the electrolyte upon discharging/charging; electrons doing so similarly through the outer electrical circuit.[41]

Why Lithium-ion batteries are so important for portable applications? Motivations came from Lithium, of course. It is the third lightest element known, which means low influence of the total mass in a market where the device weight is a crucial aspect. Moreover, the oxidation potential Li^+/Li is the highest of all known elements with 3 V above the standard hydrogen potential. Therefore, Li-ion batteries offer a good perspective for developing high energy and high-power batteries. These batteries offer versatility, suitable lifetime for a wide range of applications.

However, it exists something alarming for this technology. Undeniably, Lithium can be viewed as the gold of the next century because it is a material with a relatively low abundance on earth. This low abundance coupled with a complete shift from oil-dependent internal combustion engine to Li-ion batteries-propelled "electric" vehicles, could have dramatic impact. Indeed, if there will be enough lithium on planet to feed the whole automobile market, the price will become unaffordable for the final buyers or for the EV manufacturers. The Lithium price is expected to be multiplied by five within ten years from 5.42 in 2010 to 25.50 $/kg in 2020. To date, the price increased to a value of 9.1 $/kg with is less than expected by the scientific community.[45]

New materials developments are needed and a lot of research groups around the world are focused on this thematic to find the new "killer" materials concerning the chemical nature of cathode, anode, and electrolyte. For example, it is possible to find investigations on Sodium-ion batteries[46–48], Lithium-Sulphur batteries[49–51], metal-air batteries[52].

1.2.4.2. Supercapacitors: competitors or allies of batteries?[11,18,29,31–34,53–56]

"Electrochemical Capacitors", "Supercapacitors", "Ultra-Capacitors"; all these appellations are used for the same technology. Different manufacturers gave the name according to the commercial device: "Supercapacitors" for Nippon

Electric Company (NEC) and “Ultra-Capacitors” for Pinnacle Research Institute (PRI). In this thesis, the appellation “Supercapacitors” will be used through all the document.

Supercapacitors must be differentiated from two other types of capacitors: electrostatic capacitors (typically made of two metal electrodes, in a parallel configuration, separated by a dielectric) and electrolytic capacitors (like electrolytic capacitors but they use conductive electrolyte salt in direct contact with the electrodes instead of the dielectric).

As it can be seen in Figure 1. 11, Supercapacitors fill the gap between conventional capacitors and batteries. Indeed, they can store more energy than that of conventional capacitors, and can deliver more power than that of batteries.

Supercapacitors use highly reversible electrostatic charge storage mechanism which allows to be charged/discharged over an almost unlimited number of cycles. Unfortunately, Supercapacitors suffer from the low energy density in comparison with batteries which leads to an ambivalent solution for the choice of the electrochemical energy storage devices required for an application. Indeed, using only batteries, the storage must be oversized to manage the peak demand while, using supercapacitors only, the storage must be oversized to store a sufficient amount of energy to deal with the intermittence of the renewable energy sources. Therefore, batteries and supercapacitors are not in competition one against the other, but they can be seen as allies to overcome the current challenges of energy storage / power delivery systems due to the existing synergy between these two technologies.

This thesis work is focused on the synthesis and development of new materials to increase Supercapacitors performances. In the next chapter, Supercapacitor technology will be described in addition with materials used for electrodes fabrication.

REFERENCES

(1) U.S. Energy Information Administration. *International Energy Outlook 2016*; 2016.
(2) Enerdata. Global Energy Statistical Yearbook 2016.
(3) Technology Roadmap: Energy Storage. *Energy Rep.* **2014**, 64.
(4) Dell, R.; Rand, D. A. J. Energy Storage - a Key Technology for Global Energy Sustainability. *J. Power Sources* **2001**, *100* (1–2), 2–17.
(5) Yang, Z.; Zhang, J.; Kintner-Meyer, M. C. W.; Lu, X.; Choi, D.; Lemmon, J. P.; Liu, J. Electrochemical Energy Storage for Green Grid. *Chem. Rev.* **2011**, *111*, 3577–3613.
(6) Ibrahim, H.; Ilinca, A.; Perron, J. Energy Storage Systems-Characteristics and Comparisons. *Renew. Sustain. Energy Rev.* **2008**, *12* (5), 1221–1250.
(7) Eller, A.; Gauntlett, D. Energy Storage Trends and Opportunities in Emerging Markets. *Energy Rep.* **2017**.
(8) Commercialisation of Energy Storage. *REPORT* **2015**, No. March.
(9) Ribeiro, P. F.; Johnson, B. K.; Crow, M. L.; Arsoy, A.; Liu, Y. L. Energy Storage Systems for Advanced Power Applications. *Proc. IEEE* **2001**, *89* (12), 1744–1756.
(10) Nehrir, M. H.; Wang, C.; Strunz, K.; Aki, H.; Ramakumar, R.; Bing, J.; Miao, Z.; Salameh, Z. A Review of Hybrid Renewable/alternative Energy Systems for Electric Power Generation: Configurations, Control, and Applications. *IEEE Trans. Sustain. Energy* **2011**, *2* (4), 392–403.
(11) Hall, P. J.; Bain, E. J. Energy-Storage Technologies and Electricity Generation. *Energy Policy* **2008**, *36* (12), 4352–4355.
(12) Abbey, C.; Joos, G. Supercapacitor Energy Storage for Wind Energy Applications. *IEEE Trans. Ind. Appl.* **2007**, *43* (3), 769–776.
(13) Decourt, B.; Debarre, R. *Electricity Storage: Factbook*, Schlumberg.; Paris, 2013.
(14) IEA, A.; EPRI. *Electrical Energy Storage Technology Options*; Palo Alto, 2010.
(15) Chen, H.; Cong, T. N.; Yang, W.; Tan, C.; Li, Y.; Ding, Y. Progress in Electrical Energy Storage System: A Critical Review. *Prog. Nat. Sci.* **2009**, *19* (3), 291–312.
(16) Beaudin, M.; Zareipour, H.; Schellenberglabe, A.; Rosehart, W. Energy Storage for Mitigating the Variability of Renewable Electricity Sources. *Energy Sustain. Dev.* **2010**, *14*, 302–314.
(17) Liu, C.; Li, F.; Ma, L.-P.; Cheng, H.-M. Advanced Materials for Energy Storage. *Adv. Mater.* **2010**, *22* (8), E28–E62.
(18) Whittingham, M. S. History, Evolution, and Future Status of Energy Storage. *Proc. IEEE* **2012**, *100*, 1518–1534.
(19) Cook, T. R.; Dogutan, D. K.; Reece, S. Y.; Surendranath, Y.; Teets, T. S.; Nocera, D. G. Solar Energy Supply and Storage for the Legacy and Non Legacy Worlds. *Chem. Rev.* **2010**, *110* (11), 6474–6502.
(20) Díaz-González, F.; Sumper, A.; Gomis-Bellmunt, O.; Villafáfila-

Robles, R. A Review of Energy Storage Technologies for Wind Power Applications. *Renew. Sustain. Energy Rev.* **2012**, *16* (4), 2154–2171.
(21) Luo, X.; Wang, J.; Dooner, M.; Clarke, J. Overview of Current Development in Electrical Energy Storage Technologies and the Application Potential in Power System Operation. *Appl. Energy* **2015**, *137*, 511–536.
(22) Bailey, K. 3 steps Blueprint to 100% Renewable Jamaica http://kimroybailey.com/renewable_blueprint/ (accessed Aug 1, 2017).
(23) Vazquez, S.; Lukic, S. M.; Galvan, E.; Franquelo, L. G.; Carrasco, J. M. Energy Storage Systems for Transport and Grid Applications. *IEEE Trans. Ind. Electron.* **2010**, *57* (12), 3881–3895.
(24) Lund, H.; Salgi, G. The Role of Compressed Air Energy Storage (CAES) in Future Sustainable Energy Systems. *Energy Convers. Manag.* **2009**, *50* (5), 1172–1179.
(25) Hebner, R.; Beno, J.; Walls, A. Flywheel Batteries Come around Again. *IEEE Spectr.* **2002**, *39* (4), 46–51.
(26) Lukic, S. M.; Cao, J.; Bansal, R. C.; Rodriguez, F.; Emadi, A. Energy Storage Systems for Automotive Applications. *IEEE Trans. Ind. Electron.* **2008**, *55* (6), 2258–2267.
(27) Lazarewicz, M.; Arseneaux, J. Flywheel-Based Frequency Regulation Demonstration Projects Status. In *Proceedings of EESAT conference*; San Francisco, 2005; pp 1–22.
(28) Ragone, D. Review of Battery Systems for Electrically Powered Vehicles. *SAE Tech. Pap.* **1968**, No. 680453.
(29) Winter, M.; Brodd, R. J. What Are Batteries, Fuel Cells, and Supercapacitors? *Chem. Rev.* **2004**, *104* (10), 4245–4269.
(30) Khaligh, A.; Li, Z. Battery, Ultracapacitor, Fuel Cell, and Hybrid Energy Storage Systems for Electric, Hybrid Electric, Fuel Cell, and Plug-in Hybrid Electric Vehicles: State of the Art. *IEEE Trans. Veh. Technol.* **2010**, *59* (6), 2806–2814.
(31) Burke, A. Batteries and Ultracapacitors for Electric, Hybrid, and Fuel Cell Vehicles. *Proc. IEEE* **2007**, *95* (4), 806–820.
(32) Miller, J. R.; Simon, P. Electrochemical Capacitors for Energy Management. *Science* **2008**, *321*, 651–652.
(33) Whittingham, M. S. Materials Challenges Facing Electrical Energy Storage. *MRS Bull.* **2008**, *33* (4), 411–419.
(34) Simon, P.; Gogotsi, Y.; Dunn, B. Where Do Batteries End and Supercapacitors Begin? *Science.* **2014**, *343* (3), 1210–1211.
(35) Burke, A. Ultracapacitors: Why, How, and Where Is the Technology. *J. Power Sources* **2000**, *91* (1), 37–50.
(36) Choi, N. S.; Chen, Z.; Freunberger, S. A.; Ji, X.; Sun, Y. K.; Amine, K.; Yushin, G.; Nazar, L. F.; Cho, J.; Bruce, P. G. Challenges Facing Lithium Batteries and Electrical Double-Layer Capacitors. *Angew. Chemie - Int. Ed.* **2012**, *51* (40), 9994–10024.
(37) Grosjean, C.; Herrera Miranda, P.; Perrin, M.; Poggi, P. Assessment of World Lithium Resources and Consequences of Their Geographic Distribution on the Expected Development of the Electric Vehicle

Industry. *Renew. Sustain. Energy Rev.* **2012**, *16* (3), 1735–1744.
(38) Thackeray, M. M.; Wolverton, C.; Isaacs, E. D. Electrical Energy Storage for Transportation—approaching the Limits Of, and Going Beyond, Lithium-Ion Batteries. *Energy Environ. Sci.* **2012**, *5* (7), 7854.
(39) Dubal, D. P.; Ayyad, O.; Ruiz, V.; Gómez-Romero, P. Hybrid Energy Storage: The Merging of Battery and Supercapacitor Chemistries. *Chem. Soc. Rev.* **2015**, *44* (7), 1777–1790.
(40) Larcher, D.; Tarascon, J.-M. Towards Greener and More Sustainable Batteries for Electrical Energy Storage. *Nat. Chem.* **2014**, *7* (1), 19–29.
(41) Palacín, M. R. Recent Advances in Rechargeable Battery Materials: A Chemist's Perspective. *Chem. Soc. Rev.* **2009**, *38* (9), 2565–2575.
(42) Hofmann, A.; Uhlmann, N.; Ziebert, C.; Wiegand, O.; Schmidt, A.; Hanemann, T. Preventing Li-Ion Cell Explosion during Thermal Runaway with Reduced Pressure. *Appl. Therm. Eng.* **2017**, *124*, 539–544.
(43) Wang, Q.; Ping, P.; Zhao, X.; Chu, G.; Sun, J.; Chen, C. Thermal Runaway Caused Fire and Explosion of Lithium Ion Battery. *J. Power Sources* **2012**, *208*, 210–224.
(44) Chi, J.; Kim, Y.-W.; Kim, B.; Lee, J.-G.; Park, B. A Breakthrough in the Safety of Lithium Seconday Batteries by Coating the Cathode Material with $AlPO_4$ Nanoparticles. *Angew. Chemie - Int. Ed.* **2003**, *42* (14), 1618–1621.
(45) Metalary.Lithium price https://www.metalary.com/lithium-price/ (accessed Jul 24, 2017).
(46) Ellis, B. L.; Nazar, L. F. Sodium and Sodium-Ion Energy Storage Batteries. *Curr. Opin. Solid State Mater. Sci.* **2012**, *16* (4), 168–177.
(47) Pan, H.; Hu, Y.-S.; Chen, L. Room-Temperature Stationary Sodium-Ion Batteries for Large-Scale Electric Energy Storage. *Energy Environ. Sci.* **2013**, *6* (8), 2338.
(48) Slater, M. D.; Kim, D.; Lee, E.; Johnson, C. S. Sodium-Ion Batteries. *Adv. Funct. Mater.* **2013**, *23* (8), 947–958.
(49) Xin, S.; Gu, L.; Zhao, N.; Yin, Y.; Zhou, L.; Guo, Y.; Wan, L. Smaller Sulfur Molecules Promise Better Lithium − Sulfur Batteries. *J. Am. Chem. Soc.* **2012**, *134*, 2–5.
(50) Manthiram, A.; Fu, Y.; Su, Y.-S. Challenges and Prospects of Lithium–Sulfur Batteries. *Acc. Chem. Res.* **2013**, *46* (5), 1125–1134.
(51) Manthiram, A.; Fu, Y.; Chung, S.; Zu, C.; Su, Y. Rechargeable Lithium − Sulfur Batteries. *Chem. Rev.* **2014**, *114*, 11751–11787.
(52) Cheng, F.; Chen, J. Metal–air Batteries: From Oxygen Reduction Electrochemistry to Cathode Catalysts. *Chem. Soc. Rev.* **2012**, *41* (6), 2172.
(53) Thounthong, P.; Raël, S.; Davat, B. Energy Management of Fuel Cell/battery/supercapacitor Hybrid Power Source for Vehicle Applications. *J. Power Sources* **2009**, *193* (1), 376–385.
(54) Zhou, H.; Bhattacharya, T.; Tran, D.; Siew, T. S. T.; Khambadkone, A. M. Composite Energy Storage System Involving Battery and

Ultracapacitor with Dynamic Energy Management in Microgrid Applications. *IEEE Trans. Power Electron.* **2011**, *26* (3), 923–930.

(55) Conway, B. E. Transition from "Supercapacitor" to "Battery" behavior in Electrochemical Energy Storage. *J. Electrochem. Soc.* **1991**, *138* (6), 1539–1548.

(56) Sharma, P.; Bhatti, T. S. A Review on Electrochemical Double-Layer Capacitors. *Energy Convers. Manag.* **2010**, *51* (12), 2901–2912.

Chapter 2

Graphene-based supercapacitors

In this chapter, fundamentals of supercapacitors are described. Then, historical background of graphene is reported. The outstanding properties of this material are highlighted alongside the scalable production methods. Finally, the state-of-the-art of graphene-based supercapacitors are reviewed and the comparison between Electrical Double-Layers Capacitors and Hybrid Supercapacitors containing conductive polymers, transition metal oxides, and transition metal dichalcogenides is presented.

2.1. Supercapacitors: general background

Supercapacitors can be found in different cell architectures: coin cell, stacked, wound, or pouch cell configurations as shown in Figure 2.1.

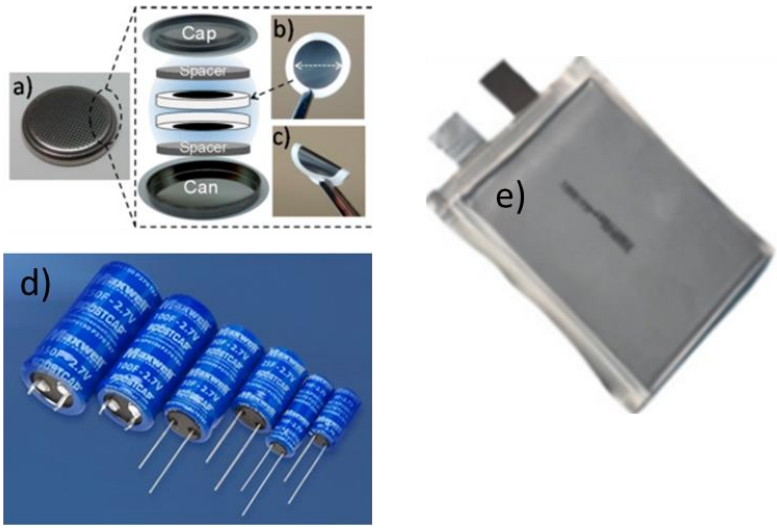

Figure 2. 1. (a, b, c) coin cell architecture[1], (d) wound supercapacitor[2], and (e) pouch cell supercapacitor[3].

Even if the configurations are different, components are the same for all supercapacitors. The most important components are: electrodes, electrolyte, current collectors, separator.

Electrodes represent the core of the supercapacitor as the active material composing them, mainly defines the device deliverable performances, thus becoming the focus of attention for materials scientists. Electrodes are generally carbonaceous materials such as activated carbon, amorphous carbon, carbon nanotubes, carbon aerogels, and, of course, graphene. Materials must have high porosity and be electrically conductive.

Electrolyte consists of dissolved chemicals in a solvent that can be aqueous or organic. Recently, ionic liquids have also attracted much attention due to their large operating voltage. Electrolyte contains cations and anions that allow charge separation in Electrical Double Layers Capacitors and can participate to the Faradaic processes in Pseudocapacitors (e.g. intercalation).

Separator is a physical barrier used to avoid any contact between the two electrodes of the supercapacitors. This contact would produce short-circuit that can have terrible consequences such as explosions and fire for examples.

Current Collectors are typically a metal foil (Copper, Aluminium, Nickel, Stainless Steel…) onto electrodes are deposited. This current collector must have high electrical conductivity. This part of the supercapacitors is also used to connect the supercapacitors to the electrical circuit in which it is applied.

2.2. Graphene: a "World-Famous Teenager"

"A single carbon layer of the graphite structure, describing its nature by analogy to a polycyclic aromatic hydrocarbon of quasi infinite size".[4]

This simple definition resumes two centuries of research works, which finally lead to the first isolation of a monolayer

of graphene, made by Geim's research group in Manchester (2004), and to the Nobel prize awarded to A. Geim and K.S. Novoselov in 2010.

Graphene, the carbon-based wonder material, is now 13 years old and has attracted attention from all around the world making itself a "World-Famous Teenager". To understand why the first isolation of a graphene monolayer was such an achievement for the science development, it is important to understand the general historic background of this material.

2.2.1. Historical Background[5–7]

The pencil commonly used today since the childhood, finds its origin in the 16th century, in England, with the discovery of *Plumbago*, which is the Latin appellation for "lead ore". They also understood the writing capabilities of this material making *Plumbago* the basis of the European development in substitution for quill and ink. It is only two centuries later that Carl Sheele, Swedish chemist, demonstrates the real composition of *Plumbago*. Indeed, the material discovered by the English was Carbon, not lead. Then, in an appropriated way, Abraham Gottlob Werner, German geologist, has suggested to change the name of the material to "graphite", which means "to write" in Greek.

In 1859, Benjamin Brodie, British chemist, has oxidized the graphite in "graphon" using strong acids. This new molecule with a molecular weight of 33 g/mol was actually graphene oxide.[8] In fact, due to the oxidation, graphite sheets surface was covered with hydroxyl and epoxides groups.[9] Graphene oxide suspension was observed for the first time using Transmission Electron Microscopy in 1948 by G. Ruess and F. Vogt.[10] Ulrich Hofmann and Hanns-Peter Boehm observed for the first time monolayers of reduced Graphene Oxide in 1962. The term "Graphene" has been introduced in 1986 by Boehm and co-workers. Graphene is the combination of

"Graphite" with the suffix referring to polycyclic aromatic hydrocarbons.[11]

In 1985, Harry Kroto, Robert Curl, and Richard E. Smalley have discovered a molecule containing 60 atoms of carbon in a spatial configuration of a soccer ball: fullerene.[12] They received the Nobel prize in Chemistry in 1996.

The first paper on mechanical exfoliation of graphite was published by Heinrich Kurz's group in 1990. They reported ultra-thin graphite obtained by peeling off layers using transparent tape to study carrier dynamics in graphite.[13] The year after, 1991, helical microtubules of graphite carbon with honeycomb lattice, read "Carbon Nanotubes" were identified by Sumio Iijima.[14]

According to a theoretical point of view, Phil Wallace reported the band structure of a "monolayer of graphite" to understand the electronic properties of bulk graphite.[15]

Practically, the isolation of graphene was envisaged by Rodney Ruoff and Reginald Little before the work published by Geim and co-workers.[16,17] However, the first isolation was demonstrated only in 2004 using an optical microscope even if the graphene was present in our daily life, such as in our pencil trace for example.[18]

2.2.1.1. Andre Geim: "Random Walk to Graphene".[6]

Andre Geim has completed his Ph.D. in 1987 at the Institute of Solid State Physics, Chernogolovka (U.S.S.R.). His Ph.D. thesis's title was: "*Investigation of mechanisms of transport relaxation in metals by a helicon resonance method*". He defined its thesis himself a "*zombie project*" because "*the project was dead a decade before he started the Ph.D.*".

After his Ph.D., Andre Geim became a staff member at Chernogolovska before moved across Europe for post-doc positions. He moved from U.S.S.R. to Nottingham (UK) [two times], Bath (UK) and Copenhagen (Denmark). During these years, he changed his researcher philosophy moving from the

research of a new phenomenon to the development of new experimental systems.

In 1994, he became Associate Professor at the University of Nijmegen (The Netherlands) working on the mesoscopic superconductivity. Alongside to its research niche, he started with some collaborators the so-called "*Friday Night Experiments*". These projects are of course much longer than one night with 6 months long for the shorter one. Most of them was abandoned after "*miserable failure*". Nevertheless, three of them were hits: levitation, gecko tape,[19] and graphene.

The levitation of non-magnetic materials is probably the funniest work. To study the diamagnetism, Geim and co-workers use expensive instrumentation. To reduce the experiments-cost they were forced to work during the night. To make the story brief, one night, they put water in an electromagnet at its maximum power and, surprisingly, the water drop does not finish on the floor but levitates between the magnets. To demonstrate that the ever-present diamagnetism is not negligible; and everything (and everybody) is magnetic; Geim and its collaborator Michael Berry show the same phenomenon with a frog. The levitated frog is shown in Figure 2.2. The physics behind the stability of diamagnetic levitation is reported in the review published by Geim in Physics Today.[20] In 2000, Geim and Berry were recognized by the Ig Nobel Prize for their "unprofessional" behaviour. So, Andre Geim was the first to won both Nobel and Ig Nobel Prize.

Figure 2. 2. Levitated frog during the "Friday Night Experiments" demonstrating the magnetism of "nonmagnetic things"

In 2001, Andre Geim earned a Full Professor position at The University of Manchester. His "research lab" was storage rooms filled with ancient equipment with no value. After earning some grants and building a fully functional laboratory, its first Ph.D. student arrived in 2002. Da Jiang, Chinese student, will work on the mesoscopic properties of graphite "as thin as possible"; only if he will be able to prepare such sample.

2.2.1.2. The Scotch Tape Legend[6,21]

Da Jiang started his Ph.D. thesis with a tablet of pyrolytic graphite with the following dimensions: 1 inch of diameter (± 2.5 cm) and several mm of thickness. After months of hard work with a polishing machine, Da has declared that he obtained the minimal thickness possible. The sample, placed at the bottom of a Petri dish, was observed carefully by means of an optic microscope. Result was unequivocal with a thickness around 10 µm. This project was a failure and, as it happens often, frustration entails nervousness and teasing remarks. Moreover, the unfortunate student threw away all the powder he does not use during the polishing, which means that no other sample is available to continue the work.

In the lab, Oleg Shklyarevskii was present and bring over a tape from a litter bin. This tape has graphite flakes attached on it because the tape was used to prepare a clean surface for STM (Scanning Tunneling Microscope) analysis. This technique was used for years but no one has never had the idea to look at the graphite leftovers (See Figure 2.3.a). The result was surprisingly much thinner than the sample prepared using the polishing machine. So, "*Polishing was dead, long live Scotch tape!*".

Promising results were obtained and, to go further, more people are needed. Kostya (Konstantin S. Novoselov) jumped at the opportunity to start this new project. The first measurements were performed on graphite flakes transferred by Novoselov onto glass slides using tweezers.

Then, Geim had the idea to transfer the materials to oxidised Si wafers, that give interference colours useful for the indication of the thickness. Indeed, some fragments were optically transparent with a thickness of few nanometres as shown in Figure 2.3.b. This result is the first discovery but not the eureka moment.

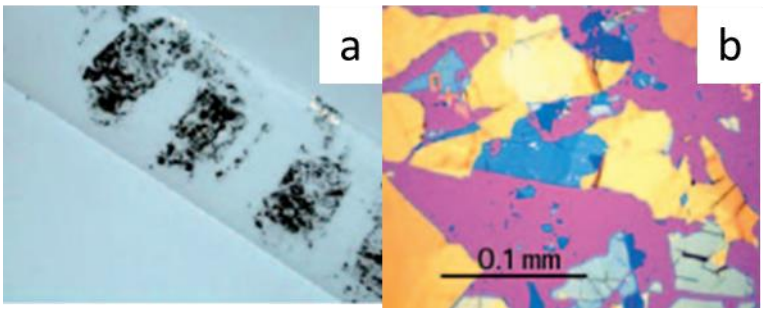

Figure 2. 3. (a) picture of the left-over graphene on tape and (b) microscopy image of as-isolated graphene

2.2.1.3. EUREKA Moment

The "Scotch Tape" method is generally reminded for the first isolation and identification of graphene. This method is reported in Figure 2.4. However, the objective was to find some breakthrough results.

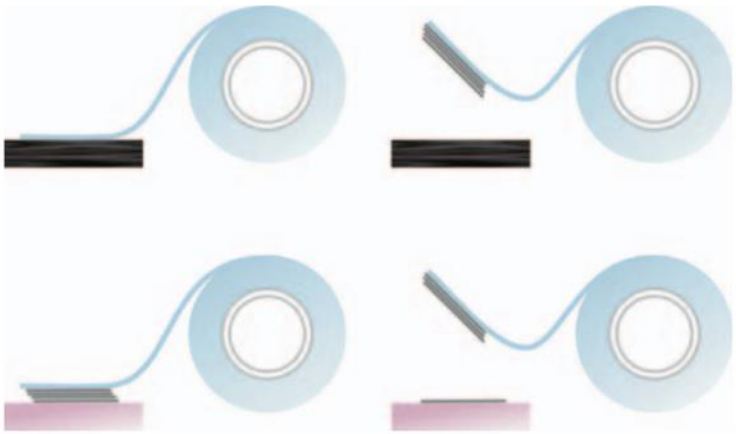

Figure 2. 4. Schematic representation of the scotch tape method to isolate graphene and to transfer it.

Surprisingly, ultra-thin graphite shows low resistance using silver paint to make electrical contacts. These results were

interesting and further measurements were carried out. The first hand-made device used 20 nm of graphite crystal in the centre part. Results were outstanding with the demonstration of an electric field effect. This is the eureka moment, when both Geim and Novoselov understood the potentiality of this preliminary measurement with a hand-made device.

Indeed, using the state-of-the-art microfabrication facilities, graphene will demonstrate its incomparable properties. Even with this discovery, reported works were rejected two times by Nature journal because, according to one referee, "*the work does not constitute a sufficient scientific advance*" before to be accepted by Science.[18]

2.2.1.4. Graphene: The mother of all Graphitics[7]

Graphene is often considered as "the mother of all graphitics" or, more precisely, of all sp^2 carbon allotropes because, starting from this single layer of carbon, it is possible to build all the other carbonaceous materials such as fullerene by wrapping (0D), carbon nanotubes by rolling(1D), and uninterestingly graphite by stacking (3D) as shown in Figure 2.5.

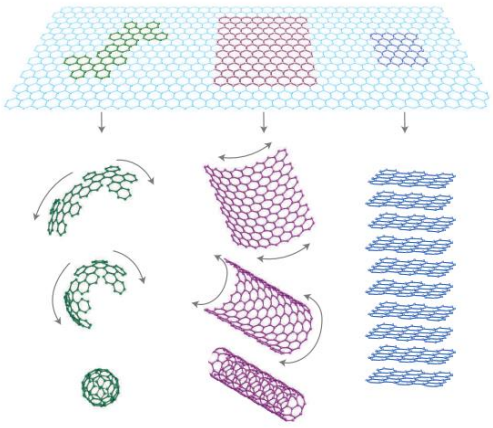

Figure 2. 5. A graphene layer (light blue) that can be used to build all the graphitics. In green, the formation of a fullerene by wrapping a part of the graphene layer. In red, the formation of carbon nanotubes by rolling a part of the graphene layer. In dark blue, formation of graphite by stacking of graphene layers.[7]

2.2.1.5. Outstanding properties of Graphene

Graphene has attracted attention due to tremendous characteristics that are superior to any other material known.[22] These characteristics are briefly described in this section.

2.2.1.5.1. Room-T Electron Mobility[23]

In 2011, Geim and co-workers fabricated a device containing a graphene layer encapsulated in hexagonal boron-nitride. This encapsulation isolates graphene from ambient atmosphere and allows the observation of an anomalous Hall effect and a pronounced negative bend resistance. Both observations are due to a room-temperature electron mobility of about 2.5 10^5 $cm^2/V.s$ of graphene layer which is superior to the theoretical limit of 2 10^5 $cm^2/V.s$ estimated previously by Morozov and colleagues.[24]

2.2.1.5.2. Mechanical Properties[25]

Lee *et al.* deposited a freestanding graphene layer onto a 5-by-5-mm array of circular wells patterned onto Si substrate. This "suspended" graphene permits to measure the mechanical properties by nanoindentation in an atomic force microscopy. A SEM image of the graphene is shown in Figure 2.6, A; non-contact mode AFM image in B; schematic representation of the nanoindentation on "suspended" graphene in C; and AFM image of a fractured membrane in D. Using this method, they determine a Young modulus for graphene of 1 TPa and an intrinsic strength of 130 GPa.

2.2.1.5.3. Other properties

Balandin reported and compared the thermal conductivity of carbonaceous material. Graphene has demonstrated a thermal conductivity higher than 3,000 W/mK.[26] Graphene demonstrated also high transparency as reported by Geim and colleagues. The optical absorption of a single layer of graphene is about 2.3% as shown in Figure 2.7.[27]

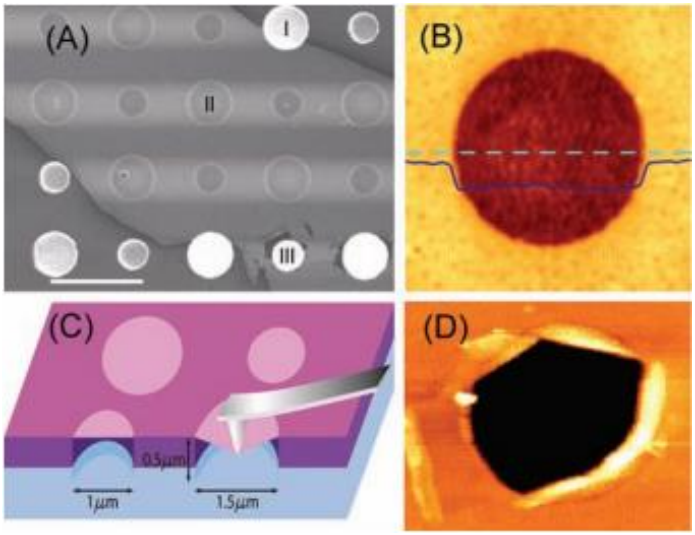

Figure 2. 6. (A) "suspended" graphene deposited on patterned Si containing holes with a diameter comprised between 1 µm and 1.5 µm. Area I show a hole partially covered by graphene, II totally covered by graphene, and III is fractured from indentation. Scale bare: 3 µm; (B) Non-contact AFM image; (C) schematic representation of the nanoindentation procedure; and (D) AFM image of a fractured graphene layer.[25]

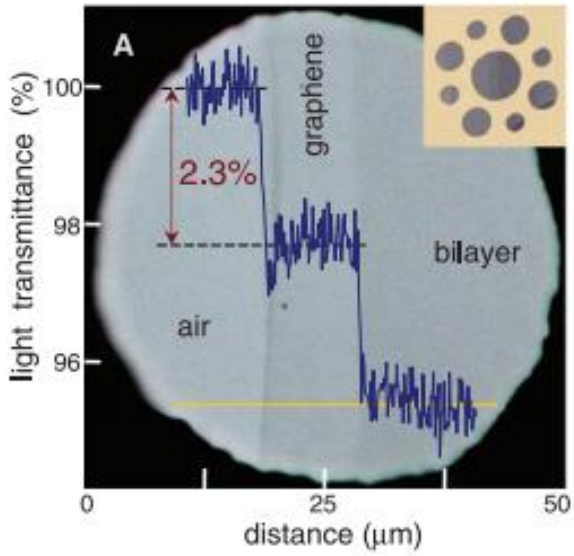

Figure 2. 7. Photograph of a 50-µm aperture partially covered by graphene and its bilayer.[27]

McEuen's research group demonstrated that graphene is also impermeable to gazes including Helium.[28]

2.2.2. Production Methods

2.2.2.1. Introduction

The synthesis of graphene, due to its tremendous properties, focused attention of both scientific community and political power since 2004. Today, there are various pathways to synthesize graphene with different quality levels, controlled dimensions (flakes lateral size), number and type of defects. The final application is, of course, strongly coupled with the graphene quality and cost of production. Figure 2.8 summarizes graphically the current scalable synthesis technique and the possible final application.[22]

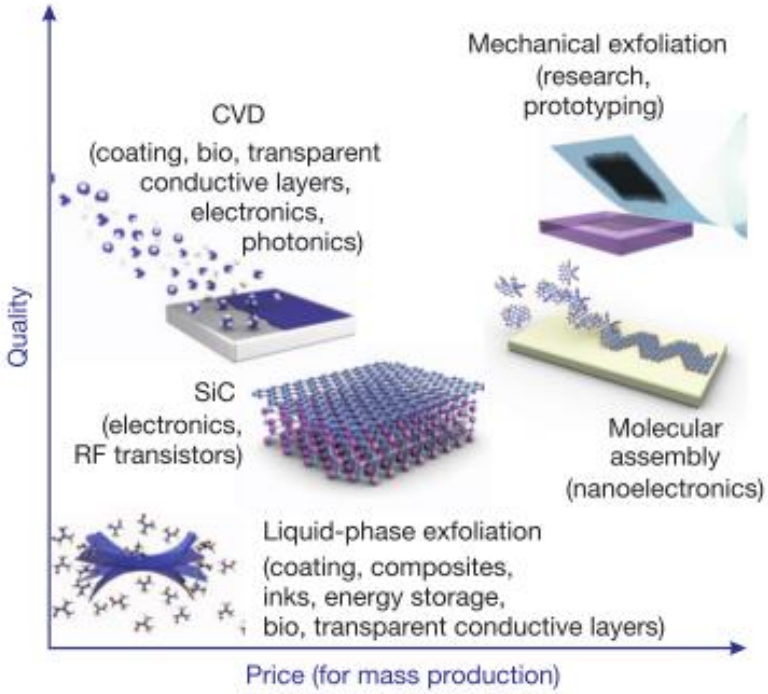

Figure 2. 8. Illustration of the current scalable and available synthesis technique and their possible applications in function of the graphene quality and the relative mass production price.[22]

Synthesis approaches are typically divided in two categories: "top-down" and "bottom-up". The most relevant techniques are discussed in this section.

2.2.2.2. "Top-Down" approaches

The "top-down" approaches start from graphite, a cheap and widely available raw material. They are advantageous due to their high yields, but they struggle looking forward to a large-scale production.[29]

2.2.2.2.1. Mechanical Exfoliation[30–32]

The mechanical exfoliation is the most famous production technique since the scotch-tape legend awarded with the Nobel prize in 2010 for Geim and Novoselov (See Section 2.2.1).[18] This micromechanical cleavage of graphite opens the door to the graphene world. This approach is nevertheless restricted to fundamental research due to the very limited quantity of graphene that can be produced.

Some improvement has been developed by mounting a single micropillar on an AFM cantilever. Kim and co-workers applied a sheer force about 300 nN/µm² to break the inter-layer Van der Waals interactions which have an energy of about 2 eV/nm².[33] However, it remains challenging to bring this technique to a viable large-scale production.

2.2.2.2.2. Liquid-phase exfoliation[22,29,30,32]

This approach is promising for a large-scale production of high quality graphene.[34] Graphite is exposed to a solvent with a surface tension which induces an increase of the exposed graphite crystallites. By sonication, Van der Waals interactions break down and multi-layers of graphene start to form a suspension. After sufficient exposure time to ultrasound, mono- and few-layers graphene are dispersed in suspension.[35,36]

Direct exfoliation can be carried out in polyvinylpyrrolidone[37], but N-methylpyrrolidone (NMP)[35] or dimethylformamide (DMF)[38] are typically used because the yield is known to be higher. Liu *et al.* further improved the in DMF-based liquid-phase exfoliation by using supercritical DMF.[39] Recently, electrochemical exfoliation has been

investigated using aqueous electrolyte. Results are promising and avoid the use of toxic organic solvent such as NMP and DMF.[40,41]

Another approach to exfoliate graphite in liquid-phase is to combine intercalation of chemical species or use of a surfactant followed by the sonication step.[42]

It is however important to keep in mind that this approach has some significant drawbacks such as low-yield, use of expensive intercalation reactants. Finally, the graphene conductivity might be decreased due to residual traces of the surfactant.

2.2.2.2.3. Unzipping of Carbon Nanotubes[22,30,32,43]

As aforementioned in the paragraph 2.2.1.4, graphene can be considered as the "mother" of all sp^2 carbon allotropes. Indeed, it is possible to build fullerenes, carbon nanotubes, and more easily (and without any interest) graphite starting from graphene layers. Interestingly, graphene can be reversibly produced from carbon nanotubes by unzipping them as shown in Figure 2.9.

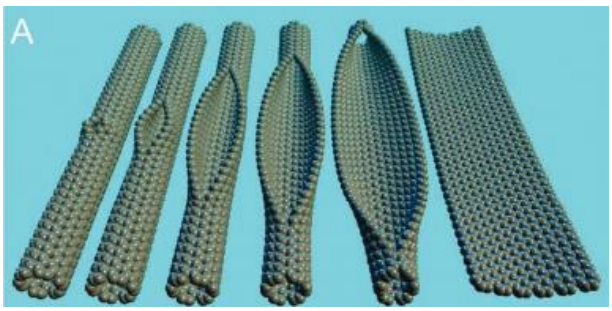

Figure 2. 9. Unzipping of CNTs to produce Graphene Nanoribbons (GNRs).[44]

Graphene Nanoribbons are a "thin elongated strip of graphene"[32] and can be produced by unzipping of SWCNTs. This production pathway allows to control the level and type of chemical functionalization, and, more importantly, to obtain high quality of the graphene edge.[44–46]

Recently, Tanaka and co-workers have demonstrated that the unzipping of CNTs to obtain graphene nanoribbons is more

efficient if it starts from DWCNTs instead of SWCNTs or MWCNTs.[47]

2.2.2.2.4. The "Graphene Oxide way"

Graphene is a wonderful material for a lot of research fields. However, its synthesis and preparation are costly and time-expensive. Moreover, for some applications, the handling of graphene layers is not straightforward. For example, a typical example is the hydrothermal synthesis of graphene-based supercapacitors. Due to the absence of carbon-oxygen moieties on the surface of the single layer of carbon, graphene is hydrophobic, and consequently not easily dispersible in water. To overcome this issue, the "graphene oxide way" is often considered.

First, graphene oxide is a cheap material, which can be prepared starting from graphite and using strong oxidizing chemical reactants. Several methods are reported in literature, but the most famous is probably the Hummers method.[48] After the oxidation step, the chemical structure of the carbonaceous material contains many oxygen functionalities such as epoxy, ketones, carboxylic acids. The chemical model of GO was developed by Lerf-Klinowski and shown in Figure 2.10.

The as-prepared material is already attractive from a general chemical point of view[9] or focusing on energy storage applications.[49]

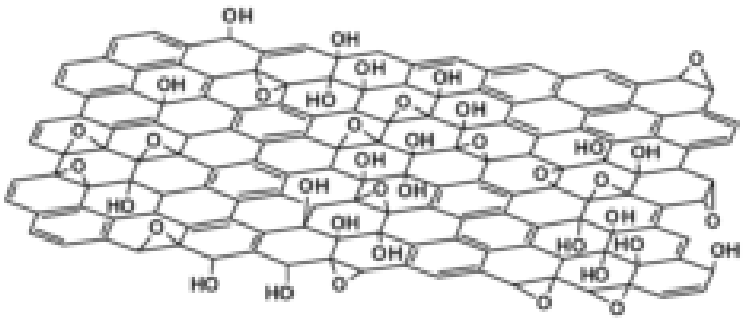

Figure 2. 10. Lerf-Klinowski model for the representation of GO.[9]

However, it is crucial to restore the sp^2 hybridization of carbon atoms to restore the electrical properties of the graphene layer. A lot of approaches have been investigated to reduce GO to rGO (or graphene-like material) with the use of H_2S, hydrazine, or other chemical reactants.[50] Notwithstanding their efficiencies, new reduction pathways have to be developed to reduce the use of toxic chemical reactants and to obtain more eco-friendly reduction of GO. Two recent reviews report the different approaches for a green reduction of GO.[51,52] To summarize the "graphene oxide way", Figure 2.11 reports the different step from graphite to rGO.

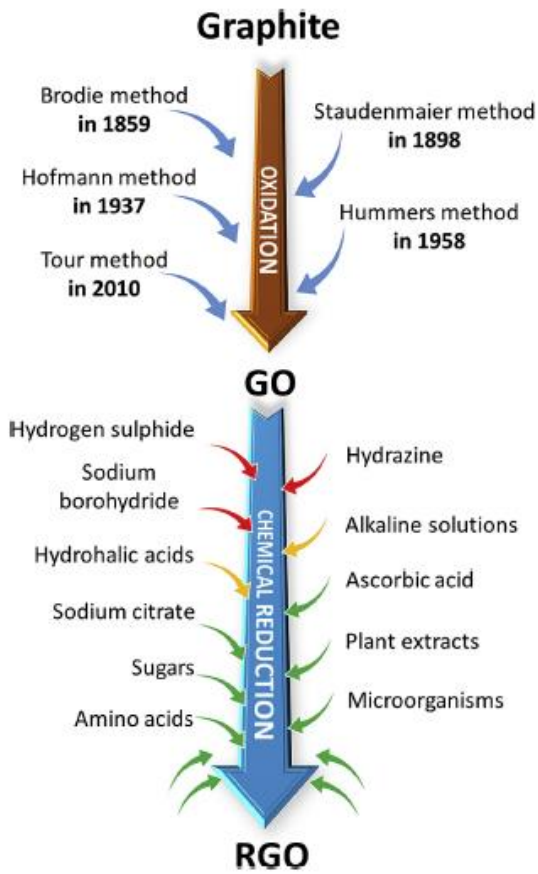

Figure 2. 11. Schematic illustration of the "graphene oxide way" starting from graphite to obtain GO and successively rGO. The arrows colours for the reduction step are in accordance with their sustainability (red: bad; yellow: medium; green: good).[51]

2.2.2.3. "Bottom-Up" approaches

This synthesis pathway starts from carbon precursors to produce *in-situ* the graphene. These approaches have generally a better control of the level and types of defects and can produce high-quality graphene with a good yield.

2.2.2.3.1. Chemical Vapor Deposition [22,29,30,43,53–55]

Chemical Vapor Deposition (CVD) is probably the most famous technique used for the "bottom-up" synthesis of graphene. The main factors are the type and thickness of the metal catalyst, hydrocarbon precursors, and the synthesis temperature.[56] The transition metal catalysts are usually copper, nickel or ruthenium.[57–61] The most used by far is copper because of its low solubility to carbon which allows to improve the control of the graphene growth.[53] Moreover, Ruoff and co-workers have demonstrated that the deposition of graphene on Cu is self-limited to a single layer.[57] The hydrocarbon precursor is usually methane (CH_4) due to its high energy activation for the adsorption and dehydrogenation on metal catalyst which delays these phenomena until the temperature reaches 1000°C.[62]

Gas precursors are adsorbed on the surface of a metal catalyst followed by a pyrolytic decomposition, which leads to the formation of adsorption sites promoting the growth of a continuous thin film as illustrated in Figure 2.12.[63]

The CVD technique has demonstrated high-scalability with the production of square meters of graphene on copper foils using a roll-to-roll setup. The 30-inch graphene-film is shown in Figure 2.13.[65] However, this technique is relatively expensive and this is an obstacle to its industrial application. In addition, the underlayer metal catalyst removal and the graphene transfer increase the total cost.

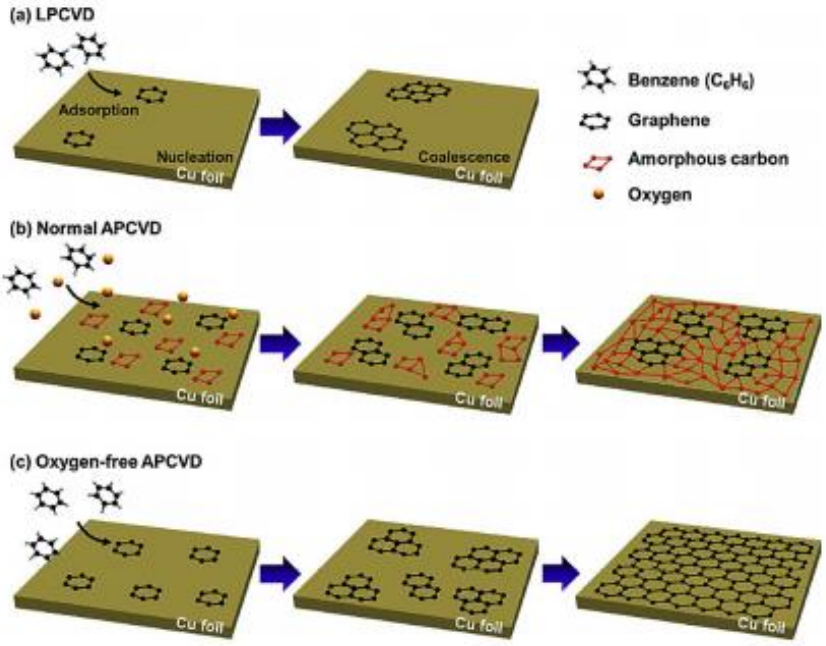

Figure 2. 12. Schematic representation of the growth of a single-layer of graphene using (a) Low-Pressure CVD, (b) Ambient-Pressure CVD, and (c) Oxygen-free Ambient-Pressure CVD.[64]

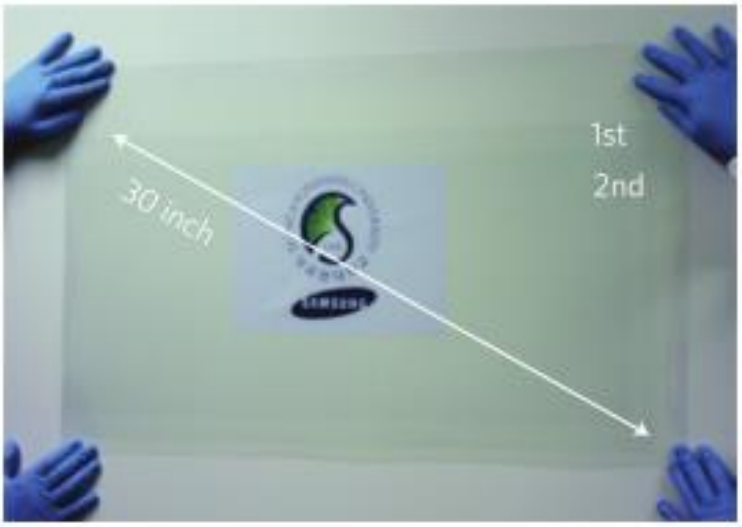

Figure 2. 13. 30-inch graphene film prepared using the CVD technique and roll-to-roll transfer.[65]

A first approach is to use different gas precursor to decrease the reaction temperature. Nandamuri *et al.* investigated the use of acetylene as precursor and decrease significantly the

temperature reaction.[66] Other approaches are focused on the reaction condition. Yuan and Wang developed a Plasma Enhanced Chemical Vapor Deposition (PECVD) which allows to decrease the reaction temperature due to the production of gaseous radicals, acting as precursors.[67,68]

Others developments were investigated such as Microwave-Plasma-Enhanced-CVD (MWPECVD)[69] and Radio-Frequency-CVD (RF-CVD)[70],but they struggle in comparison with the Ambient Pressure CVD. Indeed, this method is relatively low-cost and, more importantly, scalable. Reina *et al.* have demonstrated this feasibility with a graphene film with a size of about 1 cm^2 on Ni substrate.[71] An improved APCVD was studied by Jang and co-workers. They started from benzene as precursor which allows to reduce reaction temperature between 100 and 300°C. Moreover, by removing oxygen using repeated pumping and purging steps (Oxygen-Free APCVD), they increased the quality of the produced single layer graphene.[64]

2.2.2.3.2. Epitaxial growth[22,29,43]

This technique is based on Silicon Carbide (SiC) wafers which are widely employed in high-power electronics. By annealing at high temperature and under vacuum the wafer, a graphitization of the support occurs due to the sublimation of Si.[72] Indeed, the sublimation rate of Si is higher than C.[73,74] Consequently, the carbon remains and rearranges itself to create graphitic layers. These polycrystalline layers were initially randomly oriented.[75,76]

However, thanks to Otha and co-workers, it is now possible to control the number of layers deposited.[77] The deposition can take place either on Si or C faces.[78] Deng and co-workers investigated the use of commercially available polycrystalline SiC granules. After the annealing process, they obtained freestanding single-layer of graphene.[79]

This technique allows the production of high-quality graphene with a crystallite size of about 100 µm.[80]

Nevertheless, its application is not compatible for large scale production in some sector such as electronics due to the high cost of the wafer and the operating conditions.

2.2.2.4. Global perspective for graphene production

The first isolation of a single layer of carbon with tremendous properties has attracted a worldwide attention. Many countries have invested huge amount of money in the research and upgraded the research centre to dispose of the state-of-the-art technologies.[81] The Figure 2.14 reports the substantial investments in the main countries. Interestingly, some of them have already invested before that Geim and Novoselov received the Nobel prize in Physics.

Even if the "killer application" of graphene has not been found to date, many enterprises are born to produce large-area graphene films and to improve the actual production technique.[82]

Interestingly, this "gold Rush" induces a significant decrease of the graphene price. Geim estimated the price around 1000$/cm² in 2008.[5] In 2014, 2D Carbon Tech produced a graphene film with a dimension of 10x10cm² at the price of ¥1000 (≈ 150$). It corresponds to a decrease of almost 700 times the price in only 6 years. However, the price is still not competitive in comparison with ITO conductive film, which is about 300-450 ¥/m². Hopefully, a breakthrough achievement will arrive to decrease dramatically the price of graphene and make possible its large-scale application.

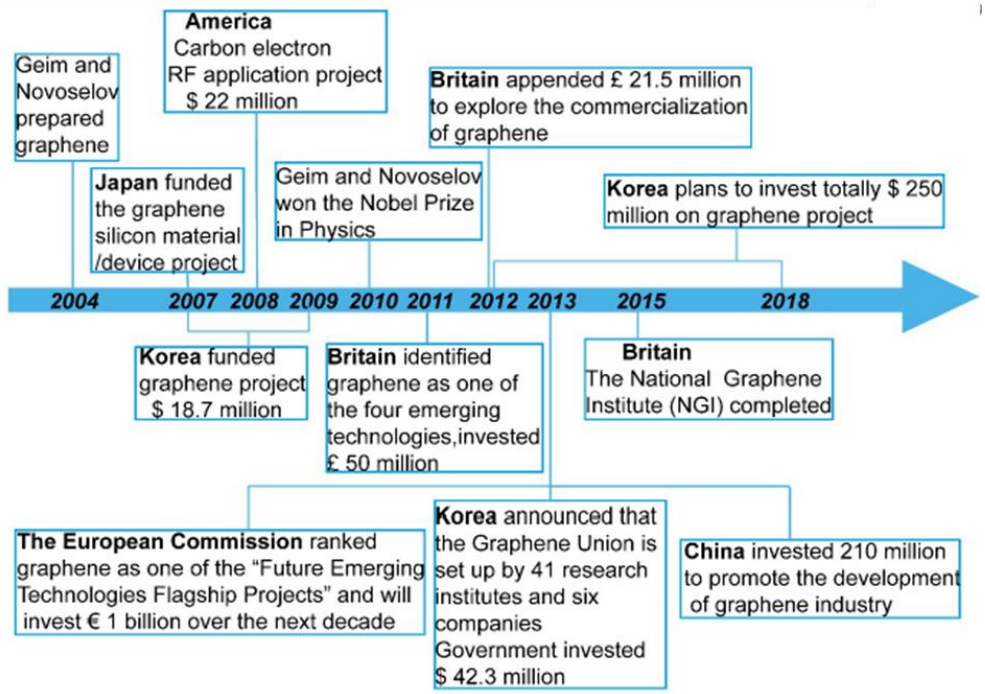

Figure 2. 14. Worldwide investment in the field of graphene since its first isolation in 2004.[55]

2.3. Graphene-based Supercapacitors

Since its first isolation in 2004, Graphene has attracted attention for electrochemical energy storage applications due to its high specific surface area, high conductivity, flexibility, and outstanding mechanical properties. Several reviews have been focused on the presentation of graphene-based materials for supercapacitors applications.[83–94]

However, the comparison of performance between materials become rapidly difficult due to diverse factors such as: specific capacitance expressed in function of the weight, the area or the volume of electrode; supercapacitors tested in a symmetric or asymmetric configuration; electrolyte used can be gel, aqueous, organic, and/or ionic liquids; measurements performed in a two- or three-electrodes cell.

Therefore, in the following sections, research works will be presented for symmetric supercapacitors in two-electrode cell configuration. Finally, the specific capacitance, expressed in F/g, are compared.

2.3.1. Electrochemical Double Layer Capacitors

Two research groups have pioneered the development of pure EDLC with graphene as active materials. Groups were leaded by Rao[95] and Ruoff[96]. In 2008, both published independent research works. The first reports the preparation of graphene by three different approaches: (1) thermal exfoliation of graphitic oxide, (2) by heating a nanodiamond at 1650°C in inert atmosphere, and (3) thermal decomposition of camphor on Ni particles. The thermally-rGO demonstrated the best performance with 117 F/g in 1M H_2SO_4 and 75 F/g using an organic electrolyte. These performances are significantly higher than Single-Walled Carbon Nanotubes (SWCNT) and Multi-Walled Carbon Nanotubes (MWCNT) with 60 and 14 F/g in the same condition, respectively.[95] Ruoff's research group has reported the chemical reduction of GO suspension using hydrazine. A TEM image of the obtained graphene is shown in Figure 2.15 with a schematic representation of the typically cell used for the electrochemical measurement. At a same scan rate of the Rao's research work but in basic condition (5.5M KOH), a specific capacitance of 102 F/g was measured while the maximum value was obtained by charge/discharge measurement with 135 F/g at 10 mA/g. Using an ionic liquid as electrolyte, TEA BF_4, a specific capacitance of 99 F/g is measured both using CV at 20 mV/s and charge/discharge at 10 mA/g.[96]

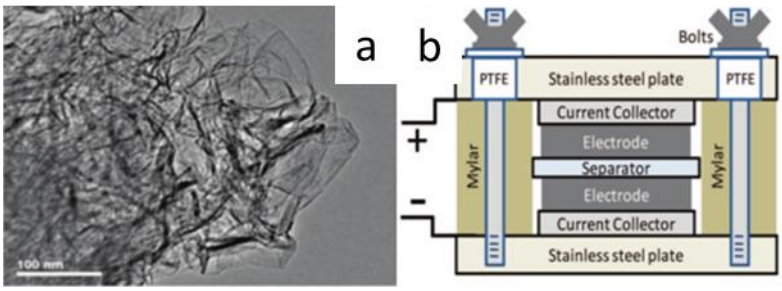

Figure 2. 15. (a) TEM image of the chemically-reduced graphene oxide using hydrazine as reducing agent, and (b) schematic representation of a typical two-electrode cell configuration.[96]

The next year, Wang and co-workers published the solid-gas reduction of GO using hydrazine. After 3 days of reduction, a more suitable reduction was obtained leading to higher specific capacitance with 205 F/g at 100 mA/g.[97] Lv and collaborators demonstrated the production of rGO in low-temperature (200°) and high-vacuum condition material synthesized using this more suitable and safer way shows a specific capacitance of 279 F/g at 10 mV/s.[98]

Since these pioneering researches, many approaches were investigated to further improve the performance of supercapacitors alongside to the doping of graphene or the fabrication of composite. These research topics are presented in the following sections.

2.3.1.1. Thermal reduction of GO

In 2010, Ruoff's research group developed a new approach for the reduction of GO and its use as electrodes in supercapacitor applications. The first way is a thermal treatment in an oil bath at 150°C for 12h allows the reduction of GO dispersed in polycarbonate. After a filtration, the material was tested and shown 127 F/g at 5 mV/s.[99]

Lei and co-workers considered a new approach with the use of a mesoporous carbon spheres-GO dispersion as template for the grown of 3D rGO structure. Unfortunately, this approach displayed only 40 F/g at 10 mA/g.[100] Mishra and Ramaprabhu reported a thermal exfoliation of GO under hydrogen atmosphere leading to a moderate supercapacitive behaviour with 80 F/g at 10 mV/s. To further increase the performance, they used HNO_3 to reintroduce carbon-oxygen functionalities which enhance the performance, with 125 F/g at the same scan rate. This "functionalized-graphene" was used as support for the synthesis of graphene-metal oxides composites that will be presented in the section 2.3.2.2.[101]

Zhi's research group reported a fast-thermal reduction of GO followed by an annealing step. The controlled reduction allows to maintain several carbon-oxygen functionalities

which add pseudocapacitive contributions to EDL capacitance, thus leading to a higher specific capacitance. The measured value was 417 F/g at 5 mA/g in 6M KOH electrolyte.[102] Ye *et al.* studied a fast thermal expansion/reduction of GO in an incubator at 200° for 10 minutes. The obtained performance was promising with 315 F/g at 100 mA/g in 1M KOH electrolyte.[103]

Yoon and collaborators studied the production of non-stacked GO assembly before the thermal reduction. They first precipitated GO using cold hexane, which is a non-polar aprotic anti-solvent for the hydrophilic GO. Therefore, a non-stacked structure is obtained due to the hydrogen bonding between the oxygen moieties onto GO. After the evaporation of hexane, crumped flakes are dried using a typical thermal treatment. The resulting rGO porous framework has a high specific surface area (1435.4 m^2/g) and high pore volume (4.11 cm^3/g) crucial for supercapacitor applications. 240 F/g were measured at 2 A/g in 6M KOH electrolyte.[104] Jang's research group had also investigated the formation of crumped graphene. They used an aerosol precursor to atomize GO followed by an evaporation triggering a self-assembly procedure. After the thermal reduction, crumpled graphene shows lower specific capacitance with 156 F/g at 100 mA/g in 5M KOH electrolyte.[105]

Ervin and collaborators reported the use of GO as ink for inkjet printing. Interestingly, the deposition can be realized without binder until considerable thickness. After the thermal reduction, 192 F/g was measure using CV at a scan rate of 20 mV/s in acidic condition (1M H_2SO_4).[106] A freestanding 3D structure of mesoporous partially reduced GO was realized by Li *et al.*. They activated/reduced GO produced by means of the Hummers method using CO in a horizontal quartz tube reactor. The performance was significantly improved with 291 F/g at 1 A/g using an ionic liquid as electrolyte.[107] In another work, Lu and colleagues investigated a vacuum-assisted thermal exfoliation-

reduction of GO. The rGO produced by this industrial-compatible approach has suitable performance in ionic liquid as electrolyte with 284 F/g at 1 A/g.[108]

Tamilarasan and Ramaprabhu used graphene produced by thermal reduction of GO to fabricate an all-solid-state supercapacitor. They synthesized a robust electrolyte using PAN/[BMIM][TFSI]. Specific capacitance calculated from CV curves at 10 mV/s was 127 F/g.[109] Sun *et al.* produced graphene oxide paper. After a thermal shock, porous graphene paper was obtained. In 1M H_2SO_4, a specific capacitance of 100 F/g at 100 mV/s was obtained.[110]

Wang and collaborators reported the carbonization of freeze-dried coagulated GO/polyethyleneimine solution to obtain a macroporous graphene network. This as-prepared active material showed a specific capacitance of 160 F/g at 100 mA/g in 6M KOH.[111] Pachfule *et al.* investigated the use of MOF-74 as a template. The MOF structure was first grown at room temperature. Then, a pyrolysis was carried out to obtain carbon nanorods. Finally, carbon nanostructures were exfoliated and thermally activated using KOH to obtain graphene nanoribbons. The schematic representation of the synthesis pathway is reported in Figure 2.16. The electrochemical characterization performed using 1M H_2SO_4 as electrolyte displayed interesting performance with 193 F/g and 198 F/g from CV and charge-discharge measurements, respectively.[112]

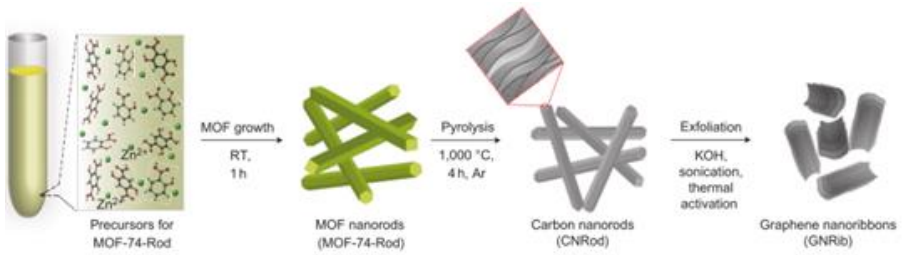

Figure 2. 16.schematic representation of the synthesis pathway from MOF to graphene nanoribbons.[112]

As reported previously, KOH activation is usually used to improve the electrochemical performance. Chen's research

group reported the KOH activation of thermally-reduced GO in a PVA-crosslinked membrane. Interestingly, they used GO-doped ion gel membrane as gel electrolyte to fabricate an all-solid-state supercapacitor. The performance was promising with 190 F/g at 1 A/g.[113] Huang *et al.* used an electrochemically exfoliated graphene mixed with cellulose to form a 3D framework. Then, a thermal process with KOH was carried out resulting in the formation of a micro- and mesoporous activated carbon covering graphene flakes. This particular structure demonstrated suitable performance with 300 F/g at 5 mV/s.[114] Wang's research group studied the controlled orientation of GO using sodium alginate forming 'salt bridge'. GO-sodium alginate mixture was then carbonized and activated using KOH. An outstanding performance was measured at 10 A/g with 240 F/g in aqueous electrolyte.[115] Abdelkader and collaborators investigated another way to activate graphene-based material. They reported an electrochemical activation at low temperature in molten salts. The 3D-graphene structure shown good electrochemical behaviour with 275 F/g at 100 mA/g in basic aqueous electrolyte.[116]

Kraner's research group partially reduced GO dispersion using a thermal process. The obtained rGO microgel was filtered under vacuum to form a membrane followed by a freezing in liquid nitrogen to form ice crystals. These ice crystals were removed, avoiding the collapse of the structure, by sublimation at low temperature and low pressure. The resulting structure was further thermally reduced prior to be used as electrode for supercapacitor applications. The synthesis procedure is reported in Figure 2.17. In acidic aqueous solution, the as-synthesized sample showed suitable performance with 284 F/g at 1 A/g.[117]

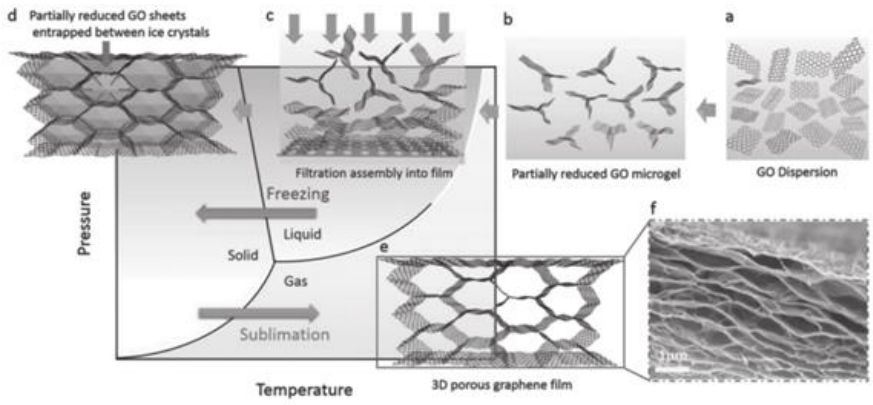

Figure 2. 17. Schematic representation of the mechanism to produce 3D porous microstructure[117]

Jha *et al.* reported the use of focused solar light for a concomitant reduction and exfoliation of GO. Indeed, the focused radiation has a power of 5.4 W and induce an increase of the temperature up to 204°C. Charge-discharge measurements showed good electrochemical behaviour with 266 F/g at 1 A/g in 6M KOH as electrolyte.[118]

2.3.1.2. Microwave reduction of GO

Ruoff and collaborators used a commercial microwave oven to both reduce and exfoliate GO within 1 minute. Interestingly, this fast way is suitable for electrode manufacturing with 191 F/g measured at 150 mA/g in 5M KOH electrolyte.[119] The same group later investigated a microwave-assisted exfoliation of GO followed by an activation of the rGO in concentrated KOH.[120] This procedure is typically used for the activation of carbon material.[121] The activated-rGO showed good electrochemical behaviour with 165 F/g at 1.4 A/g and 173 F/g at 2.1 A/g using BMIM BF_4[120] or EMIM TFSI[122] as electrolyte, respectively.

The same research group reported a similar approach to fabricate compressible electrode allowing a higher density and small pore size leading to performance enhancement. The compressed electrode showed suitable electrochemical behaviour with 158 F/g at 1.22 A/g in BMIM BF_4.[123] Simon and collaborators investigated the stability of a microwave-

assisted exfoliated rGO sample in ionic liquid in a temperature window from -50° to 80°. Sample demonstrated outstanding performance in the whole range of temperature. At room temperature, 130 F/g at 1 mV/s was measured using $(PIP_{13}\text{-}FSI)_{0.5}(PYR_{14}\text{-}FSI)_{0.5}$ as electrolyte.[124]

Shulga *et al.* studied the use of microwave-assisted exfoliated rGO as active material for supercapacitor application. They performed the electrochemical analysis using 1M H_2SO_4 as electrolyte using a GO membrane as separator. Measured specific capacitance was 280 F/g at 1 A/g.[125] Subramanya and Bhat reported a one-pot green approach for the exfoliation of graphite using a W-based catalyst before the microwave reduction of epoxidized-graphite and the catalyst regeneration. The measured specific capacitance was 219 F/g at 1 A/g in EMIM BF_4.[126]

2.3.1.3. Hydrothermal reduction of GO

Liu *et al*. described a hydrothermal reduction of GO produced by means of the Hummers method using hydrazine as reducing agent. EDLC displayed a better energy density even at high current density with 154 F/g at 1 A/g using an ionic liquid as electrolyte (EMIM BF_4).[127]

A self-assembly procedure was studied by Shi and colleagues through a one-pot hydrothermal reduction of GO. Briefly, they dispersed the hydrophilic GO in water at different concentration and placed the suspension in a Teflon reactor contained in a stainless-steel autoclave. Reactor was heated at 180°C, varying reaction time. As shown in Figure 2.18, the resulting rGO-based hydrogel structure is strictly correlated to the concentration of the GO dispersion and the reaction time. The more suitable parameters are 2 mg/mL of GO for a hydrothermal reduction during 12 hours at 180°C. These parameters lead to a specific capacitance of 175 F/g at 10 mV/s. Moreover, the rate capability was demonstrated with a calculated value of 160 F/g at 1 A/g measured by charge/discharge.[128]

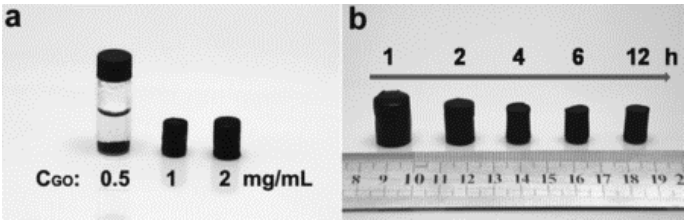

Figure 2. 18. Resulting hydrogels prepared (a) with different concentrations or (b) different reaction time[128]

Alshareef's research group investigated the effect of pH adjustment after the hydrothermal synthesis. Electrochemical performance was superior for the rGO adjusted to a neutral pH with 230 F/g at 1 A/g. The characterization was carried out using 6.9M KOH as electrolyte.[129] Gao *et al.* used wet-spun GO to fabricate oriented graphene hydrogel films using hydrothermal synthesis. Measurement in acid condition shows high specific capacitance with 208 F/g at 200 mA/g.[130] Pirri's research group used the suitable interaction between copper and graphene to develop a flexible supercapacitor by self-assembly. Clean copper wires were placed in the autoclave with the GO dispersion before the hydrothermal reaction. During the reaction, rGO flakes tend to wind around the copper wire with suitable adhesion for flexible supercapacitors. The gravimetric performance using PVP/NaI as gel electrolyte is low with 62.5 F/g at 5 mV/s due to a collapsed porous framework. However, devices demonstrated high flexibility and stability, under working conditions.[131]

Significant decrease of the supercapacitive performance were observed at high discharge rate by Shi and colleagues. This phenomenon is due to a huge number of residuals carbon-oxygen moieties onto the rGO flakes. To overcome this issue, they investigated the further chemical reduction of the self-assembled using hydroiodic acid (HI) or hydrazine as reducing agent. A noteworthy enhancement of the performance was observed with 187 F/g and 220 F/g at 1 A/g for HI and hydrazine, respectively.[132] Kim *et al.* used the

hydrothermal reduction assisted with hydrazine to produce extremely durable and flexible supercapacitors operating at high temperature (>100°C). They doped H_3PO_4 electrolyte with PBI (2,20-m-phenylene-5,50-bibenzimidazole) to improve the ion transport. At 160°C, a gravimetric capacitance of 170 F/g was measured at 1 A/g. Moreover, a stability up to 100,000 cycles with a retention of 92% was demonstrated.[133]

Chong and collaborators synthesized rGO using the same *modus operandi* of the previous work. However, they further functionalized rGO using aminopyrene through π-π interaction. This non-covalent functionalization induces electron transfer from the amine group of aminopyrene (electron donating group) and graphene (electron acceptor). In 6M KOH, rGO-functionalized shown good performance with 160 F/g at 5mV/s.[134] Park *et al*. described the functionalization of GO with Nafion® (perfluorinated resin) followed by the complementary reduction using hydrazine. The rGO produced was then used as electrodes in all-solid-state flexible supercapacitors showing suitable performance with 118 F/g at 1 A/g.[135]

Zhao *et al.* introduced the use of urea as reducing agent for the hydrothermal synthesis of rGO. Urea is a good candidate for environmental friendly reducing agent due to the absence of toxicity or safety concerns. As synthesized rGO showed suitable performance with 226 F/g at 100 mA/g in 6M KOH.[136] Another green alternative for the production of rGO was proposed by Balkus Jr.'s research group. They developed an alkaline hydrothermal deoxygenation using concentrated KOH solution. Measured gravimetric capacitance was 145 F/g at 1 A/g using LiTFSI as electrolyte.[137]

Duan *et al.* investigated the use of L-ascorbic acid, the Vitamin C, as reducing agent for the hydrothermal synthesis of rGO hydrogel. They reported a specific capacitance of 186 F/g at 1 A/g using PVA/H_2SO_4 as gel electrolyte.[138] Du and co-workers studied the reduction of GO deposited on Ni foam

using the same reactant. Obtained results were nevertheless lower with 152 F/g at 1 A/g in basic aqueous electrolyte.[139] An *et al.* reported the hydrothermal reduction of GO suspension using L-ascorbic acid. To further improve the electrochemical performance, they non-covalently functionalized rGO hydrogel using alizarin, which is a multi-electron redox centre derived from anthraquinone. Measured gravimetric capacitance was 285 F/g at 1 A/g in acidic aqueous electrolyte.[140] Another approach was investigated by Duan's research group. They reduced GO by hydrothermal synthesis in presence of H_2O_2. After the natural cooling down to room temperature, a post-treatment to further reduce the holey graphene framework by hydrothermal reaction in 1M sodium ascorbate at 100°C for 2 hours. High specific capacitance measured in 6M KOH was 310 F/g at 1 A/g.[141] Bo *et al.* reported the use of a green reducing agent for the reduction of GO by hydrothermal synthesis. Indeed, they used caffeic acid, which is an organic compound containing both acrylic and phenolic moieties. The resulting hydrogel showed modest electrochemical performance with 136 F/g at 1 A/g in neutral electrolyte (1M KCl).[142]

Feng *et al.* studied the hydrothermal reduction of GO using ammonia and hydrazine as reducing agent. The as-synthesized rGO flakes were then filtered through a membrane to form a continuous film. This active layer was carefully putted in contact with the current collector using vertically oriented graphene flakes produced by means of a PECVD technique. Electrochemical performance was measured in 6M KOH and a gravimetric capacitance of 186 F/g was calculated from charge-discharge curve at 10 mV/s.[143] Li's research group fabricated a binder-free freestanding 3D hydrogel by filling the as-prepared rGO hydrogel with an aqueous NaI solution. A specific capacitance of 169 F/g at 1.5 A/g was measured using a basic electrolyte.[144]

Duan's research group reported the concomitant reduction and functionalization of GO using hydroquinone during the hydrothermal synthesis. The 3D-porous framework demonstrated superior electrochemical performance with 441 F/g at 1 A/g in 1M H_2SO_4.[145] Zhang *et al.* investigated the hydrothermal synthesis of concentrated GO gel onto PTFE tapes. The as-prepared rGO@PTFE was then freeze-dried to obtain a rGO-based aerogel. The active material was peeled off to be tested in a two-cell supercapacitor configuration using PVA/H_2SO_4 as gel electrolyte. A gravimetric capacitance of 282 F/g was measured at 500 mA/g.[146] Fan *et al.* studied the dispersion of mesoporous carbon with GO before the hydrothermal process in autoclave. The as-prepared hydrogel was then freeze-dried to obtain aerogel. Using PVA/KOH as gel electrolyte, good performance was observed with 272 F/g at 100 mA/g.[147] Figueiredo *et al.* synthesized carbon xerogel by hydrothermal reduction of a mixture of glucose and GO. The resulting hydrogel was thoroughly washed and dried under ambient conditions. The resulting xerogel was activated using concentrated KOH. Performance was evaluated using acidic electrolyte. Gravimetric capacitance of 223 F/g was calculated from charge-discharge curve at 100 mA/g.[148]

2.3.1.4. Graphene production by exfoliation

An and colleagues smartly transformed an apparent drawback of graphitic material to an advantage. Indeed, it is well-known that graphite and graphene are hydrophobic and cannot be properly dispersed in water. However, using a non-covalent functionalization of the upper layer of the graphitic structure with PCA (1-pyrenecarboxylic acid), it is possible to obtain a graphene dispersion *via* π-stacking mechanism. A schematic representation of this intercalation-functionalisation-exfoliation is shown in Figure 2.19. As-exfoliated graphene displayed promising performance with 120 F/g at 2 A/g in 6M KOH electrolyte.[149]

A similar approach was investigated by Talapatra *et al.* to produce thin EDLC. Using the same electrolyte, they measured a gravimetric capacitance of 202 F/g at 10 mV/s.[150] Müllen's research group reported the exfoliation of graphite in aqueous solution of inorganic salts. In only 3-5 minutes, applying a direct current voltage of +10 V, oxidation of graphite flakes occurs with ions intercalation between flakes. An expansion of graphite occurs, and flakes start to detach from each other leading to an exfoliate graphene solution. After a careful washing of the electrochemically exfoliated graphene flakes, they are re-dispersed in DMF to further be coated onto a flexible support using a paintbrush. Specific capacitance of 57 F/g using a gel electrolyte (PVA/H_2SO_4) was measured by CV curves at a scan rate of 10 mV/s.[41]

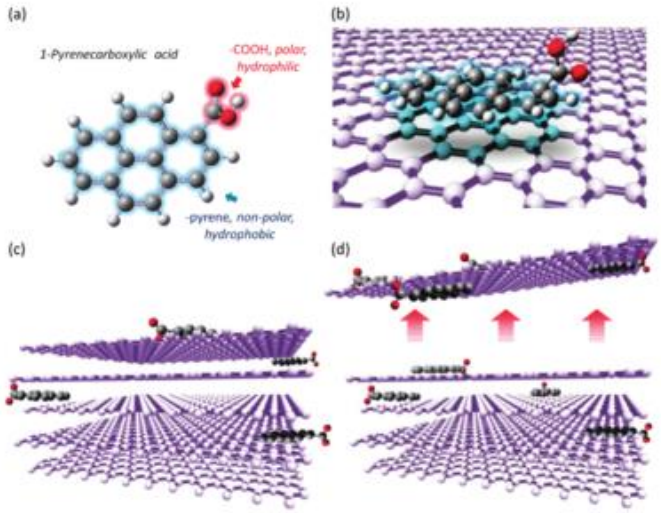

Figure 2. 19. Schematic representation of the exfoliation mechanism using PCA[149]

The same group later investigated the use of anti-oxidant to reduce the defect formation during the electrochemical exfoliation. A major efficiency was obtained using TEMPO ((2,2,6,6-tetramethylpiperidin-1-yl)oxyl) as anti-oxidant. However, a lower specific capacitance was obtained with 22 F/g at 2 mV/s using the same electrolyte as previously reported.[151]

Kong *et al.* studied the use of acidic and basic solution to minimize the graphene oxidation during the electrochemical exfoliation. They used a two-electrode configuration using graphite rods both as cathode and anode. Applying alternatively ±1 V, exfoliation process occurs quickly. Using charge-discharge measurement at a current density of 1 A/g in acidic condition, a gravimetric capacitance of 325 F/g was obtained.[152] Tascón *et al.* developed a straightforward method for the electrochemical exfoliation of graphite to produce graphene using halide-based aqueous electrolyte. They measured good electrochemical performance using acidic electrolyte with 50 F/g at 100 mA/g.[153] Dryfe *et al.* reported a one-step simultaneous electrochemical exfoliation and functionalization of graphene. They exfoliated graphite rod by means of a chronoamperometry method applying – 4 V vs Ag during 2 hours in presence of 4-nitrobenzenediazonium tetrafluoroborate which induces a chemical functionalization. A gravimetric capacitance of 19 F/g was measured at 100 mV/s in basic electrolyte (6 M KOH).[154]

Hersam and collaborators reported the production of graphene by high shear mixing. They started from graphite dispersed in ethyl cellulose and ethanol. The high shear process occurs during 2 hours at 10,230 rpm in an ice water bath. After centrifugation steps and flocculation using NaCl solution, the as-exfoliated graphene was washed carefully and deposited by inkjet printing. Solid-state supercapacitor showed a specific capacitance of 64 F/g at 500 mA/g with PVA/H_3PO_4 as gel electrolyte.[155] Fray *et al.* intercalate Li^+ and H^+ using high temperature procedure. The as-obtained graphene sheets-nanoscrolls have suitable electrochemical performance of 213 F/g at 1 A/g using an ionic liquid as electrolyte (TEA BF_4).[156] Amiri *et al.* reported a microwave-assisted functionalization of graphite using $AlCl_3$ as Lewis acid followed by the addition of HCl. After an *in-situ* exfoliation, as-prepared graphene was tested as active

material. Gravimetric capacitance of 354 F/g at 5 mV/s was obtained using 6M KOH as electrolyte.[157]

2.3.1.5. Reduction using plasma

Qiu *et al.* investigated the simultaneous reduction and exfoliation of GO under a dielectric barrier discharge (DBD) plasma. The as-produced graphene sheets were tested in a two-cell configuration using 6M KOH as electrolyte. A specific capacitance of 290 F/g at 50 mA/g was measured.[158] Fan and co-workers produced graphene by means of a plasma-assisted procedure at room temperature. The best performance was obtained using CH_4 as gas during the plasma process. A gravimetric capacitance of 192 F/g at 1 A/g was measured using basic electrolyte.[159] Bo *et al.* investigated an instantaneous reduction of GO paper using a positive-column cathode. The possible reduction mechanism and the experimental setup are schematically represented in Figure 2.20. Reduction occurs due to a synergy between high-density energetic electrons and surface touch direct heating. Using an ionic liquid as electrolyte (TEA BF_4), a specific capacitance of 162 F/g was measured at 1 A/g.[160]

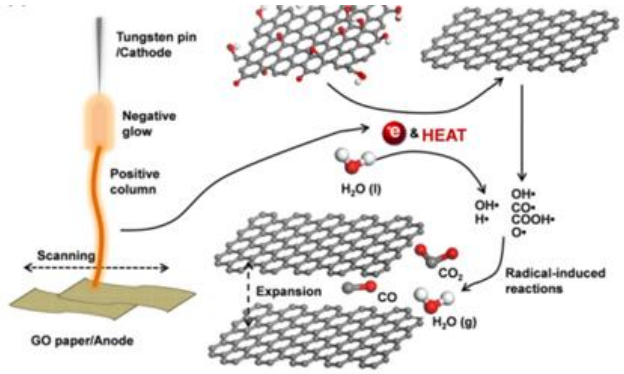

Figure 2. 20. schematic representation of the apparatus used (left) and possible mechanism of the plasma-assisted reduction of GO (right).[160]

Ostrikov *et al.* reported a green approach starting from honeycomb to obtain graphene by means of a plasma technique. This sustainable elemental lifecycle synthesis allows to produce vertically oriented graphene sheets with

high electrochemical performance (240 F/g at 5 mV/s in neutral electrolyte).[161]

2.3.1.6. Graphene production using CVD

Chemical Vapor Deposition is a procedure typically used to produce high quality graphene. Chou *et al.* used this technique to produce laminated ultrathin graphene film using four different films. A SEM image illustrating the as-prepared laminated graphene films is shown in Figure 2.21. A specific capacitance of 17 F/g at 200 mV/s using PVA/H_2SO_4 as gel electrolyte.[162]

Qin *et al.* synthesized 3D-graphene continuous structure on nanoporous copper catalyst. The as-prepared graphene was used in a flexible solid-state supercapacitor with PVA/H_3PO_4. A gravimetric capacitance of 305 F/g was calculated from charge-discharge measurement at 100 mA/g.[163] Jang *et al.* reported the CVD-growth of uniform high-quality graphene on graphite paper. Then, the active material was used to fabricate a fully flexible, lightweight all-solid-state supercapacitor with high performance (260 F/g at 5 mV/s in acidic condition).[164]

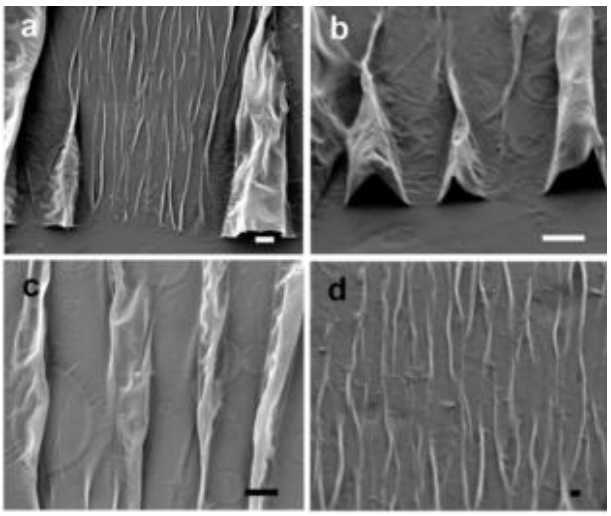

Figure 2. 21. SEM pictures of the laminate graphene produced by CVD[162]

Jung and co-workers produced graphene ball on Ni particles using CVD technique. Then, the Ni was removed by etching.

A schematic representation of the synthesis flowchart is shown in Figure 2.22. Graphene ball supported on GO flakes were assembled and tested in acidic condition. A specific capacitance of 170 F/g was measured at 500 mA/g.[165]

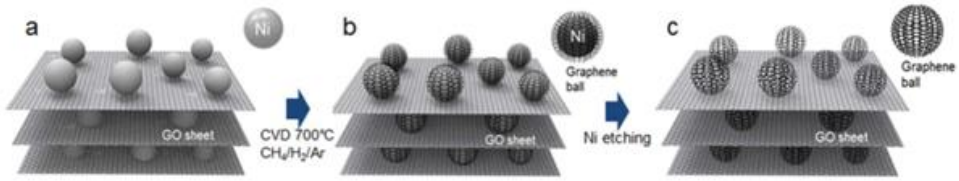

Figure 2. 22. schematic representation of the synthesis flowchart: (a) Ni-particles supported on GO flakes, (b) graphene synthesized by CVD on Ni particles, and (c) self-supported graphene ball after the etching of Ni.[165]

2.3.1.7. Others approaches for EDLC

Ajayan and co-workers investigated a different device geometry to avoid the only partial exploitation available specific surface area in the stacked configuration, which is typically used for electrochemical tests. In this research, they deposited multi-layer GO films using a layer-by-layer technique. GO flakes are oriented perpendicularly from the current collector as shown in Figure 2.23. Then, a classic chemical reduction was carried out using hydrazine. This configuration displayed high performance with 247 F/g at 110 mV/s using PVA/H_3PO_4 as gel electrolyte.[166]

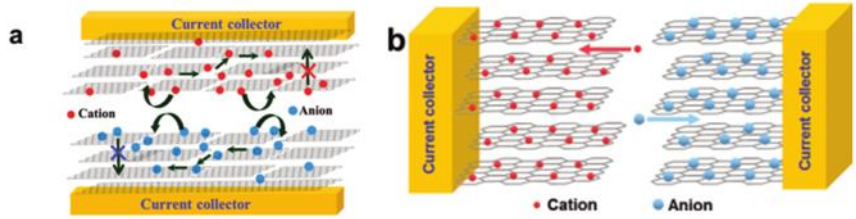

Figure 2. 23. Schematic representation of the (a) classic stacked configuration and (b) vertically oriented active material [166]

Zhang *et al.* studied a new deposition method to enhance the supercapacitive performance of the graphene-based supercapacitors. They reported a vacuum filtration deposition process to depose graphene on Ni-foam. A gravimetric capacitance of 152 F/g at 10 mV/s was measured using a basic aqueous electrolyte.[167] Then, Zhang and Pan investigated the reduction of GO using a pure hydrogen gas

environment. Using the same electrolyte, obtained performances are nevertheless lower with 110 F/g at 10 mV/s.[168] Qin and co-workers fabricated graphene using explosive reactions between alkaline earth elements (Mg and Ca) and CO_2 (from dry ice) as C precursor. Suitable electrochemical performance was measured by charge-discharge curve with 220 F/g at a current density of 100 mA/g in 6 M KOH.[169] Xue *et al.* reported a safer procedure to obtain flexible supercapacitor. They used a UV-lamp to photoreduce GO in desired positions to fabricate a rGO/GO composite. A specific capacitance of 140 F/g at 1 A/g was measured using PVA/H_3PO_4 as gel electrolyte.[170] The synthesis procedure and photoreduced GO-based architecture are reported in Figure 2.24.

Wang and collaborators studied a laser-induced reduction of GO to fabricate electrodes for supercapacitors. Interestingly, the reduction occurs simultaneously with the exfoliation leading to high specific capacitance (236 F/g at 250 mA/g in 6M KOH).[171] Yang and Bock, instead, investigated the reduction of GO dispersion using an excimer laser irradiation with a wavelength at 248 nm. However, this process seems to be less efficient with a measured specific capacitance of 130 F/g at 5 mV/s in neutral electrolyte.[172]

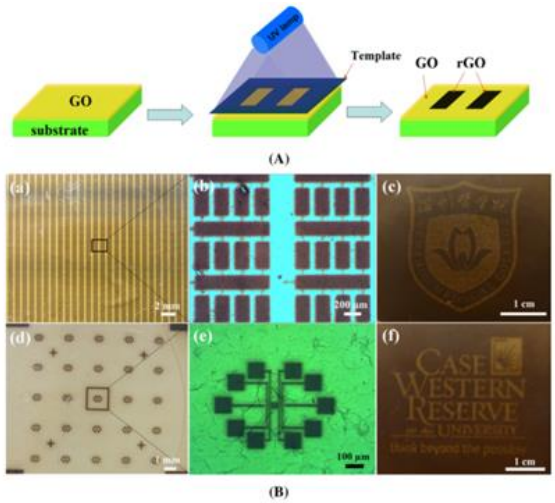

Figure 2. 24. Illustration of the photoreduction of GO in rGO and some patterned rGO electrodes[170]

Kaner and co-workers reduced freeze-dried GO using an ordinary camera flash. This lamp allows a photothermal reduction process of GO. Using an ionic liquid as electrolyte (TEA BF_4), a gravimetric capacitance of 64 F/g was measured at 1 A/g.[173] Xiang *et al.* reported a novel approach to reduce efficiently GO. They used a far-infrared (FIR) thermal reduction to fabricate electrode for supercapacitor applications. High specific capacitance was obtained with 320 F/g at 200 mA/g in basic aqueous electrolyte.[174]

Li *et al.* synthesized a GO/Graphene nanoribbon hybrid aerogel by a simple freeze-drying procedure. Then, a chemical reduction using gaseous hydrazine for 24 hours at 90°C was carried out. A gravimetric capacitance of 256 F/g at 2 mV/s was obtained using 2M KCl as neutral electrolyte.[175] Ye *et al.* investigated the *in-situ* chemical reduction of GO suspension using HI and CH_3COOH heated at 60°C for 1h. They fabricated foldable graphene paper. Specific capacitance of 90 F/g[176] and 87 F/g[177] were calculated from charge-discharge measurements at 1 A/g in 6M KOH electrolyte. Zhu and collaborators 3D-printed graphene-based aerogel. They dispersed silica powder and graphene nanoplatelets as sacrificial template and conductive additive, respectively. The 3D-printing procedure occurs in isooctane and allows to design periodic macropores. After gelation, supercritical drying, and carbonization, an etching in HF allows to remove the silica template. The synthesis flowchart is reported in Figure 2.25. A specific capacitance of 56 F/g was calculated by charge-discharge measurement at 100 mA/g in 3M KOH.[178]

Electrochemical exfoliation of graphite is often considered as an easy and fast approach to produce graphene as shown previously. However, it is important to underline that an electrochemical reduction of GO to rGO is feasible and probably easier to control in comparison with the exfoliation process. Zhong *et al.* reported the electrochemical reduction of GO suspension at 60°C applying a potential of -1 V vs Ag/AgCl electrode for 2 hours. Interestingly, this procedure

allows to depose directly the active material onto the current collector. In neutral electrolyte, a specific capacitance of 88 F/g was calculated from CV curve at a scan rate of 1 V/s.[179]

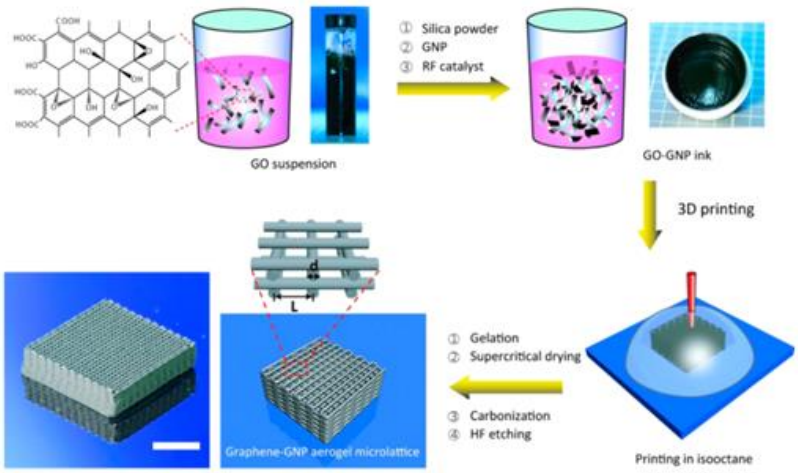

Figure 2. 25. Procedure pathways followed to 3D-printed supercapacitors[178]

Further improvement was shown by Dickerson and co-workers. They used the same electrochemical setup for the electrochemical reduction. By controlling the pH of the solution, electrodeposited/reduced GO demonstrated better performance with 165 F/g at 1 A/g in acidic aqueous electrolyte.[180]

As described previously, hydrothermal synthesis is one of the main procedure used to reduce GO suspension. However, a modification of the solvent composition may induce structural and/or performance variation. Lei *et al.* reported a solvothermal reduction of GO using a solvent composed by a mixture of water and ethylene glycol. This green synthesis followed by a freeze-drying step, allows to obtain holey graphene aerogel with good electrochemical properties. A gravimetric capacitance of 178 F/g at 200 mA/g was measured in 6M KOH.[181] Another approach was proposed by Pauzauskie *et al.* with the dispersion of GO in acetonitrile followed by an ultrasonic-assisted solvothermal reduction at low temperature (28-43°C) in presence of resorcinol, formaldehyde and HCl. The resulting wet rigid gel was further dried using supercritical CO_2 followed by a thermal

annealing. A specific capacitance of 62 F/g at 500 mA/g was measured in TEA BF_4 electrolyte.[182] Gao *et al.* reported a solvothermal reduction of GO/graphene nanosheets dispersion in DMF followed by a chemical reduction using hydrazine. The as-synthesized graphene nanoscrolls were tested in acidic aqueous electrolyte. A specific capacitance of 167 F/g was measured at 1 A/g.[183] Hao *et al.* investigated an ionothermal synthesis dissolving [BMIm][H_2PO_4] in GO dispersion to obtain a gel which will be transferred in an autoclave for reduction. After KOH activation, high specific capacitance was obtained with 313 F/g at 500 mA/g in 6M KOH electrolyte.[184]

2.3.1.8. Graphene-Carbonaceous composites

Graphene and reduced graphene oxide flakes are prone to restack due to the π→π interaction limiting the specific surface area and, consequently, the performance of the active material. To avoid this restacking, graphene-carbonaceous composites are considered. Indeed, the carbonaceous material such as carbon nanotubes, carbon black, activated carbon, etc. allows to reduce the restacking of graphene flakes. Moreover, it gives a contribution to the EDLC with their high specific surface area and conductivity.

2.3.1.8.1. Carbon Nanotubes

Yu and Dai used a cationic polymer [poly(ethyleneimine)] as stabilizer for the chemically-rGO assisted with hydrazine. The graphene dispersion positively charged was then mixed with negatively charged acid-treated MWCNTs resulting in a self-assembly procedure. Measured specific capacitance was 125 F/g at 10 mV/s in aqueous electrolyte.[185] Kim *et al.* reported the self-assembly of GO and MWCNT on a Ti substrate by drop-casting. Active materials were dispersed together by mixing. After the deposition, a thermal treatment followed by an annealing were carried out. In acidic condition, high specific capacitance were measured with 428 F/g at 500

mA/g.[186] A similar approach was investigated by Li and co-workers. Indeed, they prepared a sandwiched GO/MWCNT by filtration through a membrane after the mixing of both carbonaceous material. Then, the film was peeled-off the membrane and thermally treated to obtain rGO/MWCNT. A gravimetric capacitance of 250 F/g was measured at the same scan rate than the previous work but in basic aqueous electrolyte.[187] Silva's research group fabricated a rGO/MWCNT membrane by vacuum filtration. In this work, the GO was reduced chemically using hydrazine. After the drying, gold was sputtered on the edges to serve as current collector. Then, a scratch was manually created in the centre of the membrane to obtain a gap that separates physically the two electrodes. The in-plane supercapacitor showed suitable electrochemical performance in ionic liquid (EMI TFSI) with 154 F/g at 200 mA/g.[188] Huang *et al.* sonicated GO in presence of MWCNT until a homogeneous dispersion was obtained. Then, they add urea and performed a hydrothermal synthesis. The resulting N-doped rGO/MWCNT composite was tested in basic aqueous solution. A specific capacitance of 181 F/g was calculated from charge-discharge curve at a current density of 100 mA/g.[189]

Tamailarasan and Ramaprabhu thermally reduced GO and, in parallel, grew CNT by catalytic CVD. They, dispersed both carbonaceous material with BMIM TFSI (ionic liquid) in isopropanol containing 5% of Nafion®. Active materials were brush coated on stainless steel sheets (current collectors). SEM and TEM images of the nanocomposite are shown in Figure 2.26. The solid-like nanocomposite was tested using the same ionic liquid as electrolyte. A specific capacitance of 280 F/g was measured at 5 mV/s.[190]

Chen *et al.* reported the microwave-assisted reduction and exfoliation of GO prior to be mixed with SWCNT by probe sonication. In a stacked configuration with an acidic aqueous electrolyte, a specific capacitance of 306 F/g was obtain at a scan rate of 20 mV/s.[191]

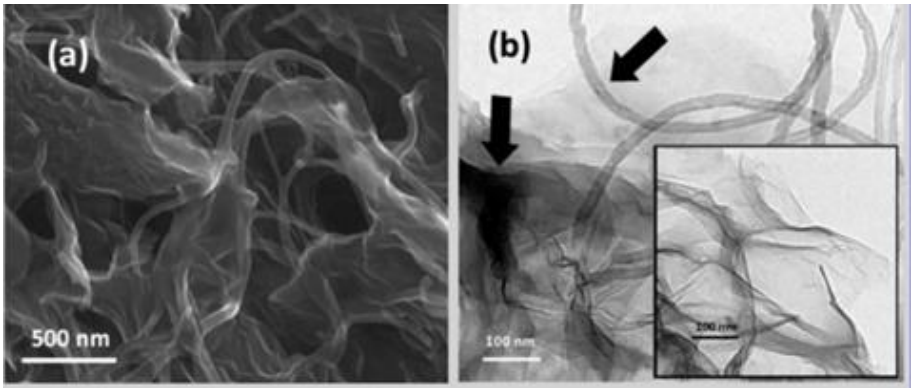

Figure 2. 26. (a) SEM and (b) TEM images of the rGO/MWCNT nanocomposite. Black arrows indicate CNTs.[190]

Derby *et al.* investigated the use of a rGO/MWCNT mixture solidified at low temperature. The active material was used to prepare a 3D-printable ink. After the deposition step, solvent was removed by sublimation resulting in a graphene-based aerogel containing MWCNT. In 1M H_2SO_4, a gravimetric capacitance of 305 F/g was obtained at 1 A/g.[192] Lee and co-workers used grafted-SWCNT by a cationic surfactant (CTAB: cetyltrimethylammonium bromide) for a self-assembly procedure using the Coulombic interaction with the negatively charged carbon-oxygen moieties onto GO flakes. The SWCNT-bridged graphene 3D-structure was electrochemically tested with EMIM BF_4 as electrolyte after a thermal activation. A specific capacitance of 199 F/g was calculated from charge-discharge curve at 500 mA/g.[193] Qin *et al.* hydrothermally reduced GO to obtain rGO hydrogel, and finally the rGO-based aerogel. However, they enhanced the performance by dispersing SWCNT with GO before the reduction step. Indeed, CNTs can be used as conductive spacer leading to higher electrochemical performance for the resulting aerogel. In basic aqueous electrolyte, they measured a gravimetric capacitance of 245 F/g at 2.5 A/g.[194] Ozkan *et al.* have grown simultaneously graphene sheets and CNTs by CVD. Interestingly, cohesive structure and robust contact between carbonaceous materials were obtained thanks to this concomitant synthesis. CNTs were vertically

oriented (pillar) on a graphene (floor) sheet. Outstanding specific capacitance was calculated from cyclic voltammetry at 10 mV/s in basic condition.[195] A similar approach was later investigated by Lee and collaborators. Indeed, they used a GO film containing 5 wt.% SWCNT. Then, they rolled the GO film to obtain a cylinder and they cut it to obtain thin film of vertically-aligned GO. Finally, a thermal reduction was carried out to obtain VArGO (Vertically Aligned reduced Graphene Oxide). A schematic representation of the ions diffusion through VArGO and a SEM image of the obtained structure are shown in Figure 2.27. In basic aqueous electrolyte, a gravimetric capacitance of 145 F/g was measured at 500 mA/g.[196]

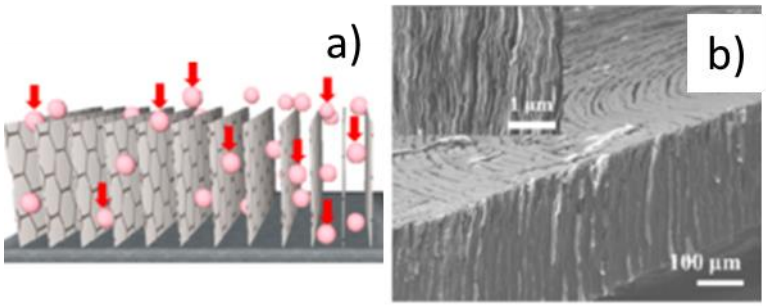

Figure 2. 27.(left) schematic representation of the ions diffusion through vertically aligned reduced graphene oxide film and (right) SEM image of the as-produced structure.[196]

Ostrikov *et al.* investigated the plasma-assisted production of vertically aligned graphene nanosheets starting from butter. Then, CNTs were growth on graphene sheets by a thermal CVD process. A specific capacitance of 278 F/g was calculated from CV at 10 mV/s in neutral electrolyte.[197] Li's research group reported a scalable and high yield production of exfoliated graphene by ultrasonication at room temperature under inert atmosphere. This solution was drop-casted onto a SWCNT-based buckypaper to be used as electrode. The electrolyte was PVA/H_2SO_4 containing exfoliated graphene and was coated on the electrode to fabricate all-solid-state supercapacitor. The electrochemical performance was nevertheless relatively low with only 50 F/g

at 1mV/s.[198] Yi *et al.* studied the deposition of microwave-assisted rGO on CNT layer coated onto a pre-strained substrate. This configuration allows to obtain a omnidirectionally stretchable supercapacitor with outstanding stability. A specific capacitance of 329 F/g was calculated from charge-discharge curve at 150 mA/g using PVA/H_3PO_4 as gel electrolyte.[199]

Chen and colleagues reported the synthesis of porous CNT-based network directly on crumpled graphene balls. This spatial configuration allows a better percolation of electrons through carbonaceous material in addition with a good mass transfer. A gravimetric capacitance of 165 F/g was obtained at 10 mV/s in 6M KOH.[200] Ozkan *et al.* grown simultaneously graphene and CNTs to obtain nanocomposite directly on Ni foam. Then, a thermal process was carried out on the sample before the electrochemical characterization in 6M KOH. A gravimetric capacitance of 270 F/g[201] and 275 F/g[202] was calculated from CV curves at 5 mV/s and 10mV/s, respectively. Chen's research group reported an *in-situ* synthesis of graphene-SWCNT nanocomposite by arc-discharge. This thermal procedure followed by KOH activation allows to fabricate supercapacitor with good properties such as 339 F/g at 1 mV/s in TEA BF_4.[203]

2.3.1.8.2. Carbon Black

Lian *et al.* first reported the use of carbon black as spacers to avoid the restacking of graphene flakes. GO was hydrothermally reduced using ammonia and hydrazine prior to be mixed with commercially available carbon black. After a mixing assisted by ultrasonication, the solution was filtered through a PVDF membrane and dried in air at 100°C. The electrochemical test was performed in 6M KOH. A specific capacitance of 138 F/g was calculated from CV curve at 10 mV/s.[204] A similar investigation was carried out by Wang *et al.* to fabricate flexible supercapacitors. After the hydrothermal reduction followed by the mixing with carbon

black, the nanocomposite was filtered and dried. Then, the film was peeled off and transferred to a PET substrate allowing flexibility. An all-solid-state supercapacitor using PVA/H_2SO_4 as gel electrolyte demonstrated interesting performance with 155 F/g at 100 mA/g.[205] Jia *et al.* dispersed carbon black with GO before the reduction process. In this work, a hydrazine-assisted solvothermal reaction, with DMF as solvent, was carried out to obtain the carbonaceous nanocomposite. A gravimetric capacitance of 130 F/g at 5 mV/s was measured in 1M H_2SO_4 electrolyte.[206]

2.3.1.8.3. Activated Carbon

Ma *et al.* reported the non-covalent functionalization of GO using PPD (p-phenylene diamine) prior to a solvothermal reduction in DMF. Then, a KOH activation was carried out before a carbonization step at 800°C for 1h under Ar. The resulting graphene-activated carbon nanocomposite was tested using an ionic liquid, EMIM BF_4, as electrolyte. The higher performance was obtained at 80°C with 180 F/g at 500 mA/g.[207] Pan and collaborators investigated the use of commercially available activated carbon to obtain high performance nanocomposite. Prior to mix it with GO, they activated newly the commercially available reactant with KOH. The nanocomposite rGO/AC was obtained by hydrothermal reduction of the GO/AC dispersion followed by a freeze-drying under vacuum. A specific capacitance of 205 F/g was calculated from charge-discharge curve at 2 A/g in 6M KOH.[208]

Jin *et al.* prepared activated carbon using waste particleboards as raw materials. After a carbonization step, a KOH activation was carried out. Then, carbonaceous material was mixed with GO and thermally reduced to obtain the nanocomposite. Electrochemical characterization in 7M KOH showed good performance with 265 F/g at 50 mA/g.[209] Zhao *et al.* reported a sustainable and green approach to fabricate graphene/N-doped activated carbon

nanocomposite. They produced activated carbon from corn straw and soy protein by carbonization followed by KOH activation in presence of GO flakes. The as-obtained nanocomposite demonstrated high electrochemical performance using 6M KOH as electrolyte. Indeed, specific capacitance of 299 F/g at 5 mV/s and 379 F/g at 50 mA/g was calculated from CV and charge-discharge curves, respectively.[210]

2.3.1.8.4. Mesoporous Carbon

Ogal *et al.* synthesized 3D-hexaporous nanocomposite using a catalyst-free approach. They first produced graphene-like sheets by inter-chain cyclization between maleic acid units from poly(4-styrene-sulfonic acid-co-maleic acid) sodium salt. After a pyrolysis step, units tend to assembly forming hexagonal pores leading to 3D-hexaporous nanocomposite. In acidic condition, a specific capacitance of 154 F/g was measured at 500 mA/g.[211] Zhao *et al.* grown mesoporous carbon by CVD using a sacrificial template. This positively charged carbonaceous material self-assembled with GO flakes (negatively charged). After a thermal reduction, 144 F/g was measured at 200 mA/g in EMIM BF_4 electrolyte.[212] Another self-assembly procedure was later reported by Zhao and colleagues. In this research, they used resols as carbon source, triblock co-polymer Pluronic® F-127 as soft template, and graphene aerogel as macroporous template. The graphene aerogel was produced by hydrothermal reduction of GO. The resulting nanocomposite contains interconnected macroporous graphene sheets linked to mesoporous carbon with a uniform pore size of 9.6 nm. After a carbonization step, electrochemical characterization using PVA/H_2SO_4 as gel electrolyte was carried out. Nevertheless, low specific capacitance was obtained with only 44 F/g in 5 mV/s.[213]

2.3.1.9. Graphene doping

The intentional introduction of heteroatoms to tailor the electrical properties of a semi-conductor is referred as doping. In this section, the doping with different heteroatoms will be presented.

2.3.1.9.1. N-doped Graphene

The doping using nitrogen as heteroatom is by far the most reported in literature for graphene-based supercapacitors. Kim *et al.* reported the N-doping of graphene by hydrothermal reduction of graphene oxide using hexamethylenetetramine. Three different type of doping was obtained with pyrrolic-N, pyridinic-N, and quaternary-N as shown in Figure 2.28. The electrochemical performance was evaluated in 6M KOH. A specific capacitance of 28 F/g was calculated from CV curve at 5 mV/s.[214]

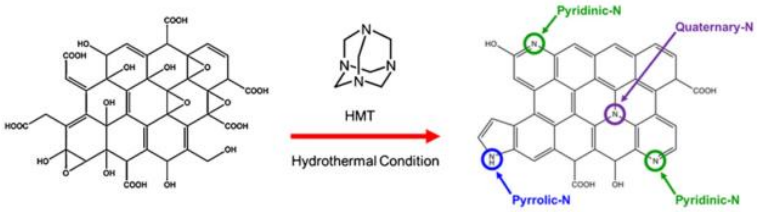

Figure 2. 28. N-doped reduced graphene oxide produced by hydrothermal synthesis using hexamethylenetetramine as doping agent.[214]

Chen *et al.* investigated the production of N-doping using the same doping agent. However, in this work, GO was spread on HMT. Then, the doping agent was burned. The exfoliation, reduction, and N-doping processes occur simultaneously using this procedure. Interestingly, the performance was enhanced with 205 F/g at 100 mA/g using the same electrolyte.[215] Several doping agents were studied for hydrogel production by means of hydrothermal reduction and are reported in Table 2.1.

Han's research group used ammonia as doping agent to obtain N-doped hydrogel. They further freeze-dried the as-synthesized material to obtain N-doped aerogel. In acidic aqueous electrolyte, a gravimetric capacitance of 223 F/g

was calculated from charge-discharge curve at 200 mA/g.[220] Guan *et al.* recently reported the fabrication of N-doped aerogel using a greener doping agent: urea. Before the hydrothermal synthesis, they dispersed iron (III) nitrate. The as-produced hydrogel was freeze-dried to obtain N-doped aerogel. Then, it was crushed and calcinated before removing iron oxide particles by HCl etching. Nevertheless, the specific capacitance was lower with only 48 F/g at 500 mA/g in neutral electrolyte.[221]

Doping Agent	Electrolyte	Specific Capacitance	Ref
Ethylenediamine	5M KOH	115 F/g @ 140 A/g	[216]
Ammonia	5M KOH	100 F/g @ 80 A/g	[216]
	6M KOH	230 F/g @ 330 mA/g	[217]
Ethylenetriamine	5M KOH	92 F/g @ 100 A/g	[216]
Tetraethylenepentamine	5M KOH	120 F/g @ 20 A/g	[216]
Propylamine	5M KOH	131 F/g @ 80 A/g	[216]
Butylamine	5M KOH	96 F/g @ 20 A/g	[216]
Ammonium carbonate	BMIM PF_6	163 F/g @ 1 A/g	[218]
1,4-butanediamine	6M KOH	269 F/g @ 300 mA/g	[219]

Table 2. 1. Electrochemical performance of N-doped graphene-based supercapacitors using different doping agent.

Kang *et al.* doped graphene with nitrogen from urea by means of a microwave-assisted hydrothermal reaction. Hydrazine was added to further reduce GO and enhance the electrochemical performance. A specific capacitance of 96 F/g was calculated from charge-discharge curve at 100 mA/g in 1M $LiPF_6$ electrolyte.[222] Li's research group investigated the solvothermal reduction of GO in ethanol using hydroxylamine as doping agent. The performance of the as-prepared hydrogel was evaluated in 6M KOH. A gravimetric capacitance of 205 F/g was measured at 1 mV/s.[223]

Lu *et al.* firstly reduced GO paper using gaseous hydrazine. Then, the self-standing film was thermally treated in concentrated ammonia environment to obtained N-doped rGO film. A solid-state supercapacitor was fabricated using PVA/H_2SO_4 as gel electrolyte. A specific capacitance of 55 F/g

was calculated from CV curve at 5 mV/s.[224] Gomez *et al.* investigated the graphene doping using 2-aminoterephtalic acid. They started by dispersing GO and the doping agent in water. After removing the water at low temperature, a thermal treatment in a ceramic quartz boat at 750°C for 60 minutes under inert atmosphere was carried out to obtain N-doped rGO. Specific capacitance, in 0.5M H_2SO_4 electrolyte, was evaluated from both CV and charge discharge curves. Obtained values are 323 F/g at 20 mV/s and 286 F/g at 200 mA/g, respectively.[225]

Zhang *et al.* polymerized polydopamine on montmorillonite, which is used as sacrificial template. After a carbonization step, crumpled N-doped graphene was obtained and tested in EMIM BF_4 electrolyte. A specific capacitance of 128 F/g was calculated from charge-discharge curve at 1 A/g.[226] Wang and co-workers reported a modified-molten salts method to produce N-doped reduced graphene oxide. This method allows to prevent restacking together with the activation of graphene using KNO_3. The electrochemical performance was evaluated using EMIM BF_4 as electrolyte. The best performance was 130 F/g at a current density of 1 A/g.[227]

2.3.1.9.2. B, S, or P doping

Sun *et al.* reported the synthesis of B-doped graphene. They mixed GO with boric acid prior using a DBD plasma with hydrogen as the working gas. The electrochemical performance was interesting with 446 F/g at 500 mA/g in 6M KOH.[228] Yang *et al.* investigated the sulfonation of graphite using tosyl. The reaction occurs at the edges of the carbonaceous material. After exfoliation by sonication and thermal treatment, a S-doped graphene was obtained. A good electrochemical behaviour was observed with 180 F/g at 500 mA/g in 6M KOH.[229]

Dhathathreyan *et al.* reduced GO prior to impregnate it with phosphoric acid. This procedure allows to obtain P-doped rGO after drying step at 220°C. The active material showed

good performance with 365 F/g at 5 mV/s in acidic aqueous solution.[230] A similar approach was investigated by Hulicova-Jurcakova's research group. They reported a P-doping with an atomic concentration of 1.3%, which allows to extend the electrochemical windows. The specific capacitance calculated from charge-discharge curve at 50 mA/g was 115 F/g in 1M H_2SO_4.[231]

2.3.1.9.3. N-B and N-S-co-doped Graphene

Müllen *et al.* firstly reported the simultaneous co-doping of rGO. They reduced hydrothermally GO in presence of ammonia – boron trifluoride (NH_3BF_3). The resulting hydrogel was freeze-dried to obtain N-B-co-doped graphene aerogel. An all-solid-state supercapacitor was fabricated using PVA/H_2SO_4 as gel electrolyte. Good electrochemical behaviour was demonstrated with 239 F/g at 5 mV/s.[232] Chung's research group used ammonia borane (also called borazane [BH_3NH_3]) as versatile agent for the reduction of GO together with its N-B-co-doping. Interestingly, this compound can be used both in aqueous or in organic environment. The electrochemical performance was evaluated using an ionic liquid as electrolyte: TEA BF_4. A specific capacitance of 110 F/g was calculated from charge-discharge curve at 1 A/g.[233]

Jia *et al.* reported the one-pot hydrothermal synthesis of N-S-co-doped graphene using L-cysteine, an amino acid, as doping agent. Interestingly, they demonstrated that the co-doping has a synergistic effect leading to higher performance in comparison with singly S- and N-doped graphene. In basic aqueous electrolyte, a specific capacitance of 186 F/g was obtained at 5 A/g.[234] Dou and collaborators mixed ultra large GO flakes with 3-aminobenzenesulfonic acid in water to obtain an homogeneous dispersion. Then, sample was heated firstly at low temperature followed by a treatment at high temperature to obtain N-S-co-doped graphene paper. High specific capacitance was measured in 6M KOH electrolyte

(305 F/g at 100 mV/s).[235] Recently, Wong *et al.* reported the use of ammonium sulphide to act both as reducing agent and doping agent for the one-pot hydrothermal synthesis of N-S-co-doped rGO. The resulting hydrogel was tested in 6M KOH electrolyte. A gravimetric capacitance of 251 F/g was calculated from charge-discharge curve at 500 mA/g.[236]

2.3.1.10. Graphene produced from green precursor

In this section, research works focusing on the fabrication of electrochemical double-layer capacitors using green source of carbon will be presented.

Qiu *et al.* firstly investigated a green approach for the fabrication of EDLC. They produced coal-derived graphite oxide starting from anthracite coal. After a DBD plasma step, graphene-like material was obtained and tested in 6M KOH. A specific capacitance of 195 F/g was measured at 50 mA/g.[237] Chen *et al.* reported the hydrothermal reduction of GO dispersion mixed with biomass or polymer. Then, carbonaceous composite was carbonized and activated with KOH to obtain a 3D-porous graphene-based material. Using an ionic liquid as electrolyte, a specific capacitance of 225 F/g was calculated from charge-discharge curve at 1 A/g.[238] Bando *et al.* synthesized graphene starting from glucose and ammonium chloride. Under controlled temperature, a molten syrup was obtained and chemically released gas (such as melanoidin) induces bubbles formation. Then, a thermal annealing was carried out to obtain graphene. The flowchart of the synthesis procedure is reported in Figure 2.29. In acidic aqueous electrolyte, a specific capacitance of 250 F/g was measured at a current density of 100 mA/g.[239]

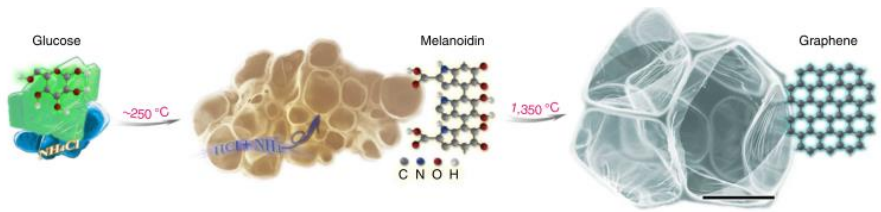

Figure 2. 29. synthesis flowchart of the green production of graphene starting from glucose.[239]

Wilson and Islam investigated the infiltration of CNTs using D-glucose prior to carried out a thermal annealing. Electrochemical measurement using RTIL electrolyte showed interesting performance with 120 F/g at 20 mV/s.[240] Fu *et al.* reported the production of graphene-like sheets starting from coconut shell. The synthesis procedure required the use of Fe and Zn as catalyst of graphitization and activating agent, respectively. After the graphitization, both metals are removed, and 3D-porous framework of graphene-like sheets is obtained. A modest gravimetric capacitance of 69 F/g at 1 A/g was measured in 6M KOH.[241] Zhang and colleagues used shrimp shells to produce N-doped graphene-like sheets. After the carbonization of the bio-polymer layers, the biochar is rinsed with an acidic solution to remove mineralized layers contained in the starting material. After a sonicated-assisted exfoliation, electrochemical characterization in basic electrolyte was carried out. Interestingly, this green approach leads to high specific capacitance with 322 F/g at 500 mA/g.[242]

Kale's research group produced perforated graphene-like sheets starting from bougainvillea flowers. First, flowers were washed with water and dried at low temperature. After a crushing step to obtain a fine powder, thermal treatment was carried out to obtain graphene-like sheets with unique naturally perforated structure. Electrochemical characterization in neutral electrolyte demonstrated high specific capacitance with 458 F/g at 2.28 A/g.[243] Another green approach was investigated by Yu and co-workers. They carbonized humic acid and they oxidized the resulting powder to obtain carbonaceous material similar to graphene oxide. After a thermal concomitant exfoliation/reduction step, the graphene-like material was obtained. A specific capacitance of 254 F/g was calculated from charge-discharge curve at 50 mA/g in 3M KOH.[244]

Aimed by a sustainable production of energy storage devices, Kumar and co-workers extracted graphite from used primary

cell. The 'second-hand' graphite was used as starting material for the fabrication of eco-friendly supercapacitor. Graphite was exfoliated/reduced using microwave-assisted process. An all-solid-state supercapacitor using PVA/H_3PO_4 was fabricated with this active material. The performance was interesting with 201 F/g at 2 mV/s and 208 F/g at 200 mA/g from CV and charge-discharge curves, respectively.[245]

2.3.2. Hybrid Graphene-based Supercapacitors

It is well-known that the specific capacitance (and energy density) of EDLC can be improved creating hybrid graphene-based supercapacitors which combine both EDLC and pseudocapacitors.

However, during the last decade, the number of publication reporting graphene-based supercapacitors containing conductive polymers, metal oxides, and/or metal dichalcogenides has increased exponentially. For sake of comparability, only advances dealing with hybrid supercapacitors containing both EDLC, assignable to graphene (or reduced graphene oxide), and pseudocapacitors are presented.

2.3.2.1. Conductive Polymers

Conductive polymers have attracted attention due to their electrical conductivity. However, they suffer of poor cyclability due to non-perfectly reversible Faradaic reactions. By forming a composite with graphene, the specific capacitance of the graphene-based material is enhanced alongside the cycle life of the pseudocapacitive material. The most studied conductive polymers are Polyaniline (PANI), Polypyrrole (PPy), and Poly(3,4-ethylenedioxythiophene) (PEDOT).

2.3.2.1.1. PANI

Shi's research group first investigated the fabrication of a composite using PANI as pseudocapacitive material. They

deposited nanofibers of PANI by interfacial polymerization onto chemically converted graphene. A specific capacitance of 214 F/g was calculated from charge-discharge curve at a current density of 300 mA/g using 1M H_2SO_4 as electrolyte.[246] Three years later, Li and co-workers investigated to polymerization of aniline onto graphene nanoribbons synthesized from MWCNTs. The PANI nanorods allows an increase of the gravimetric capacitance, which reaches a value of 340 F/g at 250 mA/g using the same electrolyte.[247]

Jiang *et al.* studied an easy one-step electrosynthesis by fabricating a two-electrode configuration using GO and aniline as active material and a separator soaked in 1M H_2SO_4. By applying an alternative potential, they simultaneously reduced GO in rGO and polymerized aniline in PANI. The electrochemical performance was interesting with 243 F/g at 100 mV/s.[248] Jing's research synthesized rGO-PANI composite using a sacrificial template. Indeed, they deposited silica homogeneously onto GO. After an annealing, they obtained rGO-SiO_2. Aniline was then polymerized onto the silica layer followed by the removal of the template to obtain rGO-PANI. Nevertheless, the measured gravimetric capacitance was not improved with 127 F/g measured at 500 mA/g.[249] Xie *et al.* investigated a "dipping and drying" strategy to coat GO with PANI before an hydrothermal synthesis to reduce GO. This synthesis pathway occurs directly on carbon fibers and allow the supercapacitor to be highly flexible and even foldable. Interestingly, the electrochemical performance was high with a specific capacitance of 464 F/g at 1 A/g in 1M H_2SO_4.[250]

Another approach was followed by Xu and co-workers using the inkjet printing technique. They started from graphene powder and they mixed it with previously polymerized PANI. Nevertheless, the specific capacitance is not as high as expected with only 70 F/g at 5 mV/s.[251] Chi *et al.* also used the inkjet printing technology, but using a different synthesis pathways as shown in Figure 2.30. The specific capacitance

was significantly improved with 864 F/g at 1 A/g using the same electrolyte.[252]

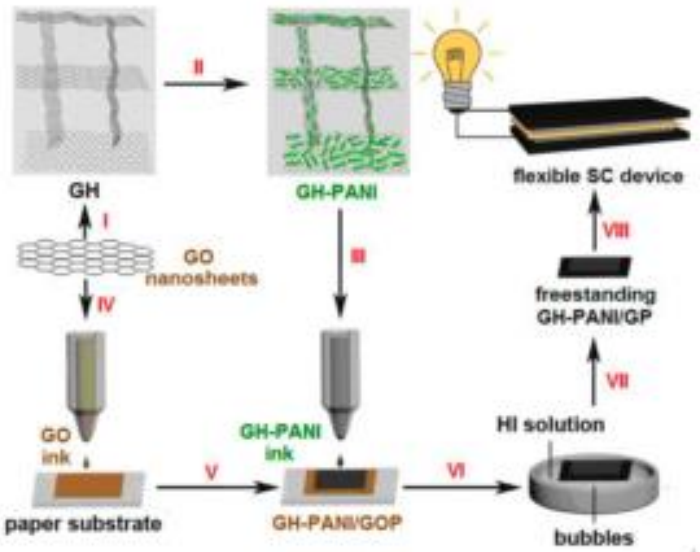

Figure 2. 30. Synthesis pathways for the fabrication of the flexible rGO-PANI supercapacitor device by inkjet printing. (I) formation of 3D-hydrogel by self-assembly procedure, (II) in-situ polymerization of PANI onto graphene hydrogel, (III) homogenization of the GH-PANI mixture to prepare the ink, (IV) inkjet-printed GO solution on paper substrate, (V) printing step of the GH-PANI ink, (VI) soaking by HI solution, (VII) concomitant reduction and peeling of the GH-PANI@GO paper, and (VIII) fabrication of the supercapacitor device.[252]

Gong's research group later fabricated a freestanding electrode for flexible all-solid-state supercapacitors. They deposited aniline on as-prepared oriented graphene hydrogel. Then, they performed the *in-situ* polymerization to obtain G-PANI composite. The specific capacitance was interesting with 530 F/g at 500 mA/g, but using a gel electrolyte (PVA/H_2SO_4) instead of the liquid electrolyte.[253] Sekar *et al.* reported a close approach. Indeed, they prepared pillared graphene by chemical reduction of GO using $NaBH_4$. Then, they *in-situ* polymerized aniline in presence of phytic acid to prepare the nanocomposite. The gravimetric capacitance was close to the previous report with 652 F/g at 10 mV/s, but they use 0.5M H_2SO_4 in this work.[254]

Recently, Lei's research group studied the oxidation polymerization of aniline on graphene nanomesh synthesized

by means of a CVD technique. The as-prepared PANI is composed by nanorods structure. The electrochemical performance is interesting with 452 F/g at 1 A/g.[255] Hong and co-workers reported the layer-by-layer deposition of GO to obtain a 3D-rGO-based structure by hydrothermal synthesis. Then, they *in-situ* polymerized aniline to obtain rGO-PANI nanocomposite. The specific capacitance was high with 438.8 F/g at 500 mA/g using 1M H_2SO_4.[256] Zhang's research group further enhance the electrochemical performance by dispersing already prepared PANI fibers in GO solution before a hydrothermal reduction. In this case, the 3D-nanocomposite displayed a specific capacitance of 808 F/g at 1 A/g using the same electrolyte.[257]

2.3.2.1.2. PPy

Biswas and Drzal first reported the use of PPy (Polypyrrole) as pseudocapacitive materials to fabricate graphene-PPy composite and use it for supercapacitor applications. They synthesized PPy nanowires by chemical polymerization using Pyrrole as precursor. Then, they produced an emulsion by sonication of an aqueous dispersion of PPy nanowires, which adsorb at the liquid-liquid interface after adding chloroform. They transferred the PPy films formed at the interface to the graphene and they use this composite as electrode. The specific capacitance was 165 F/g at 1 A/g using 1M NaCl as electrolyte.[258] Later, Swager *et al.* studied the concomitant reduction of GO and polymerization of pyrrole. The as-prepared rGO-PPy nanocomposite film is freestanding and has good electrochemical properties with a specific capacitance of 277 F/g at 10 mV/s in 1M KCl.[259] Qu's research group investigated a similar idea using electro-polymerization instead of chemical polymerization. Interestingly, the as-prepared electrolyte is tolerant to high compression without significant decrease of the electrochemical performance. Moreover, without

compression, the specific capacitance was evaluated of about 350 F/g at 1.5 A/g using 3M $NaClO_4$ as electrolyte.[260]

Ding and co-workers investigated the use of rGO-PPy nanocomposite as active material for the fabrication of all-solid-state supercapacitors. They first dispersed GO and pyrrole to create a suspension. Then, they reduced GO and simultaneously polymerized pyrrole in PPy. The chemical reduction occurred in presence of iron (III) chloride and hydroiodic acid. The specific capacitance, using PVA/H_2SO_4, was 72 F/g at 150 mA/g.[261] Li *et al.* reported a similar approach. Nevertheless, they synthesized PPy nanofibers before to mix them with GO and to chemically reduced it with HI. An improvement of the specific capacitance, in comparison with the previous work, was observed using PVA/H_3PO_4 as gel electrolyte. A value of 345 F/g was calculated from discharge curve at a current density of 1 A/g.[262] Finally, Du and colleagues fabricated supercapacitor starting from pyrrole and GO. The *in-situ* polymerization was carried out using p-toluenesulfonate (p-TsOH) acid instead of HI. A schematic illustration of the synthesis pathways is shown in Figure 2.31. A good electrochemical behaviour was observed with a specific capacitance of 255.7 F/g at 200 mA/g using 3M KCl as electrolyte.[263]

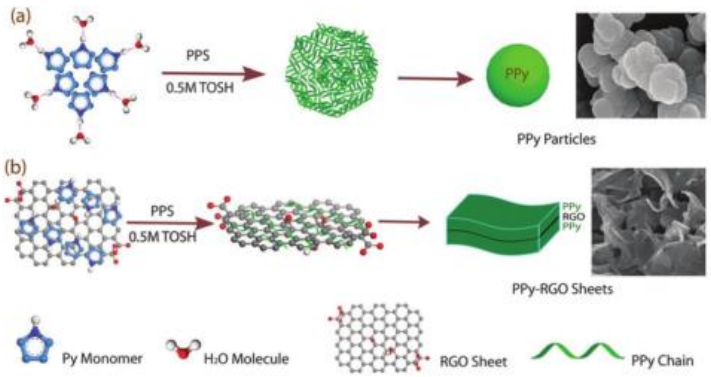

Figure 2. 31. Schematic representation of the synthesis pathways of the PPy and PPy-rGO composites.[263]

2.3.2.1.3. PEDOT

Despite the several works reported using PEDOT as pseudocapacitive material coupled with graphene, only two of them report the gravimetric capacitance. The others report the areal capacitance.

Pandey and Rastogi investigated graphene-PEDOT nanocomposite for supercapacitor applications in 2013. They started from graphene nanoplatelets and EDOT(monomer of PEDOT). By a single electrochemical step, they obtain graphene-PEDOT nanocomposite. They tested it by using $BMImBF_4$, after gelification, as gel electrolyte. They obtained good electrochemical performance with 110 F/g at 10 mV/s.[264] Later, in 2015, Chen's research group investigated PEDOT doped with PSS as pseudocapacitive material. They first mix it with GO before a solvothermal reduction at 60°C for 24 hours in diethylene glycol and phosphoric acid. The specific capacitance, using PVA/H_3PO_4 as gel electrolyte, was lightly inferior with 82 F/g at 10 mV/s. Interestingly, this approach permits to obtain large film with high flexibility as shown in Figure 2.32.[265]

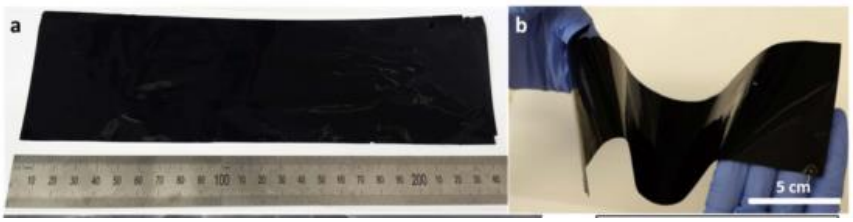

Figure 2. 32. Photographs of the as-prepared PEDOT:PSS film (30x7 cm)[265]

2.3.2.2. Transition Metal Oxides

Transition Metal Oxides are attractive pseudocapacitive material to create hybrid supercapacitor with high specific capacitance, and consequently high energy density. Indeed, they possess a wide range of oxidation states which allows this material to contribute to the specific capacitance with near-surface reversible redox reactions. However, they sometimes struggle due to a poor electrical conductivity which limits the deliverable performance.

2.3.2.2.1. Ruthenium Oxide

The first report was published by Mishra and Ramprabhu in 2011. They deposited Ruthenium (III) Chloride [$RuCl_3$] on hydrogen exfoliated graphene. By addition of NaOH, Ruthenium Oxide was obtained on graphene. The specific capacitance was measured by both CV and CCCD in 1M H_2SO_4. Capacitance of 265 F/g at 10 mV/s and 220 F/g at 10 A/g were calculated, respectively.[101] The same year, a similar approach was reported by Alshareef's research group. They evaluated a specific capacitance of about 365F/g at 20 mV/s in 10M NaOH electrolyte.[266]

Lin *et al.* investigated the synthesis of rGO-RuO_2 starting from GO and $RuCl_3$. After the homogeneous suspension was obtained, a hydrothermal synthesis was carried out to reduce graphene followed by a thermal annealing to increase the crystallinity of the pseudocapacitive materials. A gravimetric capacitance of 551 F/g was calculated from charge-discharge curve at 1 A/g in acidic aqueous electrolyte.[267] Liu and co-workers studied a controllable nanosheets reassembly process between RuO_2 nanosheets and graphene nanosheets previously prepared and mixed together to obtain the nanocomposite. However, the specific capacitance is significantly lower with 100 F/g at a current density of 5 A/g.[268]

Dickerson's research group mixed GO with $RuCl_3$ before adding NaOH inducing the formation of RuO_2. By addition of NaOH again, and by ageing the solution for long time, a deoxygenation of the GO occurs inducing the formation of the rGO-RuO_2 nanocomposite. Using 1M H_2SO_4, they measured a specific capacitance of 500 F/g at a current density of 1 A/g.[269] They reported the same year a specific capacitance of 418 F/g with a gel electrolyte (PVA/H_3PO_4) in the same condition.[270]

The last report was published by Wang and co-workers. They prepared a Ru hydrosol starting from $RuCl_3$ and adding $NaBH_4$. Then, they add GO and chemically reduced it using

hydrazine to obtain rGO-RuO_2 nanocomposite. An outstanding specific capacitance of 1099 F/g was measured at 500 mA/g using 1M H_2SO_4 as electrolyte.[271]

2.3.2.2.2. Manganese Oxide

Ruthenium is an attractive pseudocapacitive material. However, it is expensive which limits its industrial-scale application. Manganese is a good candidate to substitute it.

Majid and co-workers investigated the formation of a rGO-wrapped-MnO_2 nanocomposite. They dispersed GO in water, adding L-ascorbic acid as reducing agent, and manganese (II) acetate. They obtained the desired nanocomposite by electrodeposition. A specific capacitance of 378 F/g was measured at a scan rate of 1 mV/s using 1M Na_2SO_4.[272] Li's research group investigated another approach. Indeed, they hydrothermally synthesized nanobelts β-MnO_2 starting from manganese (II) sulfate and ammonium sulfate. Then, they mixed it with GO and hydrothermal reduced the GO. A gravimetric capacitance of 362 F/g at a current density of 1 A/g with a basic aqueous electrolyte (6M NaOH).[273] Kuang *et al.* reported the one-pot hydrothermal synthesis starting from the same precursors. The electrochemical performance was consistent with the previous report. Indeed, the specific capacitance of about 321 F/g at a current density of 0.5 A/g using 1M NaOH.[274]

Another manganese oxide has focused attention for energy storage application: Mn_3O_4. Deng *et al.* reported the synthesis of rGO-Mn_3O_4 nanocomposite starting from manganese (II) nitrate and mix it with microwave-assisted reduced GO. They hydrothermally treated the mixture followed by a microwave step. Then, the nanocomposite was tested using 5M KOH as electrolyte. A specific capacitance of 345 F/g was calculated from charge-discharge current at a current density 1 A/g.[275] Wang's research group fabricated an all-solid-state supercapacitor based on vertically aligned graphene decorated with Mn_3O_4 nanoparticles. They

hydrothermally synthesized the pseudocapacitive material starting from manganese (II) acetate. After the hydrothermal step, they annealed the nanocomposite to increase the crystallinity of the manganese oxide. A specific capacitance of 562 F/g was measured at a current density of 0.7 A/g using PVA/H_3PO_4 as gel electrolyte.[276]

2.3.2.2.3. Molybdenum Oxide

Following the idea to reduce the cost of the active material, Molybdenum Oxide has attracted much attention due to its oxidation states comprised between +2 and +6. Chen *et al*. first reported the synthesis of a nanocomposite α-MoO_3-decorated graphene sheets tested in a two-electrode configuration. They electrochemically exfoliated graphite rods using a solution of sodium molybdate as electrolyte. The as-obtained composite was then dried and finally annealed at 200°C in air for 2 hours. A schematic representation of the synthesis pathways is shown in Figure 2.33. The electrochemical characterization was carried out using 6M KOH as electrolyte. A maximal gravimetric capacitance of 86.3 F/g was obtained at a current density of 100 mA/g.[277]

Another approach was investigated by Zhou and co-workers using the same precursor of Mo (sodium molybdate). Indeed, they carried out a one-pot solvothermal synthesis using GO and sodium molybdate as precursor. The resulting solvogel was freeze-dried to obtain MoO_3-graphene aerogel. The as-prepared Molybdenum Oxide (VI) has a nanometric size and was covalently linked with the reduced Graphene Oxide by oxygen bonding. The specific capacitance was significantly improved, even using a gel electrolyte (PVA/H_2SO_4), with a specific capacitance of 373 F/g at 1 A/g.[278]

Chiu *et al*. reported the preparation of MoO_3-graphene nanocomposite by a facile solvothermal synthesis. They first exfoliated graphene starting from graphite flakes by a typical liquid exfoliation procedure. Then, they dispersed as-prepared graphene flakes with ammonium molybdate as Mo

precursor in ethylene glycol. This solvent allows to avoid the use of DMF which is more toxic. The resulting solvogel was centrifugated and dried before a thermal treatment to increase the crystallinity of the molybdenum oxide. A specific capacitance of 148 F/g was measured at 5 mV/s in 1M Na_2SO_3.[279] The same work was recently published with more structural and electrochemical characterizations.[280]

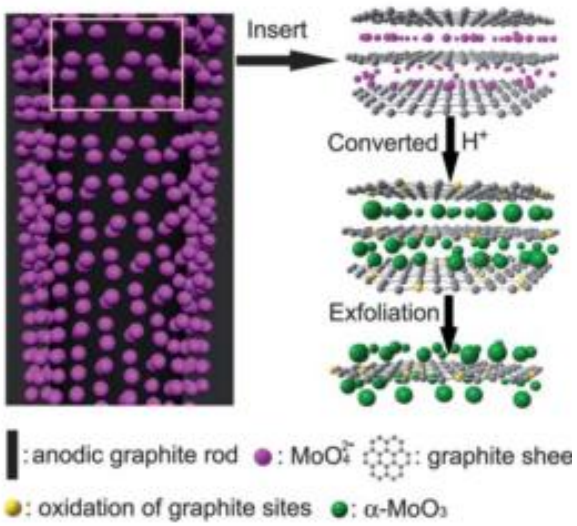

Figure 2. 33. Schematic representation of the production of α-MoO_3-decorated graphene sheets.[277]

Giardi *et al.* investigated the hydrothermal synthesis of Molybdenum Oxide (IV) instead of Molybdenum Oxide (VI). Indeed, the less oxidized specie is more conductive which allows to decrease the equivalent series resistance (ESR) of the nanocomposite. They hydrothermally synthesized MoO_2-decorated rGO aerogel starting from GO and phosphomolybdic acid as Mo precursor. The resulting hydrogel was rapidly frozen in liquid nitrogen followed by a freeze-dying procedure. XRD confirmed the monolithic phase of MoO_2 nanoparticles onto graphene sheets. The electrochemical characterization was performed using 1M Na_2SO_4 as aqueous electrolyte. A gravimetric capacitance of 381 F/g was measured at a scan rate of 0.5 mV/s.[281] A similar

approach was investigated in chapter 4 in comparison with the *in-situ* synthesized MoS_2 sample, in chapter 5 with the addition of L-ascorbic acid as reducing agent, and in chapter 6 as active material for micro-supercapacitor applications.

2.3.2.2.4. Cobalt Oxide

Cobalt Oxide (Co_3O_4) has also attracted much attention due to the wide range of oxidation states of the Co centre (from +1 to +5). Wang *et al*. reported the one-pot hydrothermal synthesis of Co_3O_4-decorated rGO hydrogels. They used cobalt acetate (II) as Co precursor. A specific capacitance of about 250 F/g was measured at a current density of 0.5 A/g using 6M KOH as electrolyte.[282] A similar approach was later investigated by Liu and co-workers. They started from the same precursors, but they adjusted the pH value to 9.5 using ammonia solution. The as-obtained Co_3O_4-decorated rGO hydrogels were electrochemically tested using 2M KOH as electrolyte. A gravimetric capacitance of 263 F/g was calculated from charge-discharge curve at a current density of 0.2 A/g.[283] Liao *et al.* fabricated an all-solid-state with outstanding performance (580 F/g at 1 A/g using PVA/KOH as gel electrolyte). They used carbon fabric as support to growth vertically aligned graphene nanosheets by microwave plasma enhanced chemical vapor deposition (MPECVD). Then, they hydrothermally synthesized Co_3O_4 nanoparticles on VAGN@CF using cobalt acetate (II) as precursor. SEM images of the different steps are shown in Figure 2.34.[284]

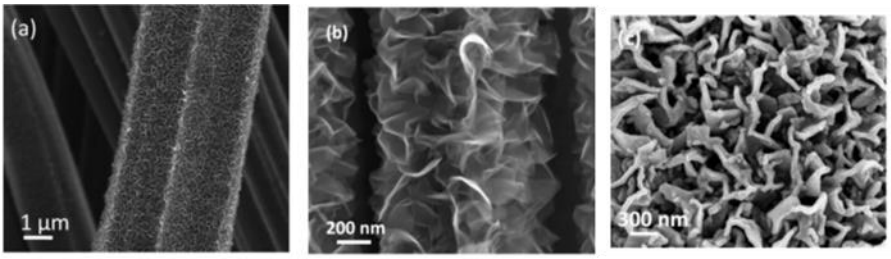

Figure 2. 34. (a) Low-magnification and (b) high-magnification SEM images of the VAGN@CF; (c) high-magnification SEM image of the as-synthesized Co3O4 nanoparticles on VAGN@CF.[284]

2.3.2.2.5. Others Transition Metal Oxides

Ping Wong *et al.* investigate tungsten trioxide as pseudocapacitive material to produce nanocomposite with enhanced properties. In the first report, they synthesized WO_3 by hydrothermal synthesis starting from ammonium paratungstate as W precursor. Then, they mixed the as-prepared nanoparticles with chemically reduced GO. In the second, they reported the one-pot hydrothermal synthesis starting from the same W precursor. Electrochemical measurements were carried out using 1M Na_2SO_3 as neutral electrolyte. The specific capacitance, calculated from charge-discharge curves at a current density of 0.7 mA/g, was 85.7 F/g[285] and 274 F/g[286], respectively.

Yuan and co-workers reported the hydrothermal synthesis of $Ni(OH)_2$ starting from Nickel Nitrate (II) and sodium hydroxide. The resulting hydrogel was then freeze-dried to obtain $Ni(OH)_2$-decorated rGO aerogel with outstanding properties (1461 F/g at 5 mV/s).[287] Another group, supervised by Shi, reported the fabrication of NiO-graphene composite by using alcohols-rGO as substrate. They used the same precursor for Nickel. However, after the hydrothermal synthesis, the product was dried in an oven followed by a microwave treatment at 300°C for 1 minute. Good gravimetric performance was obtained with 530 F/g at 1 A/g using 2M KOH as electrolyte.[288]

Li *et al.* studied ZnO as pseudocapacitive material to fabricate hybrid supercapacitors. They synthesized ZnO-decorated hydrogel by hydrothermal synthesis using hydrazine as reducing agent. The precursor of ZnO was zinc nitrate (II). They fabricated all-solid-state supercapacitors using PVA-H_2SO_4 as gel electrolyte. The obtained performance was interesting with 156 F/g at 5 mV/s.[289] Zhang and co-workers investigated a different approach to fabricate ZnO-rGO nanocomposite. Indeed, they mixed GO with zinc acetate (II) under microwave irradiation until the solvent was fully removed. Then, another microwave

irradiation was carried out during 5 minutes at 1000 W. A specific capacitance of 125 F/g was calculated from charge-discharge curve at 1 A/g using 1M Na_2SO_4 as neutral electrolyte.[290]

Ma *et al.* synthesized maghemite (γ-Fe_2O_3) starting from Iron Chloride (III) as Fe precursor. First, they mixed GO with the Fe precursor to decorate GO with Fe^{3+} cations. After removing the excess of cations, they treated thermally the sample in inert atmosphere for 2 hours at 350°C. The as-prepared nanocomposite demonstrated interesting electrochemical properties with 175 F/g at 0.2 A/g in 6M KOH.[291] In another report, Gholipour-Ranjbar and co-workers synthesized Fe_3O_4-decorated-N-doped rGO. First, they prepared N-doped rGO by hydrothermal synthesis in presence of ammonia solution. Then, they add Iron sulfate (II) as Fe precursor and they synthesized the nanocomposite by a facile sonochemical method. The magnetite-based nanocomposite showed high gravimetric capacitance with 355 F/g at 2 mV/s.[292] Sharma's research group investigated the synthesis of magnetite nanoplatelets over holey graphene for supercapacitor applications. They produced GO nanoribbon by unzipping of MWCNT using strong oxidizing species. Then, they mixed GO with 2 different precursors of Fe: iron sulfate (II) and iron chloride (III). They finally prepared the nanocomposite using a typical hydrothermal synthesis. An all-solid-state supercapacitor was fabricated using PVA/H_2SO_4 as gel electrolyte. A specific capacitance of 64 F/g was measured at a current density of 1 A/g.[293]

Vanadium has also attracted attention for energy storage applications. Interestingly, V_2O_5 can be found in various spatial configurations such as nanowires, microspheres, etc., as shown in Figure 2.35.

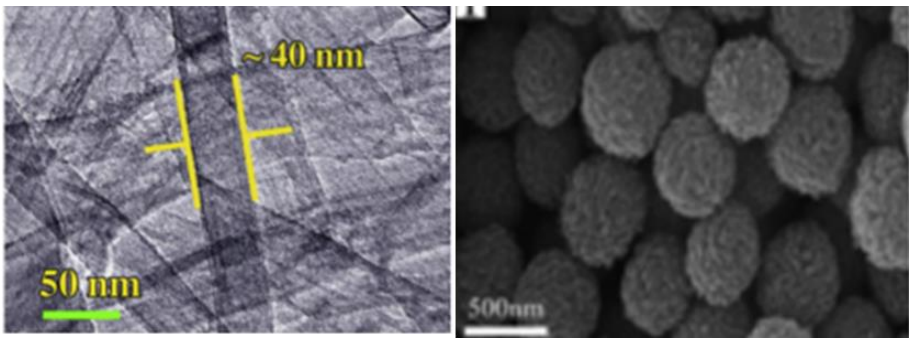

Figure 2. 35. V_2O_5 nanostructures: (left) TEM image of V_2O_5 nanowires on alkaline deoxygenated GO[294]; (right) SEM image of pure V_2O_5 microspheres.[295]

Balkus *et al*. reported the synthesis of V_2O_5 nanowires on alkaline deoxygenated GO. They solvothermally produced the pseudocapacitive materials starting from vanadium oxytriisopropoxide (V) as V precursor in presence of Pluronic®123 as surfactant. The as-prepared nanocomposite is reported in Figure 2.35 (left). The specific capacitance was evaluated using 1M LiTFSI in acetonitrile as electrolyte. A value of 80 F/g was obtained at a current density of 0.5 A/g.[294] Ai and co-workers used the same solvothermal reaction but, in this case, an annealing step was carried out at different temperature between 250 and 550°C for 30 minutes. The as-obtained microspheres (see Figure 2.35 (right)) supported by rGO flakes were tested electrochemically using 8M LiCl as neutral electrolyte. A significant improvement of the specific capacitance was obtained with 470 F/g at 1 A/g.[295] Fan's research group synthesized nanocomposite starting from GO and $VO(acac)_2$ as V precursor. After the slow mixing procedure need to obtain homogeneous suspension, a hydrothermal synthesis was carried out during 24 hours at 180°C. To further improve the electrochemical performance, a hydrogen thermal processing was performed to reduce partially V_2O_3 to VO_x nanostructures. The resulting graphene bridged V_2O_3/VO_x core-shell nanostructured electrode has an electronic conductivity several orders of magnitude higher than common vanadium oxide. The structure of the electrode is

shown in Figure 2.36. The specific capacitance, evaluated using neutral aqueous electrolyte, was significantly improved with a value of 590 F/g at a scan rate of 5 mV/s.[296]

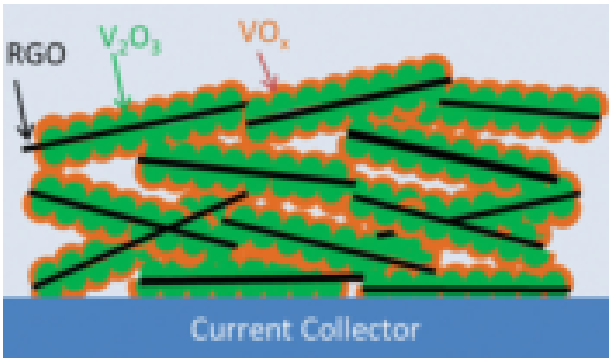

Figure 2. 36. schematic representation of the graphene bridged V_2O_3/VO_x core-shell nanostructured electrode obtained after the hydrogen thermal treatment.[296]

2.3.2.3. Transition Metal Dichalcogenides

2.3.2.3.1. General background[297–305]

Since the first isolation of graphene in 2004 by Geim and Novoselov, 2D materials which are analogues to graphene have attracted much attention due to the development of new techniques for the isolation of layered structures. Beyond graphene, it exists a large family of 2D-materials such as Transition Metal Dichalcogenides (TMDs), hexagonal-Boron Nitride (h-BN), X-ene such as silicene and germanene, black phosphorous, etc. Figure 2.37 indicates the chemical composition of these 2D materials starting from the periodic table.

In this section, Transition Metal Dichalcogenides (TMDs) are presented. TMDs are a family composed by around 40 members which some of them have a layered spatial configuration (predominantly from group 4-7 in the periodic table) while others display non-layered structures (mainly from group 8-10). The most interesting TMDs for energy storage applications are layered due to their outstanding properties (transparency, flexibility, electrical behaviour, etc.) when isolated.

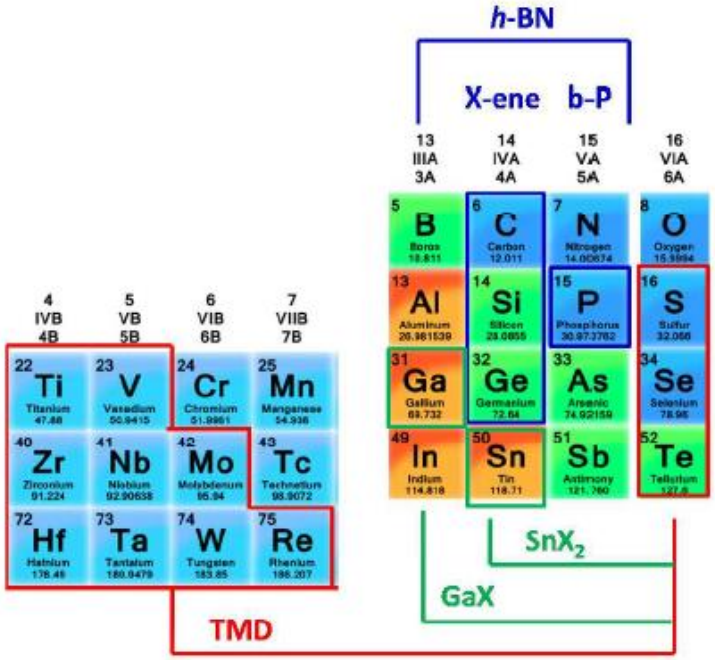

Figure 2. 37. Chemical composition of the 2D materials starting from the periodic table.[303]

Starting from the definition, a single layer of TMD is composed by a single sheet of transition-metal atoms sandwiched between two layers of chalcogens. A schematic representation of the chemical structure is shown in Figure 2.38. The resulting structure has a thickness around of 6~7 Å. The intra-layer chemical bonds are predominantly covalent (strong bonds) while the stacking of the different layers is governed by Van der Waals forces. Consequently, it is possible to cleave the bulk structure to isolate a layer of TMD following a similar approach developed to obtain the graphene from graphite.

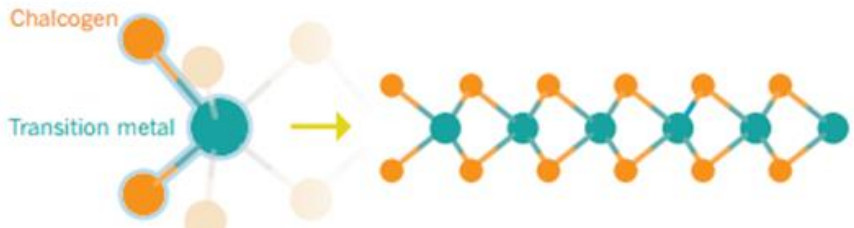

Figure 2. 38. schematic representation of the chemical structure of a layered transition metal dichalcogenide.[304]

The metal coordination of layered TMDs can be either trigonal prismatic or octahedral as illustrated in Figure 2.39. Typically, TMDs are found naturally as the 2H polytype because the 1T-phase is metastable. As demonstrated by Chhowalla *et al.*, it is possible to reversibly transform the 2H phase in 1T using a chemical process. This transformation can be partial or complete according to the experimental procedure.[306,307]

Figure 2. 39. metal coordination for layered TMDs. Atom colour code: purple, metal; yellow, chalcogen.[297]

Interestingly, some TMDs are chemically active (such as MoS_2 and WS_2) and can store energy through fast and reversible redox reactions using the transition-metal. In addition, the layered structure facilitates the ions intercalations. Layered TMDs are materials which combine both double-layer capacitor and pseudocapacitor behaviours.[308]

To obtain layered TMDs, two main approaches are typically envisaged: CVD and liquid exfoliation. The first way is a "bottom-up" approach which allows to growth extremely pure MoS_2 nanoflakes with controlled size and thickness. However, the scalability of this method from lab scale to industrial scale is limited by the rigid experimental conditions such as high temperature, high vacuum, etc.[309–311]

The other approach is a "top-down" liquid exfoliation starting from bulk TMDs. This method is more suitable for high quantity production of single layer or multi-layers TMDs. By sonication, it is possible to break the Van der Waals forces which maintain together the different TMDs layers. These methods used typically dimethylformamide or *N*-methyl-2-pyrrolidone as solvent. This way demonstrated high efficiency for a wide range of 2D materials: MoS_2, WS_2, $MoSe_2$, $NbSe_2$, $TaSe_2$, $NiTe_2$, $MoTe_2$, h-BN, Bi_2Te_3, and graphene.[35,312]

TMDs, and in particular MoS_2, since its first application as single layer-transistor developed by Kis *et al.*[313], have been investigated in a wide range of applications such as catalysis, sensing, electronic devices, energy storage, etc.

2.3.2.3.2. Molybdenum Disulfide

Molybdenum Disulfide (MoS_2) is the most studied TMD for energy storage application. Indeed, Mo as transition-metal is highly interesting due to its wide range of oxidation states from +2 to +6. The theoretical specific capacitance was evaluated about 1000 F/g.[314,315] A focus on this material is reported in Chapter 4.

Dryfe *et al.* reported the preparation of MoS_2/graphene composite for supercapacitor applications. They first exfoliated MoS_2 in NMP by a typical phase exfoliation and prepared graphene flakes from graphene powder. An illustration of the exfoliation procedure is shown in Figure 2.40. Then, both active materials were mixed together according to different weight ratios. The best performance was obtained in a coin-cell with 1M Na_2SO_4 as neutral electrolyte for the MoS_2/graphene composite with a weight ratio of 3:1. A gravimetric capacitance of 11 F/g was measured at 5 mV/s.[1]

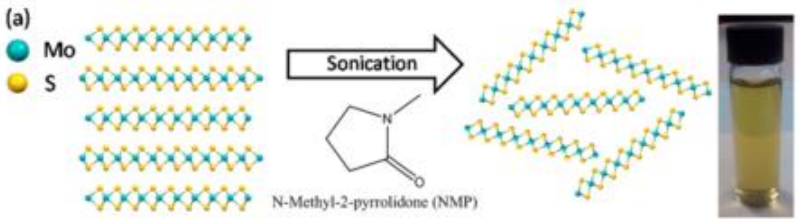

Figure 2. 40. schematic representation of the exfoliation procedure in NMP starting from bulk MoS_2.[1]

The same group reported later the synthesis of 1H-MoS_2-graphene@Oleylamine by hot-injection thermolysis of a single precursor ($[Mo_2O_2S_2(S_2COEt)_2]$). This approach demonstrated more suitable performance for supercapacitor electrodes with 50 F/g calculated from charge-discharge

curve at a current density of 0.37 A/g with the same electrolyte.[316]

Lamberti *et al.* investigated a new approach to produce MoS_2-graphene nanocomposite. They deposited commercially available 2H-MoS_2 on a polyimide substrate following by a laser treatment. The MoS_2-laser induced graphene nanocomposite showed interesting areal capacitance, but the gravimetric capacitance cannot be evaluated. The experimental setup with FESEM images of the as-prepared sample are reported in Figure 2.41.[317]

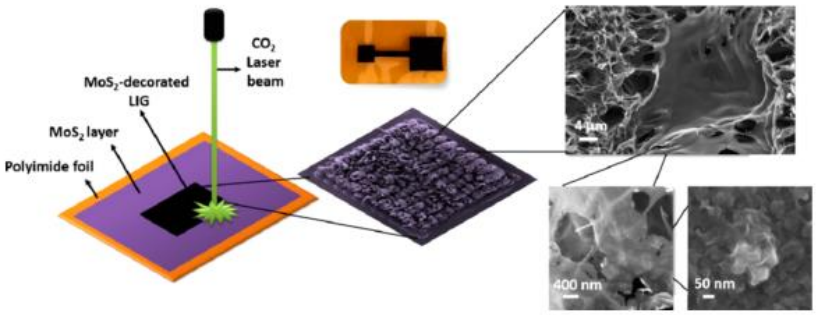

Figure 2. 41. Experimental setup (left) and FESEM images of the as-prepared sample at different magnification (right).[317]

Jena's research group reported the hydrothermal synthesis of rGO-MoS_2 starting from GO, ammonium heptamolybdate as Mo precursor, and thiourea as sulphur precursor. The as-prepared MoS_2 was hollow spherical instead of the layered structure usually targeted. However, the specific capacitance was significantly improved with 318 F/g at 1 mV/s in neutral aqueous electrolyte.[318]

A similar approach was investigated using L-cysteine as S precursor, which allows to avoid the use of the toxic thiourea. Experimental setup, results, and discussions are reported in Chapter 4.

2.3.2.3.3. Tungsten Disulfide

Ratha and Rout firstly reported the hydrothermal synthesis of rGO/WS_2 nanocomposite. They mixed GO, WCl_6 as W precursor, and thioacetamide as S precursor. The as-

prepared nanocomposite displayed undistinguishable nanoflakes of rGO and WS_2 intimately mixed together. This homogeneous composite showed high gravimetric capacitance with 350 F/g at 2 mV/s using 1M Na_2SO_4 as aqueous electrolyte.[319]

Min's research group recently reported the fabrication of a flexible all-solid-state supercapacitor with ultralarge graphene nanosheets and liquid exfoliated tungsten disulfide as active materials. The electrical energy storage devices showed interesting areal capacitance with 312.4 mF/cm^2 which is promising for the future use of this TMD in energy storage application. Unfortunately, it was not possible to compare the gravimetric capacitance due to the lack of information in the published paper.[320]

2.3.2.3.4. Vanadium Diselenide

Behera *et al.* investigated the one-step hydrothermal synthesis of vanadium diselenide (VSe_2)-rGO nanocomposite. They started from GO, sodium metavanadate ($NaVO_3$), and selenium dioxide (SeO_2). The as-prepared VSe_2 has a 3D-cuboidal structure as shown in Figure 2.42. The nanocomposite was electrochemically tested in a neutral aqueous electrolyte and demonstrated a specific capacitance of about 680 F/g at 1 A/g, which is about 5 and 6 fold higher than bare rGO and bare VSe_2.[321]

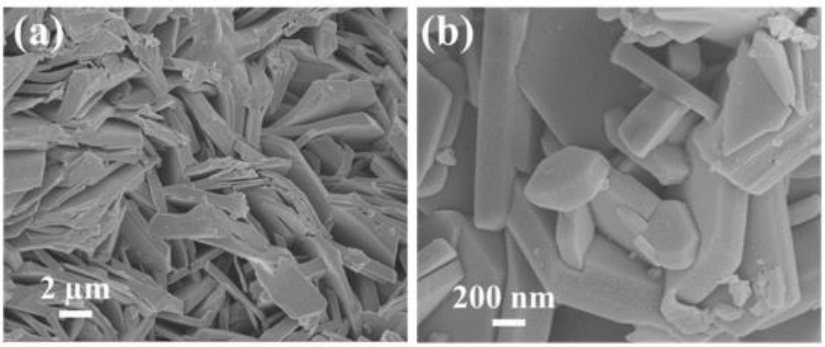

Figure 2. 42. FESEM images of the pristine VSe_2 sample at (a) low and (b) high magnification.[321]

2.3.3. Performance comparison

All the specific capacitance aforementioned in Section 2.3.1 and 2.3.2 are reported in Figure 2.43 and 2.44 from galvanostatic charge-discharge and cyclic voltammetry measurements, respectively. Both graphs have the same scale for the specific capacitance axis to be confrontable directly.

Higher is the scatter in the graph, better is the specific capacitance. Righter is the scatter, quicker the supercapacitor is able to deliver the stored energy, and more attractive for real applications.

From both graphs, interesting information can be observed. First, EDLCs have typically a specific capacitance comprised between 100 and 500 F/g, which seems to be the practical limit of graphene-based supercapacitors. In Figure 2.43, it can be noticed that hybrid supercapacitors using metal oxides or polymer conductive as pseudocapacitive materials allow to increase the specific capacitance as expected. Most promising results are obtained for Ru-based and PANI-based hybrid supercapacitors. Although this improvement of gravimetric capacitance, it seems that hybrid supercapacitors struggle for applications using high current density in comparison to ELDCs materials. Indeed, Faradaic processes require a more important to occur instead of the double-layers.

From Figure 2.44, a similar observation can be expressed. However, for this type of measurements, Ni-based supercapacitors seem to be more attractive followed by PANI-based hybrid supercapacitors.

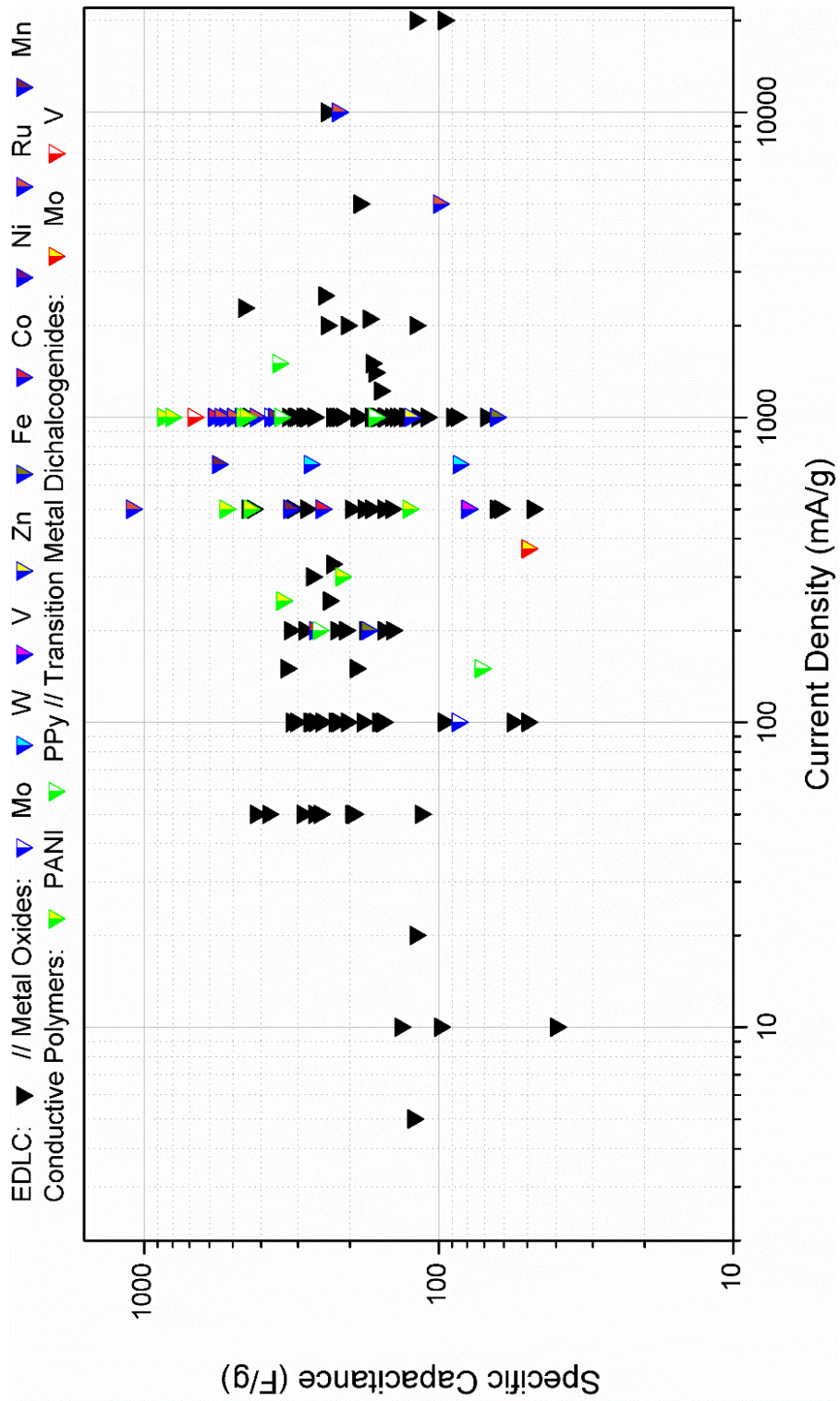

Figure 2. 43. Comparison of the specific capacitance calculated from constant current charge discharge

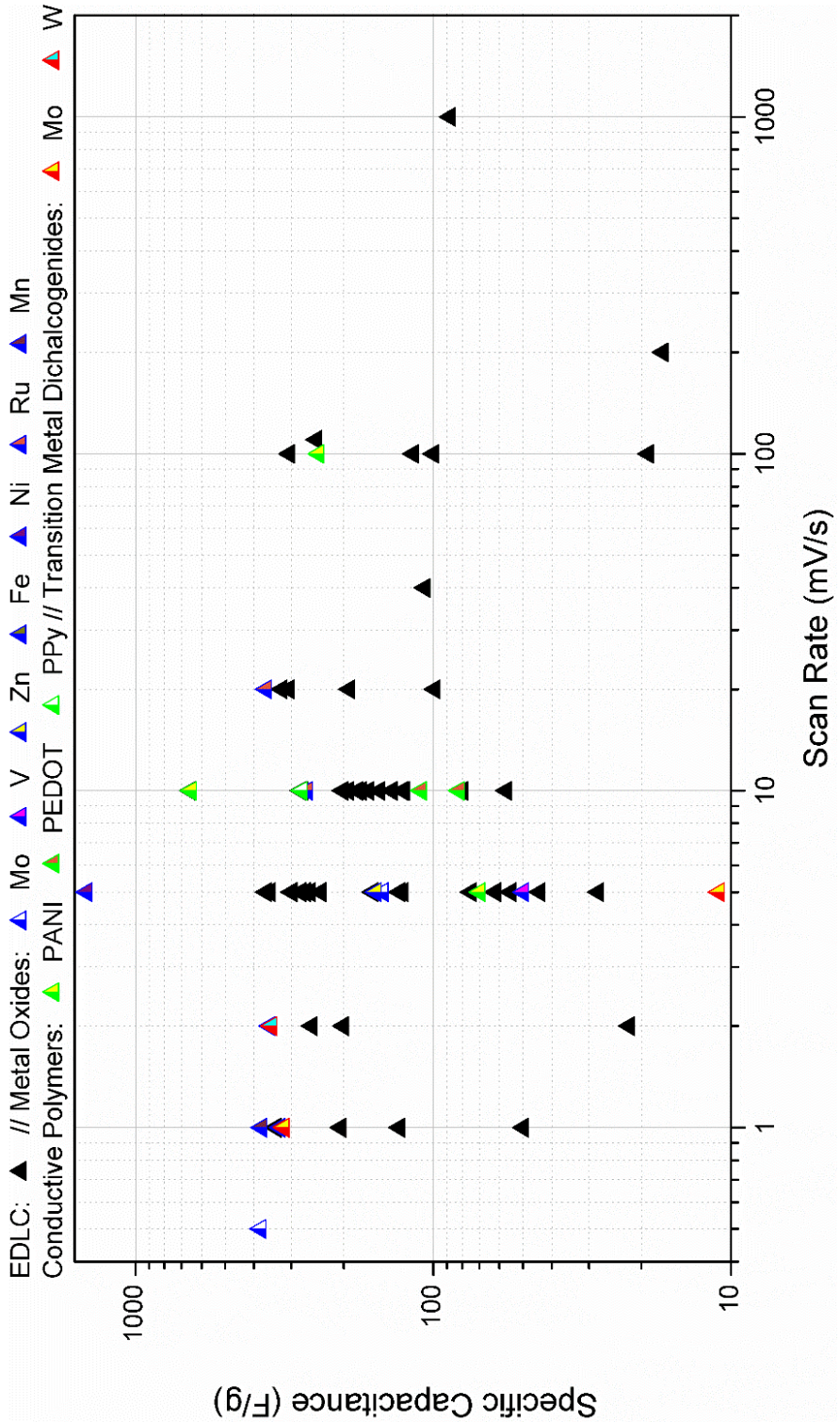

Figure 2. 44. Comparison of the specific capacitance calculated from cyclic voltammetry measurements

REFERENCES

(1) Bissett, M. A.; Kinloch, I. A.; Dryfe, R. A. W. Characterization of MoS_2 –Graphene Composites for High-Performance Coin Cell Supercapacitors. *ACS Appl. Mater. Interfaces* **2015**, *7* (31), 17388–17398.

(2) Harrop, P. Change of Leadership of the Global Market Value of Supercapacitors? *IDTechEx* **2013**.

(3) Yu, A. Aiping Yu, University of Waterloo, Chemical Engineering, Researc http://chemeng.uwaterloo.ca/ayu/research.html.

(4) Fitzer, E.; Kochling, K.-H.; Boehm, H. P.; Marsh, H. Recommended Terminology for the Description of Carbon as a Solid (IUPAC Recommendations 1995). *Pure Appl. Chem.* **1995**, *67* (3), 491.

(5) Geim, A. K.; Kim, P. Carbon Wonderland. *Sci. Am.* **2008**, *298*, 90–97.

(6) Geim, A. K. Random Walk to Graphene. In *The Nobel Prize 2010*; Grandin, K., Ed.; Stockholm, 2010; pp 70–95.

(7) Geim, A. K.; Novoselov, K. S. The Rise of Graphene. *Nat. Mater.* **2007**, *6* (3), 183–191.

(8) Brodie, B. C. On the Atomic Weight of Graphite. *Philos. Trans. R. Soc. London* **1859**, *149*, 249–259.

(9) Dreyer, D. R.; Park, S.; Bielawski, C. W.; Ruoff. The Chemistry of Graphene Oxide. *Chem. Soc. Rev.* **2010**, *39*, 228–240.

(10) Ruess, G.; Vogt, F. Höchstlamellarer Kohlenstoff Aus Graphitoxyhydroxyd. *Monatshefte für Chemie und verwandte Teile anderer Wissenschaften* **1948**, *78* (3–4), 222–242.

(11) Boehm, H. P.; Setton, R.; Stumpp, E. Nomenclature and Terminology of Graphite Intercalation Compounds. *Carbon N. Y.* **1986**, *24* (2), 241–245.

(12) Kroto, H. W.; Heath, J. R.; O'Brien, S. C.; Curl, R. F.; Smalley, R. C. C60:Buckminsterfullerene. *Nature* **1985**, *318* (6042), 162–163.

(13) Seibert, K.; Cho, G. C.; Kutt, W.; Kurz, H.; Reitze, D. H.; Dadap, J. I.; Ahn, H.; Downer, M. C.; Malvezzi, A. M. Femtosecond Carrier Dynamics in Graphite. *Phys. Rev. B* **1990**, *42* (5), 2842–2851.

(14) Iijima, S. Helical Microtubules of Graphitic Carbon. *Nature* **1991**, *354* (6348), 56–58.

(15) Wallace, P. R. The Band Theory of Graphite. *Phys. Rev.* **1947**, *71* (9), 622–634.

(16) Lu, X.; Yu, M.; Huang, H.; Ruoff, R. S. Tailoring Graphite with the Goal of Achieving Single Sheets. *Nanotechnology* **1999**, *10* (3), 269–272.

(17) Little, P. R. Mechanistic Aspects of Carbon Nanotube Nucleation and Growth. *J. Clust. Sci.* **2003**, *14* (2), 135–185.

(18) Novoselov, K. S.; Geim, A. K.; Morozov, S. V.; Jiang, D.; Zhang, Y.; Dubonos, S. V.; Grigorieva, I. V.; Firsov, A. A. Electric Field Effect

in Atomically Thin Carbon Films. *Science* **2004**, *306*, 666–669.

(19) Geim, A. K.; Dubonos, S. V.; Grigorieva, I. V.; Novoselov, K. S.; Zhukov, A. A.; Shapoval, S. Y. Microfabricated Adhesive Mimicking Gecko Foot-Hair. *Nat. Mater.* **2003**, *2*, 461–463.

(20) Geim, A. K. Everyone's Magnetism. *Phys. Today* **1998**, *51* (9), 36–39.

(21) Novoselov, K. S. Graphene: Materials in Flatland. In *The Nobel Prize 2010*; K., G., Ed.; Stockholm, 2010; pp 106–131.

(22) Novoselov, K. S.; Fal'ko, V. I.; Colombo, L.; Gellert, P. R.; Schwab, M. G.; Kim, K. A Roadmap for Graphene. *Nature* **2012**, *490* (7419), 192–200.

(23) Mayorov, A. S.; Gorbachev, R. V.; Morozov, S. V.; Britnell, L.; Jalil, R.; Ponomarenko, L. A.; Blake, P.; Novoselov, K. S.; Watanabe, K.; Taniguchi, T.; Geim, A. K. Micrometer-Scale Ballistic Transport in Encapsulated Graphene at Room Temperature. *Nano Lett.* **2011**, *11* (6), 2396–2399.

(24) Morozov, S. V.; Novoselov, K. S.; Katsnelson, M. I.; Schedin, F.; Elias, D. C.; Jaszczak, J. A.; Geim, A. K. Giant Intrinsic Carrier Mobilities in Graphene and Its Bilayer. *Phys. Rev. Lett.* **2008**, *100* (1), 11–14.

(25) Lee, C.; Wei, X.; Kysar, J. W.; Hone, J. Measurement of the Elastic Properties and Intrinsic Strength of Monolayer Graphene. *Science (80-.).* **2008**, *321* (July), 385–388.

(26) Balandin, A. A. Thermal Properties of Graphene and Nanostructured Carbon Materials. *Nat. Mater.* **2011**, *10* (8), 569–581.

(27) Nair, R. R.; Blake, P.; Grigorenko, A. N.; Novoselov, K. S.; Booth, T. J.; Stauber, T.; Peres, N. M. R.; Geim, A. K. Fine Structure Constant Defines Visual Transparency of Graphene. *Science.* **2008**, *320* (5881), 1308–1308.

(28) Bunch, J. S.; Verbridge, S. S.; Alden, J. S.; Van Der Zande, A. M.; Parpia, J. M.; Craighead, H. G.; McEuen, P. L. Impermeable Atomic Membranes from Graphene Sheets. *Nano Lett.* **2008**, *8* (8), 2458–2462.

(29) Huang, X.; Qi, X.; Chiang, F. Y.; Zhang, H. Graphene-Based Composites. *Chem. Soc. Rev.* **2012**, *41*, 666–686.

(30) Kim, H.; Abdala, A. A.; MacOsko, C. W. Graphene/polymer Nanocomposites. *Macromolecules* **2010**, *43* (16), 6515–6530.

(31) Soldano, C.; Mahmood, A.; Dujardin, E. Production, Properties and Potential of Graphene. *Carbon N. Y.* **2010**, *48* (8), 2127–2150.

(32) Lee, H. C.; Liu, W.-W.; Chai, S.-P.; Mohamed, A. R.; Aziz, A.; Khe, C.-S.; Hidayah, N. M. S.; Hashim, U. Review of the Synthesis, Transfer, Characterization and Growth Mechanisms of Single and Multilayer Graphene. *RSC Adv.* **2017**, *7* (45), 15644–15693.

(33) Zhang, Y.; Small, J. P.; Pontius, W. V.; Kim, P. Fabrication and Electric-Field-Dependent Transport Measurements of Mesoscopic Graphite Devices. *Appl. Phys. Lett.* **2005**, *86* (7), 1–3.

(34) Choi, W.; Lahiri, I.; Seelaboyina, R.; Kang, Y. S. Synthesis of Graphene and Its Applications: A Review. *Crit. Rev. Solid State Mater. Sci.* **2010**, *35* (1), 52–71.

(35) Hernandez, Y.; Nicolosi, V.; Lotya, M.; Blighe, F. M.; Sun, Z.; De, S.; McGovern, I. T.; Holland, B.; Byrne, M.; Gun'Ko, Y. K.; Boland, J. J.; Niraj, P.; Duesberg, G.; Krishnamurthy, S.; Goodhue, R.; Hutchison, J.; Scardaci, V.; Ferrari, A. C.; Coleman, J. N. High-Yield Production of Graphene by Liquid-Phase Exfoliation of Graphite. *Nat. Nanotechnol.* **2008**, *3* (9), 563–568.

(36) Blake, P.; Brimicombe, P. D.; Nair, R. R.; Booth, T. J.; Jiang, D.; Schedin, F.; Ponomarenko, L. A.; Morozov, S. V.; Gleeson, H. F.; Hill, E. W.; Geim, A. K.; Novoselov, K. S. Graphene-Based Liquid Crystal Device. *Nano Lett.* **2008**, *8* (6), 1704–1708.

(37) Bourlinos, A. B.; Georgakilas, V.; Zboril, R.; Sterioti, T. A.; Stubos, A. K. Liquid-Phase Exfoliation of Graphite Towards Solubilized Graphenes. *Small* **2009**, *5* (16), 1841–1845.

(38) Zhu, L.; Zhao, X.; Li, Y.; Yu, X.; Li, C.; Zhang, Q. High-Quality Production of Graphene by Liquid-Phase Exfoliation of Expanded Graphite. *Mater. Chem. Phys.* **2013**, *137* (3), 984–990.

(39) Liu, C.; Hu, G.; Gao, H. Preparation of Few-Layer and Single-Layer Graphene by Exfoliation of Expandable Graphite in Supercritical N,N-Dimethylformamide. *J. Supercrit. Fluids* **2012**, *63*, 99–104.

(40) Parvez, K.; Li, R.; Puniredd, S. R.; Hernandez, Y.; Hinkel, F.; Wang, S.; Feng, X.; Mullen, K. Electrochemically Exfoliated Graphene as Solution-Processable, Highly Conductive Electrodes for Organic Electronics. *ACS Nano* **2013**, *7* (4), 3598–3606.

(41) Parvez, K.; Wu, Z. S.; Li, R.; Liu, X.; Graf, R.; Feng, X.; Mullen, K. Exfoliation of Graphite into Graphene in Aqueous Solutions of Inorganic Salts. *J. Am. Chem. Soc.* **2014**, *136* (16), 6083–6091.

(42) Lotya, M.; Hernandez, Y.; King, P. J.; Smith, R. J.; Nicolosi, V.; Karlsson, L. S.; Blighe, M.; De, S.; Wang, Z.; Mcgovern, I. T.; Duesberg, G. S.; Coleman, J. N. Liquid Phase Production of Graphene by Exfoliation of Graphite in Surfactant / Water Solutions. *J. Am. Chem. Soc.* **2009**, *131* (11), 3611–3620.

(43) Guo, S.; Dong, S. Graphene Nanosheet: Synthesis, Molecular Engineering, Thin Film, Hybrids, and Energy and Analytical Applications. *Chem. Soc. Rev.* **2011**, *40* (5), 2644–2672.

(44) Jiao, L.; Zhang, L.; Wang, X.; Diankov, G.; Dai, H. Narrow Graphene Nanoribbons from Carbon Nanotubes. *Nature* **2009**, *458* (7240), 877–880.

(45) Hirsch, A. Unzipping Carbon Nanotubes: A Peeling Method for the Formation of Graphene Nanoribbons. *Angew. Chemie - Int. Ed.* **2009**, *48* (36), 6594–6596.

(46) Kosynkin, D. V.; Higginbotham, A. L.; Sinitskii, A.; Lomeda, J. R.; Dimiev, A.; Price, B. K.; Tour, J. M. Longitudinal Unzipping of Carbon Nanotubes to Form Graphene Nanoribbons. *Nature* **2009**, *458* (7240), 872–876.

(47) Tanaka, H.; Arima, R.; Fukumori, M.; Tanaka, D.; Negishi, R.; Kobayashi, Y.; Kasai, S.; Yamada, T. K.; Ogawa, T. Method for Controlling Electrical Properties of Single-Layer Graphene Nanoribbons via Adsorbed Planar Molecular Nanoparticles. *Sci. Rep.* **2015**, *5* (November 2014).

(48) Hummers, W. S.; Offeman, R. E. Preparation of Graphitic Oxide. *J. Am. Chem. Soc.* **1958**, *80* (6), 1339–1339.

(49) Li, F.; Jiang, X.; Zhao, J.; Zhang, S. Graphene Oxide: A Promising Nanomaterial for Energy and Environmental Applications. *Nano Energy* **2015**, *16*, 488–515.

(50) Pei, S.; Cheng, H. M. The Reduction of Graphene Oxide. *Carbon N. Y.* **2012**, *50* (9), 3210–3228.

(51) De Silva, K. K. H.; Huang, H.-H.; Joshi, R. K.; Yoshimura, M. Chemical Reduction of Graphene Oxide Using Green Reductants. *Carbon N. Y.* **2017**, *119*, 190–199.

(52) Aunkor, M. T. H.; Mahbubul, I. M.; Saidur, R.; Metselaar, H. S. C. The Green Reduction of Graphene Oxide. *RSC Adv.* **2016**, *6*, 27807–27828.

(53) Naghdi, S.; Rhee, K. Y.; Park, S. J. A Catalytic, Catalyst-Free, and Roll-to-Roll Production of Graphene via Chemical Vapor Deposition: Low Temperature Growth. *Carbon N. Y.* **2018**, *127*, 1–12.

(54) Chen, X.; Wu, B.; Liu, Y. Direct Preparation of High Quality Graphene on Dielectric Substrates. *Chem. Soc. Rev.* **2016**, *45* (8), 2057–2074.

(55) Lin, X.-H.; Gai, J.-G. Synthesis and Applications of Large-Area Single-Layer Graphene. *RSC Adv.* **2016**, *6* (22), 17818–17844.

(56) Cabrero-Vilatela, A.; Weatherup, R. S.; Braeuninger-Weimer, P.; Caneva, S.; Hofmann, S. Towards a General Growth Model for Graphene CVD on Transition Metal Catalysts. *Nanoscale* **2016**, *8* (4), 2149–2158.

(57) Li, X.; Cai, W.; An, J.; Kim, S.; Nah, J.; Yang, D.; Piner, R.; Velamakanni, A.; Jung, I.; Tutuc, E.; Banerjee, S. K.; Colombo, L.; Ruoff, R. S. Large-Area Synthesis of High-Quality and Uniform Graphene Films on Copper Foils. *Science.* **2009**, *324* (5932), 1312–1314.

(58) Kim, K. S.; Zhao, Y.; Jang, H.; Lee, S. Y.; Kim, J. M.; Kim, K. S.; Ahn, J.-H.; Kim, P.; Choi, J.-Y.; Hong, B. H. Large-Scale Pattern Growth of Graphene Films for Stretchable Transparent Electrodes. *Nature* **2009**, *457* (7230), 706–710.

(59) Sutter, P. W.; Flege, J. I.; Sutter, E. A. Epitaxial Graphene on Ruthenium. *Nat. Mater.* **2008**, *7* (5), 406–411.

(60) Xiao, N.; Dong, X.; Song, L.; Liu, D.; Tay, Y.; Wu, S.; Li, L. J.; Zhao, Y.; Yu, T.; Zhang, H.; Huang, W.; Hng, H. H.; Ajayan, P. M.; Yan, Q. Enhanced Thermopower of Graphene Films with Oxygen Plasma Treatment. *ACS Nano* **2011**, *5* (4), 2749–2755.

(61) Dong, X.; Li, B.; Wei, A.; Cao, X.; Chan-Park, M. B.; Zhang, H.; Li, L. J.; Huang, W.; Chen, P. One-Step Growth of Graphene-Carbon Nanotube Hybrid Materials by Chemical Vapor Deposition. *Carbon N. Y.* **2011**, *49* (9), 2944–2949.

(62) Lee, E.; Lee, H. C.; Jo, S. B.; Lee, H.; Lee, N. S.; Park, C. G.; Lee, S. K.; Kim, H. H.; Bong, H.; Cho, K. Heterogeneous Solid Carbon Source-Assisted Growth of High-Quality Graphene via CVD at Low Temperatures. *Adv. Funct. Mater.* **2016**, *26* (4), 562–568.

(63) Reinke, M.; Kuzminykh, Y.; Hoffmann, P. Low Temperature Chemical Vapor Deposition Using Atomic Layer Deposition Chemistry. *Chem. Mater.* **2015**, *27* (5), 1604–1611.

(64) Jang, J.; Son, M.; Chung, S.; Kim, K.; Cho, C.; Lee, B. H.; Ham, M. H. Low-Temperature-Grown Continuous Graphene Films from Benzene by Chemical Vapor Deposition at Ambient Pressure. *Sci. Rep.* **2015**, *5* (November), 1–7.

(65) Bae, S.; Kim, H. K.; Lee, Y.; Xu, X.; Park, J.-S.; Zheng, Y.; Balakrishnan, J.; Im, D.; Lei, T.; Song, Y. Il; Kim, Y. J.; Kim, K. S.; Özyilmaz, B.; Ahn, J.-H.; Hong, B. H.; Iijima, S. 30 Inch Roll-Based Production of High-Quality Graphene Films for Flexible Transparent Electrodes. *Nat. Nanotechnol.* **2010**, *5* (August), 574–578.

(66) Nandamuri, G.; Roumimov, S.; Solanki, R. Chemical Vapor Deposition of Graphene Films. *Nanotechnology* **2010**, *21* (14).

(67) Yuan, G. D.; Zhang, W. J.; Yang, Y.; Tang, Y. B.; Li, Y. Q.; Wang, J. X.; Meng, X. M.; He, Z. B.; Wu, C. M. L.; Bello, I.; Lee, C. S.; Lee, S. T. Graphene Sheets via Microwave Chemical Vapor Deposition. *Chem. Phys. Lett.* **2009**, *467* (4–6), 361–364.

(68) Wang, Y.; Xu, X.; Lu, J.; Lin, M.; Bao, Q.; Özyilmaz, B.; Loh, K. P. Toward High Throughput Interconvertible Graphane-to-Graphene Growth and Patterning. *ACS Nano* **2010**, *4* (10), 6146–6152.

(69) Malesevic, A.; Vitchev, R.; Schouteden, K.; Volodin, A.; Zhang, L.; Tendeloo, G. Van; Vanhulsel, A.; Haesendonck, C. Van. Synthesis of Few-Layer Graphene via Microwave Plasma-Enhanced Chemical Vapour Deposition. *Nanotechnology* **2008**, *19* (30).

(70) Dervishi, E.; Li, Z.; Watanabe, F.; Biswas, A.; Xu, Y.; Biris, A. R.; Saini, V.; Biris, A. S. Large-Scale Graphene Production by RF-cCVD Method. *Chem. Commun.* **2009**, No. 27, 4061.

(71) Reina, A.; Jia, X.; Ho, J.; Nezich, D.; Son, H.; Bulovic, V.; Dresselhaus, M. S.; Jing, K. Large Area, Few-Layer Graphene Films on Arbitrary Substrates by Chemical Vapor Deposition. *Nano Lett.* **2009**, *9* (1), 30–35.

(72) Emtsev, K. V.; Bostwick, A.; Horn, K.; Jobst, J.; Kellogg, G. L.; Ley, L.; McChesney, J. L.; Ohta, T.; Reshanov, S. A.; Röhrl, J.; Rotenberg, E.; Schmid, A. K.; Waldmann, D.; Weber, H. B.; Seyller, T. Towards Wafer-Size Graphene Layers by Atmospheric Pressure Graphitization of Silicon Carbide. *Nat. Mater.* **2009**, *8* (3), 203–207.

(73) Shivaraman, S.; Barton, R. A.; Yu, X.; Alden, J.; Herman, L.; Chandrashekhar, M. S. V; Park, J.; McEuen, P. L.; Parpia, J. M.; Craighead, H. G.; Spencer, M. G. Free-Standing Epitaxial Graphene. *Nano Lett.* **2009**, *9* (9), 3100–3105.

(74) Aristov, V. Y.; Urbanik, G.; Kummer, K.; Vyalikh, D. V.; Molodtsova, O. V.; Preobrajenski, A. B.; Zakharov, A. A.; Hess, C.; Hänke, T.; Büchner, B.; Vobornik, I.; Fujii, J.; Panaccione, G.; Ossipyan, Y. A.; Knupfer, M. Graphene Synthesis on Cubic SiC/Si Wafers. Perspectives for Mass Production of Graphene-Based Electronic Devices. *Nano Lett.* **2010**, *10* (3), 992–995.

(75) Berger, C.; Song, Z.; Li, T.; Li, X.; Ogbazghi, A. Y.; Feng, R.; Dai, Z.; Marchenkov, A. N.; Conrad, E. H.; First, P. N.; de Heer, W. a. Ultrathin Epitaxial Graphite: 2D Electron Gas Properties and a Route toward Graphene-Based Nanoelectronics. *J. Phys. Chem. B* **2004**, *108* (52), 19912–19916.

(76) Berger, C. Electronic Confinement and Coherence in Patterned Epitaxial Graphene. *Science.* **2006**, *312* (5777), 1191–1196.

(77) Ohta, T. Controlling the Electronic Structure of Bilayer Graphene. *Science.* **2006**, *313* (5789), 951–954.

(78) Forbeaux, I.; Themlin, J.-M.; Debever, J.-M. Heteroepitaxial Graphite on 6H-SiC(0001): Interface Formation through Conduction-Band Electronic Structure. *Phys. Rev. B* **1998**, *58* (24), 16396–16406.

(79) Deng, D.; Pan, X.; Zhang, H.; Fu, Q.; Tan, D.; Bao, X. Freestanding Graphene by Thermal Splitting of Silicon Carbide Granules. *Adv. Mater.* **2010**, *22* (19), 2168–2171.

(80) Virojanadara, C.; Syväjarvi, M.; Yakimova, R.; Johansson, L. I.; Zakharov, A. A.; Balasramanian, T. Homogeneous Large-Area Graphene Layer Growth on 6H-SiC(0001). *Phys. Rev. B - Condens. Matter Mater. Phys.* **2008**, *78* (24), 1–6.

(81) Ribeiro-Soares, J.; Dresselhaus, M. S. News and Views: Perspectives on Graphene and Other 2D Materials Research and Technology Investments. *Brazilian J. Phys.* **2014**, *44* (2–3), 278–282.

(82) Ren, W.; Cheng, H. M. The Global Growth of Graphene. *Nat. Nanotechnol.* **2014**, *9* (10), 726–730.

(83) Cao, X.; Yin, Z.; Zhang, H. Three-Dimensional Graphene Materials: Preparation, Structures and Application in Supercapacitors. *Energy Environ. Sci.* **2014**, *7* (6), 1850–1865.

(84) Ren, J.; Bai, W.; Guan, G.; Zhang, Y.; Peng, H. Flexible and Weaveable Capacitor Wire Based on a Carbon Nanocomposite Fiber. *Adv. Mater.* **2013**, *25* (41), 5965–5970.

(85) Palaniselvam, T.; Baek, J.-B. Graphene Based 2D-Materials for Supercapacitors. *2D Mater.* **2015**, *2* (3), 32002.

(86) Yang, W.; Ni, M.; Ren, X.; Tian, Y.; Li, N.; Su, Y.; Zhang, X. Graphene in Supercapacitor Applications. *Curr. Opin. Colloid Interface Sci.* **2015**, *20* (5–6), 416–428.

(87) Mendoza-Sánchez, B.; Gogotsi, Y. Synthesis of Two-Dimensional Materials for Capacitive Energy Storage. *Adv. Mater.* **2016**, 6104–6135.

(88) Shi, Q.; Cha, Y.; Song, Y.; Lee, J.-I.; Zhu, C.; Li, X.; Song, M.-K.; Du, D.; Lin, Y. 3D Graphene-Based Hybrid Materials: Synthesis and Applications in Energy Storage and Conversion. *Nanoscale* **2016**, *8* (34), 15414–15447.

(89) Shen, J.; Zhu, Y.; Jiang, H.; Li, C. 2D Nanosheets-Based Novel Architectures: Synthesis, Assembly and Applications. *Nano Today* **2016**, *11* (4), 483–520.

(90) El-Kady, M. F.; Shao, Y.; Kaner, R. B. Graphene for Batteries, Supercapacitors and beyond. *Nat. Rev. Mater.* **2016**, *1* (7), 16033.

(91) Peng, L.; Zhu, Y.; Li, H.; Yu, G. Chemically Integrated Inorganic-Graphene Two-Dimensional Hybrid Materials for Flexible Energy Storage Devices. *Small* **2016**, *12* (45), 6183–6199.

(92) Guo, X.; Zheng, S.; Zhang, G.; Xiao, X.; Li, X.; Xu, Y.; Xue, H.; Pang, H. Nanostructured Graphene-Based Materials for Flexible Energy Storage. *Energy Storage Mater.* **2017**, *9* (July), 150–169.

(93) Tan, K. L.; Reeves, S.; Hashemi, N.; Thomas, D. G.; Kavak, E.; Montazami, R.; Hashemi, N. Graphene as Flexible Electrode: Review of Fabrication Approaches. *J. Mater. Chem. A* **2017**, *5*, 17777–17803.

(94) Liu, T.; Ding, J.; Su, Z.; Wei, G. Porous Two-Dimensional Materials for Energy Applications: Innovations and Challenges. *Mater. Today Energy* **2017**, *6*, 79–95.

(95) Vivekchand, S. R. C.; Rout, C. S.; Subrahmanyam, K. S.; Govindaraj, A.; Rao, C. N. R. Graphene-Based Electrochemical Supercapacitors. *J. Chem. Sci.* **2008**, *120* (1), 9–13.

(96) Stoller, M. D.; Park, S.; Yanwu, Z.; An, J.; Ruoff, R. S. Graphene-Based Ultracapacitors. *Nano Lett.* **2008**, *8* (10), 3498–3502.

(97) Wang, Y.; Shi, Z.; Huang, Y.; Ma, Y.; Wang, C.; Chen, M.; Chen, Y. Supercapacitor Devices Based on Graphene Materials. *J. Phys. Chem. C* **2009**, *113*, 13103–13107.

(98) Lv, W.; Tang, D. M.; He, Y. B.; You, C. H.; Shi, Z. Q.; Chen, X. C.; Chen, C. M.; Hou, P. X.; Liu, C.; Yang, Q. H. Low-Temperature Exfoliated Graphenes: Vacuum-Promoted Exfoliation and Electrochemical Energy Storage. *ACS Nano* **2009**, *3* (11), 3730–3736.

(99) Chen, D. Z.; Zhu, Y.; Stoller, M. D.; Cai, W.; Velamakanni, A.; Piner, R. D.; Chen, D.; Ruoff, R. S. Exfoliation of Graphite Oxide in Propylene Carbonate and Thermal Oxide Platelets. *ACS Nano* **2010**, *4* (2), 1227–1233.

(100) Lei, Z.; Christov, N.; Zhao, X. S. Intercalation of Mesoporous Carbon Spheres between Reduced Graphene Oxide Sheets for Preparing High-Rate Supercapacitor Electrodes. *Energy Environ. Sci.* **2011**, *4* (5), 1866–1873.

(101) Mishra, A. K.; Ramaprabhu, S. Functionalized Graphene-Based Nanocomposites for Supercapacitor Application. *J. Phys. Chem. C* **2011**, *115* (29), 14006–14013.

(102) Fang, Y.; Luo, B.; Jia, Y.; Li, X.; Wang, B.; Song, Q.; Kang, F.; Zhi, L. Renewing Functionalized Graphene as Electrodes for High-Performance Supercapacitors. *Adv. Mater.* **2012**, *24* (47), 6348–6355.

(103) Ye, J.; Zhang, H.; Chen, Y.; Cheng, Z.; Hu, L.; Ran, Q. Supercapacitors Based on Low-Temperature Partially Exfoliated and Reduced Graphite Oxide. *J. Power Sources* **2012**, *212*, 105–110.

(104) Yoon, Y.; Lee, K.; Baik, C.; Yoo, H.; Min, M.; Park, Y.; Lee, S. M.; Lee, H. Anti-Solvent Derived Non-Stacked Reduced Graphene Oxide for High Performance Supercapacitors. *Adv. Mater.* **2013**, *25* (32), 4437–4444.

(105) Jo, E. H.; Choi, J. H.; Park, S. R.; Lee, C. M.; Chang, H.; Jang, H. D. Size and Structural Effect of Crumpled Graphene Balls on the Electrochemical Properties for Supercapacitor Application. *Electrochim. Acta* **2016**, *222*, 58–63.

(106) Ervin, M. H.; Le, L. T.; Lee, W. Y. Inkjet-Printed Flexible Graphene-Based Supercapacitor. *Electrochim. Acta* **2014**, *147*, 610–616.

(107) Li, Z. .; Yang, B. .; Li, K. .; Wang, H. .; Lv, X. .; Guo, Y. .; Zhang, Z. .; Su, Y. . Freestanding 3D Mesoporous Graphene Oxide for High Performance Energy Storage Applications. *RSC Adv.* **2014**, *4* (93), 51640–51647.

(108) Yang, H.; Kannappan, S.; Pandian, A. S.; Jang, J. H.; Lee, Y. S.; Lu, W. Nanoporous Graphene Materials by Lowerature Vacuum-Assisted Thermal Process for Electrochemical Energy Storage. *J. Power Sources* **2015**, *284*, 146–153.

(109) Tamilarasan, P.; Ramaprabhu, S. Graphene Based All-Solid-State Supercapacitors with Ionic Liquid Incorporated Polyacrylonitrile Electrolyte. *Energy* **2013**, *51*, 374–381.

(110) Li, Q.; Guo, X.; Zhang, Y.; Zhang, W.; Ge, C.; Zhao, L.; Wang, X.; Zhang, H.; Chen, J.; Wang, Z.; Sun, L. Porous Graphene Paper for Supercapacitor Applications. *J. Mater. Sci. Technol.* **2017**, *33* (8), 793–799.

(111) Xiong, Z.; Liao, C.; Wang, X. A Self-Assembled Macroporous Coagulation Graphene Network with High Specific Capacitance for Supercapacitor Applications. *J. Mater. Chem. A* **2014**, *2* (45), 19141–19144.

(112) Pachfule, P.; Shinde, D.; Majumder, M.; Xu, Q. Fabrication of Carbon Nanorods and Graphene Nanoribbons from a Metal–organic Framework. *Nat. Chem.* **2016**, *8* (7), 718–724.

(113) Yang, X.; Zhang, L.; Zhang, F.; Zhang, T.; Huang, Y.; Chen, Y. A High-Performance All-Solid-State Supercapacitor with Graphene-Doped Carbon Material Electrodes and a Graphene Oxide-Doped Ion Gel Electrolyte. *Carbon N. Y.* **2014**, *72*, 381–386.

(114) Huang, J.; Wang, J.; Wang, C.; Zhang, H.; Lu, C.; Wang, J. Hierarchical Porous Graphene Carbon-Based Supercapacitors. *Chem. Mater.* **2015**, *27* (6), 2107–2113.

(115) Liu, D.; Jia, Z.; Wang, D. Preparation of Hierarchically Porous Carbon Nanosheet Composites with Graphene Conductive Scaffolds for Supercapacitors: An Electrostatic-Assistant Fabrication Strategy. *Carbon N. Y.* **2016**, *100*, 664–677.

(116) Zoromba, M. S.; Abdel-Aziz, M. H.; Bassyouni, M.; Gutub, S.; Demko, D.; Abdelkader, A. Electrochemical Activation of Graphene at Low Temperature: The Synthesis of Three-Dimensional Nanoarchitectures for High Performance Supercapacitors and Capacitive Deionization. *ACS Sustain. Chem. Eng.* **2017**, *5* (6), 4573–4581.

(117) Shao, Y.; El-Kady, M. F.; Lin, C. W.; Zhu, G.; Marsh, K. L.; Hwang, J. Y.; Zhang, Q.; Li, Y.; Wang, H.; Kaner, R. B. 3D Freeze-Casting of Cellular Graphene Films for Ultrahigh-Power-Density Supercapacitors. *Adv. Mater.* **2016**, 6719–6726.

(118) Mohanapriya, K.; Ghosh, G.; Jha, N. Solar Light Reduced Graphene as High Energy Density Supercapacitor and Capacitive Deionization Electrode. *Electrochim. Acta* **2016**, *209*, 719–729.

(119) Zhu, Y.; Murali, S.; Stoller, M. D.; Velamakanni, A.; Piner, R. D.; Ruoff, R. S. Microwave Assisted Exfoliation and Reduction of Graphite Oxide for Ultracapacitors. *Carbon*. Elsevier Ltd 2010, pp 2118–2122.

(120) Zhu, Y.; Murali, S.; Stoller, M. D.; Ganesh, K. J.; Cai, W.; Ferreira, P. J.; Pirkle, A.; Wallace, R. M.; Cychosz, K. a; Thommes, M.; Su, D.; Stach, E. a; Ruoff, R. S. Carbon-Based Supercapacitors Produced by Activation of Graphene. *Science.* **2011**, *332* (June), 1537–1542.

(121) Wang, J.; Kaskel, S. KOH Activation of Carbon-Based Materials for Energy Storage. *J. Mater. Chem.* **2012**, *22* (45), 23710.

(122) Kim, T.; Jung, G.; Yoo, S.; Suh, K. S.; Ruoff, R. S. Activated Graphene-Based Carbons as Supercapacitor Electrodes with Macro- and Mesopores. *ACS Nano* **2013**, *7* (8), 6899–6905.

(123) Murali, S.; Quarles, N.; Zhang, L. L.; Potts, J. R.; Tan, Z.; Lu, Y.; Zhu, Y.; Ruoff, R. S. Volumetric Capacitance of Compressed Activated Microwave-Expanded Graphite Oxide (a-MEGO) Electrodes. *Nano Energy* **2013**, *2* (5), 764–768.

(124) Tsai, W. Y.; Lin, R.; Murali, S.; Li Zhang, L.; McDonough, J. K.; Ruoff, R. S.; Taberna, P. L.; Gogotsi, Y.; Simon, P. Outstanding Performance of Activated Graphene Based Supercapacitors in Ionic Liquid Electrolyte from -50 to 80°C. *Nano Energy* **2013**, *2* (3), 403–411.

(125) Shulga, Y. M.; Baskakov, S. A.; Baskakova, Y. V.; Volfkovich, Y. M.; Shulga, N. Y.; Skryleva, E. A.; Parkhomenko, Y. N.; Belay, K. G.; Gutsev, G. L.; Rychagov, A. Y.; Sosenkin, V. E.; Kovalev, I. D. Supercapacitors with Graphene Oxide Separators and Reduced Graphite Oxide Electrodes. *J. Power Sources* **2015**, *279*, 722–730.

(126) Subramanya, B.; Bhat, D. K. Novel One-Pot Green Synthesis of Graphene in Aqueous Medium under Microwave Irradiation Using a Regenerative Catalyst and the Study of Its Electrochemical Properties. *New J. Chem.* **2015**, *39* (1), 420–430.

(127) Liu, C.; Yu, Z.; Neff, D.; Zhamu, A.; Jang, B. Z. Graphene-Based Supercapacitor with an Ultrahigh Energy Density. *Nano Lett.* **2010**, *10* (12), 4863–4868.

(128) Xu, Y.; Sheng, K.; Li, C.; Shi, G. Self-Assembled Graphene Hydrogel *via* a One-Step Hydrothermal Process. *ACS Nano* **2010**, *4* (7), 4324–4330.

(129) Bai, Y.; Rakhi, R. B.; Chen, W.; Alshareef, H. N. Effect of pH-Induced Chemical Modification of Hydrothermally Reduced Graphene Oxide on Supercapacitor Performance. *J. Power Sources* **2013**, *233*, 313–319.

(130) Kou, L.; Liu, Z.; Huang, T.; Zheng, B.; Tian, Z.; Deng, Z.; Gao, C. Wet-Spun, Porous, Orientational Graphene Hydrogel Films for High-Performance Supercapacitor Electrodes. *Nanoscale* **2015**, *7* (9), 4080–4087.

(131) Lamberti, A.; Gigot, A.; Bianco, S.; Fontana, M.; Castellino, M.; Tresso, E.; Pirri, C. F. Self-Assembly of Graphene Aerogel on Copper Wire for Wearable Fiber-Shaped Supercapacitors. *Carbon N. Y.* **2016**, *105*, 649–654.

(132) Zhang, L.; Shi, G. Preparation of Highly Conductive Graphene Hydrogels for Fabricating Supercapacitors with High Rate Capability. *J. Phys. Chem. C* **2011**, *115* (34), 17206–17212.

(133) Kim, S. K.; Kim, H. J.; Lee, J. C.; Braun, P. V.; Park, H. S. Extremely Durable, Flexible Supercapacitors with Greatly Improved Performance at High Temperatures. *ACS Nano* **2015**, *9* (8), 8569–8577.

(134) Teo, E. Y. L.; Lim, H. N.; Jose, R.; Chong, K. F. Aminopyrene Functionalized Reduced Graphene Oxide as a Supercapacitor Electrode. *RSC Adv.* **2015**, *5* (48), 38111–38116.

(135) Choi, B. G.; Hong, J.; Hong, W. H.; Hammond, P. T.; Park, H. Facilitated Ion Transport in All-Solid-State Flexible Supercapacitors. *ACS Nano* **2011**, *5* (9), 7205–7213.

(136) Lei, Z.; Lu, L.; Zhao, X. S. The Electrocapacitive Properties of Graphene Oxide Reduced by Urea. *Energy Environ. Sci.* **2012**, *5* (4), 6391–6399.

(137) Perera, S. D.; Mariano, R. G.; Nijem, N.; Chabal, Y.; Ferraris, J. P.; Balkus, K. J. Alkaline Deoxygenated Graphene Oxide for Supercapacitor Applications: An Effective Green Alternative for Chemically Reduced Graphene. *J. Power Sources* **2012**, *215*, 1–10.

(138) Xu, Y.; Lin, Z.; Huang, X.; Liu, Y.; Huang, Y.; Duan, X. Flexible Solid-State Supercapacitors Based on Three-Dimensional Graphene Hydrogel Films. *ACS Nano* **2013**, *7* (5), 4042–4049.

(139) Luo, G.; Huang, H.; Lei, C.; Cheng, Z.; Wu, X.; Tang, S.; Du, Y. Facile Synthesis of Porous Graphene as Binder-Free Electrode for Supercapacitor Application. *Appl. Surf. Sci.* **2016**, *366*, 46–52.

(140) An, N.; An, Y.; Hu, Z.; Guo, B.; Yang, Y.; Lei, Z. Graphene Hydrogels Non-Covalently Functionalized with Alizarin: An Ideal Electrode Material for Symmetric Supercapacitors. *J. Mater. Chem. A* **2015**, *3* (44), 22239–22246.

(141) Xu, Y.; Lin, Z.; Zhong, X.; Huang, X.; Weiss, N. O.; Huang, Y.; Duan, X. Holey Graphene Frameworks for Highly Efficient Capacitive Energy Storage. *Nat. Commun.* **2014**, *5* (4554), 1–8.

(142) Bo, Z.; Shuai, X.; Mao, S.; Yang, H.; Qian, J.; Chen, J.; Yan, J.; Cen, K. Green Preparation of Reduced Graphene Oxide for Sensing and Energy Storage Applications. *Sci. Rep.* **2015**, *4* (1), 4684.

(143) Bo, Z.; Zhu, W.; Ma, W.; Wen, Z.; Shuai, X.; Chen, J.; Yan, J.; Wang, Z.; Cen, K.; Feng, X. Vertically Oriented Graphene Bridging Active-Layer/current-Collector Interface for Ultrahigh Rate Supercapacitors. *Adv. Mater.* **2013**, *25* (40), 5799–5806.

(144) Zuo, Z.; Kim, T. Y.; Kholmanov, I.; Li, H.; Chou, H.; Li, Y. Ultra-Light Hierarchical Graphene Electrode for Binder-Free Supercapacitors and Lithium-Ion Battery Anodes. *Small* **2015**, *11* (37), 4922–4930.

(145) Xu, Y.; Lin, Z.; Huang, X.; Wang, Y.; Huang, Y.; Duan, X. Functionalized Graphene Hydrogel-Based High-Performance Supercapacitors. *Adv. Mater.* **2013**, *25* (40), 5779–5784.

(146) Zhang, L.; Yang, C.; Hu, N.; Yang, Z.; Wei, H.; Chen, C.; Wei, L.; Xu, Z. J.; Zhang, Y. Steamed Water Engineering Mechanically Robust Graphene Films for High-Performance Electrochemical Capacitive Energy Storage. *Nano Energy* **2016**, *26*, 668–676.

(147) Ju, H.-F.; Song, W.-L.; Fan, L.-Z. Rational Design of Graphene/porous Carbon Aerogels for High-Performance Flexible All-Solid-State Supercapacitors. *J. Mater. Chem. A* **2014**, *2* (28), 10895–10903.

(148) Enterría, M.; Martín-Jimeno, F. J.; Suárez-García, F.; Paredes, J. I.; Pereira, M. F. R.; Martins, J. I.; Martínez-Alonso, A.; Tascón, J. M. D.; Figueiredo, J. L. Effect of Nanostructure on the Supercapacitor Performance of Activated Carbon Xerogels Obtained from Hydrothermally Carbonized Glucose-Graphene Oxide Hybrids. *Carbon N. Y.* **2016**, *105*, 474–483.

(149) An, X.; Simmons, T.; Shah, R.; Wolfe, C.; Lewis, K. M.; Washington, M.; Nayak, S. K.; Talapatra, S.; Kar, S. Stable Aqueous Dispersions of Noncovalently Functionalized Graphene from Graphite and Their Multifunctional High-Performance Applications. *Nano Lett.* **2010**, *10* (11), 4295–4301.

(150) Ghosh, S.; An, X.; Shah, R.; Rawat, D.; Dave, B.; Kar, S.; Talapatra, S. Effect of 1-Pyrene Carboxylic-Acid Functionalization of Graphene on Its Capacitive Energy Storage. *J. Phys. Chem. C* **2012**, *116* (39), 20688–20693.

(151) Yang, S.; Brüller, S.; Wu, Z. S.; Liu, Z.; Parvez, K.; Dong, R.; Richard, F.; Samorì, P.; Feng, X.; Müllen, K. Organic Radical-Assisted Electrochemical Exfoliation for the Scalable Production of High-Quality Graphene. *J. Am. Chem. Soc.* **2015**, *137* (43), 13927–13932.

(152) Jung, S. M.; Mafra, D. L.; Lin, C.-T.; Jung, H. Y.; Kong, J. Controlled Porous Structures of Graphene Aerogels and Their Effect on Supercapacitor Performance. *Nanoscale* **2015**, *7* (10), 4386–4393.

(153) Munuera, J. M.; Paredes, J. I.; Enterría, M.; Pagán, A.; Villar-Rodil, S.; Pereira, M. F. R.; Martins, J. I.; Figueiredo, J. L.; Cenis, J. L.; Martínez-Alonso, A.; Tascón, J. M. D. Electrochemical Exfoliation of Graphite in Aqueous Sodium Halide Electrolytes toward Low Oxygen Content Graphene for Energy and Environmental Applications. *ACS Appl. Mater. Interfaces* **2017**, *9* (28), 24085–24099.

(154) Ejigu, A.; Kinloch, I. A.; Dryfe, R. A. W. Single Stage Simultaneous Electrochemical Exfoliation and Functionalization of Graphene. *ACS Appl. Mater. Interfaces* **2017**, *9* (1), 710–721.

(155) Li, L.; Secor, E. B.; Chen, K. S.; Zhu, J.; Liu, X.; Gao, T. Z.; Seo, J. W. T.; Zhao, Y.; Hersam, M. C. High-Performance Solid-State Supercapacitors and Microsupercapacitors Derived from Printable Graphene Inks. *Adv. Energy Mater.* **2016**, *6* (20), 1–8.

(156) Kim, H.-K.; Kamali, A. R.; Roh, K. C.; Kim, K.-B.; Fray, D. J. Dual Coexisting Interconnected Graphene Nanostructures for High Performance Supercapacitor Applications. *Energy Environ. Sci.* **2016**, *9* (7), 2249–2256.

(157) Amiri, A.; Shanbedi, M.; Ahmadi, G.; Eshghi, H.; Kazi, S. N.; Chew, B. T.; Savari, M.; Zubir, M. N. M. Mass Production of Highly-Porous Graphene for High-Performance Supercapacitors. *Sci. Rep.* **2016**, *6* (1), 32686.

(158) Zhou, Q.; Zhao, Z.; Chen, Y.; Hu, H.; Qiu, J. Low Temperature Plasma-Mediated Synthesis of Graphene Nanosheets for Supercapacitor Electrodes. *J. Mater. Chem.* **2012**, *22* (13), 6061–6066.

(159) Wang, K.; Xu, M.; Shrestha, M.; Gu, Z.; Fan, Q. H. Plasma-Assisted Fabrication of Graphene in Ambient Temperature for Symmetric Supercapacitors Application. *Mater. Today Energy* **2017**, *4*, 7–13.

(160) Bo, Z.; Zhu, W.; Tu, X.; Yang, Y.; Mao, S.; He, Y.; Chen, J.; Yan, J.; Cen, K. Instantaneous Reduction of Graphene Oxide Paper for Supercapacitor Electrodes with Unimpeded Liquid Permeation. *J. Phys. Chem. C* **2014**, *118* (25), 13493–13502.

(161) Seo, D. H.; Pineda, S.; Yick, S.; Bell, J.; Han, Z. J.; Ostrikov, K. (Ken). Plasma-Enabled Sustainable Elemental Lifecycles: Honeycomb-Derived Graphenes for next-Generation Biosensors and Supercapacitors. *Green Chem.* **2015**, *17* (4), 2164–2171.

(162) Xu, P.; Kang, J.; Choi, J. B.; Suhr, J.; Yu, J.; Li, F.; Byun, J. H.; Kim, B. S.; Chou, T. W. Laminated Ultrathin Chemical Vapor Deposition Graphene Films Based Stretchable and Transparent High-Rate Supercapacitor. *ACS Nano* **2014**, *8* (9), 9437–9445.

(163) Qin, K.; Kang, J.; Li, J.; Liu, E.; Shi, C.; Zhang, Z.; Zhang, X.; Zhao, N. Continuously Hierarchical Nanoporous Graphene Film for Flexible Solid-State Supercapacitors with Excellent Performance. *Nano Energy* **2016**, *24*, 158–164.

(164) Ramadoss, A.; Yoon, K. Y.; Kwak, M. J.; Kim, S. I.; Ryu, S. T.; Jang, J. H. Fully Flexible, Lightweight, High Performance All-Solid-State Supercapacitor Based on 3-Dimensional-Graphene/graphite-Paper. *J. Power Sources* **2017**, *337*, 159–165.

(165) Kim, K. H.; Yang, M.; Cho, K. M.; Jun, Y.-S.; Lee, S. B.; Jung, H.-T. High Quality Reduced Graphene Oxide through Repairing with Multi-Layered Graphene Ball Nanostructures. *Sci. Rep.* **2013**, *3* (1), 3251.

(166) Yoo, J. J.; Balakrishnan, K.; Huang, J.; Meunier, V.; Sumpter, B. G.; Srivastava, A.; Conway, M.; Reddy, A. L. M.; Yu, J.; Vajtai, R.; Ajayan, P. M. Ultrathin Planar Graphene Supercapacitors. *Nano Lett.* **2011**, *11* (4), 1423–1427.

(167) Zhang, S.; Li, Y.; Pan, N. Graphene Based Supercapacitor Fabricated by Vacuum Filtration Deposition. *J. Power Sources* **2012**, *206*, 476–482.

(168) Zhang, S.; Pan, N. Supercapacitor Performance of Crumpled and Planar Graphene Materials Produced by Hydrogen Gas Reduction of Graphene Oxide. *J. Mater. Chem. A* **2013**, *1* (27), 7957–7962.

(169) Zhang, J.; Tian, T.; Chen, Y.; Niu, Y.; Tang, J.; Qin, L. C. Synthesis of Graphene from Dry Ice in Flames and Its Application in Supercapacitors. *Chem. Phys. Lett.* **2014**, *591*, 78–81.

(170) Xue, Y.; Zhu, L.; Chen, H.; Qu, J.; Dai, L. Multiscale Patterning of Graphene Oxide and Reduced Graphene Oxide for Flexible Supercapacitors. *Carbon N. Y.* **2015**, *92*, 305–310.

(171) Wang, D.; Min, Y.; Yu, Y.; Peng, B. Laser Induced Self-Propagating Reduction and Exfoliation of Graphite Oxide as an Electrode Material for Supercapacitors. *Electrochim. Acta* **2014**, *141*, 271–278.

(172) Yang, D.; Bock, C. Laser Reduced Graphene for Supercapacitor Applications. *J. Power Sources* **2017**, *337*, 73–81.

(173) Wang, L. J.; El-Kady, M. F.; Dubin, S.; Hwang, J. Y.; Shao, Y.; Marsh, K.; McVerry, B.; Kowal, M. D.; Mousavi, M. F.; Kaner, R. B. Flash Converted Graphene for Ultra-High Power Supercapacitors. *Adv. Energy Mater.* **2015**, *5* (18), 1–8.

(174) Xiang, F.; Zhong, J.; Gu, N.; Mukherjee, R.; Oh, I. K.; Koratkar, N.; Yang, Z. Far-Infrared Reduced Graphene Oxide as High Performance Electrodes for Supercapacitors. *Carbon N. Y.* **2014**, *75*, 201–208.

(175) Wang, C.; He, X.; Shang, Y.; Peng, Q.; Qin, Y.; Shi, E.; Yang, Y.; Wu, S.; Xu, W.; Du, S.; Cao, A.; Li, Y. Multifunctional Graphene Sheet–nanoribbon Hybrid Aerogels. *J. Mater. Chem. A* **2014**, *2* (36), 14994–15000.

(176) Ye, X.; Zhou, Q.; Jia, C.; Tang, Z.; Zhu, Y.; Wan, Z. Producing Large-Area, Foldable Graphene Paper from Graphite Oxide Suspensions by in-Situ Chemical Reduction Process. *Carbon N. Y.* **2017**, *114*, 424–434.

(177) Ye, X.; Zhu, Y.; Tang, Z.; Wan, Z.; Jia, C. In-Situ Chemical Reduction Produced Graphene Paper for Flexible Supercapacitors with Impressive Capacitive Performance. *J. Power Sources* **2017**, *360*, 48–58.

(178) Zhu, C.; Liu, T.; Qian, F.; Han, T. Y. J.; Duoss, E. B.; Kuntz, J. D.; Spadaccini, C. M.; Worsley, M. A.; Li, Y. Supercapacitors Based on Three-Dimensional Hierarchical Graphene Aerogels with Periodic Macropores. *Nano Lett.* **2016**, *16* (6), 3448–3456.

(179) Liu, X.; Qi, X.; Zhang, Z.; Ren, L.; Hao, G.; Liu, Y.; Wang, Y.; Huang, K.; Wei, X.; Li, J.; Huang, Z.; Zhong, J. Electrochemically Reduced Graphene Oxide with Porous Structure as a Binder-Free Electrode for High-Rate Supercapacitors. *RSC Adv.* **2014**, *4* (26), 13673–13679.

(180) Pham, V. H.; Gebre, T.; Dickerson, J. H. Facile Electrodeposition of Reduced Graphene Oxide Hydrogels for High-Performance Supercapacitors. *Nanoscale* **2015**, *7* (14), 5947–5950.

(181) Zang, P.; Gao, S.; Dang, L.; Liu, Z.; Lei, Z. Green Synthesis of Holey Graphene Sheets and Their Assembly into Aerogel with Improved Ion Transport Property. *Electrochim. Acta* **2016**, *212*, 171–178.

(182) Lim, M. B.; Hu, M.; Manandhar, S.; Sakshaug, A.; Strong, A.; Riley, L.; Pauzauskie, P. J. Ultrafast Sol-Gel Synthesis of Graphene Aerogel Materials. *Carbon N. Y.* **2015**, *95*, 616–624.

(183) Zheng, B.; Xu, Z.; Gao, C. Mass Production of Graphene Nanoscrolls and Their Application in High Rate Performance Supercapacitors. *Nanoscale* **2016**, *8* (3), 1413–1420.

(184) Hao, X.-F.; Yan, Y.; Gao, L.-G.; Mu, W.-S.; Hao, C. Ionothermal Synthesis of Graphene-Based Hierarchically Porous Carbon for High-Energy Supercapacitors with Ionic Liquid Electrolyte. *Electrochim. Acta* **2017**, *241*, 124–131.

(185) Yu, D.; Dai, L. Self-Assembled Graphene/carbon Nanotube Hybrid Films for Supercapacitors. *J. Phys. Chem. Lett.* **2010**, *1* (2), 467–470.

(186) Huang, Z.-D.; Zhang, B.; Oh, S.-W.; Zheng, Q.-B.; Lin, X.-Y.; Yousefi, N.; Kim, J.-K. Self-Assembled Reduced Graphene Oxide/carbon Nanotube Thin Films as Electrodes for Supercapacitors. *J. Mater. Chem.* **2012**, *22* (8), 3591–3599.

(187) Li, Y. F.; Liu, Y. Z.; Yang, Y. G.; Wang, M. Z.; Wen, Y. F. Reduced Graphene oxide/MWCNT Hybrid Sandwiched Film by Self-Assembly for High Performance Supercapacitor Electrodes. *Appl. Phys. A Mater. Sci. Process.* **2012**, *108* (3), 701–707.

(188) Trigueiro, J. P. C.; Lavall, R. L.; Silva, G. G. Nanocomposites of Graphene Nanosheets/Multiwalled Carbon Nanotubes as Electrodes for In-Plane Supercapacitors. *Electrochim. Acta* **2016**, *187*, 312–322.

(189) Ban, F. Y.; Jayabal, S.; Lim, H. N.; Lee, H. W.; Huang, N. M. Synthesis of Nitrogen-Doped Reduced Graphene Oxide-Multiwalled Carbon Nanotube Composite on Nickel Foam as Electrode for High-Performance Supercapacitor. *Ceram. Int.* **2017**, *43* (1), 20–27.

(190) Tamailarasan, P.; Ramaprabhu, S. Carbon Nanotubes-Graphene-Solidlike Ionic Liquid Layer-Based Hybrid Electrode Material for High Performance Supercapacitor. *J. Phys. Chem. C* **2012**, *116* (27), 14179–14187.

(191) Antiohos, D.; Romano, M. S.; Razal, J. M.; Beirne, S.; Aitchison, P.; Minett, A. I.; Wallace, G. G.; Chen, J. Performance Enhancement of Single-Walled Nanotube–microwave Exfoliated Graphene Oxide Composite Electrodes Using a Stacked Electrode Configuration. *J. Mater. Chem. A* **2014**, *2* (36), 14835–14843.

(192) Lin, Y.; Liu, F.; Casano, G.; Bhavsar, R.; Kinloch, I. A.; Derby, B. Pristine Graphene Aerogels by Room-Temperature Freeze Gelation. *Adv. Mater.* **2016**, *28* (36), 7993–8000.

(193) Pham, D. T.; Lee, T. H.; Luong, D. H.; Yao, F.; Ghosh, A.; Le, V. T.; Kim, T. H.; Li, B.; Chang, J.; Lee, Y. H. Carbon Nanotube-Bridged Graphene 3D Building Blocks for Ultrafast Compact Supercapacitors. *ACS Nano* **2015**, *9* (2), 2018–2027.

(194) Shao, Q.; Tang, J.; Lin, Y.; Li, J.; Qin, F.; Yuan, J.; Qin, L. C. Carbon Nanotube Spaced Graphene Aerogels with Enhanced Capacitance in Aqueous and Ionic Liquid Electrolytes. *J. Power Sources* **2015**, *278*, 751–759.

(195) Ghazinejad, M.; Guo, S.; Wang, W.; Ozkan, M.; Ozkan, C. S. Synchronous Chemical Vapor Deposition of Large-Area Hybrid Graphene–carbon Nanotube Architectures. *J. Mater. Res.* **2013**, *28* (7), 958–968.

(196) Yoon, Y.; Lee, K.; Kwon, S.; Seo, S.; Yoo, H.; Kim, S.; Shin, Y.; Park, Y.; Kim, D.; Choi, J. Y.; Lee, H. Vertical Alignments of Graphene Sheets Spatially and Densely Piled for Fast Ion Diffusion in Compact Supercapacitors. *ACS Nano* **2014**, *8* (5), 4580–4590.

(197) Seo, D. H.; Yick, S.; Han, Z. J.; Fang, J. H.; Ostrikov, K. Synergistic Fusion of Vertical Graphene Nanosheets and Carbon Nanotubes for High-Performance Supercapacitor Electrodes. *ChemSusChem* **2014**, *7* (8), 2317–2324.

(198) Chen, I. W. P.; Chen, Y. S.; Kao, N. J.; Wu, C. W.; Zhang, Y. W.; Li, H. T. Scalable and High-Yield Production of Exfoliated Graphene Sheets in Water and Its Application to an All-Solid-State Supercapacitor. *Carbon N. Y.* **2015**, *90*, 16–24.

(199) Nam, I.; Bae, S.; Park, S.; Yoo, Y. G.; Lee, J. M.; Han, J. W.; Yi, J. Omnidirectionally Stretchable, High Performance Supercapacitors Based on a Graphene-Carbon-Nanotube Layered Structure. *Nano Energy* **2015**, *15*, 33–42.

(200) Mao, B. S.; Wen, Z.; Bo, Z.; Chang, J.; Huang, X.; Chen, J. Hierarchical Nanohybrids with Porous CNT-Networks Decorated Crumpled Graphene Balls for Supercapacitors. *ACS Appl. Mater. Interfaces* **2014**, *6* (12), 9881–9889.

(201) Wang, W.; Guo, S.; Ruiz, I.; Ozkan, M.; Ozkan, C. S. Three Dimentional Graphene-CNTs Foam Architectures for Electrochemical Capacitors. *ECS Trans.* **2012**, *50* (43), 37–44.

(202) Wang, W.; Guo, S.; Penchev, M.; Ruiz, I.; Bozhilov, K. N.; Yan, D.; Ozkan, M.; Ozkan, C. S. Three Dimensional Few Layer Graphene and Carbon Nanotube Foam Architectures for High Fidelity Supercapacitors. *Nano Energy* **2013**, *2* (2), 294–303.

(203) Wu, Y.; Zhang, T.; Zhang, F.; Wang, Y.; Ma, Y.; Huang, Y.; Liu, Y.; Chen, Y. In Situ Synthesis of Graphene/single-Walled Carbon Nanotube Hybrid Material by Arc-Discharge and Its Application in Supercapacitors. *Nano Energy* **2012**, *1* (6), 820–827.

(204) Wang, G.; Sun, X.; Lu, F.; Sun, H.; Yu, M.; Jiang, W.; Liu, C.; Lian, J. Flexible Pillared Graphene-Paper Electrodes for High-Performance Electrochemical Supercapacitors. *Small* **2012**, *8* (3), 452–459.

(205) Fei, H.; Yang, C.; Bao, H.; Wang, G. Flexible All-Solid-State Supercapacitors Based on Graphene/carbon Black Nanoparticle Film Electrodes and Cross-Linked Poly(vinyl Alcohol)-H_2SO_4 Porous Gel Electrolytes. *J. Power Sources* **2014**, *266*, 488–495.

(206) Wang, Y.; Chen, J.; Cao, J.; Liu, Y.; Zhou, Y.; Ouyang, J. H.; Jia, D. Graphene/carbon Black Hybrid Film for Flexible and High Rate Performance Supercapacitor. *J. Power Sources* **2014**, *271*, 269–277.

(207) Chen, Y.; Zhang, X.; Zhang, H.; Sun, X.; Zhang, D.; Ma, Y. High-Performance Supercapacitors Based on a Graphene–activated Carbon Composite Prepared by Chemical Activation. *RSC Adv.* **2012**, *2* (20), 7747–7753.

(208) Yu, S.; Li, Y.; Pan, N. KOH Activated Carbon/graphene Nanosheets Composites as High Performance Electrode Materials in Supercapacitors. *RSC Adv.* **2014**, *4* (90), 48758–48764.

(209) Li, Y.; Shang, T.-X.; Gao, J.-M.; Jin, X.-J. Nitrogen-Doped Activated Carbon/graphene Composites as High-Performance Supercapacitor Electrodes. *RSC Adv.* **2017**, *7* (31), 19098–19105.

(210) Xie, Q.; Bao, R.; Zheng, A.; Zhang, Y.; Wu, S.; Xie, C.; Zhao, P. Sustainable Low-Cost Green Electrodes with High Volumetric Capacitance for Aqueous Symmetric Supercapacitors with High Energy Density. *ACS Sustain. Chem. Eng.* **2016**, *4* (3), 1422–1430.

(211) Yadav, P.; Banerjee, A.; Unni, S.; Jog, J.; Kurungot, S.; Ogale, S. A 3D Hexaporous Carbon Assembled from Single-Layer Graphene as High Performance Supercapacitor. *ChemSusChem* **2012**, *5* (11), 2159–2164.

(212) Lei, Z.; Liu, Z.; Wang, H.; Sun, X.; Lu, L.; Zhao, X. S. A High-Energy-Density Supercapacitor with Graphene-CMK-5 as Electrode and Ionic Liquid as Electrolyte. *J. Mater. Chem. A* **2013**, *1*, 2313–2321.

(213) Liu, R.; Wan, L.; Liu, S.; Pan, L.; Wu, D.; Zhao, D. An Interface-Induced Co-Assembly Approach towards Ordered Mesoporous Carbon/graphene Aerogel for High-Performance Supercapacitors. *Adv. Funct. Mater.* **2015**, *25* (4), 526–533.

(214) Lee, J. W.; Ko, J. M.; Kim, J. D. Hydrothermal Preparation of Nitrogen-Doped Graphene Sheets via Hexamethylenetetramine for Application as Supercapacitor Electrodes. *Electrochim. Acta* **2012**, *85*, 459–466.

(215) Liu, Y. Z.; Li, Y. F.; Su, F. Y.; Xie, L. J.; Kong, Q. Q.; Li, X. M.; Gao, J. G.; Chen, C. M. Easy One-Step Synthesis of N-Doped Graphene for Supercapacitors. *Energy Storage Mater.* **2016**, *2*, 69–75.

(216) Chen, P.; Yang, J. J.; Li, S. S.; Wang, Z.; Xiao, T. Y.; Qian, Y. H.; Yu, S. H. Hydrothermal Synthesis of Macroscopic Nitrogen-Doped Graphene Hydrogels for Ultrafast Supercapacitor. *Nano Energy* **2013**, *2* (2), 249–256.

(217) Zhu, Y.; Huang, H.; Zhou, W.; Li, G.; Liang, X.; Guo, J.; Tang, S. Low Temperature Reduction of Graphene Oxide Film by Ammonia Solution and Its Application for High-Performance Supercapacitors. *J. Mater. Sci. Mater. Electron.* **2017**, *28* (14), 10098–10105.

(218) Liu, D.; Fu, C.; Zhang, N.; Zhou, H.; Kuang, Y. Three-Dimensional Porous Nitrogen Doped Graphene Hydrogel for High Energy Density Supercapacitors. *Electrochim. Acta* **2016**, *213*, 291–297.

(219) Zhang, Y.; Wen, G.; Gao, P.; Bi, S.; Tang, X.; Wang, D. High-Performance Supercapacitor of Macroscopic Graphene Hydrogels by Partial Reduction and Nitrogen Doping of Graphene Oxide. *Electrochim. Acta* **2016**, *221*, 167–176.

(220) Sui, Z. Y.; Meng, Y. N.; Xiao, P. W.; Zhao, Z. Q.; Wei, Z. X.; Han, B. H. Nitrogen-Doped Graphene Aerogels as Efficient Supercapacitor Electrodes and Gas Adsorbents. *ACS Appl. Mater. Interfaces* **2015**, *7* (3), 1431–1438.

(221) Su, X.-L.; Cheng, M.-Y.; Fu, L.; Zheng, G.-P.; Zheng, X.-C.; Yang, J.-H.; Guan, X.-X. Facile Synthesis of 3D Nitrogen-Doped Graphene Aerogel Nanomeshes with Hierarchical Porous Structures for Applications in High-Performance Supercapacitors. *New J. Chem.* **2017**, *41* (13), 5291–5296.

(222) Yang, J.; Jo, M. R.; Kang, M.; Huh, Y. S.; Jung, H.; Kang, Y. M. Rapid and Controllable Synthesis of Nitrogen Doped Reduced Graphene Oxide Using Microwave-Assisted Hydrothermal Reaction for High Power-Density Supercapacitors. *Carbon N. Y.* **2014**, *73*, 106–113.

(223) Chang, Y.; Han, G.; Yuan, J.; Fu, D.; Liu, F.; Li, S. Using Hydroxylamine as a Reducer to Prepare N-Doped Graphene Hydrogels Used in High-Performance Energy Storage. *J. Power Sources* **2013**, *238*, 492–500.

(224) Li, C.; Hu, Y.; Yu, M.; Wang, Z.; Zhao, W.; Liu, P.; Tong, Y.; Lu, X. Nitrogen Doped Graphene Paper as a Highly Conductive, and Light-Weight Substrate for Flexible Supercapacitors. *RSC Adv.* **2014**, *4* (94), 51878–51883.

(225) Haque, E.; Islam, M. M.; Pourazadi, E.; Hassan, M.; Faisal, S. N.; Roy, A. K.; Konstantinov, K.; Harris, A. T.; Minett, A. I.; Gomes, V. G. Nitrogen Doped Graphene via Thermal Treatment of Composite Solid Precursors as a High Performance Supercapacitor. *RSC Adv.* **2015**, *5* (39), 30679–30686.

(226) Wang, J.; Ding, B.; Xu, Y.; Shen, L.; Dou, H.; Zhang, X. Crumpled Nitrogen-Doped Graphene for Supercapacitors with High Gravimetric and Volumetric Performances. *ACS Appl. Mater. Interfaces* **2015**, *7* (40), 22284–22291.

(227) Wang, J.; Ding, B.; Hao, X.; Xu, Y.; Wang, Y.; Shen, L.; Dou, H.; Zhang, X. A Modified Molten-Salt Method to Prepare Graphene Electrode with High Capacitance and Low Self-Discharge Rate. *Carbon N. Y.* **2016**, *102*, 255–261.

(228) Li, S.; Wang, Z.; Jiang, H.; Zhang, L.; Ren, J.; Zheng, M.; Dong, L.; Sun, L. Plasma-Induced Highly Efficient Synthesis of Boron Doped Reduced Graphene Oxide for Supercapacitors. *Chem. Commun.* **2016**, *52* (73), 10988–10991.

(229) Wen, P.; Gong, P.; Mi, Y.; Wang, J.; Yang, S. Scalable Fabrication of High Quality Graphene by Exfoliation of Edge Sulfonated Graphite for Supercapacitor Application. *RSC Adv.* **2014**, *4* (68), 35914–35918.

(230) Karthika, P.; Rajalakshmi, N.; Dhathathreyan, K. S. Phosphorus-Doped Exfoliated Graphene for Supercapacitor Electrodes. *J. Nanosci. Nanotechnol.* **2013**, *13* (3), 1746–1751.

(231) Wen, Y.; Wang, B.; Huang, C.; Wang, L.; Hulicova-Jurcakova, D. Synthesis of Phosphorus-Doped Graphene and Its Wide Potential Window in Aqueous Supercapacitors. *Chem. - A Eur. J.* **2015**, *21* (1), 80–85.

(232) Wu, Z. S.; Winter, A.; Chen, L.; Sun, Y.; Turchanin, A.; Feng, X.; Mullen, K. Three-Dimensional Nitrogen and Boron Co-Doped Graphene for High-Performance All-Solid-State Supercapacitors. *Adv. Mater.* **2012**, *24* (37), 5130–5135.

(233) Pham, V. H.; Hur, S. H.; Kim, E. J.; Kim, B. S.; Chung, J. S. Highly Efficient Reduction of Graphene Oxide Using Ammonia Borane. *Chem. Commun.* **2013**, *49* (59), 6665.

(234) Wang, T.; Wang, L.-X.; Wu, D.-L.; Xia, W.; Jia, D.-Z. Interaction between Nitrogen and Sulfur in Co-Doped Graphene and Synergetic Effect in Supercapacitor. *Sci. Rep.* **2015**, *5* (1), 9591.

(235) Akhter, T.; Islam, M. M.; Faisal, S. N.; Haque, E.; Minett, A. I.; Liu, H. K.; Konstantinov, K.; Dou, S. X. Self-Assembled N/S Codoped Flexible Graphene Paper for High Performance Energy Storage and Oxygen Reduction Reaction. *ACS Appl. Mater. Interfaces* **2016**, *8* (3), 2078–2087.

(236) Li, J.; Zhang, G.; Fu, C.; Deng, L.; Sun, R.; Wong, C. P. Facile Preparation of Nitrogen/sulfur Co-Doped and Hierarchical Porous Graphene Hydrogel for High-Performance Electrochemical Capacitor. *J. Power Sources* **2017**, *345*, 146–155.

(237) Zhou, Q.; Zhao, Z.; Zhang, Y.; Meng, B.; Zhou, A.; Qiu, J. Graphene Sheets from Graphitized Anthracite Coal: Preparation, Decoration, and Application. *Energy and Fuels* **2012**, *26* (8), 5186–5192.

(238) Zhang, L.; Zhang, F.; Yang, X.; Long, G.; Wu, Y.; Zhang, T.; Leng, K.; Huang, Y.; Ma, Y.; Yu, A.; Chen, Y. Porous 3D Graphene-Based Bulk Materials with Exceptional High Surface Area and Excellent Conductivity for Supercapacitors. *Sci. Rep.* **2013**, *3* (1), 1408.

(239) Wang, X.; Zhang, Y.; Zhi, C.; Wang, X.; Tang, D.; Xu, Y.; Weng, Q.; Jiang, X.; Mitome, M.; Golberg, D.; Bando, Y. Three-Dimensional Strutted Graphene Grown by Substrate-Free Sugar Blowing for High-Power-Density Supercapacitors. *Nat. Commun.* **2013**, *4* (May), 1–8.

(240) Wilson, E.; Islam, M. F. Ultracompressible, High-Rate Supercapacitors from Graphene-Coated Carbon Nanotube Aerogels. *ACS Appl. Mater. Interfaces* **2015**, *7* (9), 5612–5618.

(241) Sun, L.; Tian, C.; Li, M.; Meng, X.; Wang, L.; Wang, R.; Yin, J.; Fu, H. From Coconut Shell to Porous Graphene-like Nanosheets for High-Power Supercapacitors. *J. Mater. Chem. A* **2013**, *1* (21), 6462–6470.

(242) Tian, W.; Gao, Q.; Zhang, L.; Yang, C.; Li, Z.; Tan, Y.; Qian, W.; Zhang, H. Renewable Graphene-like Nitrogen-Doped Carbon Nanosheets as Supercapacitor Electrodes with Integrated High Energy–power Properties. *J. Mater. Chem. A* **2016**, *4* (22), 8690–8699.

(243) Panmand, R. P.; Patil, P.; Sethi, Y.; Kadam, S. R.; Kulkarni, M. V.; Gosavi, S. W.; Munirathnam, N. R.; Kale, B. B. Unique Perforated Graphene Derived from Bougainvillea Flowers for High-Power Supercapacitors: A Green Approach. *Nanoscale* **2017**, *9* (14), 4801–4809.

(244) Xing, B.; Yuan, R.; Zhang, C.; Huang, G.; Guo, H.; Chen, Z.; Chen, L.; Yi, G.; Zhang, Y.; Yu, J. Facile Synthesis of Graphene Nanosheets from Humic Acid for Supercapacitors. *Fuel Process. Technol.* **2017**, *165*, 112–122.

(245) Sudhakar, Y. N. .; Selvakumar, M. .; Bhat, D. K. .; Senthil Kumar, S. . Reduced Graphene Oxide Derived from Used Cell Graphite and Its Green Fabrication as an Eco-Friendly Supercapacitor. *RSC Adv.* **2014**, *4* (104), 60039–60051.

(246) Wu, Q.; Xu, Y.; Yao, Z.; Liu, A.; Shi, G. Supercapacitors Based on Flexible Graphene/Polyaniline Nanofiber Composite Films. *ACS Nano* **2010**, *4* (4), 1963–1970.

(247) Li, L.; Raji, A. R. O.; Fei, H.; Yang, Y.; Samuel, E. L. G.; Tour, J. M. Nanocomposite of Polyaniline Nanorods Grown on Graphene Nanoribbons for Highly Capacitive Pseudocapacitors. *ACS Appl. Mater. Interfaces* **2013**, *5* (14), 6622–6627.

(248) Jiang, X.; Setodoi, S.; Fukumoto, S.; Imae, I.; Komaguchi, K.; Yano, J.; Mizota, H.; Harima, Y. An Easy One-Step Electrosynthesis of Graphene/polyaniline Composites and Electrochemical Capacitor. *Carbon N. Y.* **2014**, *67*, 662–672.

(249) Wang, Q.; Yan, J.; Fan, Z.; Wei, T.; Zhang, M.; Jing, X. Mesoporous Polyaniline Film on Ultra-Thin Graphene Sheets for High Performance Supercapacitors. *J. Power Sources* **2014**, *247*, 197–203.

(250) Liu, L.; Niu, Z.; Zhang, L.; Zhou, W.; Chen, X.; Xie, S. Nanostructured Graphene Composite Papers for Highly Flexible and Foldable Supercapacitors. *Adv. Mater.* **2014**, *26* (28), 4855–4862.

(251) Xu, Y.; Hennig, I.; Freyberg, D.; James Strudwick, A.; Georg Schwab, M.; Weitz, T.; Chih-Pei Cha, K. Inkjet-Printed Energy Storage Device Using Graphene/polyaniline Inks. *J. Power Sources* **2014**, *248*, 483–488.

(252) Chi, K.; Zhang, Z.; Xi, J.; Huang, Y.; Xiao, F.; Wang, S.; Liu, Y. Freestanding Graphene Paper Supported Three-Dimensional Porous Graphene-Polyaniline Nanocomposite Synthesized by Inkjet Printing and in Flexible All-Solid-State Supercapacitor. *ACS Appl. Mater. Interfaces* **2014**, *6* (18), 16312–16319.

(253) Du, P.; Liu, H. C.; Yi, C.; Wang, K.; Gong, X. Polyaniline-Modified Oriented Graphene Hydrogel Film as the Free-Standing Electrode for Flexible Solid-State Supercapacitors. *ACS Appl. Mater. Interfaces* **2015**, *7* (43), 23932–23940.

(254) Sekar, P.; Anothumakkool, B.; Kurungot, S. 3D Polyaniline Porous Layer Anchored Pillared Graphene Sheets: Enhanced Interface Joined with High Conductivity for Better Charge Storage Applications. *ACS Appl. Mater. Interfaces* **2015**, *7* (14), 7661–7669.

(255) Gao, S.; Zang, P.; Dang, L.; Xu, H.; Shi, F.; Liu, Z.; Lei, Z. Extraordinarily High-Rate Capability of Polyaniline Nanorod Arrays on Graphene Nanomesh. *J. Power Sources* **2016**, *304*, 111–118.

(256) Hong, X.; Zhang, B.; Murphy, E.; Zou, J.; Kim, F. Three-Dimensional Reduced Graphene Oxide/polyaniline Nanocomposite Film Prepared by Diffusion Driven Layer-by-Layer Assembly for High-Performance Supercapacitors. *J. Power Sources* **2017**, *343*, 60–66.

(257) Zhang, L.; Huang, D.; Hu, N.; Yang, C.; Li, M.; Wei, H.; Yang, Z.; Su, Y.; Zhang, Y. Three-Dimensional Structures of Graphene/polyaniline Hybrid Films Constructed by Steamed Water for High-Performance Supercapacitors. *J. Power Sources* **2017**, *342*, 1–8.

(258) Biswas, S.; Drzal, L. T. Multilayered Nanoarchitecture of Graphene Nanosheets and Polypyrrole Nanowires for High Performance Supercapacitor Electrodes. *Chem. Mater.* **2010**, *22* (20), 5667–5671.

(259) De Oliveira, H. P.; Sydlik, S. A.; Swager, T. M. Supercapacitors from Free-Standing Polypyrrole/graphene Nanocomposites. *J. Phys. Chem. C* **2013**, *117* (20), 10270–10276.

(260) Zhao, Y.; Liu, J.; Hu, Y.; Cheng, H.; Hu, C.; Jiang, C.; Jiang, L.; Cao, A.; Qu, L. Highly Compression-Tolerant Supercapacitor Based on Polypyrrole-Mediated Graphene Foam Electrodes. *Adv. Mater.* **2013**, *25* (4), 591–595.

(261) Ding, X.; Zhao, Y.; Hu, C.; Hu, Y.; Dong, Z.; Chen, N.; Zhang, Z.; Qu, L. Spinning Fabrication of Graphene/polypyrrole Composite Fibers for All-Solid-State, Flexible Fibriform Supercapacitors. *J. Mater. Chem. A* **2014**, *2* (31), 12355–12360.

(262) Li, S.; Zhao, C.; Shu, K.; Wang, C.; Guo, Z.; Wallace, G. G.; Liu, H. Mechanically Strong High Performance Layered Polypyrrole Nano Fibre/graphene Film for Flexible Solid State Supercapacitor. *Carbon N. Y.* **2014**, *79* (1), 554–562.

(263) Zhu, J.; Xu, Y.; Wang, J.; Wang, J.; Bai, Y.; Du, X. Morphology Controllable Nano-Sheet Polypyrrole–graphene Composites for High-Rate Supercapacitor. *Phys. Chem. Chem. Phys.* **2015**, *17* (30), 19885–19894.

(264) Pandey, G. P.; Rastogi, A. C. Poly(3,4-Ethylenedioxythiophene)-Graphene Composite Electrodes For Solid-State Supercapacitors with Ionic Liquid Gel Polymer Electrolyte. *ECS Trans.* **2013**, *45* (29), 173–181.

(265) Liu, Y.; Weng, B.; Razal, J. M.; Xu, Q.; Zhao, C.; Hou, Y.; Seyedin, S.; Jalili, R.; Wallace, G. G.; Chen, J. High-Performance Flexible All-Solid-State Supercapacitor from Large Free-Standing Graphene-PEDOT/PSS Films. *Sci. Rep.* **2015**, *5* (October), 17045.

(266) Rakhi, R. B.; Chen, W.; Cha, D.; Alshareef, H. N. High Performance Supercapacitors Using Metal Oxide Anchored Graphene Nanosheet Electrodes. *J. Mater. Chem.* **2011**, *21* (40), 16197–16204.

(267) Lin, N.; Tian, J.; Shan, Z.; Chen, K.; Liao, W. Hydrothermal Synthesis of Hydrous Ruthenium Oxide/graphene Sheets for High-Performance Supercapacitors. *Electrochim. Acta* **2013**, *99*, 219–224.

(268) Deng, L.; Wang, J.; Zhu, G.; Kang, L.; Hao, Z.; Lei, Z.; Yang, Z.; Liu, Z. H. RuO2/graphene Hybrid Material for High Performance Electrochemical Capacitor. *J. Power Sources* **2014**, *248*, 407–415.

(269) Amir, F. Z.; Pham, V. H.; Dickerson, J. H. Facile Synthesis of Ultra-Small Ruthenium Oxide Nanoparticles Anchored on Reduced Graphene Oxide Nanosheets for High-Performance Supercapacitors. *RSC Adv.* **2015**, *5* (83), 67638–67645.

(270) Amir, F. Z.; Pham, V. H.; Mullinax, D. W.; Dickerson, J. H. Enhanced Performance of HRGO-RuO_2 Solid State Flexible Supercapacitors Fabricated by Electrophoretic Deposition. *Carbon N. Y.* **2016**, *107*, 338–343.

(271) Wang, P.; Liu, H.; Xu, Y.; Chen, Y.; Yang, J.; Tan, Q. Supported Ultrafine Ruthenium Oxides with Specific Capacitance up to 1099 F g^{-1} for a Supercapacitor. *Electrochim. Acta* **2016**, *194*, 211–218.

(272) Chan, P. Y.; Rusi; Majid, S. R. RGO-Wrapped MnO_2 Composite Electrode for Supercapacitor Application. *Solid State Ionics* **2014**, *262*, 226–229.

(273) Zhu, S.; Zhang, H.; Chen, P.; Nie, L.-H.; Li, C.-H.; Li, S.-K. Self-Assembled Three-Dimensional Hierarchical Graphene Hybrid Hydrogels with Ultrathin β-MnO_2 Nanobelts for High Performance Supercapacitors. *J. Mater. Chem. A* **2015**, *3* (4), 1540–1548.

(274) Zhang, N.; Fu, C.; Liu, D.; Li, Y.; Zhou, H.; Kuang, Y. Three-Dimensional Pompon-like MnO2/Graphene Hydrogel Composite for Supercapacitor. *Electrochim. Acta* **2016**, *210*, 804–811.

(275) Zhang, H.; Huang, Z.; Li, Y.; Chen, Y.; Wang, W.; Ye, Y.; Deng, P. Microwave-Assisted in Situ Synthesis of Reduced Graphene oxide/Mn_3O_4 Composites for Supercapacitor Applications. *RSC Adv.* **2015**, *5* (56), 45061–45067.

(276) Liao, Q. Y.; Li, S. Y.; Cui, H.; Wang, C. Vertically-Aligned graphene@Mn_3O_4 Nanosheets for a High-Performance Flexible All-Solid-State Symmetric Supercapacitor. *J. Mater. Chem. A* **2016**, *4* (22), 8830–8836.

(277) Hu, J.; Ramadan, A.; Luo, F.; Qi, B.; Deng, X.; Chen, J. One-Step Molybdate Ion Assisted Electrochemical Synthesis of α-MoO_3-Decorated Graphene Sheets and Its Potential Applications. *J. Mater. Chem.* **2011**, *21* (38), 15009–15014.

(278) Zhou, K.; Zhou, W.; Liu, X.; Sang, Y.; Ji, S.; Li, W.; Lu, J.; Li, L.; Niu, W.; Liu, H.; Chen, S. Ultrathin MoO_3 Nanocrystalsself-Assembled on Graphene Nanosheets via Oxygen Bonding as Supercapacitor Electrodes of High Capacitance and Long Cycle Life. *Nano Energy* **2015**, *12*, 510–520.

(279) Ho, M. Y.; Khiew, P. S.; Chiu, W. S. Green and Facile Synthesis of Molybdenum Oxide-Graphene Composite Electrodes for Supercapacitor Application. *Mater. Sci. Forum* **2016**, *863*, 90–94.

(280) Ho, M. Y.; Khiew, P. S.; Isa, D.; Chiu, W. S.; Chia, C. H. Solvothermal Synthesis of Molybdenum Oxide on Liquid-Phase Exfoliated Graphene Composite Electrodes for Aqueous Supercapacitor Application. *J. Mater. Sci. Mater. Electron.* **2017**, *28* (9), 6907–6918.

(281) Giardi, R.; Porro, S.; Topuria, T.; Thompson, L.; Pirri, C. F.; Kim, H. C. One-Pot Synthesis of Graphene-Molybdenum Oxide Hybrids and Their Application to Supercapacitor Electrodes. *Appl. Mater. Today* **2015**, *1* (1), 27–32.

(282) Yuan, J.; Zhu, J.; Bi, H.; Meng, X.; Liang, S.; Zhang, L.; Wang, X. Graphene-Based 3D Composite Hydrogel by Anchoring Co_3O_4 Nanoparticles with Enhanced Electrochemical Properties. *Phys. Chem. Chem. Phys.* **2013**, *15* (31), 12940–12945.

(283) Liu, G. J.; Fan, L. Q.; Yu, F. Da; Wu, J. H.; Liu, L.; Qiu, Z. Y.; Liu, Q. Facile One-Step Hydrothermal Synthesis of Reduced Graphene oxide/Co_3O_4 Composites for Supercapacitors. *J. Mater. Sci.* **2013**, *48* (24), 8463–8470.

(284) Liao, Q.; Li, N.; Jin, S.; Yang, G.; Wang, C. All-Solid-State Symmetric Supercapacitor Based on Co_3O_4 Nanoparticles on Vertically Aligned Graphene. *ACS Nano* **2015**, *9* (5), 5310–5317.

(285) Ping Wong, C. P.; Lai, C. W.; Lee, K. M.; Juan, J. C.; Abd Hamid, S. B. Synthesis of Reduced Graphene Oxide/tungsten Trioxide Nanocomposite Electrode for High Electrochemical Performance. *Ceram. Int.* **2016**, *42* (11), 13128–13135.

(286) Ping Wong, C. P.; Lee, K. M.; Lai, C. W. Hydrothermal Preparation of Reduced Graphene Oxide/tungsten Trioxide Nanocomposites with Enhanced Electrochemical Performance. *J Mater Sci Mater Electron* **2017**, *28* (19), 14554–14567.

(287) Yuan, B.; Zheng, X. Y.; Zhang, C.; Lu, W.; Li, B. H.; Yang, Q. H. Assembly of Ni(OH)2-Graphene Hybrids with a High Electrochemical Performance by a One-Pot Hydrothermal Method. *Xinxing Tan Cailiao/New Carbon Mater.* **2014**, *29* (6), 426–431.

(288) Deng, P.; Zhang, H.; Chen, Y.; Li, Z.; Huang, Z.; Xu, X.; Li, Y.; Shi, Z. Facile Fabrication of Graphene/nickel Oxide Composite with Superior Supercapacitance Performance by Using Alcohols-Reduced Graphene as Substrate. *J. Alloys Compd.* **2015**, *644*, 165–171.

(289) Li, Z.; Zhou, Z.; Yun, G.; Shi, K.; Lv, X.; Yang, B. High-Performance Solid-State Supercapacitors Based on Graphene-ZnO Hybrid Nanocomposites. *Nanoscale Res. Lett.* **2013**, *8* (1), 473.

(290) Guo, Y.; Chang, B.; Wen, T.; Zhao, C.; Yin, H.; Zhou, Y.; Wang, Y.; Yang, B.; Zhang, S. One-Pot Synthesis of Graphene/zinc Oxide by Microwave Irradiation with Enhanced Supercapacitor Performance. *RSC Adv.* **2016**, *6* (23), 19394–19403.

(291) Zhang, H.; Zhang, X.; Lin, H.; Wang, K.; Sun, X.; Xu, N.; Li, C.; Ma, Y. Graphene and Maghemite Composites Based Supercapacitors Delivering High Volumetric Capacitance and Extraordinary Cycling Stability. *Electrochim. Acta* **2015**, *156*, 70–76.

(292) Naderi, H. R.; Norouzi, P.; Ganjali, M. R.; Gholipour-Ranjbar, H. Synthesis of a Novel Magnetite/nitrogen-Doped Reduced Graphene Oxide Nanocomposite as High Performance Supercapacitor. *Powder Technol.* **2016**, *302*, 298–308.

(293) Lalwani, S.; Sahu, V.; Marichi, R. B.; Singh, G.; Sharma, R. K. In Situ Immobilized, Magnetite Nanoplatelets over Holey Graphene Nanoribbons for High Performance Solid State Supercapacitor. *Electrochim. Acta* **2017**, *224*, 517–526.

(294) Perera, S. D.; Liyanage, A. D.; Nijem, N.; Ferraris, J. P.; Chabal, Y. J.; Balkus, K. J. Vanadium Oxide Nanowire-Graphene Binder Free Nanocomposite Paper Electrodes for Supercapacitors: A Facile Green Approach. *J. Power Sources* **2013**, *230*, 130–137.

(295) Li, M.; Sun, G.; Yin, P.; Ruan, C.; Ai, K. Controlling the Formation of Rodlike V_2O_5 Nanocrystals on Reduced Graphene Oxide for High-Performance Supercapacitors. *ACS Appl. Mater. Interfaces* **2013**, *5* (21), 11462–11470.

(296) Pan, X.; Ren, G.; Hoque, M. N. F.; Bayne, S.; Zhu, K.; Fan, Z. Fast Supercapacitors Based on Graphene-Bridged V_2O_3/VO_x Core-Shell Nanostructure Electrodes with a Power Density of 1 MW Kg^{-1}. *Adv. Mater. Interfaces* **2014**, *1* (9), 1400398.

(297) Chhowalla, M.; Shin, H. S.; Eda, G.; Li, L.-J.; Loh, K. P.; Zhang, H. The Chemistry of Two-Dimensional Layered Transition Metal Dichalcogenide Nanosheets. *Nat. Chem.* **2013**, *5* (4), 263–275.

(298) Jariwala, D.; Sangwan, V. K.; Lauhon, L. J.; Marks, T. J.; Hersam, M. C. Emerging Device Applications for Semiconducting Two-Dimensional Transition Metal Dichalcogenides. *ACS Nano* **2014**, *8* (2), 1102–1120.

(299) Tan, C.; Zhang, H. Two-Dimensional Transition Metal Dichalcogenide Nanosheet-Based Composites. *Chem. Soc. Rev.* **2015**, *44* (July 2006), 2713–2731.

(300) Bhimanapati, G. R.; Lin, Z.; Meunier, V.; Jung, Y.; Cha, J.; Das, S.; Xiao, D.; Son, Y.; Strano, M. S.; Cooper, V. R.; Liang, L.; Louie, S. G.; Ringe, E.; Zhou, W.; Kim, S. S.; Naik, R. R.; Sumpter, B. G.; Terrones, H.; Xia, F.; Wang, Y.; Zhu, J.; Akinwande, D.; Alem, N.; Schuller, J. A.; Schaak, R. E.; Terrones, M.; Robinson, J. A. Recent Advances in Two-Dimensional Materials beyond Graphene. *ACS Nano* **2015**, *9* (12), 11509–11539.

(301) Wang, H.; Feng, H.; Li, J. Graphene and Graphene-like Layered Transition Metal Dichalcogenides in Energy Conversion and Storage. *Small* **2014**, *10* (11), 2165–2181.

(302) Zhang, X.; Lai, Z.; Tan, C.; Zhang, H. Solution-Processed Two-Dimensional MoS2Nanosheets: Preparation, Hybridization, and Applications. *Angew. Chemie - Int. Ed.* **2016**, *55* (31), 8816–8838.

(303) Xie, L. M. Two-Dimensional Transition Metal Dichalcogenide Alloys: Preparation, Characterization and Applications. *Nanoscale* **2015**, *7* (44), 18392–18401.

(304) Gibney, E. 2D or Not 2D? *Nature* **2015**, *522*, 274–276.

(305) Wu, S.; Du, Y.; Sun, S. Transition Metal Dichalcogenide Based Nanomaterials for Rechargeable Batteries. *Chem. Eng. J.* **2017**, *307*, 189–207.

(306) Eda, G.; Yamaguchi, H.; Voiry, D.; Fujita, T.; Chen, M.; Chhowalla, M. Photoluminescence from Chemically Exfoliated MoS_2. *Nano Lett.* **2011**, *11* (12), 5111–5116.

(307) Eda, G.; Fujita, T.; Yamaguchi, H.; Voiry, D.; Chen, M.; Chhowalla, M. Coherent Atomic and Electronic Heterostructures of Single-Layer MoS_2. *ACS Nano* **2012**, *6* (8), 7311–7317.

(308) Feng, J.; Sun, X.; Wu, C.; Peng, L.; Lin, C.; Hu, S.; Yang, J.; Xie, Y. Metallic Few-Layered VS_2 Ultrathin Nanosheets: High Two-Dimensional Conductivity for in-Plane Supercapacitors. *J. Am. Chem. Soc.* **2011**, *133* (44), 17832–17838.

(309) Liu, K. K.; Zhang, W.; Lee, Y. H.; Lin, Y. C.; Chang, M. T.; Su, C. Y.; Chang, C. S.; Li, H.; Shi, Y.; Zhang, H.; Lai, C. S.; Li, L. J. Growth of Large-Area and Highly Crystalline MoS_2 Thin Layers on Insulating Substrates. *Nano Lett.* **2012**, *12* (3), 1538–1544.

(310) Zhan, Y.; Liu, Z.; Najmaei, S.; Ajayan, P. M.; Lou, J. Large-Area Vapor-Phase Growth and Characterization of MoS_2 Atomic Layers on a SiO_2 Substrate. *Small* **2012**, *8* (7), 966–971.

(311) Shi, Y.; Zhou, W.; Lu, A.-Y.; Fang, W.; Lee, Y.-H.; Hsu, A. L.; Kim, S. M.; Kim, K. K.; Yang, H. Y.; Li, L.-J.; Idrobo, J.-C.; Kong, J. Van Der Waals Epitaxy of MoS_2 Layers Using Graphene As Growth Templates. *Nano Lett.* **2012**, *12* (6), 2784–2791.

(312) Coleman, J. N.; Lotya, M.; O'Neill, A.; Bergin, S. D.; King, P. J.; Khan, U.; Young, K.; Gaucher, A.; De, S.; Smith, R. J.; Shvets, I. V.; Arora, S. K.; Stanton, G.; Kim, H.-Y.; Lee, K.; Kim, G. T.; Duesberg, G. S.; Hallam, T.; Boland, J. J.; Wang, J. J.; Donegan, J. F.; Grunlan, J. C.; Moriarty, G.; Shmeliov, A.; Nicholls, R. J.; Perkins, J. M.; Grieveson, E. M.; Theuwissen, K.; McComb, D. W.; Nellist, P. D.; Nicolosi, V. Two-Dimensional Nanosheets Produced by Liquid Exfoliation of Layered Materials. *Science.* **2011**, *331* (6017), 568–571.

(313) Radisavljevic, B.; Radenovic, A.; Brivio, J.; Giacometti, V.; Kis, A. Single-Layer MoS_2 Transistors. *Nat. Nanotechnol.* **2011**, *6* (3), 147–150.

(314) Chang, K.; Chen, W. In Situ Synthesis of MoS_2/graphene Nanosheet Composites with Extraordinarily High Electrochemical Performance for Lithium Ion Batteries. *Chem. Commun.* **2011**, *47*, 4252–4254.

(315) Ma, G.; Peng, H.; Mu, J.; Huang, H.; Zhou, X.; Lei, Z. In Situ Intercalative Polymerization of Pyrrole in Graphene Analogue of MoS_2 as Advanced Electrode Material in Supercapacitor. *J. Power Sources* **2013**, *229*, 72–78.

(316) Savjani, N.; Lewis, E. A.; Bissett, M. A.; Brent, J. R.; Dryfe, R. A. W.; Haigh, S. J.; O'Brien, P. Synthesis of Lateral Size-Controlled Monolayer 1H-MoS_2@Oleylamine as Supercapacitor Electrodes. *Chem. Mater.* **2016**, *28* (2), 657–664.

(317) Clerici, F.; Fontana, M.; Bianco, S.; Serrapede, M.; Perrucci, F.; Ferrero, S.; Tresso, E.; Lamberti, A. In Situ MoS_2 Decoration of Laser-Induced Graphene as Flexible Supercapacitor Electrodes. *ACS Appl. Mater. Interfaces* **2016**, *8* (16), 10459–10465.

(318) Kamila, S.; Mohanty, B.; Samantara, A. K.; Guha, P.; Ghosh, A.; Jena, B.; Satyam, P. V.; Mishra, B. K.; Jena, B. K. Highly Active 2D Layered MoS_2-rGO Hybrids for Energy Conversion and Storage Applications. *Sci. Rep.* **2017**, *7* (1), 1–13.

(319) Ratha, S.; Rout, C. S. Supercapacitor Electrodes Based on Layered Tungsten Disulfide-Reduced Graphene Oxide Hybrids Synthesized by a Facile Hydrothermal Method. *ACS Appl. Mater. Interfaces* **2013**, *5* (21), 11427–11433.

(320) Li, J.; Liao, K.; Wang, X.; Shi, P.; Fan, J.; Xu, Q.; Min, Y. High-Performance Flexible All-Solid-State Supercapacitors Based on Ultralarge Graphene Nanosheets and Solvent-Exfoliated Tungsten Disulfide Nanoflakes. *Adv. Mater. Interfaces* **2017**, *4* (20), 1–11.

(321) Marri, S. R.; Ratha, S.; Rout, C. S.; Behera, J. N. 3D Cuboidal Vanadium Diselenide Embedded Reduced Graphene Oxide Hybrid Structures with Enhanced Supercapacitor Properties. *Chem. Commun.* **2017**, *53* (1), 228–231.

Chapter 3

Supercapacitors Performance Evaluation

The charge-transfer mechanisms of Electrical Double-Layers Capacitors and Pseudocapacitors are presented. Then, the characterization approach for supercapacitors evaluation is described. The three types of measurements (Cyclic Voltammetry, Constant Current Charge Discharge, and Electrochemical Impedance Spectroscopy) are explained. Finally, the key metrics of supercapacitors are defined and the experimental procedures to measure properly them and the correlations among them are highlighted.

This chapter was wrote using the following documents: minireview published by Stoller and Ruoff in 2010[1], review published by Zhang and Pan in 2014[2], and two books: the first wrote by Conway in 1999[3], and the second edited by Béguin and Frackowiak in 2013[4].

3.1. Charge-Storage Mechanisms

As described previously, supercapacitors can be divided in two categories: Electrical Double-Layers Capacitors (EDLCs) and Pseudocapacitors (PCs). To further improve the deliverable performance, hybrid supercapacitors which combine both EDLCs and PCs. The charge-storage mechanism is different according to the supercapacitor categories.

3.1.1. Electrical Double-Layers Capacitors (EDLCs)

The pioneer in the use of EDLC for energy storage and delivery was Becker, who filed a US Patent in 1957.[5] He

understands the possibility to develop a device which is able to store energy only by charge separations (non-Faradaic processes occur inside the cell). The first model able to explain this phenomenon was developed by Helmholtz.[6] The model was later developed by Gouy-Chapman to describe more accurately the double-layer structure. However, the charge-storage mechanism is still called "Helmholtz double-layers" in tribute to Helmholtz who first give an explanation to this phenomenon. A representation of the double-layer mechanism that explains the charging-discharging procedure in EDLCs in shown in Figure 3.1. During the charging, electrodes have either a positive (cathode) or a negative (anode) potential. Ions contained in the electrolyte moves through the separator (yellow) to counterbalance the charges in the cell. Practically, cations (blue) move to the anode while anions (green) move to the cathode.

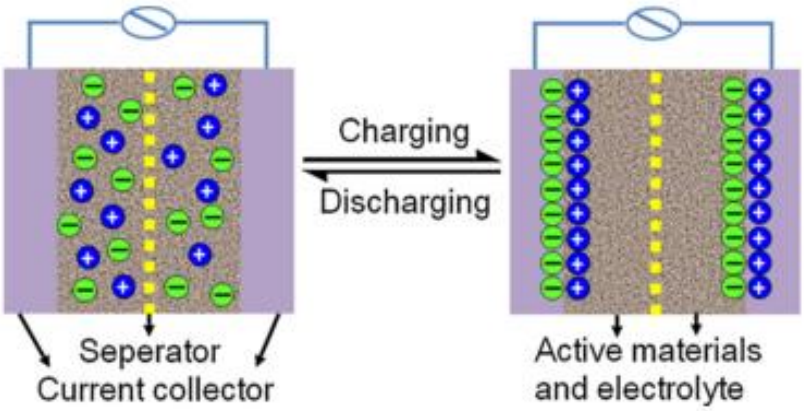

Figure 3. 1. Schematic representation of the charge-discharge mechanism in Electrical Double Layers Capacitors.[7]

3.1.2. Pseudocapacitors (PCs)

Conductive Polymers, Transition Metal Oxides, and Transition Metal Dichalcogenides are investigated as pseudocapacitive materials. Indeed, these materials store energy through Faradaic processes which are highly reversible surface reaction. These phenomena were first introduced by Trassati and co-workers.[8] It is nevertheless difficult to describe the mechanisms of those reactions

because they can differ according to the electrolyte and the pseudocapacitive materials.

3.2. Supercapacitors Performance Evaluation

Supercapacitors performance can be compared according to three main parameters: cell capacitance (also called total capacitance), operating voltage, and equivalent series resistance. However, this evaluation works essentially for commercial supercapacitor, where the materials and the cell configuration and design are all fixed. The aforementioned parameters become rapidly insufficient looking for the development of new materials, manufacturing processes, new cell designs. Indeed, the three parameters, which allow a quick comparison, are transformed in a parameters network strongly coupled together. An illustration of this network is shown in Figure 3.2.

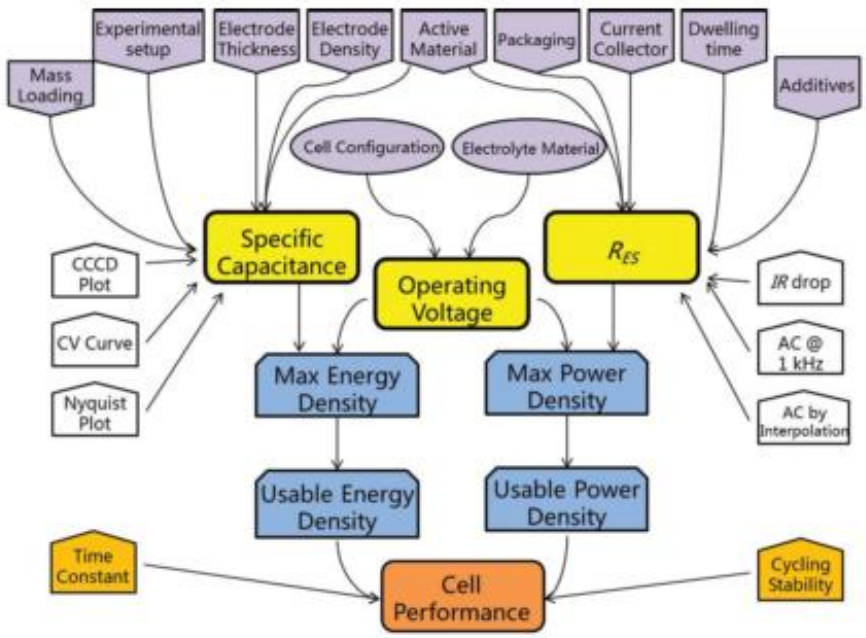

Figure 3. 2. Schematic illustration of key metrics relationship between them, the supercapacitor fabrications, and the measurements methods [2]

Looking to the Figure 3.2, which is not exclusive for the inter-parameters relationship, it can be easily understandable that

the comparison based on the deliverable performance may become inappropriate without information regarding the tests procedure. Moreover, academic, and industrial research are not focusing on the same spot inducing inconsistencies or misleading final reports.

To minimize them, several standards have been proposed with the aim to conform the evaluation procedure. A chronological review of these evaluation procedures is shown in Table 3.1.

Year	Organization	Title	Document ID
1986	DOD	Capacitors, fixed, electrolytic, double layer, carbon (metric), general specifications	DOD-C-29501
1994	DOE	Electrical vehicle capacitor test procedures manual	DOE/ID-10491
2004	DOE	FreedomCAR ultracapacitor test manual	DOE/NE-ID-11173
2006	IEC	Fixed electric double layer capacitor for use in electronic equipment	IEC 62391
2009	IEC	Electric double layer capacitors for use in hybrid electric vehicles – Test methods for electrical characteristics	IEC 62576
2012	IEC	Railway applications – Rolling stock equipment – Capacitors for power electronics – Part 3: Electric double-layer capacitors	IEC 61881-3
2013	SAE	Capacitive Energy storage device requirements for automotive propulsion applications	J3051

Table 3. 1. Chronological review of Supercapacitors evaluation procedure (DOD is US Department of Defense, DOE is US Department of Energy, IEC is International Electrochemical Commission), and SAE is Society Automotive Engineers). Adapted from [2].

As it can be seen from the organization names, proposed standards are industry-driven. In an academic research point of you, research papers are performance-driven. In some cases, particular data interpretation and/or cell configuration allow to obtain tremendous specific capacitance. However, the test procedure works for lab-scale and is not applicable for industry-scale. Therefore, some papers highlight “the good practice” for supercapacitors performance evaluation and are presented in the next section.

3.3. Measurements of Key Metrics

Electrochemical measurements are focused on three parameters: current, potential, and time. All the key metrics used for the supercapacitors performance evaluation derive

from these values. The key metrics are capacitance, equivalent series resistance, operating voltage. Typical measurements, which are cyclic voltammetry, galvanostatic charge-discharge, and electrochemical impedance spectroscopy, have their own focus and targeted parameters. These three measurements are discussed in this section.

3.3.1. Cyclic Voltammetry (CV)

Cyclic voltammetry consists in applying a linearly changed electric potential between the two electrodes, which act as positive (cathode) and negative (anode) electrodes. In a three-electrodes configuration, the electric potential is applied between the working and the reference electrodes.

The setup parameters for this measurement are scan rate (also called sweep rate) and the potential window. The scan rate is the speed of the potential change typically expressed in mV/s or V/s.

The data acquisition during CV contains the instantaneous current induced during the cathodic and anodic sweeps, the time, and the scan rate which was fixed by the operators. Typical voltammograms are plotted usually as current (A or mA) vs. potential (V) but sometimes also as current vs time (s).

The shape of the voltammograms may be different according to the charge storage mechanism. Indeed, for EDLCs, a rectangular shape is observed, while intense deviation from rectangular shape due to pronounced redox peaks can be observed for some PCs or hybrid supercapacitors containing both EDLCs and PCs. Both cases are illustrated in Figure 3.3.

However, in some cases, Faradaic processes do not produce significant change to the instantaneous current and, consequently, the resultant voltammogram shape remains rectangular. Therefore, it could be tricky to distinguish EDLCs and PCs based only on the shape of the CV curve. To overcome this issue, more quantitative and reliable methods were developed. They extract the two different contributions

(EDLCs and PCs) according to the time dependence of these phenomena. Indeed, EDL mechanism is linearly dependant on the scan rate (i f(t)) while phenomena induced by the pseudocapacitive materials, such as semi-infinite diffusion limited carbon adsorption/insertion at/near the electrode surface, are proportional to the square root of the scan rate (i $f(t^{1/2})$).[11]

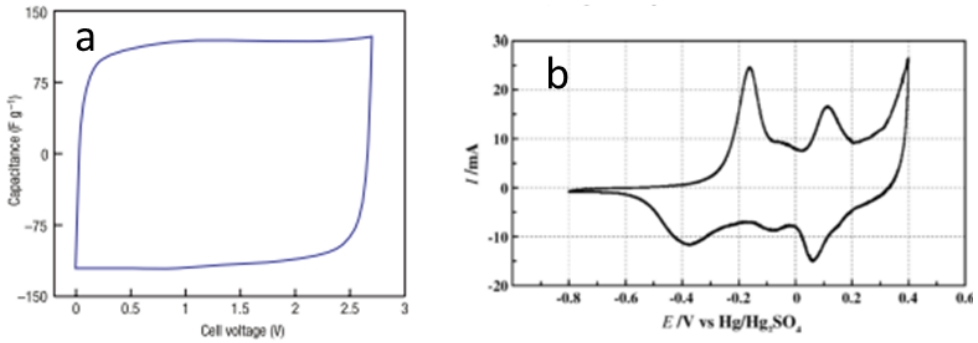

Figure 3. 3. (a) EDLC: Cyclic Voltammetry of a two-electrode cell using an ionic liquid,[9] and (b) Hybrid supercapacitors (PANI/MWCNTs) measured by CV in a three-electrode configuration using 1M H_2SO_4 as electrolyte.[10]

Nevertheless, surface-redox reactions have a time dependence roughly linear, which can create some misleading interpretation by overlapping with EDLCs phenomena.

Cyclic voltammetry is a useful technique to determine the operating voltage or potential window by increasing each time this value in a three-electrode configuration. In addition, the reversibility of phenomena contributing to the change of the instantaneous current can be investigated by cycling and observing shape change.[12] In a two-electrode configuration, the device-like performance can be estimated.

3.3.2. Galvanostatic Charge-Discharge (CCCD)

Galvanostatic charge-discharge or Constant Current Charge Discharge (CCCD) is a measurement mimicking the use of supercapacitor in real applications. Indeed, this measurement uses a constant current to charge and

discharge the device. Typically, the reported current charge-discharge is given as a current density which can be gravimetric (A/g) or using the surface of the electrode (A/cm²).

The parameters setup includes current, potential window and the dwelling time. A dwelling period corresponds to a time between charging and discharging while the peak voltage remains constant. This step can be absent of the procedure. The output graphs are usually plotted as voltage (V) vs. time (s). A triangular shape is expected for EDLCs while the observed shape for hybrid capacitors could be completely different. Both cases are illustrated in Figure 3.4.

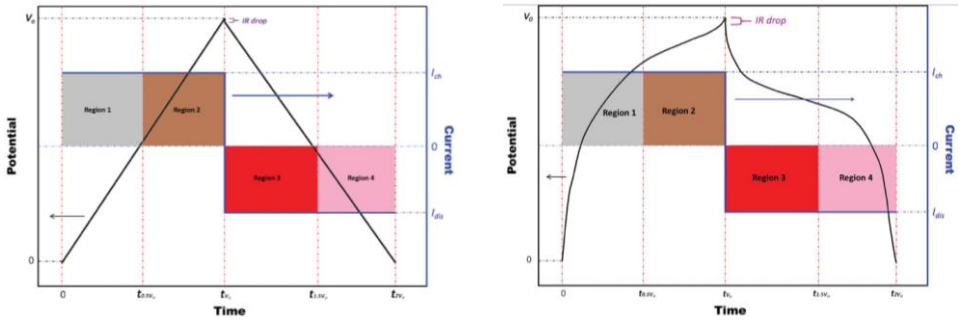

Figure 3. 4. Galvanostatic Charge-Discharge curves for: (left) EDLCs or PCs without strong Faradaic processes and (right) PCs or Hybrid Supercapacitors with strong Faradaic processes.[2]

This method is the most widely used for supercapacitor characterizations.[13] Indeed, all the three core parameters (capacitance, ESR, and operating voltage) can be tested with this method and the other key metrics can be calculated using the output data as described later.

3.3.3. Electrochemical Impedance Spectroscopy (EIS)

EIS measures the impedance of a power cell as a function of the frequency by applying a low-amplitude alternating voltage (typically 5-10 mV) superimposed on a steady-state potential.

The acquired data are usually plotted as both Bode and Nyquist plots. A Bode plot shows the variation of the phase angle with frequency while a Nyquist plot reports the

imaginary part in function of the real part of the cell impedances on a complex plane.[14,15] Typical Bode and Nyquist graphs for supercapacitor are shown in Figure 3.5.

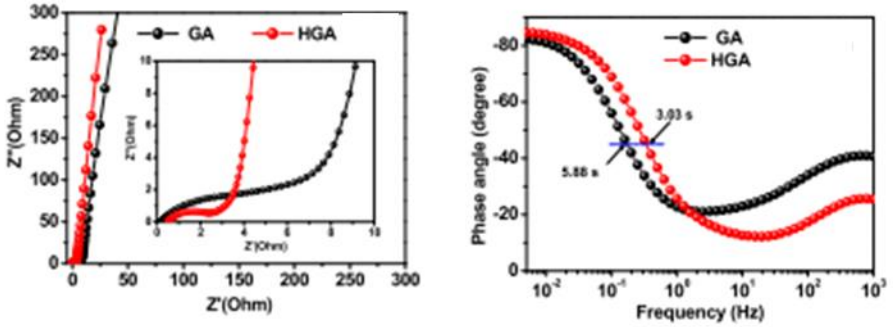

Figure 3. 5. (left) Nyquist plot and (right) Bode plots of GA (aerogel built with non-holey graphene sheets) and HGA (aerogel built with holey graphene sheets)[16]

In addition to the frequency and impedance, EIS can be used to evaluate the charge transfer, mass transport, and charge transfer mechanism. Finally, this technique can be used to determine the capacitance, energy and power densities building an equivalent circuit to represent the supercapacitor.[17,18]

However, the operator must have a good understanding of the phenomena present in the cell to build an equivalent circuit with a physical meaning. Indeed, different equivalent circuits can fit the same curve adjusting the different building blocks number and value but only one has a physical meaning and represent truly the supercapacitor cell.

3.4. Key Metrics

As illustrated above in Figure 3.2, a supercapacitor can be seen as a network of key metrics strongly coupled together and with a huge impact for the deliverable performance of the supercapacitor devices. In this section, key metrics are defined, and calculation methods are explained.

3.4.1. Capacitance

3.4.1.1. Definition

The total capacitance (C_T) is the amount of the electrical charge (ΔQ) under a given voltage change (ΔV):

$$C_T = \frac{\Delta Q}{\Delta V} \tag{3.1}$$

This value corresponds to the total charge storage ability of a supercapacitor device. However, in a research point of view, a specific capacitance (C_T) referred to the material used is preferred.

$$C_S = \frac{\Delta Q}{\Delta V . \Pi} \tag{3.2}$$

In the equation 3.2, Π is function of the relevant parameters to express the performance of the supercapacitor. It can be mass, volume, surface area of the electrode, or even the size of the electrode. Typically, the specific capacitance is expressed accordingly to the Π used: gravimetric capacitance (F/g), volumetric capacitance (F/cm³), areal capacitance (F/cm²), linear capacitance (F/cm), etc. However, the value used to transform the total capacitance in specific capacitance can corresponds to the active material, electrode, or even device. The authors must mentioned this information to avoid misleading interpretation.[19]

3.4.1.2. Calculation

3.4.1.2.1. From CV curve

Before the data acquisition necessary to calculate the capacitance from CV curve, the cell must be cycled for at least 20 cycles. Moreover, it is recommended to use the whole curve to calculate the total capacitance from CV curve.[20] In this case, the equation 3.1 evolves in 3.3 using the integration of the CV curve expressed as current (i) vs time (t).

$$C_T = \frac{\Delta Q}{\Delta V} = \frac{\int_0^{2(V_0/\upsilon)} |i| dt}{2\, V_0} \tag{3.3}$$

where V_0 is the maximum of the potential window and v is the scan rate.

3.4.1.2.2. From charge-discharge curve

To evaluate properly the capacitance from CCCD curve, the current density must be tailored to provide charge and discharge time comprised between 5 and 60 seconds.

As aforementioned, the current is constant during galvanostatic charge-discharge measurements. So, the equation 3.1 evolves in 3.4.

$$C_T = \frac{\Delta Q}{\Delta V} = \frac{i\,\Delta t}{\Delta V} \tag{3.4}$$

To calculate the capacitance, the whole discharging curve is typically used. The equation can be expressed as below:

$$C_T = \frac{i\,\Delta t}{\Delta V} = \frac{i_{dis}\,\Delta t_{V_0 \to 2V_0}}{V_0} \tag{3.5}$$

However, for a more accurate calculation, the IR drop, which is inevitable in CCCD measurements, must be excluded and the expression becomes:

$$C_T = \frac{i_{dis}\,\Delta t_{V_0 \to 2V_0}}{V_0 - V_{IR\,drop}} \tag{3.6}$$

3.4.1.2.3. From EIS

The calculation used the imaginary part of the complex impedance Im(Z) as reported in the equation 3.7.[14]

$$C_T = -\frac{1}{2\,\pi\,f\,\mathrm{Im}(Z)} \tag{3.7}$$

where f is the frequency. The frequency value is determined graphically using the frequency at which the phase angle reaches -45° or at the lowest frequency applied.

3.4.1.3. Concluding remarks

Three-electrode configuration is useful for materials understanding, and evaluation with the value of the specific capacitance. In another way, two-electrode configuration

can be seen as a device prototype in addition to be useful to compare materials performance.

It is important to underline the experimental setups because the difference can be significant. To demonstrate it,[21] gravimetric capacitance (C_x) is used with an electrode weight of m (constant for the two electrodes in the two-electrode configuration). The total capacitance for a cell is expressed as C_E.

In a three-electrode configuration, the specific capacitance ($C_{3\text{-electrode}}$) can be calculated as follow:

$$C_{3-\text{electrode}} = \frac{C_E}{m} \tag{3.8}$$

For the two-electrode configuration, the cell can be seen as two electrodes in parallel. So, the total capacitance can be calculated as follow:

$$\frac{1}{C_{T_{2-\text{electrode}}}} = \frac{1}{C_E} + \frac{1}{C_E} \tag{3.9}$$

$$C_{T_{2-\text{electrode}}} = \frac{C_E}{2} \tag{3.10}$$

Calculating the specific capacitance using the mass of both electrodes:

$$C_{2-\text{electrode}} = \frac{C_{T_{2-\text{electrode}}}}{2\,m} = \frac{C_E}{4\,m} \tag{3.11}$$

If we compare the specific capacitance calculated for two- and three-electrode configuration, knowing that:

$$m = \frac{C_E}{4\,C_{2-\text{electrode}}} \tag{3.12}$$

Introducing 3.11 in 3.8, we obtain

$$C_{3-\text{electrode}} = \frac{C_E}{m} = \frac{\cancel{C_E}}{\cancel{C_E}}\,4\,C_{2-\text{electrode}} \tag{3.13}$$

So, the specific capacitance calculated using a three-electrode configuration is four times higher than the one calculated from a two-electrode configuration for a

symmetric supercapacitor. Béguin and co-workers have validated experimentally this demonstration.[10]

3.4.2. Equivalent Series Resistance

3.4.2.1. Definition

A supercapacitor is an electrical component, which theoretically does not have a proper resistance. Actually, supercapacitors dissipate a part of the energy stored due to an internal resistance. This resistance is called by the electrochemists ESR for equivalent series resistance. Of course, the capacitance is reduced by this resistance. In a first approach, supercapacitors can be seen as a RC circuit composed of a series of capacitor and a resistor as shown in Figure 3.6.

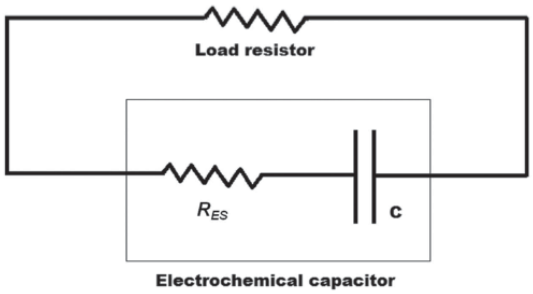

Figure 3. 6. A series RC circuit used to represented Supercapacitors.[2]

3.4.2.2. Calculation

3.4.2.2.1. From galvanostatic charge-discharge

As described previously, the IR drop is impossible to avoid during CCCD measurements. This variation of potential can be used to calculate the ESR by applying the Ohm's law:

$$\mathrm{ESR} = \frac{\Delta \mathrm{V}}{\Delta \mathrm{i}} \qquad (3.14)$$

This method is widely accepted by the scientific community to evaluate ESR. Nevertheless, the current used during the CCCD measurement has an impact on the ESR value. Indeed, a larger current tends to minimize the ESR value as demonstrated by Burke and Miller.[13]

Another approach is commonly used in the literature. This method is based on the voltage recovery behaviour after a

current interruption during a discharge process. The dc internal resistance is calculated from the equation 3.14 where the variation of current from i to 0 while the variation of potential refers to the change measured due to the i-interruption. If the data acquisition occurs at ≤ 10 ms, the resistance corresponds to the ESR of the device.[22]

3.4.2.2.2. From EIS

Two different procedures are accepted in the literature for the determination of ESR using EIS technique. In the first approach, the real part of the complex impedance at a frequency of 1 kHz corresponds to the ESR value. In the second, a linear interpolation of the low-frequency part of the Nyquist plot is drawn. The intersection between this straight line and the Im(Z) = 0 corresponds to the ESR value. The two experimental methods are illustrated in Figure 3.7.

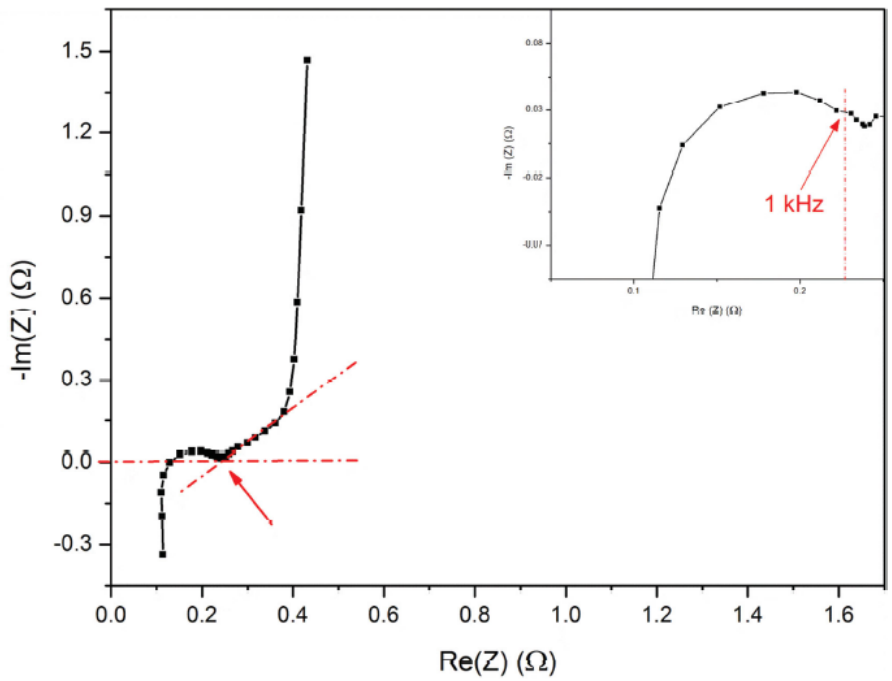

Figure 3. 7. Nyquist plot of 2.7 V / 1 F Maxwell SC with ESR determination methods highlighted in red. In the inset, the first approach to determine ESR illustrated.[2]

It is important to highlight that the ESR value obtained from EIS technique is generally much smaller than the one obtained from CCCD curves as demonstrated by Ruoff *et al.*.[23]

3.4.3. Operating Voltage

The operating voltage (V_0) is the potential window in which the supercapacitor works normally and safely. Indeed, above a certain potential value, electrolyte and even some active materials can degrade irreversibly. For example, due to the water splitting effect, the potential window of a supercapacitor using an aqueous electrolyte is strictly limited at a maximum of 1.2 V.

To determine the operating voltage of a cell, both CV and CCCD curves can be used. The procedure is simple and straightforward. Indeed, starting with a low voltage value, an incremental increase of the voltage is performed until a spike appears at the boundary of the potential window, or more dramatically, when the cell explodes.

3.4.4. Time Constants

The time constant τ indicates the ability of the supercapacitor device to respond to a solicitation. Typical range for commercial supercapacitors is 0.5 to 3.6 s.[24]

The calculation of τ is based on the equivalent circuit RC as described in the section 3.4.2.1. Practically, the time constant is the product of the ESR and the total capacitance of the device:

$$\tau = \mathrm{ESR}\, C_T \qquad (3.15)$$

The other time constant is the “relaxation time constant”, denoted τ_0. The relaxation time constant corresponds to the boundary between the capacitive and the resistive parts of the RC circuits. For supercapacitor applications, lower value of this parameter indicates a higher power delivery capability.[25]

Simon *et al.* proposed a straightforward procedure to determine this parameter based on EIS measurement.[17] They

plot the imaginary part of the complex impedance in function of the frequency. The curve contains a maximum located at a frequency f_0. Then, the relaxation time constant can be calculated with the following equation:

$$\tau_0 = \frac{1}{f_0} \tag{3.16}$$

3.4.5. Power and Energy Densities

3.4.5.1. General Background

Power and energy densities are key metrics useful regarding the final application of the supercapacitor device. As described in Chapter 1, the Ragone plot is used to represent these two key metrics. In Figure 3.8, a Ragone plot is presented with a diagonal time line, which corresponds to the so-called "characteristic time".[26] This time indicates the running time of the supercapacitor at the rated power. This value was introduced due to the rate dependence characteristic of electrical energy storage devices.

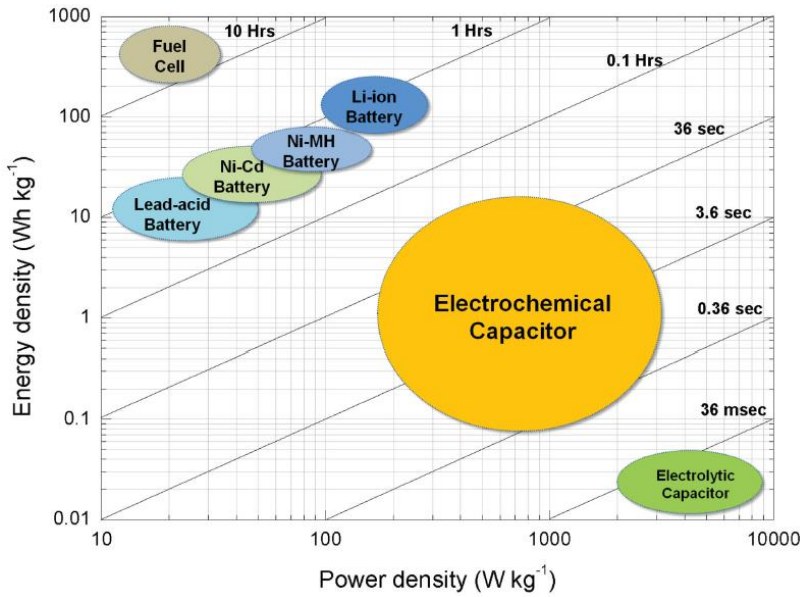

Figure 3. 8. Schematic representation of a Ragone plot containing the main electrical energy storage devices. The diagonal lines correspond to the characteristic time.[2]

3.4.5.2. Power density

The power density of supercapacitor is the characteristic which make this technology advantageous in comparison to the batteries. The power density is calculated using the following equation:

$$P_D = \frac{V_0^2}{4\,ESR\,\Pi} \qquad (3.17)$$

The maximum power delivery achievable by a supercapacitor can be performed only when the load as the identical resistance as ESR. However, this necessary match between the load and the ESR is difficult to achieve.

3.4.5.3. Energy density

Increasing the energy density is the main aim of the scientific community working on supercapacitors. Indeed, higher is this value, stronger is the supercapacitor in comparison with the battery technology.

Energy density is calculated from CCCD measurements by integration of the whole curve (charge and discharge). For EDLCs and PCs without apparent Faradaic processes, the CCCD curve is a perfect triangle as shown in Figure 3.9.

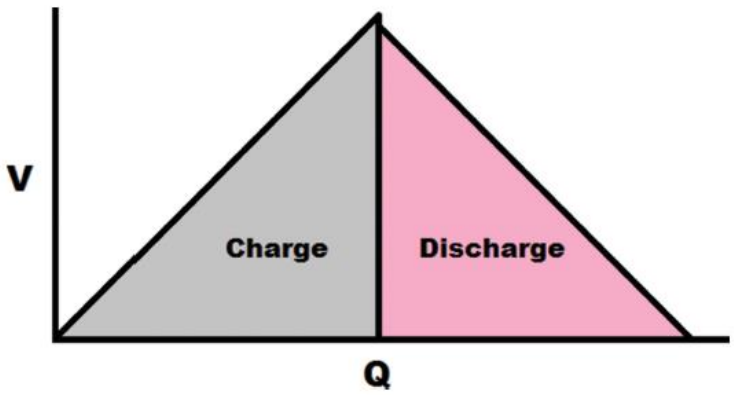

Figure 3. 9. Schematic representation of a CCCD curve for EDLCs or PCs without strong Faradaic processes.[2]

The integration of the CCCD curves corresponds to the area of the triangle. So, the expression of the energy density is:

$$E_D = \int_0^Q V_0 \, dq = \frac{1}{2} V_0 \, Q \qquad (3.18)$$

Isolating Q in the equation 3.2 and substituting it in 3.18, the expression becomes:

$$E_D = \frac{1}{2\,\Pi} C_T V_0^2 \qquad (3.19)$$

Energy is expressed in Joule/Π unit. By dividing by 3600, the unit becomes Wh/ Π and the expression is:

$$E_D = \frac{1}{7200\,\Pi} C_T V_0^2 \qquad (3.20)$$

In the case of PCs with strong Faradaic processes (Figure 3.10), the equation 3.18 evolves in 3.21:

$$E_D = \frac{1}{3600\,\Pi} \int_0^{t_Q} V \, i \, dt \qquad (3.21)$$

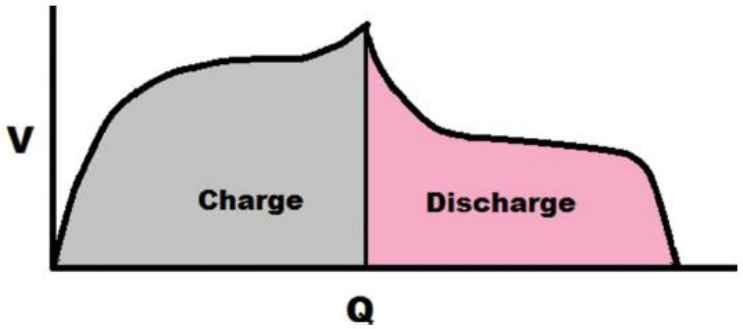

Figure 3. 10. Schematic representation of a CCCD curve for PCs or Hybrid Supercapacitors with strong Faradaic processes.[2]

3.4.5.4. Concluding remarks

For EDLCs (and PCs with triangular CCCD curves), the ratio between the energy density (3.19) and power density (3.17) is:

$$\frac{E_D}{P_D} = \frac{\frac{1}{2\,\Pi} C_T V_0^2}{\frac{V_0^2}{4\,ESR\,\Pi}} = 2\,ESR\,C_T = 2\,\tau \qquad (3.22)$$

Therefore, energy density and maximum are closely coupled by the cell time constant.

Another indicator of the supercapacitor performance is the ratio between the integral value of discharging curve and the integral value of the charging curve. Indeed, the charging corresponds to the stored electric energy while the discharging indicates the deliverable energy. The ratio of these two values is called energy efficiency of the cell.

3.4.6. Leakage and Maximum Peak currents

Before to be use in real applications, other key metrics must be known. Leakage and maximum peak currents are two important parameters in an industrial context.

The leakage current value indicates the capability of the supercapacitor device to maintain a fixed value of potential when not in use. It is typically estimated as the compensating current needed after 72 hours to recover a fully-charged state of a supercapacitor.

The maximum peak current is generally expressed on commercial product and is calculated as follow:

$$i_{max@1s} = \frac{1}{2}\frac{C_T V_0}{C_T\,ESR + 1} \qquad (3.22)$$

This key metric is evaluated by discharging a fully charged supercapacitor device from the operating voltage to the half of this value in 1 second.

3.4.7. Cycle life and Capacitance Retention Rate

Finally, the last key metrics are cycle life and capacitance retention rate. The first is one of the main advantage of this technology, which in real application leads to the so-called “fit-and-forget”. Indeed, with a cycling life higher than 1 million cycles, supercapacitor devices can be installed and almost forgotten because they would not be, theoretically, the limiting device in term of cycling life. The procedure to evaluate this key metric is easy, CCCD curves (or even CV) repeated thousands of times. The obtained value is then compared to the starting one.

Due to the high capacitance retention rate of supercapacitor, it is even difficult to evaluate properly even by cycling hundreds of thousands of time. Uno and Tanaka demonstrate this key metric by cycling a supercapacitor for 3.8 years and results showed that the capacitance retention rate decreases almost linearly with the square root of the number of cycles.[27]

3.5. Conclusions

The aim of this chapter was to give some information about the experimental setups used to calculate the key metrics of a supercapacitor. As shown in Figure 3.2, type of measurements is strongly correlated to the core parameters. Therefore, it is crucial to give all the measurements parameters such as electrode configurations (two vs three), mass of the active material, electrodes dimensions, selected electrolyte, etc.

REFERENCES

(1) Stoller, M. D.; Ruoff, R. S. Best Practice Methods for Determining an Electrode Material's Performance for Ultracapacitors. *Energy Environ. Sci.* **2010**, *3* (9), 1294–1301.

(2) Zhang, S.; Pan, N. Supercapacitors Performance Evaluation. *Adv. Energy Mater.* **2014**, *5* (6), 1401401.

(3) Conway, B. E. *Electrochemical Supercapacitors: Scientific Fundamentals and Technological Applications*; Kluwer Academic / Plenum Publisher, 1999.

(4) Beguin, F.; Frackowiak, E. *Supercapacitors: Materials, Systems and Applications*; Sons, J. W. &, Ed.; 2013.

(5) Becker, H. I. Low Voltage Electrolytic Capacitor. US2800616, 1957.

(6) Helmholtz. Ueber Einige Gesetze Der Vertheilung Elektrischer Ströme in Körperlichen Leitern Mit Anwendung Auf Die Thierisch-Elektrischen Versuche. *Ann. Phys.* **1853**, *165* (6), 211–233.

(7) Chen, T.; Dai, L. Carbon Nanomaterials for High-Performance Supercapacitors. *Mater. Today* **2013**, *16* (7–8), 272–280.

(8) Trasatti, S.; Buzzanca, G. Ruthenium Dioxide: A New Interesting Electrode Material. Solid Structure and Electrochemical Behaviour. *J. Electroanal. Chem.* **1971**, *29*, A1–A5.

(9) Simon, P.; Gogotsi, Y. Materials for Electrochemical Capacitors. *Nat. Mater.* **2008**, *7* (11), 845–854.

(10) Khomenko, V.; Frackowiak, E.; Béguin, F. Determination of the Specific Capacitance of Conducting Polymer/nanotubes Composite Electrodes Using Different Cell Configurations. *Electrochim. Acta* **2005**, *50* (12), 2499–2506.

(11) Augustyn, V.; Come, J.; Lowe, M. A.; Kim, J. W.; Taberna, P.-L.; Tolbert, S. H.; Abruña, H. D.; Simon, P.; Dunn, B. High-Rate Electrochemical Energy Storage through Li+ Intercalation Pseudocapacitance. *Nat. Mater.* **2013**, *12* (6), 518–522.

(12) Toupin, M.; Brousse, T.; Bélanger, D. Charge Storage Mechanism of MnO2 Electrode Used in Aqueous Electrochemical Capacitor. *Chem. Mater.* **2004**, *16* (16), 3184–3190.

(13) Burke, A.; Miller, M. Testing of Electrochemical Capacitors: Capacitance, Resistance, Energy Density, and Power Capability. *Electrochim. Acta* **2010**, *55* (25), 7538–7548.

(14) Miller, J. R.; Outlaw, R. A.; Holloway, B. C. Graphene Double-Layer Capacitor with Ac Line-Filtering Performance. *Science.* **2010**, *329* (5999), 1637–1639.

(15) Du, C.; Pan, N. Supercapacitors Using Carbon Nanotubes Films by Electrophoretic Deposition. *J. Power Sources* **2006**, *160* (2 SPEC. ISS.), 1487–1494.

(16) Zang, P.; Gao, S.; Dang, L.; Liu, Z.; Lei, Z. Green Synthesis of Holey Graphene Sheets and Their Assembly into Aerogel with Improved Ion Transport Property. *Electrochim. Acta* **2016**, *212*, 171–178.

(17) Taberna, P. L.; Simon, P.; Fauvarque, J. F. Electrochemical Characteristics and Impedance Spectroscopy Studies of Carbon-Carbon Supercapacitors. *J. Electrochem. Soc.* **2003**, *150* (3), A292.

(18) Dupont, M. F.; Hollenkamp, A. F.; Donne, S. W. Large Amplitude Electrochemical Impedance Spectroscopy for Characterizing the Performance of Electrochemical Capacitors. *J. Electrochem. Soc.* **2014**, *161* (4), A648–A656.

(19) Yang, X.; Cheng, C.; Wang, Y.; Qiu, L.; Li, D. Liquid-Mediated Dense Integration of Graphene Materials for Compact Capacitive Energy Storage. *Science.* **2013**, *341* (8), 534–537.

(20) Stoller, M. D.; Park, S.; Yanwu, Z.; An, J.; Ruoff, R. S. Graphene-Based Ultracapacitors. *Nano Lett.* **2008**, *8* (10), 3498–3502.

(21) Qu, D.; Shi, H. Studies of the Activated Carbons Used in Double-Layer Supercapacitors. *J. Power Sources* **1998**, *74*, 99–107.

(22) Zhao, S.; Wu, F.; Yang, L.; Gao, L.; Burke, A. F. A Measurement Method for Determination of Dc Internal Resistance of Batteries and Supercapacitors. *Electrochem. commun.* **2010**, *12* (2), 242–245.

(23) Zhu, Y.; Murali, S.; Stoller, M. D.; Ganesh, K. J.; Cai, W.; Ferreira, P. J.; Pirkle, A.; Wallace, R. M.; Cychosz, K. a; Thommes, M.; Su, D.; Stach, E. a; Ruoff, R. S. Carbon-Based Supercapacitors Produced by Activation of Graphene. *Science.* **2011**, *332* (June), 1537–1542.

(24) Burke, A.; Miller, M. The Power Capability of Ultracapacitors and Lithium Batteries for Electric and Hybrid Vehicle Applications. *J. Power Sources* **2011**, *196* (1), 514–522.

(25) Farma, R.; Deraman, M.; Awitdrus; Talib, I. A.; Omar, R.; Manjunatha, J. G.; Ishak, M. . M.; Bashri, N. H.; Dolah, B. N. M. Physical and Electrochemical Properties of Supercapacitor Electrodes Derived from Carbon Nanotube and Biomass Carbon. *Int. J. Electrochem. Sci* **2013**, *8*, 257–273.

(26) Christen, T.; Carlen, M. W. Theory of Ragone Plots. *J. Power Sources* **2000**, *91* (2), 210–216.

(27) Uno, M.; Tanaka, K. Accelerated Charge-Discharge Cycling Test and Cycle Life Prediction Model for Supercapacitors in Alternative Battery Applications. *IEEE Trans. Ind. Electron.* **2012**, *59* (12), 4704–4712.

Chapter 4

Graphene-Mo-compounds composites for enhanced supercapacitors performance

As thoroughly explained in Chapter 2, metal oxides and metal dichalcogenides are interesting to increase specific capacitance of Supercapacitors. In particular, this chapter is aimed to in-situ synthesize a hybrid 1T-2H-molybdenum disulphide and, at the same time, to reduce graphene oxide by one-pot hydrothermal synthesis. The supercapacitor resulting from this innovative hybrid demonstrates outstanding electrochemical performance, in comparison to other hybrids, in addition to a stability up to 50.000 cycles.

Part of the work described in this chapter has been previously published in ACS Applied Materials & Interfaces, 2016 (8), 32842-32852.

4.1. Motivations

Recently, Transition Metal Dichalcogenides (TMDs) have attracted attention due to their peculiar properties as described previously in the Section 2.3.2.3. Molybdenum Disulphide, MoS_2, is the most promising TMD for energy storage applications which explains the current intensive investigation for using it as materials for energy storage applications. Indeed, the first patent for using MoS_2 as cathode materials for battery applications was filled in 1980.[1] The attractivity of this TMD lies in its transition metal centre, Mo, which can assume a variety of oxidation states from +2 to +6,[2–4] and its unique 2D, graphene-like, layered

structure. It has high intrinsic ionic conductivity that guarantees for high capacitance: it can show both an electrochemical double layer (EDL) and a pseudocapacitive behaviour (PC), due to the Mo redox reactions and ability to easily promote ions insertion between layers.[5]

Since then, research was focused on the synthesis and/or production of this promising material. Typically, two approaches can be investigated: "top-down" or "bottom-up". In the first method, the starting material is bulk MoS_2 flakes stacked together due to Van der Walls interactions between flakes. Then, the idea is to exfoliate this raw material to obtain single (or few) layers of MoS_2. The exfoliation can be micromechanical using sticky tapes, which was the same technique used by Geim and Novoselov to isolate for the first time Graphene (See section 2.2.2.2.1).[6] This technique allows to produce MoS_2 flakes with random shapes, sizes, and number of layers. Nevertheless, the quality is high while the yield is very low. However, the main limitation is the inability to scale this process up for large volume production. Another way to produce MoS_2 flakes from bulk material is the liquid phase exfoliation. Solvents used are typically N-methyl-pyrrolidone (NMP) and Isopropanol (IPA). This way can be either only physical by means of sonication, shearing, grinding, bubbling, or may include chemical reactions to facilitate the process. Interestingly, the obtained amount of exfoliated materials is much higher and can be potentially be scaled up.[7] Nevertheless, the quality is much lower which can be limiting for practical applications. The last top-down approach investigated is an electrochemical exfoliation assisted by Lithium.[8]

The "bottom-up" approach can be followed using three ways: Physical Vapor Deposition, Chemical Vapor Deposition, and Solution Chemical Process. The Physical Vapor Deposition[9,10] has attracted less attention. Using high purity target of MoS_2 (>99.9%) and very low pressure ($<5.10^{-9}$ Torr), it is possible to grow continuous ultra-thin film of MoS_2 as demonstrated by Muratore *et al.*.[10] A most common method for film production is the Chemical Vapor Deposition which allows to obtain large area growth of the desired materials.

Interestingly, the deposition is uniform which makes this approach appealing for the applications market. The CVD uses chemical reactions as growth mechanism. Typically, precursors of MoS_2 can be MoO_3, Mo, or $MoCl_5$. Then, the growth mechanism occurs with a sulfurization reaction, involving H_2S as S precursor, producing layered MoS_2 structures. The last way is the solution chemical process, which is known as hydrothermal[11–22] or solvothermal[23] synthesis depending of the nature of the solvent used during the synthesis. Reactions take place typically in a stainless-steel autoclave in range of temperature from 120°C to 360°C for few hours. This *in-situ* synthesis occurs in two different steps. The first one is the decomposition of the Molybdenum precursor to form Molybdenum Oxides (IV or VI) species. Typical Mo precursors can be sodium molybdate [Na_2MoO_4],[13–16,18–22] ammonium tetrathiomolybdate [$(NH_4)_2MoS_4$],[23] ammonium heptamolybdate [$(NH_4)_6Mo_7O_{24}$],[17] phosphomolybdic acid [$H_3PMo_{12}O_{40}$],[2,24,25] molybdenum (V) chloride [$MoCl_5$].[26,27] The second step is the sulfurization of metal oxides to form metal dichalcogenides. Typical S precursor can be thiourea [H_2NCSNH_2],[14,19–21] thioacetamide [C_2H_5NS],[17] L-cysteine,[13,15,16,18,27] benzyl mercaptan [C_7H_8S].[26]

Despite of the chemical process is apparently easy; an intrinsic limitation should be taken in consideration. Indeed, MoS_2 flakes tend to wind around themselves and form fullerene-like nanoparticles or nanotube structures during the synthesis.[26] To obtain a layered structure of molybdenum disulphide, a modification of the conditions reaction is necessary. An efficient way is to introduce graphene or graphene oxide as substrate.[13,23,28] Indeed, graphene will inhibit the growth of MoS_2 flakes in the third-dimension. Moreover, the as-prepared graphene-dichalcogenide composites are hybrid materials with superior properties due to a synergetic effect between the graphene and the MoS_2 flakes.

As previously described in section 2.3.3, bulk Transition Metal Dichalcogenides exhibit a wide variety of polymorphs due to the spatial organization of the X-M-X layers of atoms

where X is for a chalcogen and M is a transition metal of groups 4-10. In this chapter, X is for Sulphur and M is for Molybdenum. Typically, three polymorphs can be encountered: 1T (trigonal), 2H (hexagonal), and 3R (rhombohedral) according to the number of S-Mo-S in the unit cell.[29,30] Crystallographic structure of polymorphs are reported in Figure 4.1.

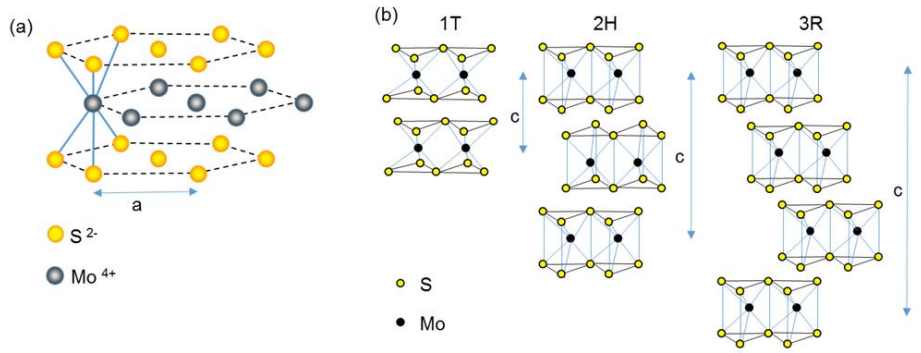

*Figure 4. 1.Schematic representation of: (**a**) Hexagonal structure of S and Mo layers and (**b**) 1T/2H/3R polymorphs unit cells of molybdenum disulphide, where "c" represents the number of layers in a repeat unit.[30]*

These three phases have different properties and stability. The most common phase is the trigonal prismatic 2H-MoS_2 phase, which is a semiconductor with a monolayer direct bandgap of ≈ 1.67 eV.[31] The 3R-MoS_2 phase is less described in literature because the metal coordination is again trigonal prismatic, like 2H-MoS_2. The 1T-MoS_2, also called distorted octahedral, is by far the most interesting for electrode materials in supercapacitor applications because this phase is metallic with a conductivity 10^7 times higher than the 2H-phase in addition to other interesting properties such as hydrophilicity, electrical conductivity and ability to intercalate different ions making this polymorph the most appealing for high efficiency supercapacitors.[32,33]

The first synthesis of the metastable 1T-MoS_2 phase was reported in 1992 by Wypich and co-workers by controlled oxidation of ternary hydrated $K_x(H_2O)_yMoS_2$ using $K_2Cr_2O_7$ in excess.[34] In the last year, lot of efforts were concentrated to improve the synthesis of the 1T polymorph. The desired phase can be find in co-existence with the 2H phase in a mixture WS_2/MoS_2 synthesized by annealing using rGO-Ni

foam coated with $(NH_4)_2MoS_4$ as precursor.[35] A solvothermal synthesis using DMF as solvent starting from the same precursor allows Lee and co-workers to observe the metastable 1T-phase.[36] The layered exfoliated 2H-MoS_2 was used also as support for the 1T phase solvothermally produced.[37] A controlled growth in a solvent mixture (DMF/H_2O) permits Wu and co-workers to coat carbon fibre cloth with 1T-MoS_2.[38] Finally, in "greener" ways, synthesis of 1T polymorph was demonstrated using L-ascorbic acid as reductant starting from $LiMoS_2$ as precursor[39] or using the intercalation of NH_4^+, produced by hydrothermal decomposition of ammonium bicarbonate, through bulk MoS_2 flakes.[40]

Despite the many research works published on the energy storage properties of graphene-dichalcogenide-based aerogels, few studies compared the performance of different materials and fabrication processes using the same experimental conditions. Consequently, the comparison is difficult, and the interpretation can be misleading.

To overcome this issue, this chapter was aimed to the identification of a hybrid aerogel to be exploited as electrode material with superior performance in terms of supercapacitance. Different aerogels are synthesized using a simple and inexpensive one-pot hydrothermal synthesis procedure that allows combining reduced Graphene Oxide and Mo–compounds, under the form of oxide (MoO_2) or dichalcogenide (MoS_2) in the final product with an attention to the use of environmental friendly reactants and synthesis conditions.

4.2. Materials and Methods

4.2.1. Acronyms

The following acronyms will be employed: **rGO-MoS_2-p** for the composite containing the 2H-MoS_2 powder commercially available added to the GO dispersion before the hydrothermal synthesis; **rGO-MoS_2-co** for the *in-situ* co-synthesized rGO-MoS_2, **MoS_2-p** for 2H-commercially available

MoS_2 powder, **MoS_2-s** for the *in-situ* synthesized MoS_2 powder, **rGO-MoO_2** for the *in-situ* co-synthesized rGO-MoO_2, **MoO_2** for the *in-situ* synthesized MoO_2 powder.

4.2.2. Synthesis procedure

Hybrid aerogels were obtained by hydrothermal reaction followed by a freeze-drying procedure. A dispersion of 2 mg/mL of commercially available Single Layer Graphene Oxide - GO (Cheaptubes Inc.) in deionised water was prepared with a total volume of 17 mL. Then, the dispersion was sonicated 30 minutes at room temperature before to be transferred in a Teflon reactor contained in a stainless-steel autoclave. The hydrothermal synthesis was carried on at 180° for 12 hours. After the reaction, the reactor was cooled down to room temperature. The resulting reduced Graphene Oxide (rGO) hydrogel was rapidly frozen in liquid nitrogen (-196°). Then, the water was removed by sublimation using a freeze-drying procedure. This procedure was carried on overnight at -50° with a pressure of $3x10^{-3}$ mbar. The resulting sample is the rGO aerogel.

The rGO-MoO_2 hybrid was obtained by adding to the pristine GO slurry after the sonication step, 0.5 g of phosphomolybdic acid ($H_3PMo_{12}O_{40}$) solution (20 wt.% in ethanol, from Sigma Aldrich). The mixture was further sonicated for 5 minutes to ensure a homogeneous dispersion of the MoO_2 precursor before the hydrothermal reduction.

The rGO-MoS_2-p aerogel was obtained by adding to the 2mg/mL aqueous dispersion the MoS_2 ultrafine powder (0.6 mg/mL (w/v)), purchased from Graphene Supermarket – Graphene Laboratories Inc. (NY-USA). Then, the slurry containing both GO and MoS_2 was subjected to the same reaction and freeze-drying procedure to obtain an aerogel with MoS_2 nanostructure dispersed on the 3D-rGO matrix. The rGO-MoS_2-co was produced by an *in-situ* synthesis of MoS_2 nanostructure together with the assembly of the rGO aerogel. 106 mg of phosphomolybdic acid hydrate

($H_3PMo_{12}O_{40}.xH_2O$, from Alfa Aesar) were added to the GO slurry as precursor of Mo. The pH was then adjusted to 6.5 by addition of NaOH 1M (Sigma Aldrich) and 170 mg of L-Cysteine (Sigma Aldrich) were added as precursor of S. The slurry was transferred to the autoclave for the hydrothermal reaction and subjected to the same freeze-drying procedure performed for all the previous aerogels.

MoO_2 and MoS_2-p and MoS_2-s were also obtained by hydrothermal synthesis and subsequent freeze-drying to study the materials without rGO contributions. The same procedures used for the corresponding hybrids were repeated without the GO powder to obtain MoO_2, MoS_2-p, and MoS_2-s.

A thermal annealing was carried out on MoS_2-s and rGO-MoS_2-co samples to promote crystallization. The annealing was performed at 800°C for 2h in N_2 (60 mL/min).

4.2.3. Methods

4.2.3.1. Physicochemical characterization

The morphology of the different aerogels was analysed by using a Field Emission Scanning Electron Microscope (FESEM Supra 40 manufactured by ZEISS), equipped with Oxford Si(Li) detector for Energy Dispersive X-ray analysis (EDX).

Transmission Electron Microscopy (TEM) measurements were performed on a FEI Tecnai G2 F20 S-TWIN microscope. Image processing was performed by means of Gatan Microscopy Suite software.

X-ray diffraction analysis (XRD, Panalytical X'Pert MRD Pro Cu Ka X-ray source) in Bragg/Brentano configuration was used to assess the structural characteristics of the hybrid aerogels and the pure transition metal compounds obtained in the same synthesis conditions.

Raman analysis was applied to study the aerogel powders carefully pressed on a glass microscope slide by means of a Renishaw InVia Reflex micro-Raman spectrometer (Renishaw plc, Wottonunder-Edge, UK), equipped with a cooled CCD

camera. The Raman source was a diode laser (λ_{ex}=514.5 nm), and samples inspection occurred through a microscope objective (50X), in backscattering light collection. 5 mW laser power, 10 s of exposure time and 1 to 3 accumulations were employed to collect each spectrum.

X-Ray Photoelectron Spectroscopy (XPS) was carried out on a PHI 5000 VersaProbe (Physical Electronics) system, with a monochromatic Al Kα radiation (1486.6 eV energy) as X-ray source. A 187.85 eV pass energy value was used for survey spectra and 23.5 eV for HR peaks. Charge compensation was accomplished with a combined electron and Ar neutralizer system. The binding energy scale was calibrated by assigning an energy value of 284.5 eV to the main C1s contribution (C-C/C-H bonds) and the background contribution in HR scans has been subtracted by means of a Shirley function.[41]

Specific surface area (SSA) measurements and pore size analysis were carried out on samples previously out-gassed for at least 4 h at 100°C, to remove water and other atmospheric contaminants, by means of N_2 isotherms at -196°C (Quantachrome Autosorb 1C instrument). BET SSA values were measured by multipoint method in the relative pressure range of P/P^0 = 0.05–0.20; cumulative pore volume curves were obtained by applying the QS-DFT method with appropriate kernel (N_2 adsorption @ -196°C onto carbon slit pores).

4.2.3.2. Electrochemical preparation setup

The electrodes were fabricated both for electrochemical measurements in analytical cell configuration (three electrodes and two-electrodes measurements) and in planar symmetric electrodes devices. To prepare them, a homogeneous solution containing the as-synthesized aerogel, finely mixed with a spacer and a binder in absolute ethanol[42] used as homogenizing solvent. The solution was carefully drop-casted onto a well-polished glassy carbon electrode (diameter of 0.3 cm, BioLogic) or onto Fluorine

doped Tin Oxide glass (diameter of 0.5 cm, Solaronix, 10 Ω/sq).

The obtained slurry had the composition of 5 mg active material, 0.4 mg acetylene black (Alfa Aesar) and 5 µL Nafion® 5% (Sigma-Aldrich).

The analytical cell setup used the glassy carbon as current collector for both two and three electrodes measurements. For the two-electrode configuration, two identical as-prepared electrodes were utilised. For the three electrode measurements, the reference electrode used was a Calomel electrode - SCE (with a potential of 240 mV vs Standard Hydrogen Electrode – SHE). The counter electrode used was a platinum bar.

For the device measurements in a symmetrical configuration, two as-prepared electrodes deposited on FTO were faced in a planar configuration. A glass-frit membrane (Whatman GF/A) was used as separator. A thermoplastic polymer (Parafilm®) was melted to be used as sealant to avoid electrolyte leakage. A schematic representation of the device is reported in Figure 4.2.

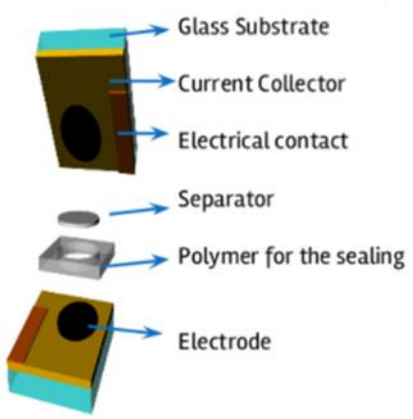

Figure 4. 2. Schematic representation of the device used for electrochemical measurements. Current collector was FTO, Electrical contact was Cu, Seperator was a glass-frit membrane, sealing polymer was Parafilm®.

To be confrontable, electrochemical measurements were performed with the same electrolyte: 1M NaCl in deionised water. Electrodes were soaked overnight before the

measurements to assure a suitable interface between the electrolyte and the electrodes.

4.2.3.3. Electrochemical characterization

All the measurements were carried out on a PGSTATM101 potentiostat–galvanostat (Metrohm Autolab, Netherlands). In three electrodes cells, cyclic voltammetry was performed between −0.7 and +0.2 V vs. SCE at multiple scan rates between 1 V s^{-1} and 3 mV s^{-1}. Galvanostatic charge-discharge cycles were performed between −0.6 and +0.1 V vs. SCE at current densities of 0.25, 0.5, 1 and 2 A g^{-1} and AC impedance spectroscopy was done at OCP (open circuit potential in the frequency range from 10 kHz to 5 mHz with 5 mV amplitude. In two electrodes cell and symmetrical device configurations, cyclic voltammetry and galvanostatic charge-discharge were carried out between −0.5 and +0.5 V at multiple scan rates and current densities, AC impedance spectroscopy was acquired at 0 V in the frequency range from 100 kHz to 5 mHz with 5 mV amplitude and the devices were aged by voltammetry for 50.000 cycles.

4.2.3.4. Effect of mass loading on performance

The mass deposited could influence dramatically the deliverable performance. Three electrodes with different mass loading were investigated. The material used for the comparison was the *in-situ* as-synthesized MoS_2 (MoS_2-s). Electrodes were prepared by drop-casting onto glassy carbon or FTO as reported above for the three- and two-electrodes analytical cell measurements. The same chemical composition was used and the same counter electrode (Pt bar). However, the reference electrode used for this measurement was a homemade Saturated Mercury-mercurous Sulphate Electrode (SMSE electrode is 680 mV vs. SHE). Electrodes were soaked in the electrolyte, 1M H_2SO_4, overnight. Cyclic Voltammetry was performed at different

scan rates between 0.1 mV s^{-1} and 1 V s^{-1} in a potential window comprised between -0.8 and +0.05 V vs SMSE.

4.3. Physicochemical Characterization

4.3.1. Morphological analysis by FESEM and atomic composition by EDX spectroscopy

Morphological characterizations were performed on the as-synthesized aerogels obtained after the hydrothermal reaction and the freeze-drying process. Figure 4.3 shows the low-magnification FESEM images of the aerogels morphology. The aerogel composed of pure rGO aerogel (Figure 4.3.a) has a similar three-dimensional architecture compared with rGO-MoO_2 (Figure 4.3.b), rGO-MoS_2-p (Figure 4.3.c), and rGO-MoS_2-co (Figure 4.3.d). The presence of other chemical species during the hydrothermal synthesis does not seems to influence the self-assembling process.

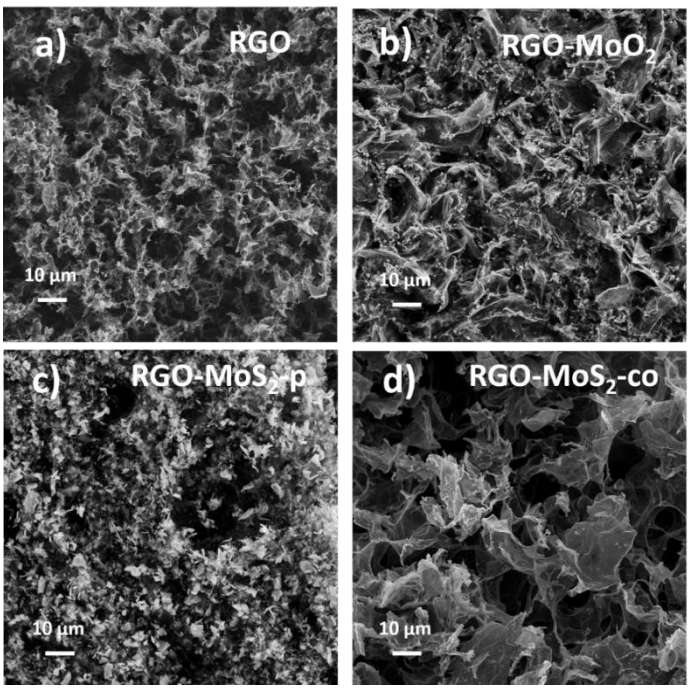

Figure 4. 3. FESEM images at low magnification for (a) rGO, (b) rGO-MoO_2, (c) rGO-MoS_2-p, and (d) rGO-MoS_2-co

Higher magnification allows the study of the micro-architecture for all the as-synthesized aerogels. Figure 4.4.a exhibits a 3D porous structure constituted of wrinkled and curled-up rGO flakes, which can be better appreciated in Figure 4.4.b. This interconnected three-dimensional structure is ideal for supercapacitor applications as reported previously[43]. Indeed, as described earlier this structural organization offers high specific surface area and accessibility by a liquid electrolyte. The nitrogen (N_2) adsorption analysis reported later confirms the suitable properties of the aerogels for supercapacitor applications.

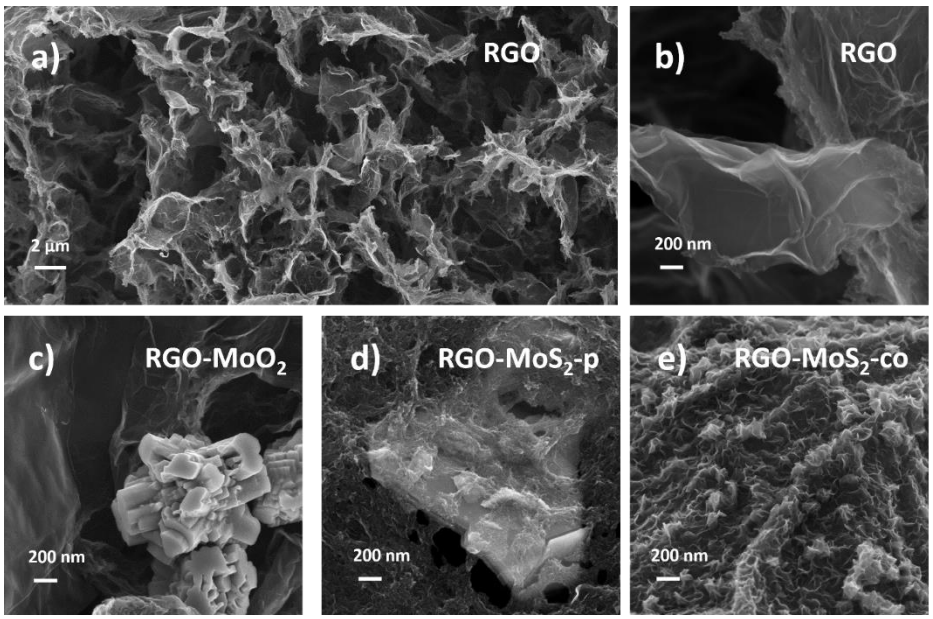

Figure 4. 4. low-magnification (a) and high-magnification (b) FESEM images of the pure rGO aerogel. High-magnification FESEM images of rGO-MoO_2 (c), rGO-MoS_2-p (d) and rGO-MoS_2-co (e) samples.

Concerning the composite containing metal oxides, rGO-MoO_2, graphene flakes are decorated by microparticles with a nanostructured surface (Figure 4.4.c). Figure 4.4.d and Figure 4.4.e are images obtained for graphene-dichalcogenide composites: rGO-MoS_2-p, starting for a commercially available powder (Figure 4.4.d), and rGO-MoS_2-co, using suitable precursors for an *in-situ* synthesis (Figure 4.4.e). rGO-MoS_2-p displays a more heterogeneous structure

in comparison with the rGO-MoS_2-co. Indeed, layered dichalcogenides structures are embedded inside the three-dimensional porous structure. Interestingly, the commercial 2H-MoS_2 powder retains its morphology. The FESEM image of the starting material is reported in Figure 4.5.a. As it can be seen, the lateral size of the commercial structure is awfully variable with a dimension range between 500 and 1500 nm, while the thickness is below 100 nm.

The graphene-dichalcogenide composite *in-situ* synthesized, rGo-MoS_2-co, displays a completely different morphology. In fact, rGO flakes and MoS_2 nanostructures became intimately connected and undistinguishable, making the composite homogeneous as it can be seen in Figure 4.5.b.

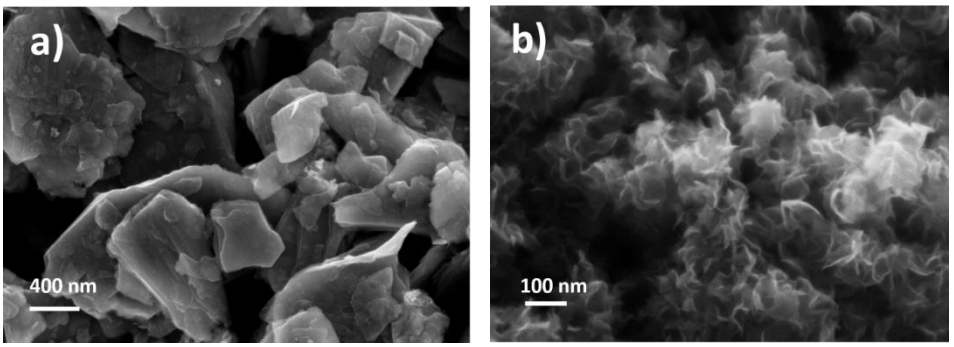

Figure 4. 5. FESEM images at high magnification for (a) commercially available 2H-MoS_2 (MoS_2-p), and (b) in-situ synthesized MoS_2 (MoS_2-s).

EDX spectroscopy analyses were carried on all the samples to investigate the atomic composition. Results are reported in Table 4.1.

Sample	C (at%)	O (at%)	Mo (at%)	S (at%)	Na (at%)
rGO	81.4	18.6	/	/	/
rGO-MoO_2	76.9	18.0	5.1	/	/
rGO-MoS_2-p	86.0	10.9	1.2	1.9	/
rGO-MoS_2-co	54.9	15.6	7.9	17.4	4.2

Table 4. 1. Atomic composition determined by EDX spectroscopy

The atomic ratio between S and Mo for the rGO-MoS_2-co is 2.2 which is close to the stoichiometric value. This data confirms the successful *in-situ* synthesis of the

dichalcogenides. Moreover, the amount of residual Na, which arises from the NaOH solution used to adjust the pH to a value of 6.5 for the proper use of L-Cysteine as S precursor, is not significant.

4.3.2. Composition analysis and phase identification by Raman scattering analysis, XRD, and XPS

4.3.2.1. Raman Analyses

Raman spectra for pure rGO aerogel, graphene-dichalcogenide composites, and the MoS_2-s powder are reported in Figure 4.6 in comparison with the starting GO spectrum. The GO spectrum, curve 1, displays typical photoluminescence at high energy shift. This phenomenon is due to band-gap emission from electron-confined sp^2 islands. The curve 2, assigned to rGO, displays a significant loss of the photoluminescence phenomenon. This decrease is the result of a reduction of GO in rGO occurred during the hydrothermal synthesis. Both GO and rGO spectra show typical peaks of carbon-based materials: D peak and G peak. The D peak is located at 1352 cm^{-1} and is devoted to the defects of sp^2 domains. These defects, containing also vacancies and distortions of sp^2 domains, provoke the decrease in size of in plane-sp^2 domains. The G peak is located at 1595 cm^{-1} and is devoted to a first-order inelastic process involving the degenerate iTO and iLO phonons at the G point (E_{2g} mode). The peak observed at 1595 cm^{-1} is broad due to a superimposition of the D' peak, at 1625cm^{-1} assignable to defects scattering. The broad band between 2600 cm^{-1} and 3300 cm^{-1} contains a superimposition of three different scattering modes: G' at 2685 cm^{-1}, D + D' combination at 2950 cm^{-1}, and the second-order of the D' peak at 3250 cm^{-1}. The G' peak is ascribable to a double resonance inter-valley scattering process involving two iTO phonons at the K point.[44]

The I_D/I_G ratio is usually calculated to evaluate the quality of the graphene-based material. The calculation was performed

for all the spectra after an appropriate subtraction of the photoluminescence background (where present). The ratio for the pristine GO (curve 1) was 0.75 and increased slightly for the rGO (curve 2) to reach a value of 0.81. The non-desired increase of the ratio during the hydrothermal synthesis is due to the formation of a 3-dimensional interconnected network of rGO flakes while the starting material was quasi-single GO flakes. The obtained rGO contains defects due to hexagonal planes distortions.[45]

By introducing commercially available 2H-MoS_2 to produce the rGO-MoS_2-p, curve 3, the ratio increased to reach a value of 0.88 while the ratio for the *in-situ* production of rGO-MoS_2-co was 0.97. This significant increase suggests the creation of new defects in the in-plane sp^2 domains ascribable to a strong reciprocal interference between the two species, rGO and MoS_2.[13,18]

Figure 4.6 reports the fingerprint region for MoS_2 material. Indeed, characteristic peaks are typically found at 279 cm^{-1} ($E1_{1g}$), 336 cm^{-1} (LA), 377 cm^{-1} ($E1_{2g}$) and 404 cm^{-1} (A_{1g}). However, only characteristic peaks of the 2H-MoS_2 are observable for the rGO-MoS_2-p (curve 3) and the MoS_2-s (curve 5) sample.[33] The peak at 404 cm^{-1} is ascribed to the out-of-plane vibration of the S atoms lying in the opposite direction along the c-axis whereas the peak at 377 cm^{-1} is associated to the opposite vibration of the Mo atom versus two S atoms.[18] The rGo-MoS_2-co spectrum does not contain typical peaks assignable to MoS_2. This result is in contradiction with the EDX analysis reported previously. Then, it can be supposed that the dichalcogenides concentration is under the limit of detection of the apparatus used and/or the nanostructures are highly dispersed in the 3D-rGO matrix preventing their observations. At this point, it was not possible to identify the phase type (1T, 2H, or both) of the MoS_2 *in-situ* co-synthesized during the hydrothermal synthesis.

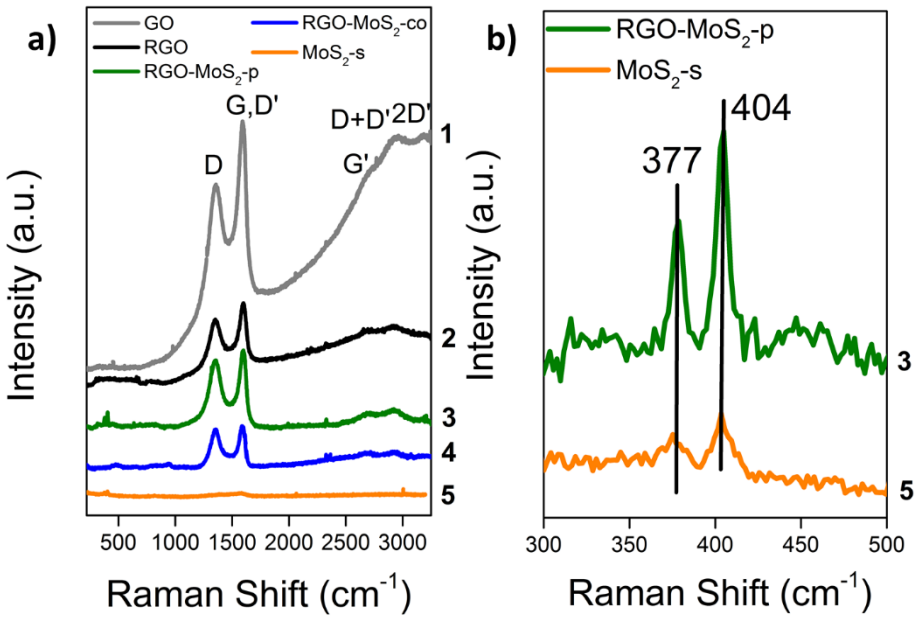

Figure 4. 6. Raman spectra collected at λ=514.5 nm excitation wavelength: curve 1 GO, curve 2 rGO, Curve 3 rGO-MoS_2-p curve 4 rGO-MoS_2-co, curve 5 MoS_2-s; (a) magnification of MoS_2 E12g and A1g mode peaks region in curve 3 and 5 (b).

Increasing the laser intensity, these peaks can nevertheless be produced and observed, as reported in Figure 4.7.a. In addition to a crystallisation of the MoS_2, the laser generates, in presence of air, a partial oxidation of the Mo-based material to form the molybdenum oxide.[21] The typical Raman peaks of MoO_2 are located at 663, 820, 993 cm^{-1} and can be observed for both MoO_2 and rGO-MoO_2 sample as reported in Figure 4.7.b.[25,46]

Regarding both MoS_2-s and rGO-MoS_2-co in Figure 4.7.a, weak E_{12g} and A_{1g} mode are observable. The relatively low intensity suggests that the nanostructures are defective and disordered. Moreover, the absence of E_{11g} and LA modes indicate the anchorage of the few-layer MoS_2 flakes onto the rGO 3D-structure.[18]

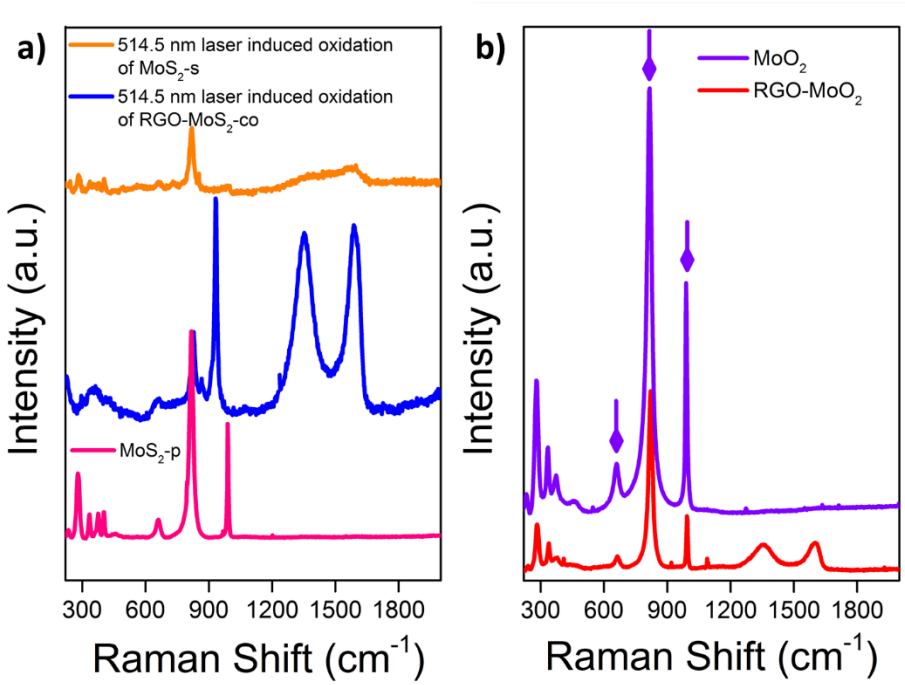

Figure 4. 7.Raman spectra collected at λ=514.5 nm excitation wavelength: comparison of rGO-MoS_2-co and MoS_2-s (with laser induced oxidation) with MoS_2-p (a) rGO-MoO_2 and MoO_2 (b).

4.3.2.2. XRD measurements

The Figure 4.8.a reports XRD spectra for the pristine GO, the rGO aerogel and the rGO-MoO_2 composite. The pristine GO displays a broad feature at 2θ ~26° ascribable to the (001) peak characteristic of GO. The diffraction spectrum of rGO displays two different bands at 2θ ~26° and 43° assignable to the (002) and (101) peaks, respectively.[16,47] The difference between the GO and the rGO spectra confirms that GO is properly reduced during the hydrothermal synthesis. For sake of comparison, the spectrum of the rGO-MoO_2 composite is reported. This spectrum shows the typical peaks of the monoclinic phase MoO_2 according to JCPDS card N° 32-0671.[25] A superimposition of the (111) peak characteristic of MoO_2 crystalline microstructures with a broad peak centred at 2θ ~26° confirms the formation of a graphene-molybdenum oxide composite.

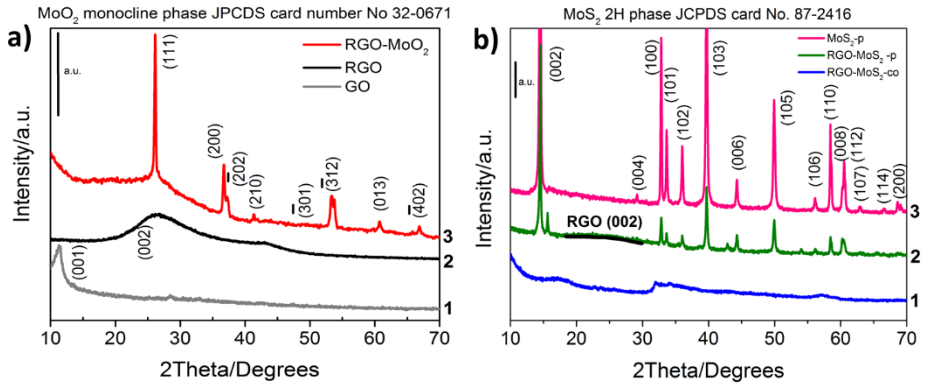

Figure 4. 8. XRD diffraction patterns of (a) pristine GO, rGO and rGO-MoO_2 and (b) MoS_2-p, rGO-MoS_2-p and rGO-MoS_2-co

Figure 4.8.b compares the diffraction pattern of the commercially available 2H-MoS_2, MoS_2-p, with the graphene-dichalcogenide composites: rGO-MoS_2-p and rGO-MoS_2-co. The spectrum of MoS_2-p confirms the 2H-phase of the MoS_2 according to JCPDS card N°87-2416 as it was expected. Interestingly, this crystallinity is maintained during the hydrothermal synthesis confirming the embedding of the dichalcogenides nanostructures in the 3D-rGO matrix. The spectrum for the *in-situ* synthesis of MoS_2 together with the reduction of GO shows a completely different pattern. Indeed, only 4 broadened peaks at 2θ = 14, 34, 40 and 58°corresponding to the (002), (100), (103) and (110) diffraction planes of MoS_2 2H phase, respectively. Moreover, the (002) feature of rGO is weak and broad, suggesting an inhibition of the long range ordered arrangement of rGO and MoS_2 layers, as already reported in literature.[16]

The spectrum of the annealed MoS_2-s is compared to the as-synthesized MoS_2-s in Figure 4.9.

The as-synthesized MoS_2 spectrum reveals a highly defective structure containing nano-sized domains along the basal planes as already observed previously.[48] Through the annealing process, a crystallization of the nanostructures take place and longer range ordered structure can be observed. Sharp and intense feature at 2θ ~ 14° and ~33° are ascribable to the (002) and (100) peaks of MoS_2 2H phase

(JCPDS card N°87-2416), respectively. Due to the presence of non-reduced oxygen functions, an oxidation occurred as side reaction. Indeed, characteristic features of MoO_2 monoclinic phase peaks, at $2\theta \sim 26°$ and ~37°, assignable to the (111) and (200) peaks, respectively in accordance with JCPDS card N°32-0671.

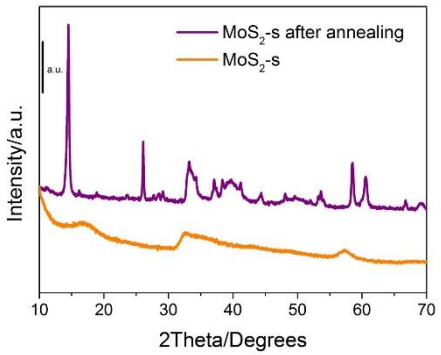

Figure 4. 9. XRD spectra for as-synthesized and annealed MoS_2-s sample.

4.3.2.3. XPS analysis

XPS measurements are particularly useful for studying the chemical composition of materials. Indeed, the sampling depth for this analysis is lower than 10 nm which allows to investigate the surface composition. It is particularly suitable for supercapacitor applications, where the performance is influenced by surface or near-surface phenomena. Figure 4.10.a plots the C1s region, studied at high resolution, for the pristine GO, the rGO, and the graphene-based composites. The reduction of GO during the hydrothermal synthesis can be undoubtedly confirmed by analysing the spectra of the pristine material and the rGO as-synthesized. Indeed, an almost complete disappearance of carbon-oxygen bonds is observed alongside with the apparition of the π-π* feature typical of few-layer graphite.[49] These phenomena can be observed for both rGO-MoO_2 and rGO-MoS_2-p samples. The HR spectrum for the *in-situ* co-synthesized rGO-MoS_2 is significantly different. Indeed, the

reduction of carbon-oxygen bonds is still present while the π-π* is not observed.

This feature is directly related to electronic band structure of the graphitic material, which is influenced by the arrangement of atoms in the basal plane and by the stacking order of layers. This band is characteristic of graphitic material because this electronic inter-band transition excited by the photo-emitted C1s core-electron,[50] corresponding to a higher binding energy (≈ 6.2 eV shift compared to the C-C component of the C1s region) due to a lower kinetic energy.

Two hypotheses might explain the absence of the π-π* feature in sample rGO-MoS_2-co. In accordance with the higher I_D/I_G ratio calculated from Raman analysis, a possible explanation could be the higher defectivity of the honeycomb lattice. The second hypothesis is related to a possible alteration of the stacking order as already reported in literature[51]. Indeed, the energy of the π → π* transition decreases according to the number of layers of graphene. As observed by FESEM analysis, rGO and MoS_2 species are undistinguishable and have a layered structure. It can be assumed that an alternation of these two components could provoke the stacking order in few-layer graphene, leading to 1-3 layers slices of perfectly ordered material. The value of the energy downshift of this typical feature is around 2eV, which leads to a π-π* feature in the C1s region shifted to ≈ 289 eV. Interestingly, the rGO-MoS_2-co sample has the higher contribution (in relative intensity) of the C=O feature. This change could be due to overlapping of this peak with a significant contribution of the downshifted π-π* feature due to perfect stacking of graphene layers confined to only 1-3 layers slices.

Mo3d/S2s and the S2p regions are the most promising for the MoX_2 phases identification. They are reported in Figure 4.10.b and Figure 4.11, respectively.

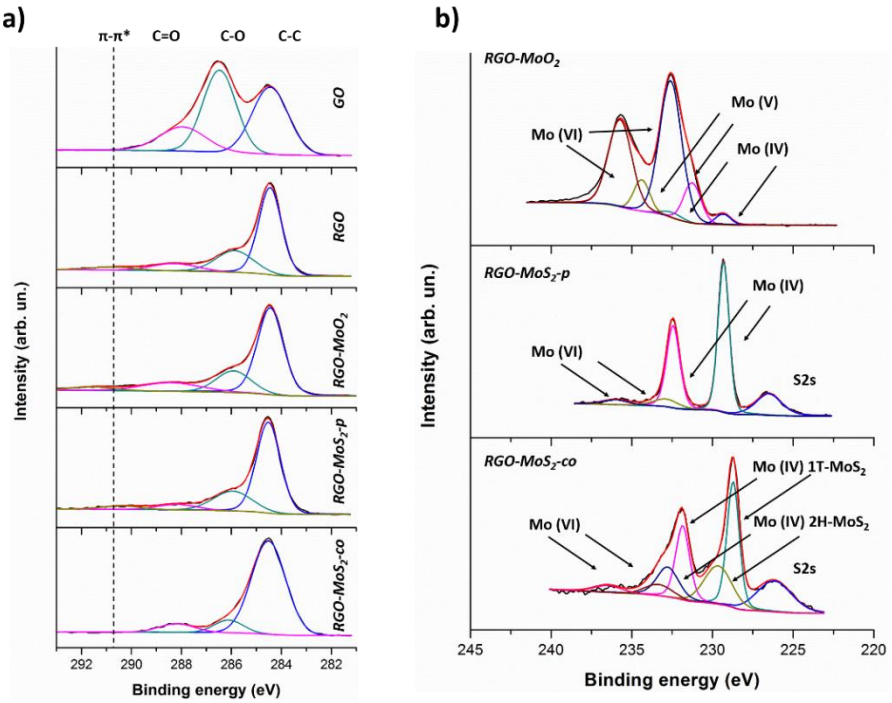

Figure 4. 10. HR XPS scans of the C1s region for each sample (a). Mo3d/S2s HR scans for sample rGO-MoO_2 rGO-MoS_2-p and rGO-MoS_2-co (b).

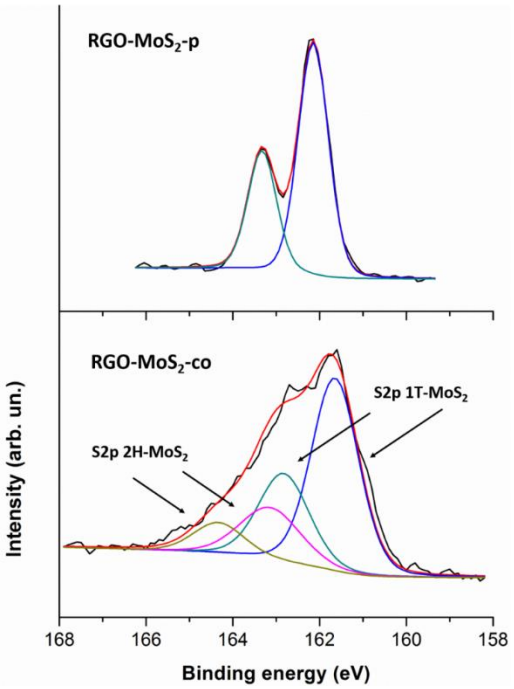

Figure 4. 11. XPS scans of the S2p regions for sample rGO-MoS_2-p and sample rGO-MoS_2-co.

Molybdenum has different oxidations number. The deconvolution of the Mo3d region, reported in Figure 4.10, for the rGO-MoO_2 sample displays three doublets. These features can be assigned to the three different molybdenum states. However, the XRD analysis displayed only monoclinic MoO_2, displaying an oxidation state of +4. We can nevertheless assume that a surface oxidation occurred on the top of sample producing an external layer of MoO_3 on the top of MoO_2 particles. The signal deconvolution gave then the three intermediate oxidation state phases, along a few nanometres scale, which is comparable to the inelastic mean free path of molybdenum oxide according to the literature.[52]

For the graphene-dichalcogenide composite, the Mo3d/S2s region contains relevant information due to the superimposition of the Mo3d region with the S2s core-level peak. For the sample containing the commercially available MoS_2, the peaks position for the Mo3d doublet (229.3 eV, 232.4 eV) and the S2s peak (226.5 eV) are compatible with the MoS_2 chemical structure.[53] The secondary Mo3d doublet is assignable to MoO_3 phase due to a surface oxidation of the sample, as described above. The absence of the secondary doublet in the S2p region excludes the presence of molybdenum oxysulfides.[54]

The spectrum deconvolution for the rGO-MoS_2-co is more complex. Indeed, the Mo3d region contains two doublets: the first at 228.7eV; 231.8eV, and the second at 229.6eV; 232.7eV. The separation is around 0.9eV and can be ascribable to the presence of both 1T and 2H MoS_2 polymorphs according to the literature.[33,55] The first doublet can be assigned to the 1T phase while the second is due to the 2H phase. The S2p region, Figure 4.11, contains also two doublets which is coherent with the Mo3d region. The third Mo3d doublet (233.3 eV, 236.5 eV) cannot be assigned to any of MoS_2 polymorphs. Moreover, the absence of its corresponding doublet in the S2p region indicates a chemical specie assignable to molybdenum oxide (VI).

The XRD spectrum of the rGO-MoS_2-co was not meaningful about the presence of a polymorph or both. The absence of signal indicates an absence of long-range organization. However, the presence of both polymorphs signals in the S2p region has revealed the co-existence of both 1T and 2H phases. Polymorphs are probably organized in a short-range ordering of atoms, giving either 1T or 2H configuration locally.

For sake of comparison, as-synthesized MoS_2 flakes without the rGO matrix spectra for the Mo3d/S2s and S2p regions are reported in Figure 4.12. Interestingly, similar deconvolutions are obtained indicating that the feature observed on the photoelectron spectrum is not influenced by the presence of GO flakes during the hydrothermal synthesis.

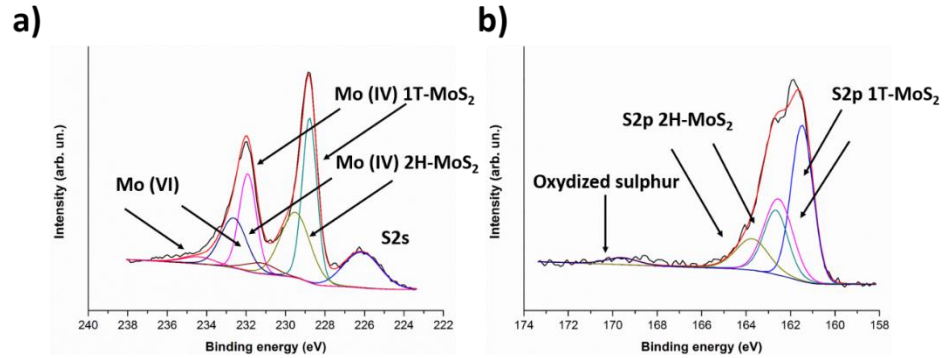

Figure 4. 12.HR spectra of the MoS_2-s sample in (a) Mo3d/S2s and (b) S2p regions

4.3.2.4. TEM analysis

Results obtained by XPS analysis indicate an interesting nanostructure containing both 1T and 2H-MoS_2 polymorphs. However, the structure analysis by FESEM analysis was not able to give information about it. To overcome this issue, TEM was used with the objective to understand the nanoscale structure of the rGo-MoS_2-co composite. A low-magnification image and its corresponding selected area diffraction (SAED) pattern are reported in Figure 4.13.a and 4.13.b, respectively. As already reported above for FESEM analysis, rGO and MoS_2 flakes are undistinguishable. The same observation can be made for the TEM analysis with low-

magnification. Then, the SAED pattern displays diffused diffraction rings. They cannot be assigned to well-defined crystalline structure (few-layer graphene or 1T/2H-MoS_2). Regarding the rGO flakes, the in-plane structure is expected to be defective.[56] Moreover, the flakes have a surface wrinkled at the nanoscale. Then, SAED pattern is expected to show diffused rings instead of the hexagonal symmetry typical of graphene material.

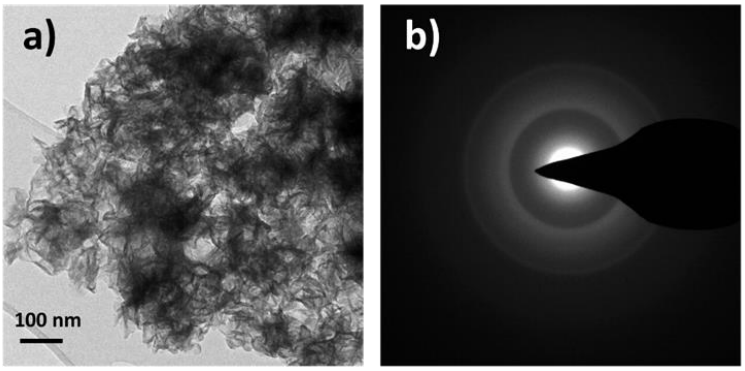

Figure 4. 13. Low magnification TEM image (a) of rGO-MoS_2-co sample and SAED pattern (b) of the same region.

For sake of deeper investigation, TEM images at different magnification and SAED patterns obtained for pure rGO and MoS_2-s (without rGO) are shown in Figure 4.14.a and 4.14.b, respectively.

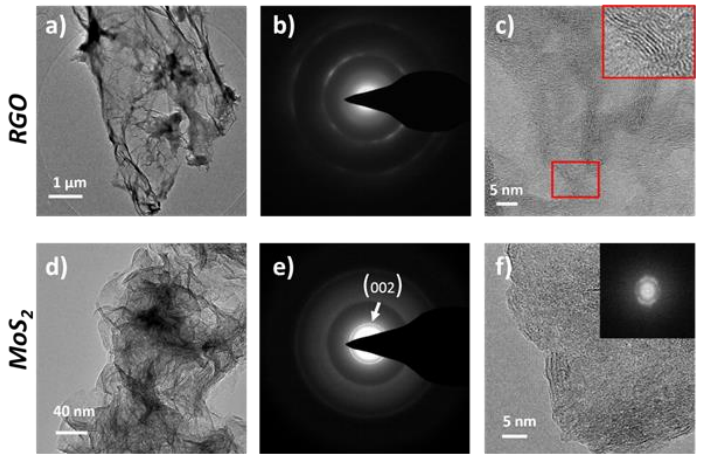

Figure 4. 14. Low-magnification (a), SAED pattern (b) and high magnification TEM images of rGO flake. Low-magnification (a), SAED pattern (b) and high magnification TEM images of MoS_2 flakes.

A single layer of rGO was characterized by TEM. The SAED pattern (b) displays a symmetry which lies with the hexagonal symmetry of the graphene. However, the rGO flake is defective as it can be seen from the low-magnification image (a). Therefore, the symmetry is not perfect. Indeed, arcs are observed instead of spots. Results obtained are in accordance with the model built for reduced Graphene Oxide flakes.[56] The high-resolution image (c) clearly indicates a few layers structure of rGO, with a interplanar distance of 3.4 Å. Concerning the MoS_2-s, the characteristic (002) ring was clearly visible in the SAED pattern (e). Its presence confirms the regular stacking of the S-Mo-S layers in this direction. The measured interplanar distance is 0.62 nm corresponds to a typical layered MoS_2 according to the literature.[57] However, this ring was not detected for the composite. Then, the presence of rGO flakes should affect the regular stacking of the dichalcogenide layers. To evaluate this hypothesis, a high-resolution image, and its corresponding fast Fourier transform (FFT) were investigated and are shown in Figure 4.15. The FFT pattern does not show any sign of periodicity at a distance corresponding the expected interplanar [002]. The interplanar distance further confirms this result. Indeed, the direct measurement on the high-resolution images does not give the typical value of 0.62 nm through all the images as measured for the pure MoS_2. The lined profile is reported in Figure 4.15.

To resume the phase identification part, the rGO-MoS_2-co contains both 1T and 2H polymorphs. The simultaneous presence of the rGO flakes during the *in-situ* synthesis of MoS_2 affects the stacking. These results are likely beneficial for materials for supercapacitor applications, as it will be presented in the next part with the electrochemical characterization.

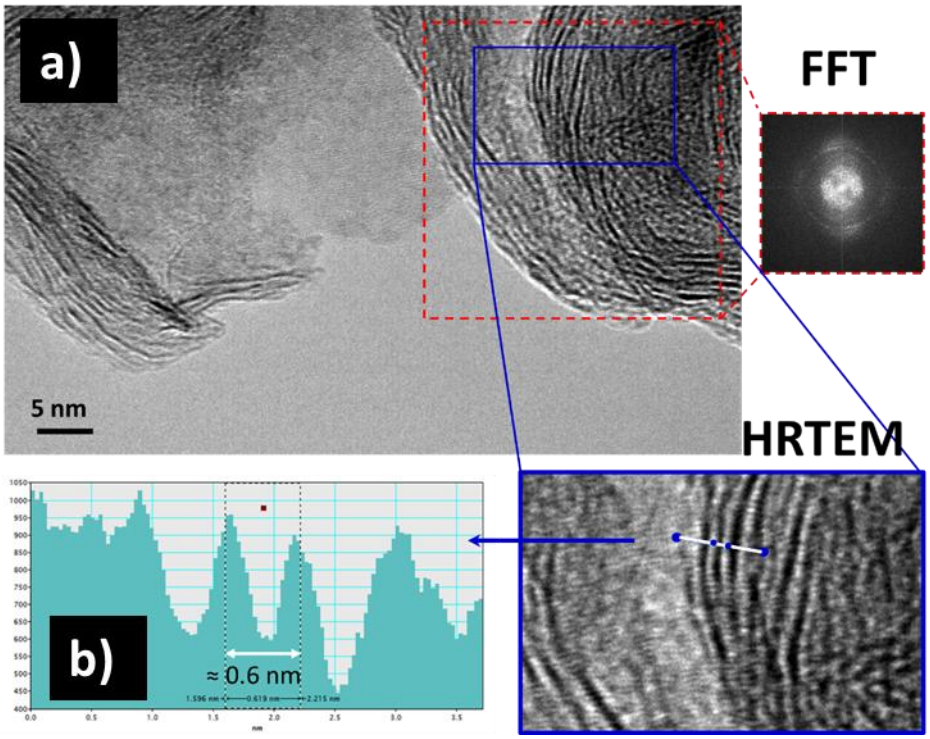

Figure 4. 15. (a) presents a high-magnification image of the hybrid alongside a fast Fourier transform of the region highlighted in red and a HRTEM view of the region highlighted in blue, allowing for a direct measurement of interplanar distance through (b) a line profile .

4.3.2.5. BET – Specific Surface Area Measurements

Specific surface area is a predominant factor for the materials performance in supercapacitor applications. N_2 adsorption/desorption isotherms at -196°C are used to measure the BET specific surface area and the cumulative pore volume of all as-synthesized samples. The obtained data are reported in Figure 4.16.a and 4.16.b, respectively.

Significant differences are observable between the samples. They can be divided in two categories according to the type of isotherms obtained. Indeed, rGO (curve 1) and rGO-MoS_2-p (curve 2) display an adsorption branch composed of Type I(b) at low relative pressure connected to a Type II at high relative pressure. Isotherms are associable to the filling of micropores in the first part connected to the filling of mesopores.[58] The hysteresis loops of both sample are characteristic of a H4 Type. The lower limit of the desorption

branch is located at a relative pressure value of 0.4 indicating the presence of mesopores accessible by the outer surface only through narrower neck. Regarding the pore size distribution, Figure 4.16.b shows that half of the total pore volume is devoted to micropores. This pore size is probably due to a partially random stacking of graphene sheets. The introduction of commercially available 2H-MoS_2 seems to not influence significantly the porous organization of the 3d-matrix since the curves of both rGO and rGO-MoS_2-p are close to each other. However, the specific surface area is significantly lower for the composite in comparison with the pure rGO (305 $m^2\ g^{-1}$ with respect to 460 $m^2\ g^{-1}$). The SSA difference is due to MoS_2, which has a high molar mass but a poor surface area.

Both rGO-MoS_2-co (curve 3) and rGO-MoO_2 (curve 4) display a different type of isotherm. Indeed, the Type II is typical of materials containing mesopores. Then, a significant decrease of BET specific surface area is observed with 80 and 50 m^2g^{-1} for rGO-MoS_2-co and rGO-MoO_2, respectively. The two samples differ from the two others by the presence of the phosphomolybdic acid in the reactor. Then, its presence probably interferes with the self-assembling of the rGO structure restricting the final microporosity of both composites.

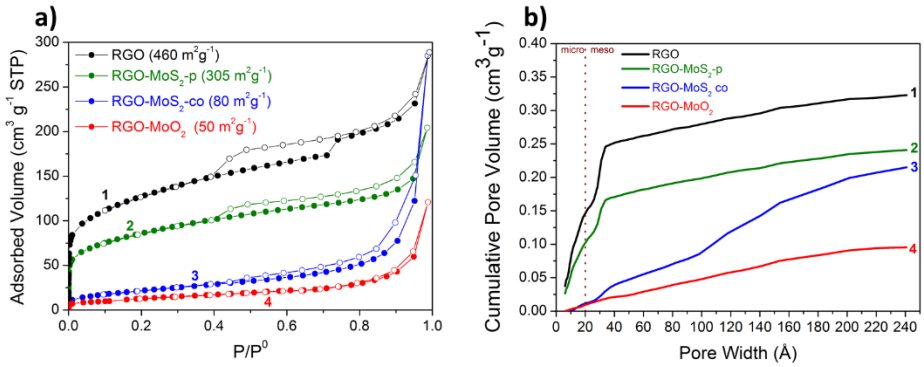

Figure 4. 16. BET SSA of rGO, rGO-MoS_2-p, rGO-MoS_2-co and rGO-MoO_2 (a) cumulative pore volume of rGO, rGO-MoS_2-p, rGO-MoS_2-co and rGO-MoO_2 (b)

Notwithstanding the lower specific surface area caused by the absence of micropores, the electrochemical performance of rGO-MoS_2-co are significantly higher than the other samples as discussed in the electrochemical characterization part.

4.4. Electrochemical Evaluation

4.4.1. Three- and two- electrode analytical cell configuration

Cyclic voltammograms (CV) for all the synthesized materials are reported in Figure 4.17.a. All the materials display characteristic cyclic voltammogram of supercapacitors. In particular, the rGO-MoS_2-co has a box-like CV typical of ideal capacitive materials. The maximum charge stored for this material was evaluated at 34 mC. The evolution of the specific capacitance with the scan rate is reported in Figure 4.17.b. The rGO-MoS_2-co sample has significantly better performance in comparison with the other materials analysed. The storage ability was particularly good that the measurements above 400 mV s^{-1} were not possible due to a current limitation of the instrument used.

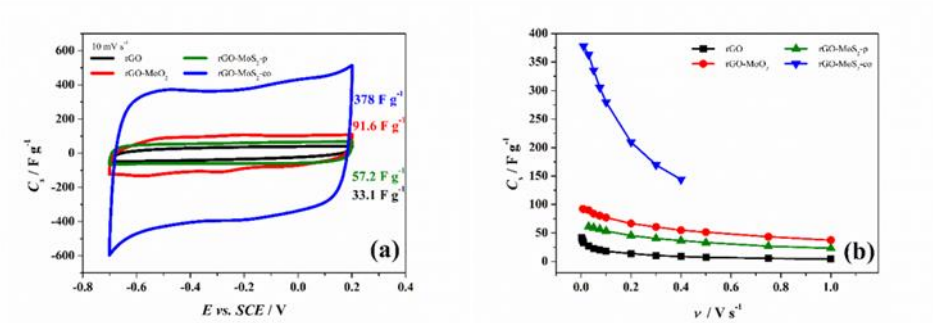

Figure 4. 17. Electrochemical behaviour of the four electrodes rGO (black), rGO-MoO_2 (red), rGO-MoS_2-p (green) and rGO-MoS_2-co (blue) in 1 M NaCl: (a) CV at 10 mV s^{-1}, (b) specific capacitance vs. scan rate

Galvanostatic charge/discharge measurements are shown in Figure 4.18.a. The chronopotentiograms are linear meaning the good capacitive behaviour of the investigated samples. Moreover, the time for the charge and the discharge are almost equal, implying the symmetric behaviour in the used

potential window. The rGO-MoS_2-co sample displays a specific capacitance up to 416 F g^{-1} during the discharge at a current density of 1 A g^{-1}.

Electrochemical Impedance Spectroscopy (EIS) is a useful technique for the characterisation of electrochemical devices. Measurements performed at open circuit potential (OCP). The equivalent circuit was defined for all the investigated materials for both three and two electrodes analytical cell configuration. The equivalent circuit was R(RQ)Q. The Nyquist plot obtained from EIS is reported in Figure 4.18.b1. The *in-situ* graphene-dichalcogenide composite, rGO-MoS_2-co, displays significant better performance in comparison with the other samples. Indeed, the deviation from the imaginary axis (Z") are more important for the other samples. The rGO-MoS_2-co, on the contrary, displays a slope nearly 90°, which is typical of an ideal polarizable electrode. Using the low-frequency data, the maximum specific capacitance can be determined using the following equation (4.1):

$$Z'' = (2\pi\omega C)^{-1} \quad (4.1)$$

where ω is the frequency, and C is the capacitance. Figure 4.18.b2 reports the specific capacitance in function of the frequency for all the samples. Results are in perfect accord with the others previously presented. Indeed, the rGO-MoS_2-co sample owns exceptional performance. Moreover, the capacitance calculated from CV and alternated current (AC) impedance are robust with 348 F g^{-1} at 5 mV s^{-1} and 325 F g^{-1} at 5 mHz, respectively.

Using the equations (4.2-4.5), real, imaginary, and total capacitance. These information are essential to design materials for supercapacitor applications in accordance with the complex capacitance model of impedance with respect to frequency.[59–61]

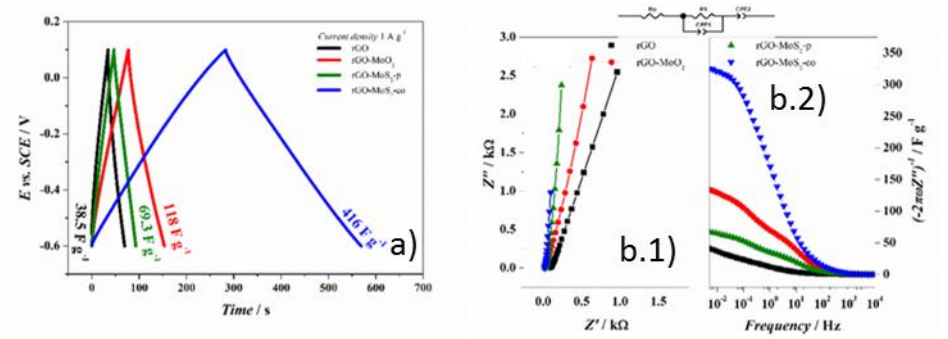

Figure 4. 18. (a) charge-discharge cycles at 1 A g^{-1} and (b.1) Nyquist plot and (b.2) capacitance vs. frequency plot

$$Z(\omega) = \frac{1}{j\omega C(\omega)} \quad (4.2)$$

$$C(\omega) = C'(\omega) - jC''(\omega) \quad (4.3)$$

$$C'(\omega) = \frac{-Z''(\omega)}{\omega|Z(\omega)|^2} \quad (4.4)$$

$$C''(\omega) = \frac{Z'(\omega)}{\omega|Z(\omega)|^2} \quad (4.5)$$

C', real part of the complex capacitance, determines the stored energy in the materials. C", imaginary part, quantifies the energy lost by dissipation. Both C' and C" are plotted in function of frequency in Figure 4.19.a and 4.19.b, respectively. For sake of comparison, C' and C" are normalized with, C_0, the proper highest capacitance of the sample. In this way, results are presented avoiding the effect of non-neglectable specific capacitance difference. Samples display a purely resistor behaviour but a different frequency, Figure 4.19.a. Indeed, for rGO and rGO-MoS_2-co, at frequencies higher than 1 Hz and, for rGO-MoS_2-p and rGO-MoO_2, at frequencies higher than 10 Hz. A formation of a small plateau is observable only for the *in-situ* co-synthesized graphene-dichalcogenide composite, rGO-MoS_2-co. This plateau, reached up to 62.5 s, describes a purely capacitor behaviour of the material. The relaxation time constant (τ_0) can be determined from the C" vs frequency plot in Figure 4.19.b. This time describes how fast the

electrode can be discharged, which is a key characteristic of supercapacitor. The frequency domains can be divided in two parts according to τ_0: resistive (when times is shorter than τ_0) and capacitive (when times is longer than τ_0). The relaxation time constant was measured to be 4.3 s for rGO-MoS_2-p and rGO-MoO_2. As-synthesized rGO and rGO-MoS_2-co displayed a slightly longer τ_0.

Bode plots are reported in Figure 4.19.c and 4.19.d. The rGO-MoS_2-co demonstrates outstanding supercapacitive performances in comparison with the other synthesized samples. Indeed, this sample displays the lowest impedance module and the maximum phase at low frequencies (84.2°). Finally, the uncompensated resistance at the working electrode was evaluated. Both i-interruption and AC impedance were carried on the rGO-MoS_2-co sample. Obtained results are consistent with 14.4 and 17.3 Ω, respectively.

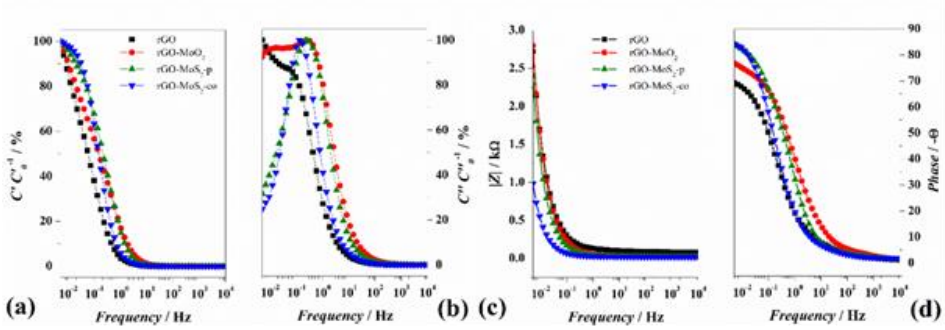

Figure 4. 19. Complex capacitance (a) real part, (b) imaginary part, Bode plots of (c) module and (d) phase as a function of frequency for the four different materials. Acquired at OCP in 1 M NaCl.

The Ragone plot, presenting the specific power in function of the specific energy, for the four materials is shown in Figure 4.20. Results used to build the Ragone plot were calculated from CV curves, at different scan rates, in the two-electrodes analytical cell. Finally, Table 4.2 contains all the capacitance values for the four materials calculated from CV, charge-discharge, together with the electrochemical performances evaluated by AC impedance. In addition, specific energy (W

h kg^{-1}) and power (W kg^{-1}), determined from the discharge cycle at 10 mV s^{-1}, are also presented.

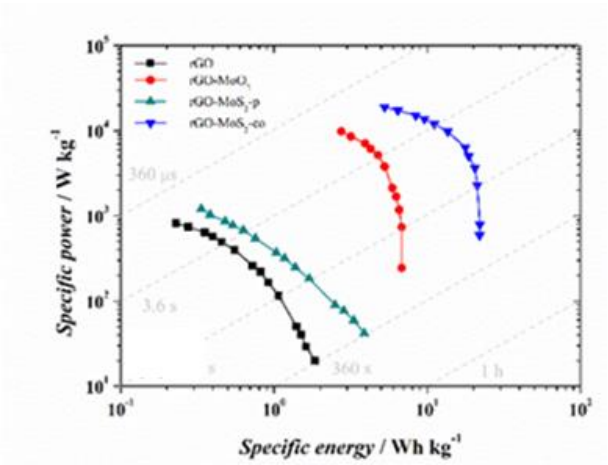

Figure 4. 20. Ragone plot of rGO (black), rGO-MoO_2 (red), rGO-MoS_2-p (green) and rGO-MoS_2-co (blue) in two electrodes cell.

4.4.2. Planar symmetric configuration

Materials were tested in device-like configuration to evaluate their stability. Measurements were carried on in a symmetric device. Three materials were tested: pure rGO, MoS_2-s, and the rGO-MoS_2-co composite. Cycling stability measurements performed over 50.000 cycles at 2 V s^{-1} are reported in Figure 4.21. Cyclic voltammograms were recorded at a scan rate of 5 mV s^{-1} every 1.000 cycles to investigate the aging effect on the devices performance. The performance of the rGO-MoS_2-co increased slightly during the first 6.000 cycles. After reached this maximum, an almost perfect stabilization is observable for the composite. This behaviour is comparable of pure rGO aerogel. For sake of comparison, pure MoS_2-s sample was investigated. This sample displays a significant decrease after 13.000 cycles. Nevertheless, the capacitance is stable over the 50.000 cycles.

Electrodes	Method	Parameter	Unit of measure	rGO-MoS_2-co	rGO-MoS_2-p	rGO-MoO_2	rGO
Three	i-Interrupt	average R_u	Ω	14.4	26.0	21.6	77.1
	Cyclic Voltammetry	C_s @ 10 mV s^{-1}	F g^{-1}	378	57.2	91.6	33.0
	Charge-Discharge	C_s @1 A g^{-1}	F g^{-1}	416	69.3	118	38.5
	AC impedance	C_s @ 9 mHz	F g^{-1}	321	65.0	130	37.3
		R_u	Ω	17.3	23.7	24.5	77.0
		τ_0	S	7.7	4.3	4.3	13.9
		-Phase	°	84.2	84.2	76.9	69.3
Two	Cyclic Voltammetry	E @ 10 mV s^{-1}	mW h kg^{-1}	22	2.5	6.8	1.4
		P @10 mV s^{-1}	mW kg^{-1}	791.9	89.93	245.3	50.39

Table 4. 2. Key metrics evaluated for each material tested in three- and two-electrode configuration.

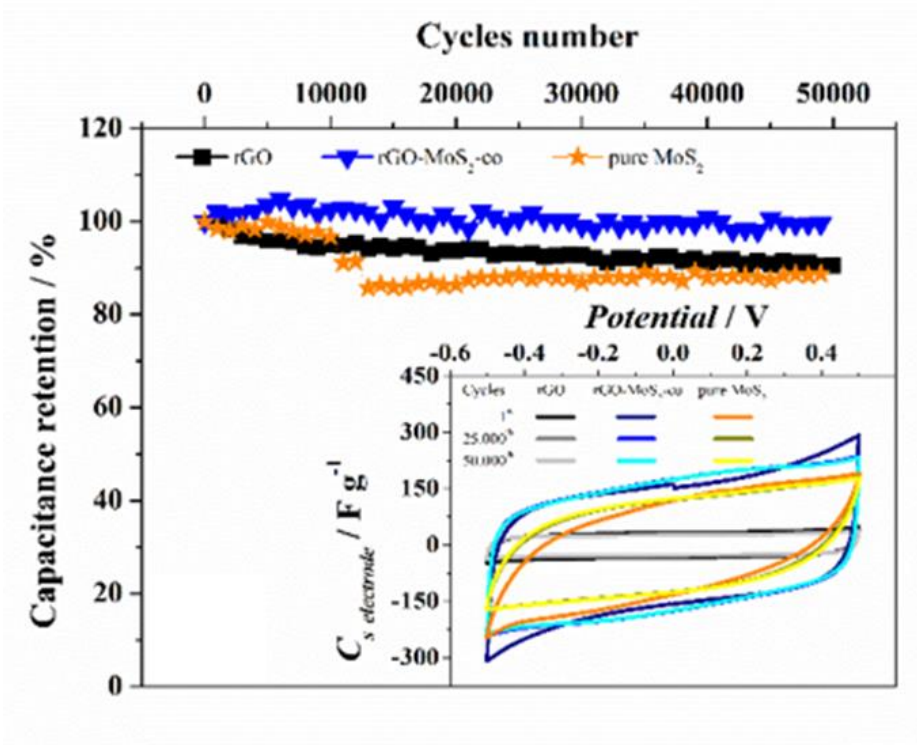

Figure 4. 21. Electrochemical stability of rGO (black) and rGO-MoS_2-co (blue) and pure MoS_2 (orange) over 50.000 cycles in symmetrical device configuration, (inset) cyclic voltammetry at 5 mV s^{-1} at cycle number 1, 25000 and 50000 for the three devices.

4.4.3. Effect of mass loading on performance

The mass loading influences significantly the capacitive performance of the material as shown in Figure 4.22.a and 4.22.b, respectively. Indeed, a box-like shape for the heavier sample, black curve, is observable while for the blue curve, corresponding to the lighter sample, shows important deviation of the ideal shape. The deviation can be ascribable to protons adsorption (from H_2SO_4) on the dichalcogenide surface, as already reported in the literature.[61] The proton diffusivity within the dichalcogenide induces a larger capacitance at slow scan rates due to the larger polarizability framework of S_2 as compared to O_2.[62] This anionic framework allows an easier migration of mobile cations, implying faster and larger capacitance than in neutral electrolytes.

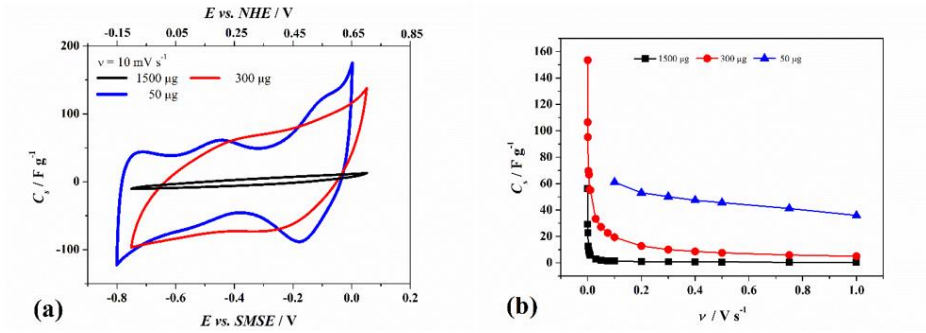

Figure 4. 22. (a) Cyclic voltammetry recorded at 10 mV s^{-1} and (b) estimated capacitance at multiple scan rates for three different masses of pure MoS_2.

The pseudo-capacitance behaviour was investigated for a potential window between at -0.1 and +0.05 V vs. normalized hydrogen electrode(NHE). The current is plotted in function of the square root of the scan rates and shown in Figure 4.23. Measured currents are linearly dependent of the $v^{1/2}$ confirming the pseudo-capacitance of the material. Results are consistent with the one recorded by Acerce *et al.* for 1T-MoS_2 phase.[33]

To resume the electrochemical characterization part, rGO-MoS_2-co displays the better performance for supercapacitor applications despite a BET specific surface area one order of magnitude lower than the other samples. Good capacitive properties reside in the win-win interaction between the 3D-rGO matrix and the pseudo-capacitive material *in-situ* synthesized. The optimum interaction between rGO and MoS_2 flakes allows a larger contact between the electrolyte available and the redox sites, which overcome the decrease of the EDL active surface resulting in an outstanding supercapacitive material.

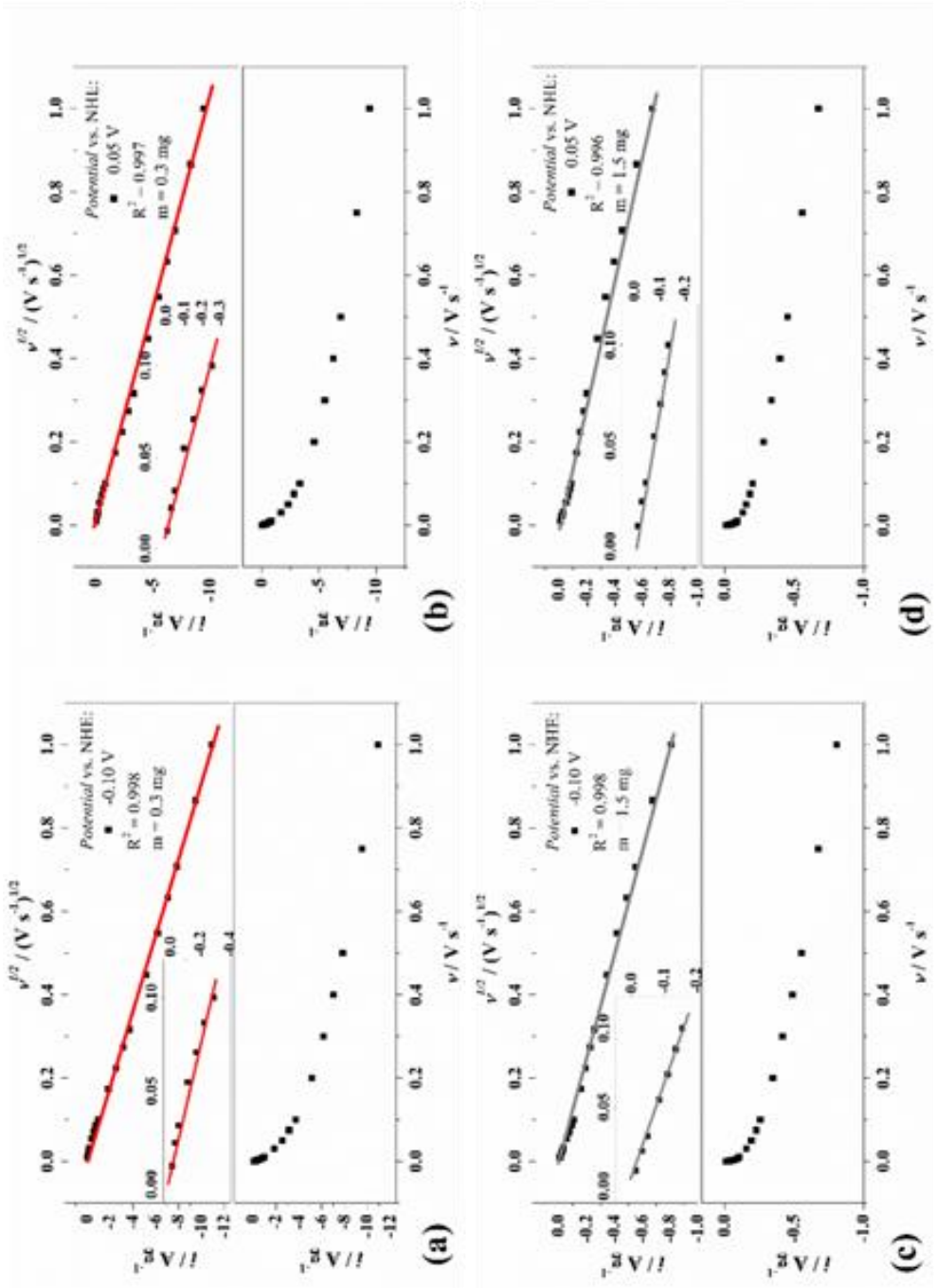

Figure 4. 23. Plots of current vs. scan rate and vs. square root of the scan rate at -0.1 V vs. NHE for samples of 0.3 mg (a) and 1.5 mg (c) and at +0.05 V vs. NHE for samples of 0.3 mg (b) and 1.5 mg (d).

4.5. Conclusions

This chapter was focused on the comparison of graphene-based aerogels for supercapacitors applications. The hydrothermal synthesis uses phosphomolybdic acid and L-cysteine as Mo and S precursors, respectively. The *in-situ* co-synthesized rGO-MoS_2-co displays an interesting morphology with rGO and MoS_2 flakes intimately mixed forming a 3D porous framework. The XPS characterization demonstrates the simultaneous presence of both 1T and 2H polymorphs, which induces higher electrochemical performance. The measured specific capacitance was up to 416 F g^{-1} was significantly higher than composite prepared with commercially available 2H-MoS_2 powder, rGO-MoS_2-p, or with the corresponding metal oxide, rGO-MoO_2. The graphene-dichalcogenide composite *in-situ* synthesized is interesting due to its hybrid behaviour with EDL charge storage mechanism assured by the large specific surface area and the Faradaic active sites of the pseudo-capacitive material provided by MoS_2. A synergetic effect occurred in the composite inducing cycling stability up to 50.000 cycles while the as-synthesized pure MoS_2 showed failure after 13.000 cycles.

To summarize, a simple one-pot green hydrothermal synthesis allows to produce graphene-dichalcogenide composite, rGO-MoS_2-co, with both 1T and 2H polymorphs organized in short-range crystalline domains. The finely mixed rGO and dichalcogenide flakes permit high exposed interface between electrolyte and active materials allowing the near surface redox reactions, resulting in the enhancement of the supercapacitive performance of the material.

REFERENCES

(1) Haering, R. R.; Stiles, J. A. R.; Brandt, K. Lithium Molybdenum Disulphide Battery Cathode. US4224390 A, 1980.

(2) Giardi, R.; Porro, S.; Topuria, T.; Thompson, L.; Pirri, C. F.; Kim, H. C. One-Pot Synthesis of Graphene-Molybdenum Oxide Hybrids and Their Application to Supercapacitor Electrodes. *Appl. Mater. Today* **2015**, *1* (1), 27–32.

(3) Ji, H.; Liu, X.; Liu, Z.; Yan, B.; Chen, L.; Xie, Y.; Liu, C.; Hou, W.; Yang, G. In Situ Preparation of Sandwich MoO_3/C Hybrid Nanostructures for High-Rate and Ultralong-Life Supercapacitors. *Adv. Funct. Mater.* **2015**, *25* (12), 1886–1894.

(4) Hu, X.; Zhang, W.; Liu, X.; Mei, Y.; Huang, Y. Nanostructured Mo-Based Electrode Materials for Electrochemical Energy Storage. *Chem. Soc. Rev.* **2015**, *44* (8), 2376–2404.

(5) Rao, C. N. R.; Maitra, U.; Waghmare, U. V. Extraordinary Attributes of 2-Dimensional MoS_2 Nanosheets. *Chem. Phys. Lett.* **2014**, *609*, 172–183.

(6) Novoselov, K. S.; Geim, A. K.; Morozov, S. V.; Jiang, D.; Zhang, Y.; Dubonos, S. V.; Grigorieva, I. V.; Firsov, A. A. Electric Field Effect in Atomically Thin Carbon Films. *Science.* **2004**, *306*, 666–669.

(7) Coleman, J. N.; Lotya, M.; O'Neill, A.; Bergin, S. D.; King, P. J.; Khan, U.; Young, K.; Gaucher, A.; De, S.; Smith, R. J.; Shvets, I. V.; Arora, S. K.; Stanton, G.; Kim, H.-Y.; Lee, K.; Kim, G. T.; Duesberg, G. S.; Hallam, T.; Boland, J. J.; Wang, J. J.; Donegan, J. F.; Grunlan, J. C.; Moriarty, G.; Shmeliov, A.; Nicholls, R. J.; Perkins, J. M.; Grieveson, E. M.; Theuwissen, K.; McComb, D. W.; Nellist, P. D.; Nicolosi, V. Two-Dimensional Nanosheets Produced by Liquid Exfoliation of Layered Materials. *Science.* **2011**, *331* (6017), 568–571.

(8) Zhang, G.; Liu, H.; Qu, J.; Li, J. Two-Dimensional Layered MoS_2: Rational Design, Properties and Electrochemical Applications. *Energy Environ. Sci.* **2016**, *9*, 1190–1209.

(9) Jaramillo, T. F.; Jorgensen, K. P.; Bonde, J.; Nielsen, J. H.; Horch, S.; Chorkendorff, I. Identification of Active Edge Sites for Electrochemical H_2 Evolution from MoS2 Nanocatalysts. *Science.* **2007**, *317* (5834), 100–102.

(10) Muratore, C.; Hu, J. J.; Wang, B.; Haque, M. A.; Bultman, J. E.; Jespersen, M. L.; Shamberger, P. J.; Mcconney, M. E.; Naguy, R. D.; Voevodin, A. A. Continuous Ultra-Thin MoS_2 Films Grown by Low-Temperature Physical Vapor Deposition. *Appl. Phys. Lett.* **2014**, *104*, 261604.

(11) Feng, C. Q.; Ma, J.; Li, H.; Zeng, R.; Guo, Z. P.; Liu, H. K. Synthesis of Molybdenum Disulfide (MoS_2) for Lithium Ion Battery Applications. *Mater. Res. Bull.* **2009**, *44*, 1811–1815.

(12) Singh, E.; Kim, K. S.; Yeom, G. Y.; Nalwa, H. S. Two-Dimensional Transition Metal Dichalcogenide-Based Counter Electrodes for Dye-Sensitized Solar Cells. *RSC Adv.* **2017**, *7* (45), 28234–28290.

(13) Chang, K.; Chen, W. L-Cysteine-Assisted Synthesis of Layered MoS_2/Graphene Composites with Excellent Electrochemical Performances for Lithium Ion Batteries. *ACS Nano* **2011**, *5* (6), 4720–4728.

(14) Huang, K. J.; Wang, L.; Liu, Y. J.; Liu, Y. M.; Wang, H. B.; Gan, T.; Wang, L. L. Layered MoS_2-Graphene Composites for Supercapacitor Applications with Enhanced Capacitive Performance. *Int. J. Hydrogen Energy* **2013**, *38* (32), 14027–14034.

(15) Huang, K. J.; Wang, L.; Li, J.; Liu, Y. M. Electrochemical Sensing Based on Layered MoS_2-Graphene Composites. *Sensors Actuators, B Chem.* **2013**, *178*, 671–677.

(16) Huang, K.-J.; Wang, L.; Zhang, J.-Z.; Xing, K. Synthesis of Molybdenum Disulfide/carbon Aerogel Composites for Supercapacitors Electrode Material Application. *J. Electroanal. Chem.* **2015**, *752*, 33–40.

(17) Murugan, M.; Kumar, M. R.; Alsalme, A.; Alghamdi, A.; Jayavel, R. Synthesis and Property Studies of Molybdenum Disulfide Modified Reduced Graphene Oxide (MoS_2-rGO) Nanocomposites for Supercapacitor Applications. *J. Nanosci. Nanotechnol.* **2017**, *17* (8), 5469–5474.

(18) Ye, J.; Ma, L.; Chen, W.; Ma, Y.; Huang, F.; Gao, C.; Lee, J. Y. Supramolecule-Mediated Synthesis of MoS_2/reduced Graphene Oxide Composites with Enhanced Electrochemical Performance for Reversible Lithium Storage. *J. Mater. Chem. A* **2015**, *3*, 6884–6893.

(19) Wang, D.; Zhou, K.; Yang, W.; Xing, W.; Hu, Y.; Gong, X. Surface Modification of Graphene with Layered Molybdenum Disulfide and Their Synergistic Reinforcement on Reducing Fire Hazards of Epoxy Resins. *Ind. Eng. Chem. Res.* **2013**, *52* (50), 17882–17890.

(20) Ma, G.; Peng, H.; Mu, J.; Huang, H.; Zhou, X.; Lei, Z. In Situ Intercalative Polymerization of Pyrrole in Graphene Analogue of MoS_2 as Advanced Electrode Material in Supercapacitor. *J. Power Sources* **2013**, *229*, 72–78.

(21) Fan, L. Q.; Liu, G. J.; Zhang, C. Y.; Wu, J. H.; Wei, Y. L. Facile One-Step Hydrothermal Preparation of Molybdenum Disulfide/carbon Composite for Use in Supercapacitor. *Int. J. Hydrogen Energy* **2015**, *40* (32), 10150–10157.

(22) Zhou, X.; Xu, B.; Lin, Z.; Shu, D.; Ma, L. Hydrothermal Synthesis of Flower-like MoS_2 Nanospheres for Electrochemical Supercapacitors. *J. Nanosci. Nanotechnol.* **2014**, *14* (9), 7250–7254.

(23) Li, Y.; Wang, H.; Xie, L.; Liang, Y.; Hong, G.; Dai, H. MoS_2 Nanoparticles Grown on Graphene: An Advanced Catalyst for the Hydrogen Evolution Reaction. *J. Am. Chem. Soc* **2011**, *133*, 7296–7299.

(24) Gigot, A.; Fontana, M.; Serrapede, M.; Castellino, M.; Bianco, S.; Armandi, M.; Bonelli, B.; Pirri, C. F.; Tresso, E.; Rivolo, P. Mixed 1T-2H Phase MoS_2/reduced Graphene Oxide as Active Electrode for Enhanced Supercapacitive Performance. *ACS Appl. Mater. Interfaces* **2016**, *8*, 32842–32852.

(25) Marasso, S. L.; Rivolo, P.; Giardi, R.; Mombello, D.; Gigot, A.; Serrapede, M.; Benetto, S.; Enrico, A.; Cocuzza, M.; Tresso, E.; Pirri, C. F. A Novel Graphene Based Nanocomposite for Application in 3D Flexible Micro-Supercapacitors. *Mater. Res. Express* **2016**, *3* (6), 65001.

(26) Firmiano, E. G. S.; Cordeiro, M. A. L.; Rabelo, A. C.; Dalmaschio, C. J.; Pinheiro, A. N.; Pereira, E. C.; Leite, E. R. Graphene Oxide as a Highly Selective Substrate to Synthesize a Layered MoS_2 Hybrid Electrocatalyst. *Chem. Commun.* **2012**, *48* (62), 7687–7689.

(27) Sun, W.; Li, P.; Liu, X.; Shi, J.; Sun, H.; Tao, Z.; Li, F.; Chen, J. Size-Controlled MoS2 Nanodots Supported on Reduced Graphene Oxide for Hydrogen Evolution Reaction and Sodium-Ion Batteries. *Nano Res.* **2017**, *10* (7), 2210–2222.

(28) Hwang, H.; Kim, H.; Cho, J. MoS_2 Nanoplates Consisting of Disordered Graphene-like Layers for High Rate Lithium Battery Anode Materials. *Nano Lett.* **2011**, *11*, 4826–4830.

(29) Chhowalla, M.; Shin, H. S.; Eda, G.; Li, L.-J.; Loh, K. P.; Zhang, H. The Chemistry of Two-Dimensional Layered Transition Metal Dichalcogenide Nanosheets. *Nat. Chem.* **2013**, *5* (4), 263–275.

(30) Ye, M.; Winslow, D.; Zhang, D.; Pandey, R.; Yap, Y. Recent Advancement on the Optical Properties of Two-Dimensional Molybdenum Disulfide (MoS_2) Thin Films. *Photonics* **2015**, *2* (1), 288–307.

(31) Splendiani, A.; Sun, L.; Zhang, Y.; Li, T.; Kim, J.; Chim, C. Y.; Galli, G.; Wang, F. Emerging Photoluminescence in Monolayer MoS_2. *Nano Lett.* **2010**, *10* (4), 1271–1275.

(32) Kan, M.; Wang, J. Y.; Li, X. W.; Zhang, S. H.; Li, Y. W.; Kawazoe, Y.; Sun, Q.; Jena, P. Structures and Phase Transition of a MoS_2 Monolayer. *J. Phys. Chem. C* **2014**, *118* (3), 1515–1522.

(33) Acerce, M.; Voiry, D.; Chhowalla, M. Metallic 1T Phase MoS_2 Nanosheets as Supercapacitor Electrode Materials. *Nat. Nanotechnol.* **2015**, *10* (4), 313–318.

(34) Wypych, F.; Sollmann, K.; Schöllhorn, R. Metastable Layered Chalcogenides 1T-MoS_2, 2M-WS_2 and 1T-$Mo_{1/2}W_{1/2}S_2$: Electrochemical Study on Their Intercalation Reactions. *Mater. Res. Bull.* **1992**, *27* (5), 545–553.

(35) Kim, S. K.; Song, W.; Ji, S.; Lim, Y. R.; Lee, Y. B.; Myung, S.; Lim, J.; An, K.-S.; Lee, S. S. Synergetic Effect at the Interfaces of Solution Processed MoS_2-WS_2 Composite for Hydrogen Evolution Reaction. *Appl. Surf. Sci.* **2017**, *425*, 241–245.

(36) Lee, J. E.; Jung, J.; Ko, T. Y.; Kim, S.; Kim, S.-I.; Nah, J.; Ryu, S.; Nam, K. T.; Lee, M. H. Catalytic Synergy Effect of MoS_2/reduced Graphene Oxide Hybrids for a Highly Efficient Hydrogen Evolution Reaction. *RSC Adv.* **2017**, *7* (9), 5480–5487.

(37) Yang, J.; Wang, K.; Zhu, J.; Zhang, C.; Liu, T. Self-Templated Growth of Vertically Aligned 2H-1T MoS_2 for Efficient Electrocatalytic Hydrogen Evolution. *ACS Appl. Mater. Interfaces* **2016**, *8* (46), 31702–31708.

(38) Wu, M.; Zhan, J.; Wu, K.; Li, Z.; Wang, L.; Geng, B.; Wang, L.; Pan, D. Metallic 1T MoS2 Nanosheet Arrays Vertically Grown on Activated Carbon Fiber Cloth for Enhanced Li-Ion Storage Performance. *J. Mater. Chem. A* **2017**, *5*, 14061–14069.

(39) Meng, N.; Cheng, J.; Zhou, Y.; Nie, W.; Chen, P. Green Synthesis of Layered 1T-MoS_2/reduced Graphene Oxide Nanocomposite with Excellent Catalytic Performances for 4-Nitrophenol Reduction. *Appl. Surf. Sci.* **2017**, *396*, 310–318.

(40) Wang, D.; Zhang, X.; Bao, S.; Zhang, Z.; Fei, H.; Wu, Z. Phase Engineering of a Multiphasic 1T/2H MoS_2 Catalyst for Highly Efficient Hydrogen Evolution. *J. Mater. Chem. A* **2017**, *5* (6), 2681–2688.

(41) Shirley, D. A. High-Resolution X-Ray Photoemission Spectrum of the Valence Bands of Gold. *Phys. Rev. B* **1972**, *5* (12), 4709–4714.

(42) Agrawal, R.; Chen, C.; Hao, Y.; Song, Y.; Wang, C. *Graphene for Supercapacitors*; A. Rashid bin Mohd Yusoff, Ed.; Wiley-VCH Verlag GmbH & Co. KGaA, 2015.

(43) Yuxi Xu, Kaixuan Sheng, C. L.; Shi, G. Self-Assembled Graphene Hydrogel. *ACS Nano* **2010**, *4* (7), 4324–4330.

(44) Roppolo, I.; Chiappone, A.; Bejtka, K.; Celasco, E.; Chiodoni, A.; Giorgis, F.; Sangermano, M.; Porro, S. A Powerful Tool for Graphene Functionalization: Benzophenone Mediated UV-Grafting. *Carbon N. Y.* **2014**, *77*, 226–235.

(45) Cançado, L. G.; Jorio, A.; Ferreira, E. H. M.; Stavale, F.; Achete, C. A.; Capaz, R. B.; Moutinho, M. V. O.; Lombardo, A.; Kulmala, T. S.; Ferrari, A. C. Quantifying Defects in Graphene via Raman Spectroscopy at Different Excitation Energies. *Nano Lett.* **2011**, *11* (8), 3190–3196.

(46) Bhaskar, A.; Deepa, M.; Rao, T. N.; Varadaraju, U. V. Enhanced Nanoscale Conduction Capability of a MoO_2/Graphene Composite for High Performance Anodes in Lithium Ion Batteries. *J. Power Sources* **2012**, *216*, 169–178.

(47) Fu, C.; Zhao, G.; Zhang, H.; Li, S. Evaluation and Characterization of Reduced Graphene Oxide Nanosheets as Anode Materials for Lithium-Ion Batteries. *Int. J. Electrochem. Sci* **2013**, *8*, 6269–6280.

(48) Wu, Z.; Li, B.; Xue, Y.; Li, J.; Zhang, Y.; Gao, F. Fabrication of Defect-Rich MoS_2 Ultrathin Nanosheets for Application in Lithium-Ion Batteries and Supercapacitors. *J. Mater. Chem. A* **2015**, 1–10.

(49) Briggs, D. *Surface Analysis by Auger and X-Ray Photoelectron Spectroscopy*; IM publications, 2003.

(50) McArthur, S. L. Thin Films of Vanadium Oxide Grown on Vanadium Metal. *Surf. Interface Anal.* **2006**, *38* (c), 1380–1385.

(51) Gass, M. H.; Bangert, U.; Bleloch, A. L.; Wang, P.; Nair, R. R.; Geim, a K. Free-Standing Graphene at Atomic Resolution. *Nat. Nanotechnol.* **2008**, *3* (11), 676–681.

(52) Baltrusaitis, J.; Mendoza-Sanchez, B.; Fernandez, V.; Veenstra, R.; Dukstiene, N.; Roberts, A.; Fairley, N. Generalized Molybdenum Oxide Surface Chemical State XPS Determination via Informed Amorphous Sample Model. *Appl. Surf. Sci.* **2015**, *326*, 151–161.

(53) Bissett, M. A.; Kinloch, I. A.; Dryfe, R. A. W. Characterization of MoS_2 –Graphene Composites for High-Performance Coin Cell Supercapacitors. *ACS Appl. Mater. Interfaces* **2015**, *7* (31), 17388–17398.

(54) Benoist, L.; Gonbeau, D.; Pfister-Guillouzo, G.; Schmidt, E.; Meunier, G.; Levasseur, a. X-Ray Photoelectron Spectroscopy Characterization of Amorphous Molybdenum Oxysulfide Thin Films. *Thin Solid Films* **1995**, *258* (1–2), 110–114.

(55) Cai, L.; He, J.; Liu, Q.; Yao, T.; Chen, L.; Yan, W.; Hu, F.; Jiang, Y.; Zhao, Y.; Hu, T.; Sun, Z.; Wei, S. Vacancy-Induced Ferromagnetism of MoS_2 Nanosheets. *J. Am. Chem. Soc.* **2015**, *137* (7), 2622–2627.

(56) Pei, S.; Cheng, H.-M. The Reduction of Graphene Oxide. *Carbon N. Y.* **2012**, *50* (9), 3210–3228.

(57) Liu, Y.; Jiao, L.; Wu, Q.; Zhao, Y.; Cao, K.; Liu, H.; Wang, Y.; Yuan, H. Synthesis of rGO-Supported Layered MoS_2 for High-Performance Rechargeable Mg Batteries. *Nanoscale* **2013**, *5* (20), 9562–9567.

(58) Thommes, M.; Kaneko, K.; Neimark, A. V.; Olivier, J. P.; Rodriguez-Reinoso, F.; Rouquerol, J.; Sing, K. S. W. Physisorption of Gases, with Special Reference to the Evaluation of Surface Area and Pore Size Distribution (IUPAC Technical Report). *Pure Appl. Chem.* **2015**, *87* (9–10), 1051–1069.

(59) Taberna, P. L.; Portet, C.; Simon, P. Electrode Surface Treatment and Electrochemical Impedance Spectroscopy Study on Carbon/carbon Supercapacitors. *Appl. Phys. A* **2006**, *82* (4), 639–646.

(60) Taberna, P. L.; Simon, P.; Fauvarque, J. F. Electrochemical Characteristics and Impedance Spectroscopy Studies of Carbon-Carbon Supercapacitors. *J. Electrochem. Soc.* **2003**, *150* (3), A292.

(61) Soon, J. M.; Loh, K. P. Electrochemical Double-Layer Capacitance of MoS2 Nanowall Films. *Electrochem. Solid-State Lett.* **2007**, *10* (11), A250.

(62) Zheng, N.; Bu, X.; Feng, P. Synthetic Design of Crystalline Inorganic Chalcogenides Exhibiting Fast-Ion Conductivity. *Nature* **2003**, *426*, 3–7.

Chapter 5

Effect of L-ascorbic acid on the hydrothermal synthesis of rGO and rGO-MoO_2 aerogels

L-ascorbic acid (Vitamin C) is attractive as green reducing agent to reduce GO to rGO. In this chapter, Vitamin C is used to hydrothermally synthesize reduced graphene oxide aerogel decorated with molybdenum oxide particles. The addition of this vitamin induces a better reduction of graphene oxide and a higher reproducibility of the desired chemical reduction yield. The presence of molybdenum oxide particles permits to increase the specific capacitance exploiting Faradaic processes.

5.1. Motivations

Graphene Oxide (GO), produced by the Hummers method[1] or similar method recently developed[2], has attracted attention. Indeed, it is relatively cheap, using graphite as starting material, and it is easily dispersible in water due to the presence of the carbon-oxygen moieties onto flakes surface.[3] However, these chemical functionalities should be restored to obtain properties close to the graphene. Several *modus operandi* were developed for the reduction of GO together with the limitation of defects/vacancies in the honeycomb lattice structure.

Some physical approaches were investigated such as thermal annealing[2], microwave[4], and photoreduction.[5] Hydrothermal reduction, using water both as solvent and reducing agent, has already shown promising results.[6,7] To further improve the reduction process, many chemicals were added such as

hydrazine (N_2H_4) [8–10] sodium bisulfite ($NaHSO_3$) [11], sodium borohydride ($NaBH_4$) [12], hydriodic acid (HI) [13], sodium iodide (NaI) [14], hypophosphorous acid (H_3PO_2) and iodine (I_2) [15], hydroquinone ($C_6H_6O_2$) [11,16], pyrogallol ($C_6H_6O_3$) and potassium hydroxide (KOH).[8]

The resulting hydrogel forming by self-assembly process during the reduction of graphene oxide can nevertheless be completely different. Indeed, hydrazine and sodium borohydride induce a strong bubbling during the reaction causing a broken hydrogel as described by Hu and co-workers.[17]

The aerogel produced by freezing of the as-synthesized hydrogel is generally characterized by the C/O ratio and its electrical conductivity to compare the reduction process efficiency. For example, HI displays better performance than $NaHSO_3$[11] in addition with interesting properties such as good flexibility and enhanced tensile strength.[18]

In the last decade, green chemistry has attracted much attention. In fact, sustainable developments are appealing in both ethic and economic points of view. Indeed, this approach permits to decrease significantly the costs of both production and disposal/recycling processes. Consequently, the use of aromatic compounds such as pyrogallol and hydroquinone are prohibited because these reactants are not environmental friendly. To overcome this issue, use of green reductant is envisaged[19,20] such as lignin reported by Ye and co-workers.[21]

Phenylalanine ($C_9H_{11}NO_2$), an amino acid, was also investigated as reducing agent to produce superhydrophobic rGO-based aerogels.[22] However, the water solubility of this compound is significantly lower than other green reactant such as ascorbic acid (AA), which stereoisomer *L* is the water-soluble Vitamin C. Moreover, the dehydroascorbic acid, which is the oxidized ascorbic acid formed during the hydrothermal synthesis, is also environmental friendly.[23]

This chemical compound has already demonstrated its suitability for reducing GO nanosheets at room temperature [23] or at higher temperature (80-100°C)[8,24]. In another investigations, Zhang[25] and Hu[17] used L-AA to reduce GO suspensions at a relatively low temperature (40°C) for 16 hours to obtain rGO-based hydrogel. This process needs nevertheless a washing step, before the freeze-drying necessary to obtain the rGO-based aerogel, to remove the excess of L-AA and the oxidized by-product. L-AA can also be used as reducing agent for the already self-assembled rGO-based hydrogel produced by hydrothermal synthesis as reported by Nguyen[26] and Zhou[27].

The hydrothermal synthesis ensures a suitable reduction of GO[28–30] but, by addition of L-AA, the reduction process is more efficient and more reproducible. In addition, the resulting rGO demonstrates better performance.[31–33]

L-ascorbic acid has already been investigated for the synthesis of materials with pseudocapacitive properties such as core-shell Cu@Cu_2O[34], MnC_2O_4[35], Pt[36], SnO_2[37], and Ag[38] nanoparticles.

Molybdenum Oxide is a pseudocapacitive material interesting for redox reactions because Mo has several oxidation number as reported previously.[39] Nevertheless, L-AA was investigated only one time as reducing agent for rGO-MoO_2 hybrid for energy storage. The microspheres were prepared at 200°C and 500 Torr in 30 minutes and post-treated by annealing at 500°C.[40]

This work is aimed to study the effect of L-ascorbic acid on the hydrothermal synthesis of rGO and rGO-MoO_2 hybrid for electrodes in supercapacitor applications.

5.2. Materials and Methods

5.2.1. Preparation of rGO aerogel

The rGO aerogel was prepared using the one-pot hydrothermal synthesis reported previously.[6,28,29,41] Briefly, Graphene Oxide flakes (Cheap Tubes Inc., USA) was dispersed

in deionized H_2O at a concentration of 2 mg/mL for a total volume of 17 mL. After 30 minutes of sonication at room temperature, the solution was transferred in a stainless-steel autoclave and undergoes a hydrothermal reaction for 12 hours at 180°C. The as-prepared hydrogel was frozen in liquid nitrogen. Finally, a freeze-drying procedure at -50°C under vacuum permits to remove the water by sublimation to obtain the rGO aerogel.

5.2.2. Preparation of rGO-vitC aerogel

L-Ascorbic acid (Sigma Aldrich) was added to the GO dispersion before the sonication using the same procedure reported in the previous section (Section 5.2.1). The concentration of L-AA is equal to the GO, 2 mg/mL, for a total volume of 17 mL.

5.2.3. Preparation of rGO-MoO_2-vitC aerogel

The hybrid aerogel was synthesized using a precursor of Mo in the same reaction condition as the pure rGO aerogel. The precursor used was Phosphomolybdic acid ($H_3PMo_{12}O_{40}$) solution (20 wt.% in ethanol), purchased from Sigma Aldrich. 0.5 g of the precursor was added to the 17 mL of deionized water contained GO and L-AA at 2 mg/mL after the sonication procedure. The molar ratio between Mo and C obtained was 1/100. The suspension was sonicated for 5 minutes to ensure a homogeneous dispersion of the Mo precursor before the hydrothermal synthesis. After the hydrothermal reaction, the same freeze-drying procedure was performed to obtain the rGO-MoO_2-vitC aerogel.

5.2.4. Materials characterization

The L-AA addition during hydrothermal synthesis could modify the resulting porous framework of the aerogels. To investigate this effect, BET-Specific Surface Area measurements (SSA) and Pore Size analysis were carried out by means of N_2 isotherms at -196°C. The instrument used was

a Quantachrome Autosorb 1C. Before the analysis, samples were degassed for 4 h at 100°C to remove atmospheric contaminants and water adsorbed on the sample surface. The BET-SSA were evaluated between 0.05 and 0.20 of relative pressure P/P^0. The cumulative pore volume curves were calculated using the QS-DFT method and carbon slit pores model.

The samples morphology was studied using FESEM analysis with a Zeiss Supra 40 Microscope equipped with an energy-dispersive X-ray (EDX) analyser.

X-Ray Photoelectron Spectroscopy (XPS) was carried out on a PHI 5000 VersaProbe (Physical Electronics) system, with a monochromatic Al Kα radiation (1486.6 eV energy) as X-ray source. Different pass energy values were used for survey (187.75 eV) and HR spectra (23.5 eV). During the measurements, charge compensation was obtained by a combined electron and Ar neutralizer system. The binding energy scale was calibrated by using the main C1s contribution (C-C/C-H bonds, 284.5 eV) as reference value. Concerning the analysis of HR scans, the background contribution was modelled with a Shirley function.[42] CasaXPS software was used for peak deconvolution, semi-quantitative analysis and calculation of uncertainties by means of Monte Carlo routines. Concerning the peak fitting procedure, two types of line shapes were exploited: GL(m) and LF(α, β, w, m).

X-ray Diffraction analysis was performed using Cu Kα radiation (λ=0.15406 nm) with a PANalytical X'Pert Powder apparatus. Spectra were collected between 2θ of 10-60° at a scanning rate of 0.85°/min. XRD analysis allows to investigate the reduction following change in the interlayer distance from GO to rGO. Moreover, the crystallographic phase of MoO_2 was also determined using this technique.

5.2.5. Electrodes preparation

Electrodes were prepared by drop-casting onto a well-polished glassy carbon (diameter of 0.3 cm, BioLogic) of a slurry with the following composition: 5 mg of active material, 0.4 mg of acetylene black (Alfa Aesar) and 5 µL Nafion® 5% (Sigma-Aldrich) dispersed in absolute ethanol.[43]

Electrochemical measurements were carried out in both two- and three-electrode symmetric configuration. For the device-like configuration, Fluorine doped Tin Oxide glass (Solaronix) was used as current collector. The diameter was 0.5 cm and the resistance was 10 Ω/sq. The two prepared electrodes were faced and separated using a glass-frit membrane (Whatman GF/A). The device was sealed using a thermoplastic polymer (Parafilm®).

For the three-electrode measurements, the reference electrode used was a homemade SMSE (680 mV vs. SHE) or a SCE (240 mV vs. SHE). A platinum bar was used as counter electrode.

Electrochemical measurements were performed using 1 M NaCl for the comparison of rGO and rGO-vitC while other measurements were carried out in Na_2SO_4 using deionized water with a resistivity of 18.2 MΩ cm^{-1}. Electrodes were soaked overnight with the electrolyte before the measurements.

5.2.6. Electrochemical characterization

Electrochemical measurements were carried out on a Metrohm Autolab PGSTATM101 potentiostat–galvanostat. Cyclic voltammetry (CV) was performed at multiple scan rates while Galvanostatic charge-discharge measurements were performed at three different current densities: 85, 170 and 350 mA g^{-1}. The cycling stability was performed in device-like configuration by cyclic voltammetry at 2 V s^{-1} up to 50.000 cycles. Every 1.000 cycles, an acquisition at a slow scan rate was analysed to estimate the capacitance. Then, AC

impedance spectroscopy was performed at 0 V in the frequency range from 10 kHz to 10 mHz with 5 mV amplitude.

5.3. Results and Discussion

5.3.1. Chemical-phyisical characterization

5.3.1.1. rGO and rGO-vitC

FESEM images at different magnification are shown in Figure 5.1.a and 5.1.b for rGO and rGO-vitC, respectively. The observed morphologies are close for both aerogels.[6,29] The porous framework seems to be composed of pores with diameter from nanometre to micrometre. They contain extremely wrinkled rGO flakes in a 3D interconnected structure, which avoid the restacking of graphene sheets. However, FESEM cannot be used to evaluate quantitatively the pore size distribution and the resulting specific surface area. N_2 adsorption/desorption isotherms permits the study of the aerogels porosity. Isotherms and cumulative pore volumes are reported in Figure 5.2.a and 5.2.b, respectively.

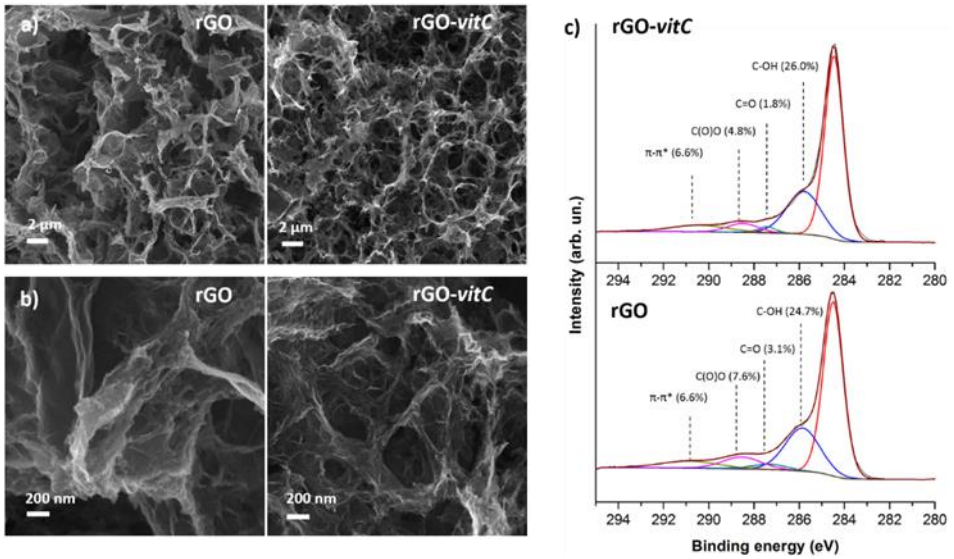

Figure 5. 1. FESEM images of rGO and rGO-vitC aerogels at low (a) and high (b) magnification (c) XPS spectra in the C1s region for rGO and rGO-vitC samples.

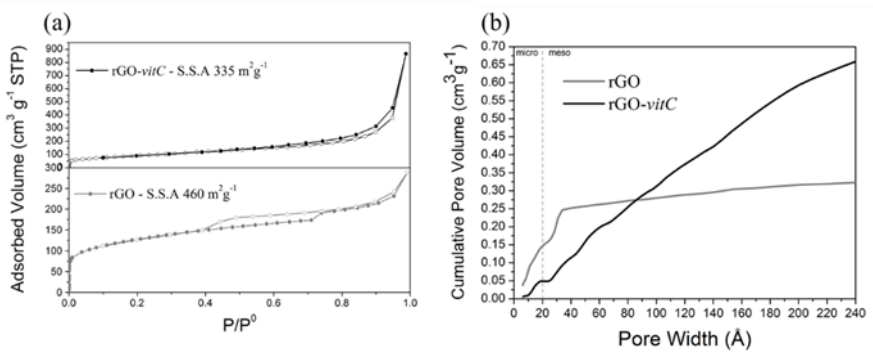

Figure 5. 2. N_2 adsorption/desorption isotherms of (lower) rGO and (upper) rGO-vitC (a); cumulative pores volume of rGO and rGO-vitC (b)

N_2 adsorption/desorption curves at 77 K are significantly different for rGO and rGO-vitC. Indeed, the rGO curve shows an adsorption branch composed of Type I(b) at low relative pressure, assignable to micropores filling, and Type II at high relative pressure, assignable to mesopores filling.[44] The hysteresis is a type H4. The lower limit of the desorption branch is observable at a relative pressure close to a value of 0.4, indicating that mesopores are accessible from the outer surface only through narrower necks. On the other hand, rGO-vitC curve displays a Type II isotherm with a limited hysteresis loop. The BET-Specific Surface Area for rGO and rGO-vitC are 460 m^2g^{-1} and 335 m^2g^{-1}, respectively. This different is significant and ascribable to the pores size. Indeed, rGO shows micropores and narrow mesopores (pore width <3nm) while rGO-vitC displays a large distribution of mesopores in the range from 2 to more than 20 nm. The hydrothermal decomposition of L-ascorbic acid seems to produce small gas bubbles (*e.g.* H_2) that induces a more open 3D structure.

As described previously in this thesis, XPS is shown in Figure 5.1.c. This technique is an important tool for the evaluation of the GO reduction by comparison of the C/O atomic ratio.[2] Finally, this technique provides information of the residual carbon-oxygen moieties by deconvolution of the C1s region.

Sample	C (at%)	O (at%)	C/O ratio
GO	65.3 ± 0.4 *	33.4 ± 0.3 *	1.95 ± 0.02
rGO	84.3 ± 0.3	15.7 ± 0.3	5.4 ± 0.1
rGO-vitC	88.3 ± 0.3	11.7 ± 0.3	7.5 ± 0.2

*Table 5. 1. atomic concentration values for C and O elements calculated from XPS spectra in the C1s region. * commercial GO atomic concentration values do not add up to 100% due to 1.3 %At of N as residual contamination of the oxidation process of graphite in commercial GO.*

Interestingly, no contamination was observed for rGO and rGO-vitC samples above the detection limit (≈ 0.1% at). The contamination present in the commercially available GO was removed during the hydrothermal synthesis and/or the freeze-drying process. Semiquantitative analysis was calculated by peak integrations in the C1s and O1s regions, using tabulated Relative Sensitivity Factors (RSF) specified by the instrument manufacturer. Obtained values are reported in Table 5.1. The C/O atomic ratio is significantly higher for rGO-vitC (≈7.5) in comparison with rGO (≈5.4) indicating a better reduction of GO. By the way, both samples display higher C/O atomic ratio in comparison with pristine GO (≈1.9) as expected. HR spectra are reported for rGO and rGO-vitC in Figure 5.1. The higher C/O atomic ratio of rGO-vitC is ascribable to the significant decrease of C=O and C(O)O moieties even if a slight increase in C-OH groups is observable.

5.3.1.2. rGO-MoO_2-vitC

FESEM images of the rGO-MoO_2-vitC are reported in Figure 5.3.a-5.3.c. The low magnification image shows that the aerogel morphology of the hybrid is close to rGO-vitC sample. Moreover, a homogeneous dispersion of micrometric MoO_2 particles, which have higher-intensity features, onto rGO flakes are obtained. Looking closer to molybdenum oxide particles (Figure 5.3.b), a nanostructured surface is observable.

The XRD pattern is reported in Figure 5.3.f. The rGO-MoO_2-vitC aerogel shows typical peaks of MoO_2 monocline phase, in accordance with JCPDS card No. 32-0671.

HR spectra in the C1s and Mo3d regions are shown in Figure 5.3.d and 5.3.e, respectively. XPS technique is used to confirm the suitable reduction of GO together with the investigation of the microparticles chemical composition. The Mo3d region contains 3 features which can be deconvoluted in different peaks ascribable to Mo (IV), Mo (V), and Mo (VI). Characteristic peaks of crystalline MoO_2 are observable with the spin-orbit doublet are located at 229.4 eV and 232.5 eV, and satellite peaks at 230.9 eV and 234.1 eV. Results are in agreement with the works reported by Scanlon and co-workers.[45] Broad asymmetric peaks located at 231.8 eV and 234.6 eV can be assigned to Mo (V) species even if the peak splitting observed is 2.8 eV instead of ≈ 3.1 eV, which is usually reported in literature. It is nevertheless important to notice that the interpretation of Mo (V) components is complicated and subject of debate in literature. The interpretation reported here is based on the peak deconvolution of the Mo3d region for mixed-oxide states using multivariate approach.[46] Finally, the doublet at higher binding energy (232.7 eV, 235.9 eV) is characteristic of MoO_3, corresponding to a Mo (VI) oxidation state.[47] To summarize, XPS results indicate the concomitant presence of diverse oxide phases with diverse oxidation states. This phenomenon was already observed previously.[29,48] XRD displays only monocline MoO_2 phase which means that the bulk is composed by this phase. However, XPS analysis (surface analysis technique) shows the presence of Mo (V) and Mo (VI). Microparticles embedded in the rGO aerogels are composed of molybdenum oxide with an oxidation state from IV (core) to (VI), due to surface oxidation by air. A schematic representation is shown in Figure 5.3.c.

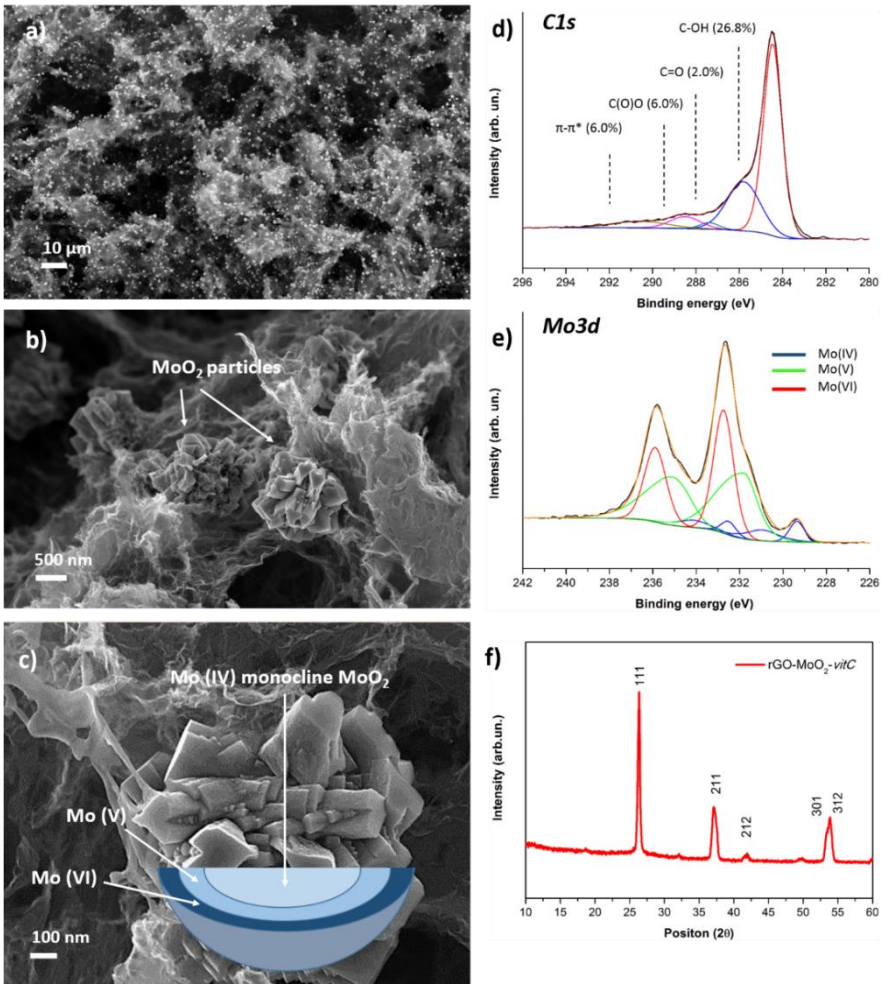

Figure 5. 3. FESEM images at low (a) and high (b) magnification of the rGO-MoO_2-vitC sample. (c) FESEM image of MoO_2 particle with a schematic representation of the gradient of Mo oxidation state. XPS HR spectra of C1s (d) and Mo3d (e) regions for rGO-MoO_2-vitC sample. (f) XRD spectrum of the hybrid aerogel.

5.3.2. Electrochemical characterization

5.3.2.1. Effect of the L-Ascorbic Acid addition

For sake of study, a comparison of the electrochemical performance in a three-electrode configuration of rGO and rGO-vitC is necessary. As reported in Figure 5.4.a, the suitable potential window differs for both samples. The rGO shows a deviation from the box-like voltammogram of pure EDLC due to the presence of non-reduced carbon-oxygen

moieties such as –C=O, -C(O)O, -C-OH, as reported previously by XPS. Interestingly, the voltammogram for rGO-vitC shows a pure EDL behaviour confirming the enhanced reduction of GO by addition of L-AA during the hydrothermal synthesis. Despite the more suitable reduction, rGO-vitC has a lower storage capability than rGO as indicated by the smaller area on the CV curves. The rate capability is reported in Figure 5.4.b for both samples. Specific capacitance is higher for rGO than rGO-vitC with a maximum of 55 F g^{-1} and 23 F g^{-1}, respectively. This significant difference is ascribable to a lower BET-specific surface area for the sample prepared using L-AA as reducing agent. However, the better rate capability confirms the pure EDLC behaviour of rGO-vitC, indicating the effect of L-AA on the GO reduction.

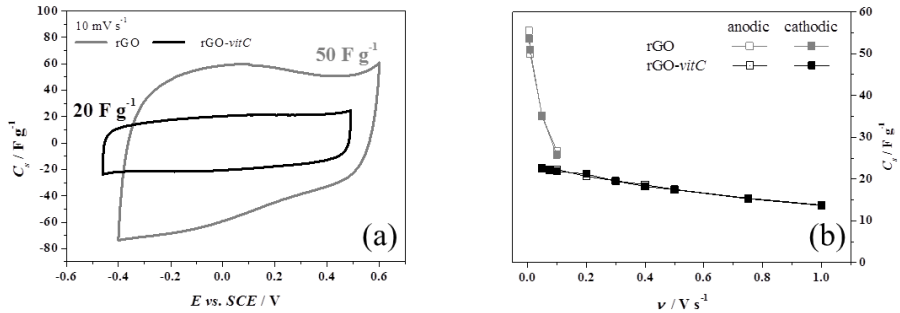

Figure 5. 4. (a) Cyclic Voltammograms acquired at 10 mV s^{-1} for rGO (gray) and rGO-vitC (black). (b) specific capacitance at multiple scan rates. Experiments carried out with 1 M NaCl as electrolyte in a three-electrode configuration.

Galvanostatic charge-discharge measurements were performed on the rGO-vitC sample. Chronopotentiograms are shown in Figure 5.5. Both cathodic and anodic behaviour were investigated at 3 current densities. For cathodic measurement, potential window starts from OCP (-0.55 V vs. SMSE) to the lower potential limit. The anodic measurement, instead, starts from OCP to the higher potential limit. Curves are perfectly linear confirming the pure EDLC behaviour. An IR drop of 8 Ω is measured.

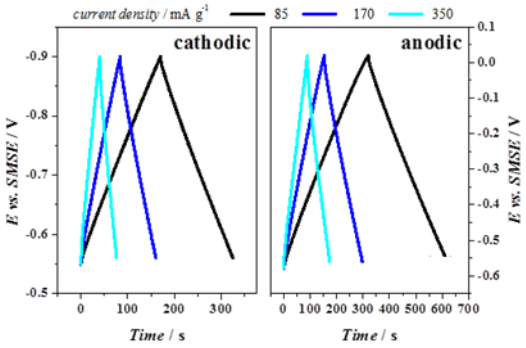

Figure 5. 5. Galvanostatic charge-discharge measurements for rGO-vitC in 1M Na_2SO_4 in a three-electrode configuration.

5.3.2.2. Effect of L-Ascorbic Acid on the hydrothermal synthesis of rGO-vitC and rGO-MoO_2-vitC

Phosphomolybdic acid is used as Mo precursor during the hydrothermal synthesis with L-AA as reducing agent. Cyclic voltammetry performed at multiple scan rates in three-electrode symmetric configuration is shown in Figure 5.6.a and 5.6.b for rGO-vitC and rGO-MoO_2-vitC, respectively.

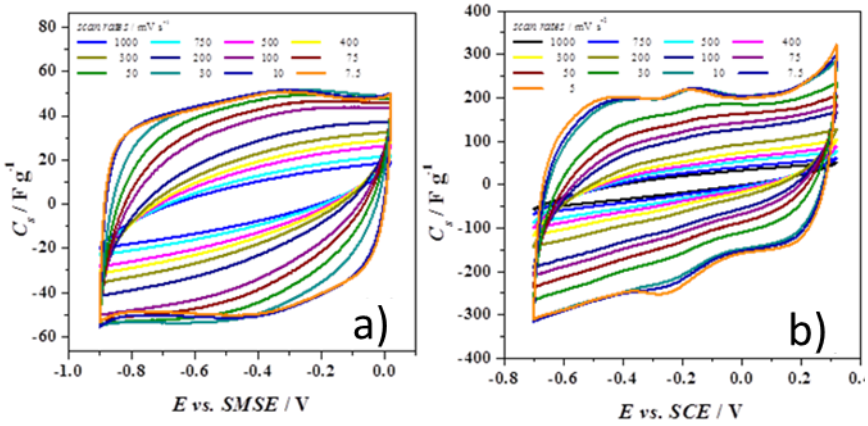

Figure 5. 6. Cyclic Voltammograms performed at multiple scan rates in the range from 1 V s^{-1} to 7.5 mV s^{-1}. Measurements were carried out in a three-electrode configuration with symmetrical electrodes in 1M Na_2SO_4.

Two information can be extrapolated from the CV curves. The shape of rGO-MoO_2-vitC shows deviation from the pure EDLC behaviour mainly at low scan rates. Indeed, redox reaction occurs at a potential about -0.2V with the anodic peak at -0.17 V and cathodic peak at -0.27 V. Consequently, measured

current is considerably increased leading to higher specific capacitance. rGO-MoO_2-vitC has a maximal storage capability of 210 F g^{-1} at 5 mV s^{-1}. These redox features progressively disappear when the sweep rate is faster. Subsequently, the calculated specific capacitance at high scan rate is close to the rGO-vitC sample because the contribution of the pseudocapacitive material is negligible.

5.3.2.3. Cycling stability evaluation for rGO-vitC and rGO-MoO_2-vitC aerogels

The cycling stability of the rGO-MoO_2-vitC material was evaluated by cyclic voltammetry at 2 V s^{-1} up to 50.000 cycles in a two-electrode configuration. Every 1.000 cycles, a cyclic voltammetry at slow scan rate followed by an AC impedance measurement were performed. EIS spectra were used to monitor the equivalent circuit of the system in the case of structural changes in the material. The capacitance retention for both samples are reported in Figure 5.7.a and 5.7.b, respectively. Nyquist plots are plotted in the insets on the same figure of the cycling stability. Complex capacitance plots, calculated according to Taberna and co-workers[49], are reported in Figure 5.7.c-5.7.f.

The capacitance was perfectly retained for both materials. However, some differences are observable from AC impedance spectra after 3.000 cycles for rGO-vitC and 8.000 cycles for rGO-MoO_2-vitC. Two hypotheses may explain those differences: activation processes and/or better wettability, which induce a larger exposed surface between the electrodes and the electrolyte. During these first cycles, values of C' and C" increased in the low frequency domain, but together the uncompensated resistance (R_u), the relaxation time constant (τ_0) and the overall capacitance were constant until the end of ageing, meaning that the charge/discharge capabilities are perfectly maintained.

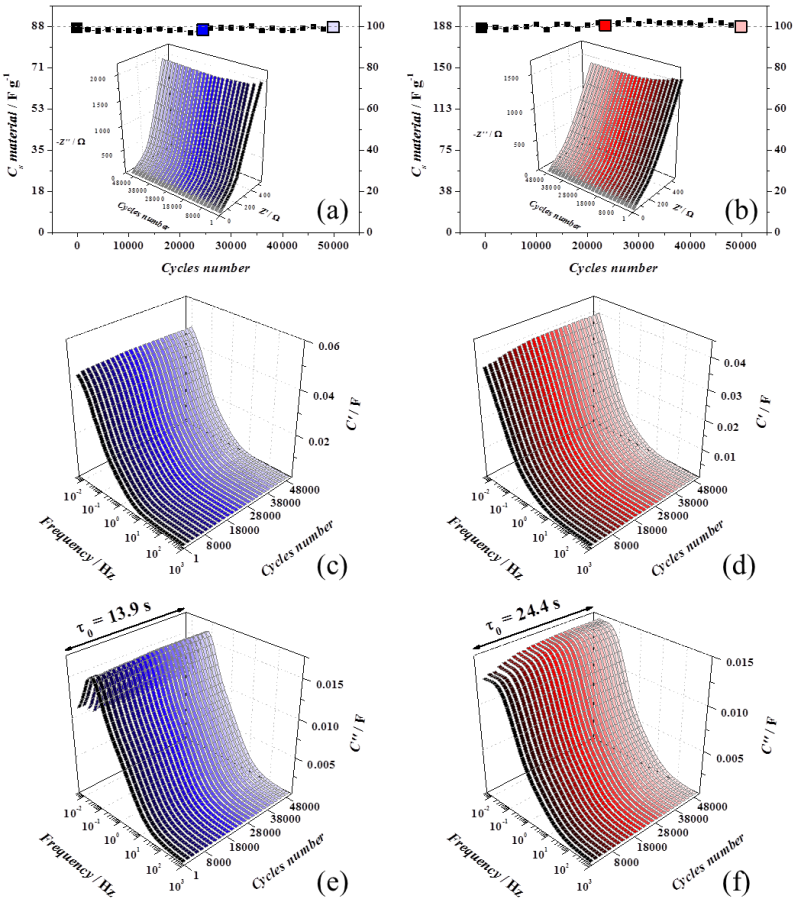

Figure 5. 7. All the ageing experiments were carried out in device with 1 M Na_2SO_4. rGO-vitC experiments are reported on the left-hand side (blue shadows) and rGO-MoO_2-vitC experiments are presented on the right-hand side (red shadows). AC impedance spectra were carried out at 0 V every 1000 cycles. (a-b) Capacitance retention and Nyquist plots in the inset, (c –d) real part of the complex capacitance spectra (C') and (e-f) imaginary part of the complex capacitance spectra (C'') with the relaxation time constant of the device.

For sake of completeness, the ageing effect on the rGO-MoO_2-vitC aerogel was investigated after 50.000 cycles by means of FESEM analysis. Images of the electrodes at different magnification are shown in Figure 5.8. At low magnification, the morphology is identical to the as-synthesized rGO-MoO_2-vitC aerogel. At higher magnification, concomitant presence of MoO_2 particles and acetylene black (from the slurry preparation) are identifiable. These

observations confirm the suitable synthesis of rGO-MoO_2 aerogels using L-AA as reducing agent during the hydrothermal reaction.

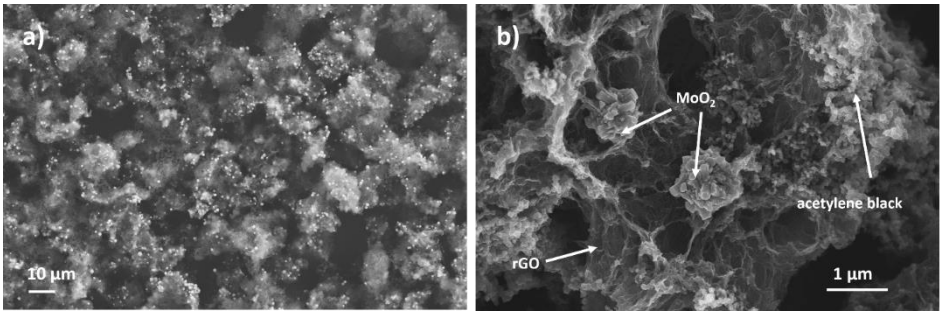

Figure 5. 8. FESEM images of the electrode material containing rGO-MoO_2-vitC, acetylene black and Nafion® after 50.000 cycles.

5.4. Conclusions

This chapter reports the use of L-Ascorbic Acid (Vitamin C) as reducing agent for the hydrothermal synthesis of rGO and rGO-MoO_2 aerogels. Both XPS and electrochemical analyses demonstrate a more suitable reduction of GO in comparison to the reduction process performed without L-AA. The specific capacitance for rGO-vitC aerogel is lower than the rGO aerogel. However, the rate capability is significantly improved due to the better reduction of GO, which eliminate the carbon-oxygen moieties onto the surface of rGO flakes.

The concomitant hydrothermal reduction with the formation of MoO_2 particles was investigated. Particles are micrometrics. Electrochemical measurements demonstrate significantly better performance of the rGO-MoO_2-vitC hybrid in comparison with the rGO-vitC. Interestingly, a perfect capacitance retention was also observed up to 50.000 cycles using cyclic voltammetry. Moreover, FESEM images of the aged slurry confirms the perfect stability of the as-synthesized rGO-MoO_2-vitC hybrid aerogel.

To conclude, L-AA demonstrates its efficiency as reducing agent to produce Graphene-Metal Oxide composites for energy storage applications.

In the next chapter, this material will be used as active material for micro-supercapacitor applications.

REFERENCES

(1) Hummers, W. S.; Offeman, R. E. Preparation of Graphitic Oxide. *J. Am. Chem. Soc.* **1958**, *80* (6), 1339–1339.

(2) Pei, S.; Cheng, H. M. The Reduction of Graphene Oxide. *Carbon N. Y.* **2012**, *50* (9), 3210–3228.

(3) Dreyer, D. R.; Park, S.; Bielawski, C. W.; Ruoff. The Chemistry of Graphene Oxide. *Chem. Soc. Rev.* **2010**, *39*, 228–240.

(4) Zhu, Y.; Murali, S.; Stoller, M. D.; Velamakanni, A.; Piner, R. D.; Ruoff, R. S. Microwave Assisted Exfoliation and Reduction of Graphite Oxide for Ultracapacitors. *Carbon*. Elsevier Ltd 2010, pp 2118–2122.

(5) Xing, L. B.; Hou, S. F.; Zhou, J.; Li, S.; Zhu, T.; Li, Z.; Si, W.; Zhuo, S. UV-Assisted Photoreduction of Graphene Oxide into Hydrogels: High-Rate Capacitive Performance in Supercapacitor. *J. Phys. Chem. C* **2014**, *118* (45), 25924–25930.

(6) Yuxi Xu, Kaixuan Sheng, C. L.; Shi, G. Self-Assembled Graphene Hydrogel via a One-Step Hydrothermal Process. *ACS Nano* **2010**, *4* (7), 4324–4330.

(7) Zhou, Y.; Bao, Q.; Tang, L. A. L.; Zhong, Y.; Loh, K. P. Hydrothermal Dehydration for The “green” reduction of Exfoliated Graphene Oxide to Graphene and Demonstration of Tunable Optical Limiting Properties. *Chem. Mater.* **2009**, *21* (13), 2950–2956.

(8) Fernández-Merino, M. J.; Guardia, L.; Paredes, J. I.; Villar-Rodil, S.; Solís-Fernández, P.; Martínez-Alonso, A.; Tascón, J. M. D. Vitamin C Is an Ideal Substitute for Hydrazine in the Reduction of Graphene Oxide Suspensions. *J. Phys. Chem. C* **2010**, *114* (14), 6426–6432.

(9) Stankovich, S.; Dikin, D. A.; Piner, R. D.; Kohlhaas, K. A.; Kleinhammes, A.; Jia, Y.; Wu, Y.; Nguyen, S. B. T.; Ruoff, R. S. Synthesis of Graphene-Based Nanosheets via Chemical Reduction of Exfoliated Graphite Oxide. *Carbon N. Y.* **2007**, *45* (7), 1558–1565.

(10) Li, D.; Müller, M. B.; Gilje, S.; Kaner, R. B.; Wallace, G. G. Processable Aqueous Dispersions of Graphene Nanosheets. *Nat. Nanotechnol.* **2008**, *3* (2), 101–105.

(11) Chen, W.; Yan, L. In Situ Self-Assembly of Mild Chemical Reduction Graphene for Three-Dimensional Architectures. *Nanoscale* **2011**, *3*, 3132–3137.

(12) Shin, H. J.; Kim, K. K.; Benayad, A.; Yoon, S. M.; Park, H. K.; Jung, I. S.; Jin, M. H.; Jeong, H. K.; Kim, J. M.; Choi, J. Y.; Lee, Y. H. Efficient Reduction of Graphite Oxide by Sodium Borohydride and Its Effect on Electrical Conductance. *Adv. Funct. Mater.* **2009**, *19* (12), 1987–1992.

(13) Pei, S.; Zhao, J.; Du, J.; Ren, W.; Cheng, H. M. Direct Reduction of Graphene Oxide Films into Highly Conductive and Flexible Graphene Films by Hydrohalic Acids. *Carbon N. Y.* **2010**, *48* (15), 4466–4474.

(14) Zhang, L.; Chen, G.; Hedhili, M. N.; Zhang, H.; Wang, P. Three-Dimensional Assemblies of Graphene Prepared by a Novel Chemical Reduction-Induced Self-Assembly Method. *Nanoscale* **2012**, *4* (22), 7038–7045.

(15) Si, W.; Wu, X.; Zhou, J.; Guo, F.; Zhuo, S.; Cui, H.; Xing, W. Reduced Graphene Oxide Aerogel with High-Rate Supercapacitive Performance in Aqueous Electrolytes. *Nanoscale Res. Lett.* **2013**, *8* (1), 247.

(16) Wang, G. X.; Yang, J.; Park, J.; Gou, X. L.; Wang, B.; Liu, H.; Yao, J. Facile Synthesis and Characterization of Graphene Nanosheets. *J. Phys. Chem. C* **2008**, *112*, 8192.

(17) Hu, H.; Zhao, Z.; Wan, W.; Gogotsi, Y.; Qiu, J. Ultralight and Highly Compressible Graphene Aerogels. *Adv. Mater.* **2013**, *25* (15), 2219–2223.

(18) Li, C.; Shi, G. Functional Gels Based on Chemically Modified Graphenes. *Adv. Mater.* **2014**, *26* (24), 3992–4012.

(19) De Silva, K. K. H.; Huang, H.-H.; Joshi, R. K.; Yoshimura, M. Chemical Reduction of Graphene Oxide Using Green Reductants. *Carbon N. Y.* **2017**, *119*, 190–199.

(20) Aunkor, M. T. H.; Mahbubul, I. M.; Saidur, R.; Metselaar, H. S. C. The Green Reduction of Graphene Oxide. *RSC Adv.* **2016**, *6*, 27807–27828.

(21) Ye, W.; Li, X.; Luo, J.; Wang, X.; Sun, R. Lignin as a Green Reductant and Morphology Directing Agent in the Fabrication of 3D Graphene-Based Composites for High-Performance Supercapacitors. *Ind. Crops Prod.* **2017**, *109*, 410–419.

(22) Xu, L. M.; Xiao, G. Y.; Chen, C. B.; Li, R.; Mai, Y. Y.; Sun, G. M.; Yan, D. Y. Superhydrophobic and Superoleophilic Graphene Aerogel Prepared by Facile Chemical Reduction. *J. Mater. Chem. A* **2015**, *3* (14), 7498–7504.

(23) Zhang, J. J.; Yang, H.; Shen, G.; Cheng, P.; Zhang, J. J.; Guo, S. Reduction of Graphene Oxide via L-Ascorbic Acid. *Chem. Commun. (Camb).* **2010**, *46* (7), 1112–1114.

(24) Lobach, S. A.; Kazakov, V. A.; Spitsyna, N. G.; Baskakov, S. A.; Dremova, N. N.; Shul'ga, Y. M. Comparative Study of Graphene Aerogels Synthesized Using Sol–Gel Method by Reducing Graphene Oxide Suspension. *High Energy Chem.* **2017**, *51* (4), 269–276.

(25) Zhang, X.; Sui, Z.; Xu, B.; Yue, S.; Luo, Y.; Zhan, W.; Liu, B. Mechanically Strong and Highly Conductive Graphene Aerogel and Its Use as Electrodes for Electrochemical Power Sources. *J. Mater. Chem.* **2011**, *21* (c), 6494.

(26) Nguyen, S. T.; Nguyen, H. T.; Rinaldi, A.; Nguyen, N. P. V; Fan, Z.; Duong, H. M. Morphology Control and Thermal Stability of Binderless-Graphene Aerogels from Graphite for Energy Storage Applications. *Colloids Surfaces A Physicochem. Eng. Asp.* **2012**, *414*, 352–358.

(27) Zhou, L.; Yang, X.; Yang, B.; Zuo, X.; Li, G.; Feng, A.; Tang, H.; Zhang, H.; Wu, M.; Ma, Y.; Jin, S.; Sun, Z.; Chen, X. Controlled Synthesis of $CuInS_2$/reduced Graphene Oxide Nanocomposites for Efficient Dye-Sensitized Solar Cells. *J. Power Sources* **2014**, *272*, 639–646.

(28) Giardi, R.; Porro, S.; Topuria, T.; Thompson, L.; Pirri, C. F.; Kim, H. C. One-Pot Synthesis of Graphene-Molybdenum Oxide Hybrids and Their Application to Supercapacitor Electrodes. *Appl. Mater. Today* **2015**, *1* (1), 27–32.

(29) Gigot, A.; Fontana, M.; Serrapede, M.; Castellino, M.; Bianco, S.; Armandi, M.; Bonelli, B.; Pirri, C. F.; Tresso, E.; Rivolo, P. Mixed 1T-2H Phase MoS_2/reduced Graphene Oxide as Active Electrode for Enhanced Supercapacitive Performance. *ACS Appl. Mater. Interfaces* **2016**, *8*, 32842–32852.

(30) Marasso, S. L.; Rivolo, P.; Giardi, R.; Mombello, D.; Gigot, A.; Serrapede, M.; Benetto, S.; Enrico, A.; Cocuzza, M.; Tresso, E.; Pirri, C. F. A Novel Graphene Based Nanocomposite for Application in 3D Flexible Micro-Supercapacitors. *Mater. Res. Express* **2016**, *3* (6), 65001.

(31) Chen, Z.-Y.; Yu, Y.-N.; Bao, S.-J.; Wang, M.-Q.; Li, Y.-N.; Xu, M.-W. Ascorbic Acid-Tailored Synthesis of Carbon-Wrapped Nanocobalt Encapsulated in Graphene Aerogel as Electrocatalysts for Highly Effective Oxygen-Reduction Reaction. *J. Solid State Electrochem.* **2017**, 1–8.

(32) Wan, W.; Zhang, F.; Yu, J.; Zhang, R.; Zhou, Y. Hydrothermal Formation of Graphene Aerogel for Oil Sorption: The Role of Reducing Agent, Reaction Time and Temperature. *New J. Chem.* **2016**, *40* (4), 3040–3046.

(33) Guanghui, W.; Ruiyi, L.; Zaijun, L.; Junkang, L.; Zhiguo, G.; Guangli, W. N-Doped Graphene/graphite Composite as a Conductive Agent-Free Anode Material for Lithium Ion Batteries with Greatly Enhanced Electrochemical Performance. *Electrochim. Acta* **2015**, *171*, 156–164.

(34) Movahed, S. K.; Dabiri, M.; Bazgir, A. A One-Step Method for Preparation of $Cu@Cu_2O$ Nanoparticles on Reduced Graphene Oxide and Their Catalytic Activities in N-Arylation of N-Heterocycles. *Appl. Catal. A Gen.* **2014**, *481*, 79–88.

(35) Liu, T.; Shao, G.; Ji, M.; Ma, Z. Composites of Olive-like Manganese Oxalate on Graphene Sheets for Supercapacitor Electrodes. *Ionics (Kiel).* **2014**, *20* (1), 145–149.

(36) Sui, Z.; Zhang, X.; Lei, Y.; Luo, Y. Easy and Green Synthesis of Reduced Graphite Oxide-Based Hydrogels. *Carbon N. Y.* **2011**, *49* (13), 4314–4321.

(37) Ye, J.; An, J.; Liu, B.; Xu, C. Facile Preparation of SnO2/graphene Nanosheet Composite with Excellent Electrochemical Performances for Lithium Storage. *Int. J. Hydrogen Energy* **2017**, *42* (8), 5199–5206.

(38) Shen, J.; Shi, M.; Yan, B.; Ma, H.; Li, N.; Ye, M. One-Pot Hydrothermal Synthesis of Ag-Reduced Graphene Oxide Composite with Ionic Liquid. *J. Mater. Chem.* **2011**, No. 21, 7795–7801.

(39) Hu, X.; Zhang, W.; Liu, X.; Mei, Y.; Huang, Y. Nanostructured Mo-Based Electrode Materials for Electrochemical Energy Storage. *Chem. Soc. Rev.* **2015**, *44* (8), 2376–2404.

(40) Palanisamy, K.; Kim, Y.; Kim, H.; Kim, J. M.; Yoon, W. S. Self-Assembled Porous MoO_2/graphene Microspheres towards High Performance Anodes for Lithium Ion Batteries. *J. Power Sources* **2015**, *275*, 351–361.

(41) Lamberti, A.; Gigot, A.; Bianco, S.; Fontana, M.; Castellino, M.; Tresso, E.; Pirri, C. F. Self-Assembly of Graphene Aerogel on Copper Wire for Wearable Fiber-Shaped Supercapacitors. *Carbon N. Y.* **2016**, *105*, 649–654.

(42) Shirley, D. A. High-Resolution X-Ray Photoemission Spectrum of the Valence Bands of Gold. *Phys. Rev. B* **1972**, *5* (12), 4709–4714.

(43) Agrawal, R.; Chen, C.; Hao, Y.; Song, Y.; Wang, C. *Graphene for Supercapacitors*; A. Rashid bin Mohd Yusoff, Ed.; Wiley-VCH Verlag GmbH & Co. KGaA, 2015.

(44) Thommes, M.; Kaneko, K.; Neimark, A. V.; Olivier, J. P.; Rodriguez-Reinoso, F.; Rouquerol, J.; Sing, K. S. W. Physisorption of Gases, with Special Reference to the Evaluation of Surface Area and Pore Size Distribution (IUPAC Technical Report). *Pure Appl. Chem.* **2015**, *87* (9–10), 1051–1069.

(45) Scanlon, D. O.; Watson, G. W.; Payne, D. J.; Atkinson, G. R.; Egdell, R. G.; Law, D. S. L. Theoretical and Experimental Study of the Electronic Structures of MoO_3 and MoO_2. *J. Phys. Chem. C* **2010**, *114* (10), 4636–4645.

(46) Baltrusaitis, J.; Mendoza-Sanchez, B.; Fernandez, V.; Veenstra, R.; Dukstiene, N.; Roberts, A.; Fairley, N. Generalized Molybdenum Oxide Surface Chemical State XPS Determination via Informed Amorphous Sample Model. *Appl. Surf. Sci.* **2015**, *326*, 151–161.

(47) Naumkin, A. V.; Kraut-Vass, A.; Gaarenstroom, S. W.; Powell, C. J. NIST X-Ray Photoelectron Spectroscopy Database. *Meas. Serv. Div. Natl. Inst. Stand. Technol.* **2012**.

(48) Liu, C.; Li, Z.; Zhang, Z. Molybdenum Oxide Film with Stable Pseudocapacitive Property for Aqueous Micro-Scale Electrochemical Capacitor. *Electrochim. Acta* **2014**, *134*, 84–91.

(49) Taberna, P. L.; Simon, P.; Fauvarque, J. F. Electrochemical Characteristics and Impedance Spectroscopy Studies of Carbon-Carbon Supercapacitors. *J. Electrochem. Soc.* **2003**, *150* (3), A292.

Chapter 6

Micro-Supercapacitors

Materials prepared in Chapter 5 are applied as active material to fabricate PDMS-based micro-supercapacitors through a simple photolithographic process. Moreover, the use of PEDOT:PSS as conductive binder is investigated. It induces the formation of a spring-like rod configuration with the embedded active material. This spatial conformation results from the filling of the interdigitated channels by capillarity. As-fabricated devices show high flexibility and good cycling stability.

Part of the work described in this chapter has been previously published in Materials Research Express, 2016 (3), 065001.

6.1. Motivations

The crucial need of portable electronic equipment stimulates the development of advanced energy storage systems. Moreover, the demand for on-chip systems and micro-power energy storage units has considerably increased in the past years. Micro-supercapacitors (MSC) are miniaturized devices that can fill the gap for portable energy storage devices thanks to the new in Micro Electro Mechanical Systems (MEMS) technologies. Several works have already demonstrated the feasibility of MSC applications with areal specific capacitance in the range of 1-100 mF cm^{-2}.[1,2]

The deliverable performance is strongly correlated to the materials used for the electrodes. Carbon-based materials have attracted much attention thanks to their outstanding properties such as good electronic conductivity, high

chemical stability, low cost and easy processing. Activated carbon, carbon nanotubes, graphene, and graphdiyne have already been investigated.[3–9] However, these materials offer capacitive performance by charge separation mechanism. It is well known that the deliverable performance can be further increased by addition of pseudocapacitive materials like metal transition oxides such as Ru, Mn, Mo;[10–12] or conductive polymers.[13,14] These materials are usually deposited to form thin film from nanometres to few micrometres of thickness. The carbonaceous material, instead, is usually grown or deposited to form a thickness between micrometres to millimetres. Graphene and activated carbon have already demonstrated the capacity to be deposited successfully to create micro-supercapacitors with high Aspect Ratio (AR) as shown by Li and co-workers.[5] The aspect ratio is a key characteristic for miniaturized devices because higher is the value of AR, higher is amount of active material that can be deposited without increasing the device footprint.

In this chapter, micro-supercapacitors are fabricated using a Lithographic, Galvanoformung, Abformung (LIGA)-like process[15] employing standard MEMS technologies. The polydimethylsiloxane (PDMS) is a good candidate for the fabrication of interdigitated structures with high aspect ratio. Indeed, PDMS has good mechanical properties allowing flexibility and deformability, which limits the accumulation of tensile stress or any plastic deformation.[16]

The hydrothermal synthesis is used in this work to reduce Graphene Oxide in a rGO-based aerogel. This 3-dimensional configuration offers high surface area for the EDL formation.[17,18] Together with this reduction, the synthesis of metal oxide particles allows to add Faradaic-active chemical species which enhance the specific capacitance.[19] Molybdenum Oxide was chosen as pseudocapacitve materials due to the wide range of oxidation number of Mo centre.[20]

Moreover, rGO flakes prevent from the formation of the Molybdenum Oxide (VI) which is more insulating.[21]

Different slurries were prepared using poly(3,4-ethylenedioxythiophene) (PEDOT) as conductive binder. The concentration ratio between rGO and MoO_2 is investigated to demonstrate the role of the composition.

The deposition of active material is often complicated but, in this case, a self-filling by capillarity is studied for the deposition of rGO/MoO_2 aerogel.[22]

6.2. Materials and Methods

6.2.1. Preparation of rGO and rGO-MoO_2 aerogels

Both aerogels were prepared using the method reported in the Section 5.2.3 of the Chapter 5. Acronyms used in this chapter are **rGO** and **rGO-MoO_2** for rGO-vitC and rGO-MoO_2-vitC, respectively.

6.2.2. Characterization of rGO and rGO-MoO_2 aerogels

The samples morphology was studied using FESEM analysis with a Zeiss Supra 40 Microscope equipped with an energy-dispersive X-ray (EDX) analyser.

Raman analyses were carried out by means of a Renishaw InVia Reflex micro-Raman spectrometer (Renishaw plc, Wottonunder-Edge, UK), equipped with a cooled CCD camera. The parameters for the data collection follows: 514.5 nm was the diode laser excitation wavelength, 50x was the microscope objective magnification, 5 mW and 10 s were the power laser and the exposure time respectively, the number of accumulations ranged between 1 and 3. Aerogels were pressed carefully on a glass microscope used as substrate to be as flat as possible to optimize the laser focus on the sample.

6.2.3. PDMS-based Micro-Supercapacitor fabrication

Standard Si wafers finished with 1 µm of SiO_2 were used for the fabrication of the master. The micro-supercapacitor (MSC) design contains interdigitated structures with 55 µm and 5 mm long channels. The distance between each channel was 20 µm. The process flow for the realization of the PDMS-based MSC is reported in Figure 6.1. A standard photolithography, using HPR 504 (Microchemicals) as photoresist, was used to pattern the replica of the interdigitated structures. The SiO_2 was etched in 6:1 Buffered Oxide Etch (BOE) solution followed by the stripping of the photoresist. The SiO_2 replica was then cleaned in a piranha solution (H_2SO_4 (99%):H_2O_2 (33%) from Sigma Aldrich, 3:1 vol. ratio).

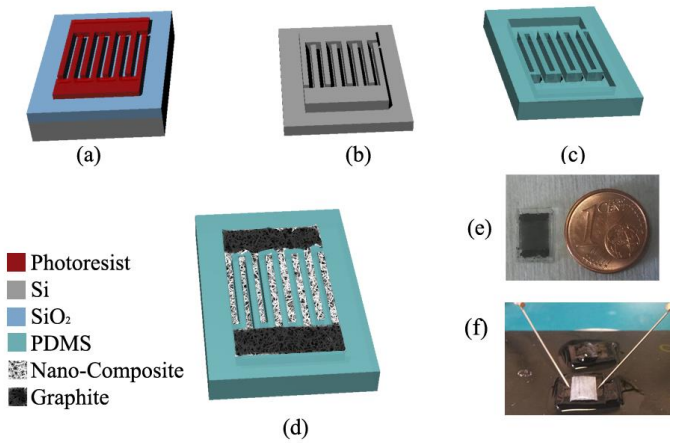

Figure 6. 1. Process flow for the fabrication of the MSC: (a) photolithographic step to design the interdigitated pattern on the SiO_2 layer; (b) Si replica after bulk micromachining in DRIE; (c) PDMS-based interdigitated structures after demoulding; (d) PDMS-based MSC with active material and collectors; (e) real device; (f) device under measurement using the characterization setup.

A Deep Reactive Ion Etching (DRIE) was performed for bulk micromachining in an Oxford Plasmalab100. Parameters used were: 60 sccm SF_6 gas flow, 6 sccm O_2 gas flow, 5 W RF power, 950 W ICP power, 10 mTorr chamber pressure, -118 °C and 10 sccm of backplate He flow. The anisotropic Si etching was 100 µm deep. Resulting interdigitated structures have an aspect

ratio (AR) of 2:1, which allows 2.5 µL maximum for the loading of each electrode.

Prior to depose the Teflon-like coating that helps the PDMS de-moulding[23], a treatment with piranha solution was performed on the Si replica. The deposition occurred in a DRIED Oxford Plasmalab100 with the following parameters: 100 sccm of C_4F_8 gas flow, 1500 W of ICP power, 11 W of RF power at 20 °C.

Next, Sylgard 184 PDMS (Dow Corning) was poured into a mould in Al fabricated by milling and fixed with a mounting wax. The ratio between the oligomer and the curing agent was 5:1 (w/w). The mould was placed under vacuum for 10 min at 1 mbar to guarantee a suitable filling of the interdigitated structures. Finally, a thermal crosslinking step at 90°C for 10 minutes was performed to form the PDMS. The PDMS-based Micro-Supercapacitor was de-moulded from the Si replica and the chip is ready to be filled with the active material.

6.2.4. Paste preparation and deposition

Different formulations were prepared: (1) PEDOT-solution:rGO (5:1) w/w; (2) PEDOT-solution:rGO decorated with MoO_2 (5:1) w/w; (3) PEDOT-solution:rGO (20:1) w/w; (4) PEDOT-solution:rGO decorated with MoO_2 (20:1) w/w; (5) pristine PEDOT used as a reference for the electrochemical measurements.

PEDOT-solution is the acronym for PEDOT:PSS. The commercially available solution (Clevios PH1000, Heraeus Conductive Polymers Division) contains poly(3,4-ethylenedioxythiophene) doped with poly(styrene sulfonate). The formulation preparation and the deposition were performed in a cleanroom with controlled temperature and humidity to avoid possible modifications of the hygroscopic PEDOT. The electrical conductivity of the PEDOT solution, used as binder, was enhanced before to be mixed with the active materials (rGO and rGO-MoO_2 aerogels). The

PEDOT:PSS was mixed with ethylene glycol [10% vol.] and dodecyl benzene sulfonic acid (DBSA) surfactant (Sigma Aldrich). Finally, the viscosity was decreased adding water to a weight ratio of 10:1.5 of H_2O:PEDOT solution according to the desired concentration.

Before to be used for micro-supercapacitor applications, rGO should be treated. The as-synthesized micron-sized powders was dispersed in ethanol before to be thoroughly mixed at 30.000 rpm for 5 minutes using an Ultraturrax Homogeniser. Ethanol was evaporated by heating the solution at 80°C. The resulting powder was carefully collected and weighed before to be mixed with the PEDOT-solution.

Prior to test the PDMS-based supercapacitors, prepared formulations were tested in planar configuration. Electrodes were prepared by doctor blading. Circular electrode with a diameter of 1 cm was deposited on current collectors, prepared in a 4 cm^2 glass microscope slide. The glass was previously cleaned using acetone and isopropanol prior to be sputtered with platinum. The sputtering procedure was carried on for 180 s with a current of 50 mA. The separator used was a disc of 1 cm diameter cut in a cleanroom paper. The electrolyte was 1M NaCl in water. Parafilm®, thermoplastic polymer, was used as sealing agent.

PDMS is hydrophobic while all prepared pastes are hydrophilic which induces filling difficulties. To overcome this issue, the hydrophilicity of the interdigitated structures was increased by oxygen plasma. The apparatus and the condition used were STS 320PC Reactive Ion Etching system for 120 s, at a power of 100 W, at a total pressure of 50 mTorr under an oxygen flow rate of 50 sccm.

To confirm the change of surface properties. Contact angle measurements were performed using water droplet on an OCAH 200 instrument (DataPhysic Instruments GmbH), equipped with a CCD camera and an automatic dosing system for the liquids. MilliQ™ H_2O (droplet volume 1.5 µL) was used for the analysis by means of the sessile droplet method in

static mode. Drop profiles were fitted through the Ellipse (high CA) and Tangent Leaning (low CA) method and contact angles between fitted function and baseline were calculated by the SCA20 software.

The filling of the different rGO-based slurries occurred by capillarity. The low viscosity formulation was carefully released on each electrode pads (5 µl per electrode).

The solvent was removed overnight in a cleanroom. This slow evaporation of water allows a minimization of the mechanical stress, which can induce adhesion problems, in comparison with evaporation process using heating and/or vacuum. Some bridges of active materials can be observed between micro-channels. They must be removed to avoid short circuits during electrochemical measurements. An Oxygen plasma procedure permits to remove these bridges. The apparatus used was STS 320PC Reactive Ion Etching system for 360 seconds, at a power of 100 W, a pressure of 50 mTorr and an oxygen flow rate of 50 sccm.

The deposition of current collectors is required on the filled PDMS-based MSC. These pads were based on ball-milled natural graphite mixed with PVDF in DMSO. The weight ratio was 1:10 to ensure the good adhesion and good electric contact between the interdigitated structures and the metal probes of the micro-manipulators used for the electrochemical characterization. The electrolyte was confined onto the PDMS-based MSC using a patch of cleanroom paper with tailored dimension (See Figure 6.1.f).

6.2.5. Electrochemical characterization

Cyclic voltammetry, Galvanostatic charge/discharge, and AC impedance spectroscopy measurements were performed on a Metrohm Autolab potentiostat / galvanostat M101. The potential window used was -0.5 V to 0.5 V and the scan rates tested were: 5, 10, 50 and 100 mV s^{-1}. Charge/discharge were performed using current densities between 1.6 µA cm^{-2} and 15.6 µA cm^{-2} in a potential window of 0.4 V. The use of two

needles supported on micromanipulators allows a good ohmic contact between device current collectors and instrument. The cycling stability was evaluated over 20.000 cycles at 5 mV s^{-1}. AC impedance was performed at OCP between 50 Hz and 5 mHz with an amplitude of 10 mV. All the experiments were performed in a two-electrode configuration after the soaking of electrodes in 1M NaCl.

6.3. Results and discussion

6.3.1. Evaluation of the slurry's supercapacitive performance in planar configuration

Different slurries were prepared and are listed in the Section 5.2.5. Their supercapacitive performances were evaluated preliminarily in planar configuration. Only the best slurry was then used for the micro-supercapacitor configuration.

Cyclic Voltammetry measurements were performed at different scan rates. The curves are reported in Figure 6.2. The specific capacitance calculated according to best practice method established by Ruoff and Stoller are reported in Table 6.1.[24]

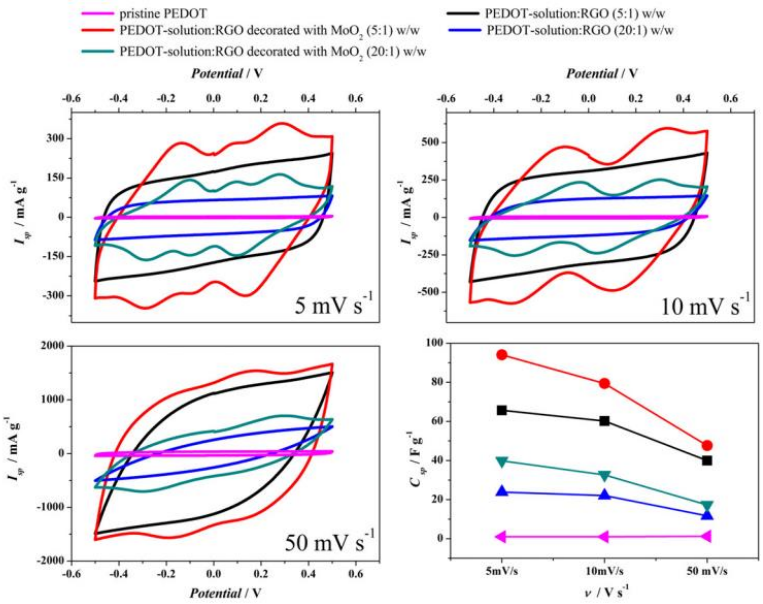

Figure 6. 2. Cyclic voltammetry in a planar configuration measured at different scan rates for all the prepared slurries and the evolution of the specific capacitance with the scan rates.

Electrodes*	C_{sp} (F g^{-1})	E_{sp} (J g^{-1})	E_{sp} (Wh Kg^{-1})
composition (1)	65.70	32.91	9.14
composition (2)	94.06	47.12	13.09
composition (3)	23.86	11.95	3.32
composition (4)	39.87	19.97	5.55
pristine PEDOT	0.96	0.48	0.13

* composition (1): 20% rGO (dispersed in a solution containing 15%wt of PEDOT)

composition (2): 20% rGO decorated with MoO_2 (dispersed in a solution containing 15%wt of PEDOT)

composition (3): 5% rGO (dispersed in a solution containing 15%wt of PEDOT)

composition (4): 5% rGO decorated with MoO_2 (dispersed in a solution containing 15%wt of PEDOT)

Table 6. 1. Specific Capacitance and energy estimated at 5 mV s^{-1} for each composite material

The use of a conductive polymer as binder does not contribute to the total measured capacitance as shown with the reference curve (pink). As expected, significant differences are observable for the different slurries. Measured values shown in Table 6.1 display an increase of almost 50% of the specific capacitance when the MoO_2 is present in the 3D-porous framework. Moreover, it is possible to triple the specific capacitance by increasing the rGO content by a factor 4.

The hybrid supercapacitor containing rGO flakes decorated with spherical micrometric particles of MoO_2 displays the best performance. The concomitance of an electric double layer capacitance and a Faradaic active material given by rGO and MoO_2, respectively, results in a significant increase of the deliverable performance. The pseudocapacitance of the MoO_2 is clearly observable looking at the CV curves shape. Indeed, a deviation of the box-like curves, typical of EDLC, can be observed with the presence of anodic and cathodic

peaks.[25] The observed phenomenon seems to be similar to the one observed previously in a two symmetrical electrodes configurations for other materials such as Ag/Ag^+.[26,27]

6.3.2. Investigation of the PDMS-based Micro-Supercapacitor morphology and filling procedure

To confirm the suitable fabrication procedure, PDMS prototypes were investigated by optical microscopy. The image of the PDMS-based MSC is reported in Figure 6.3. A final aspect ratio of 2:1 is obtained. The accessible surface for the slurry deposition is 0.32 cm^2.

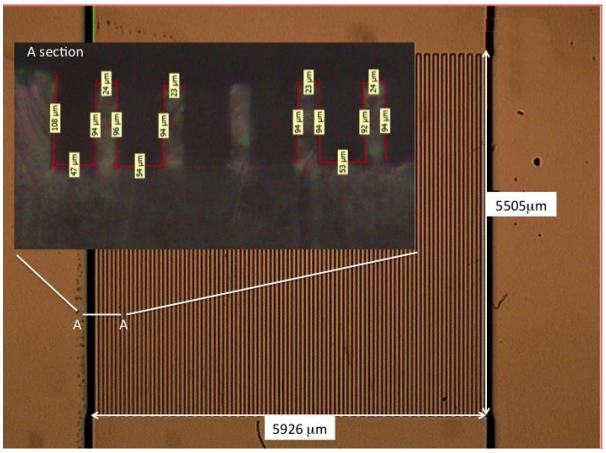

Figure 6. 3. PDMS prototype. In the inset, a cross-section is shown with the actual dimensions of microchannels and separators.

The deposition of the rGO-MoO_2 hybrid aerogel mixed with the PEDOT-solution occurs by capillarity. As described previously, a plasma oxygen treatment was performed to enhance the hydrophilicity of the PDMS-based MSC. The contact angle demonstrates the change of surface behaviour as shown in Figure 6.4. Images of the filling procedure are reported in Figure 6.5.

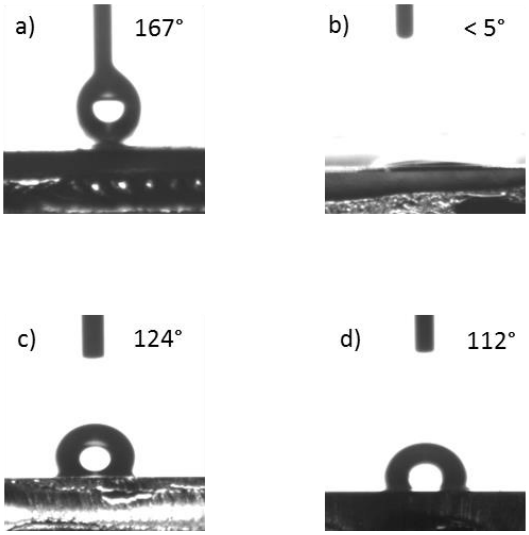

Figure 6. 4. H_2O Contact angle measured on the surface of PDMS microchannels a) before and b) after O_2 plasma treatment; H_2O contact angle measured as reference on a flat PDMS surface c) before and d) after O_2 plasma treatment

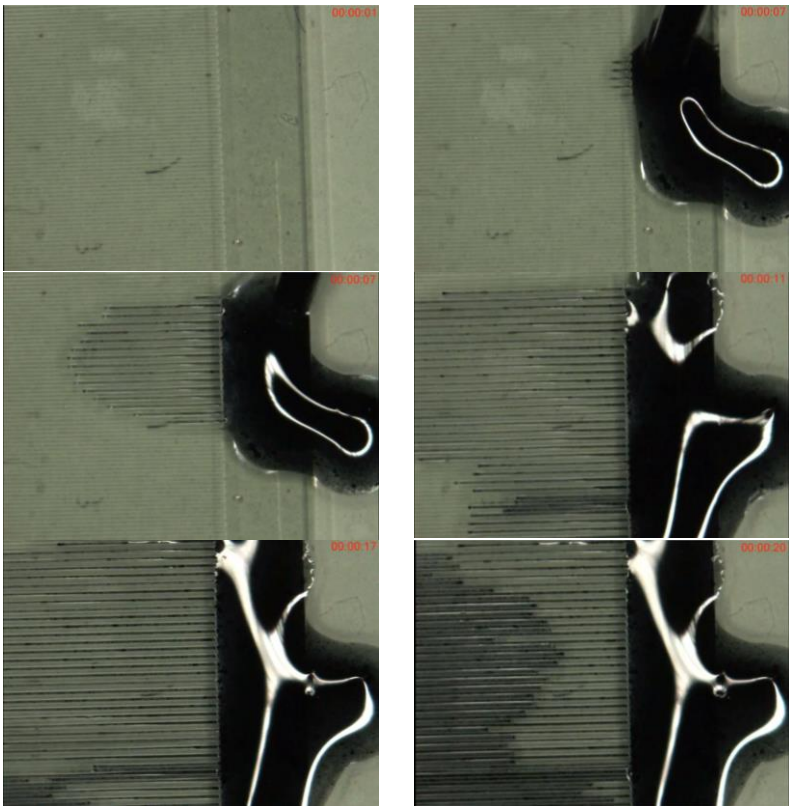

Figure 6. 5. filling of PDMS-based MSC by capillarity

After the deposition of the active material and the drying overnight in a clean room to avoid mechanical stress, current collectors were fabricated using a graphite-PVDF paste. The location of both droplets used for the deposition by capillarity and the pads for the current collectors are the same. The graphite-based paste permits to have a good electrical contact between the interdigitated electrodes and the needles of the micromanipulators used for the electrochemical measurements.

6.3.3. *Morphological and chemical investigations of the Micro-Supercapacitors filled with rGO-MoO_2*

The suitability of the filling procedure by capillarity was investigated by FESEM. A cross-sectional image of the filled MSC is shown in Figure 6.6. An uncompleted filling is clearly observable and can be ascribable to a shrinkage of the composite during the drying process. The amount of slurry deposited is nevertheless suitable for use in supercapacitor applications.

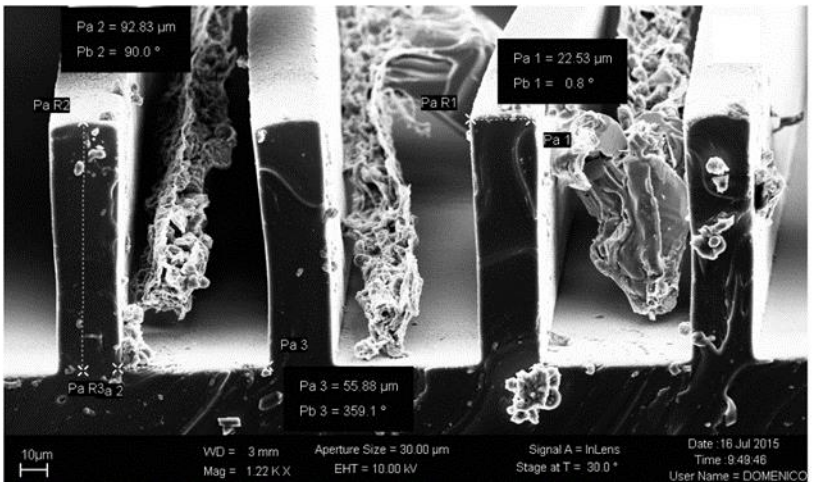

Figure 6. 6. Cross-sectional image by FESEM of the filled MSC

The dried slurry can be described as a composite formed by PEDOT-shell wrapped around the rGO-MoO_2 particles. Figure 6.7 shows a MoO_2-cluster with a large surface exposed to the electrolyte. This aspect is fundamental for faradaic reactions

allowing the enhancement of the supercapacitive performance.

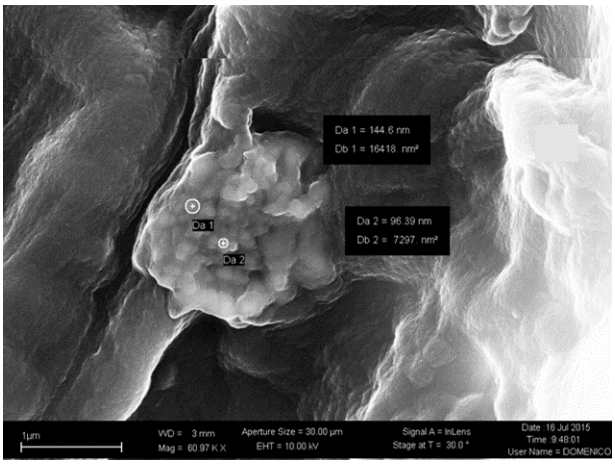

Figure 6. 7. FESEM image of a MoO_2-cluster wrapped in a PEDOT-shell. The exposed surface is large allowing good interaction with the electrolyte.

Interestingly, the PEDOT tends to form a spring-like rod configuration after the drying procedure at room temperature as shown in Figure 6.8. This spatial configuration allows high surface exposition to electrolyte which is a crucial factor in supercapacitor applications.

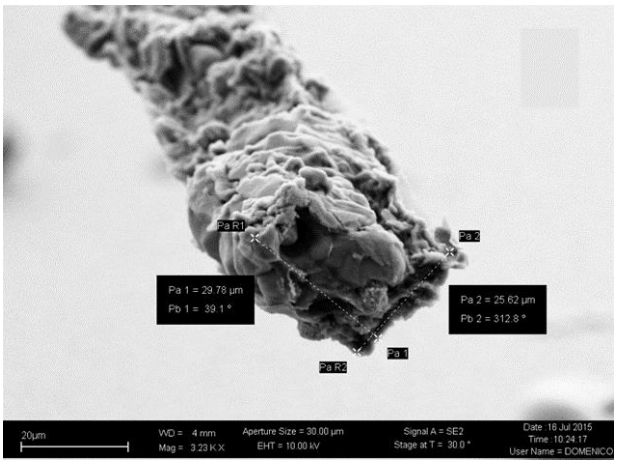

Figure 6. 8. High magnification FESEM image of the dried PEDOT forming spring-like rod structures.

A further confirmation of the suitability of the filling by capillarity was demonstrated by Raman analysis. A top-view of the filled micro-supercapacitor is shown in Figure 6.9.a. Raman analyses were performed on the sample in three

different regions marked with 1, 2, and 3 to demonstrate the presence of rGO-MoO_2 inside the channel.

The spectrum collected in region 2 shows the characteristic features of rGO-MoO_2 confirming the suitable deposition by capillarity in micro-supercapacitors. The MoO_2 features are superimposed to weak peaks typical of PDMS: 711 cm^{-1} (Si-C symmetric stretching), 1409 cm^{-1} (CH_3 asymmetric bending), 2895 cm^{-1} (CH_3 symmetric stretching), and 2954 cm^{-1} (CH_3 asymmetric stretching).[28]

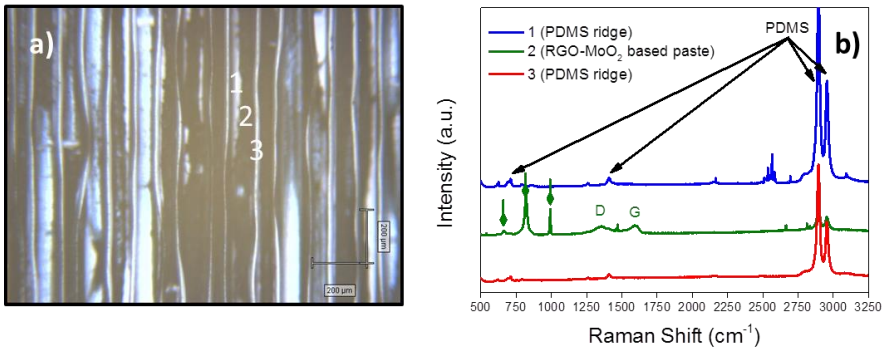

Figure 6. 9. (a) optical microscope image of PDMS interdigitated structure (5X objective), filled by rGO-MoO_2 based slurry; (b) Raman spectra collected in 1, 2, 3 regions of figure (a), corresponding to PDMS separators (1,3) and rGO-MoO_2-based slurry filled microchannel (2)

6.3.4. Electrochemical measurements of the MSC filled with the rGO-MoO_2 aerogel.

Cyclic voltammetry measurements were performed on MSC filled with the rGO-MoO_2 aerogel. Curves are reported in Figure 6.10. The inset shows the rate capability of the materials. Areal specific capacitance (Footprint area) is reported in the inset.

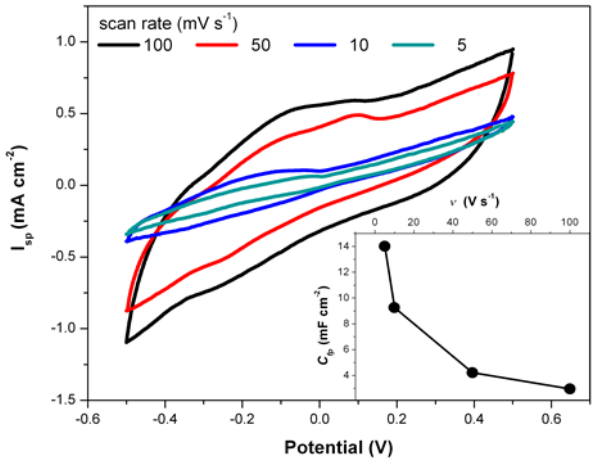

Figure 6. 10. Cyclic voltammetry at different scan rates for MSC filled with rGO-MoO_2 aerogel. In the inset, the rate capability expressed in areal capacitance versus the scan rate

The maximum areal specific capacitance was obtained a scan rate of 5 mV s^{-1} with a value of 14 mF cm^{-2}, which corresponds to a specific energy of 7 J cm^{-2}. All the calculated values are reported in Table 6.2.

Scan rate (mV s^{-1})	C_{fp} (mF cm^{-2})	E_{fp} (mJ cm^{-2})	E_{fp} (mWh cm^{-2})
100	2.9	1.5	0.4
50	4.2	2.1	0.6
10	9.2	4.6	1.3
5	14.0	7.0	1.9

Table 6. 2. Areal specific capacitance and specific energy calculated using cyclic voltammetry at different scan rates

The FESEM analysis reported in the previous section underlines a partial filling of the microchannels. The filling ratio of the slurry in the maximum accessible volume is estimated around 30%. This partial filling restricts the device's deliverable performance. Notwithstanding this limitation, the performance measured is in agreement with values reported in literature.[1,2] It is necessary to notice that a comparison between different works is tricky as supported by recent published review.[2] Indeed, the Ragone plot

typically used for electrochemical devices has sense only for the material. In this case, areal capacitance value is more significant for the comparison of the deliverable performance from devices.

Galvanostatic charge/discharge experiments were performed at different current densities. Curves are reported in Figure 6.11. Areal specific capacitance values are inserted on the same figure. A large IR drop can be observed. It might be due to an inefficient ohmic junction between the current collector and the needle from micromanipulators.

Cycling stability is a key characteristic for supercapacitors and, even more importantly, for micro-supercapacitors. The stability of the PDMS-based MSC was tested up to 20.000 cycles. The Figure 6.12 shows the capacity retention in function of the cycles number with in inset the CV curves for the 1st, 10.000th and 30.000th cycles.

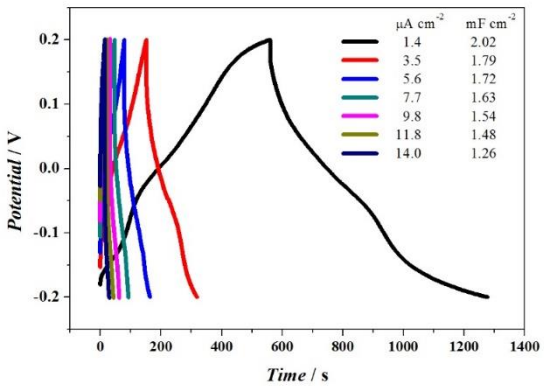

Figure 6. 11. Galvanostatic charge/discharge measurements and the calculated values of areal specific capacitance in function of the current density.

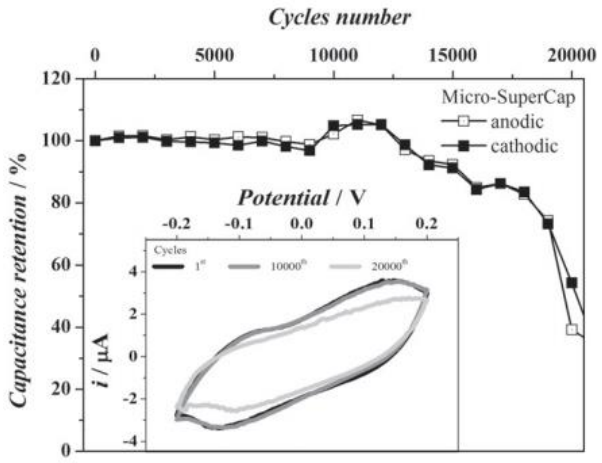

Figure 6. 12. Cyclic stability investigation measured at 2 V s^{-1} up to 20.000 cycles. In the inset, CV curves measured at 5 mV s^{-1} every 10.000 cycles.

The device demonstrates a perfect stability up 12.000 with even a slight increase of the capacity probably due to a better penetration of the liquid electrolyte within the PDMS channels and, consequently, a larger interface between the electrolyte and the active material. Then, two significant failures can be observed after 18.000 cycles and 20.000 cycles, respectively. Many factors can explain these failures such as electrolyte evaporation and salts deposition upon the electrodes. Improvement can be envisaged with the use of a cover or a packaging to avoid salt evaporation.

Electrochemical Impedance Spectroscopy (EIS) was also carried on the device. The resulting Nyquist plot is shown in Figure 6.13 with the equivalent circuit in the inset. The uncompensated resistance R_u was measured by *i*-interruption and the result is consistent with the EIS measurement with 14kΩ and 17.1kΩ, respectively. The capacitive behaviour of the material was confirmed by the shape of the Nyquist plot with a depressed semi-circle at high frequencies and a steep increase of the imaginary impedance at low frequencies. The constant phase element in series CPE2 gives rise to the capacitance and its phase angle is 82.8° (n = 0.92).

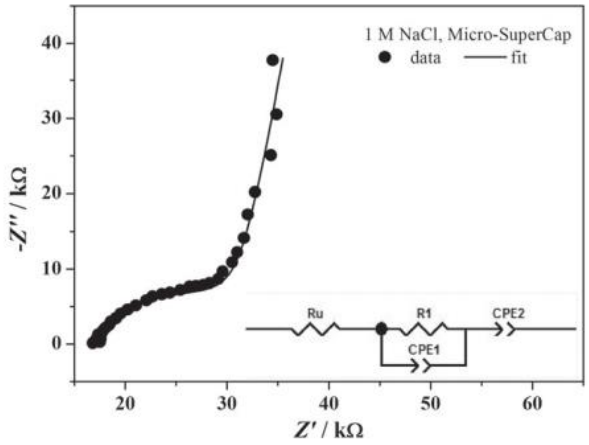

Figure 6. 13. Nyquist plot and its corresponding equivalent circuit of the PDMS-based micro-supercapacitors recorded at OCP between 50 Hz and 5 mHz with an amplitude of 10 mV. Parameters of the equivalent circuit are the following: R_u = 17.1 kΩ; R_1 = 14.0 kΩ; CPE1 Y_0 = 63.4 µMho and n = 0.793; CPE2 Y_0 = 641 µMho and n = 0.92.

It is possible to extrapolate the areal specific power using the following formula:

$$P_{sp} = \frac{\Delta V^2}{A_{fp}.4R_{eq}} \qquad (6.1)$$

where R_{eq} is the equivalent series resistance that was experimentally estimated by charge-discharge cycles to a value of 1.3 kΩ.

The areal specific power was around 1 mW cm^{-2} which is consistent with the values reported in literature.[1,2] However, obtained values are significantly lower than the calculated values from measurements in planar configuration. Indeed, deliverable performance for MSC is about four times lower. As observed previously with FESEM image (Figure 6.6), the microchannels are filled only partially with around 30% of filling. So, if the filling was completely efficient (100% filled), obtained values would be extremely consistent with the ones measured from the planar configuration.

PDMS is flexible which is an important characteristic for micro-supercapacitor applications. Bending tests were performed to investigate the flexibility of the PDMS-based

micro-supercapacitors. Cyclic voltammetry curves are reported in Figure 6.14. As shown in the inset (top), two different configurations were tested: concave and convex. The second inset shows a performance comparison between the different configurations. Obtained values of areal specific capacitance are significantly different according to the configuration. Indeed, the concave configuration provokes a decrease of 40% of the deliverable performance in comparison with the flat configuration. The convex configuration, instead, induces an increment of about 25% in respect to the initial configuration. These significant differences are mainly ascribable to the wettability of the electrodes by the electrolyte. Indeed, the spring-like rods configuration, described previously (Figure 6.8), has a larger interface with the electrolyte in the convex configuration because the interdigitated microchannels tend to get wider and the electrolyte can wet more efficiently the active materials. In an opposite way, the concave configuration induces a stretching of the interdigitated microchannels decreasing the accessibility for the electrolyte and, consequently, the deliverable performance.

6.4. Conclusion

In this chapter, an innovative PDMS-based micro-supercapacitor was fabricated through a photolithographic process. The rGO-MoO_2 hybrid material was *in-situ* synthesized using an easy one-pot hydrothermal procedure starting from Graphene Oxide and phosphomolybdic acid as Mo precursor. The active material displays both EDL (from

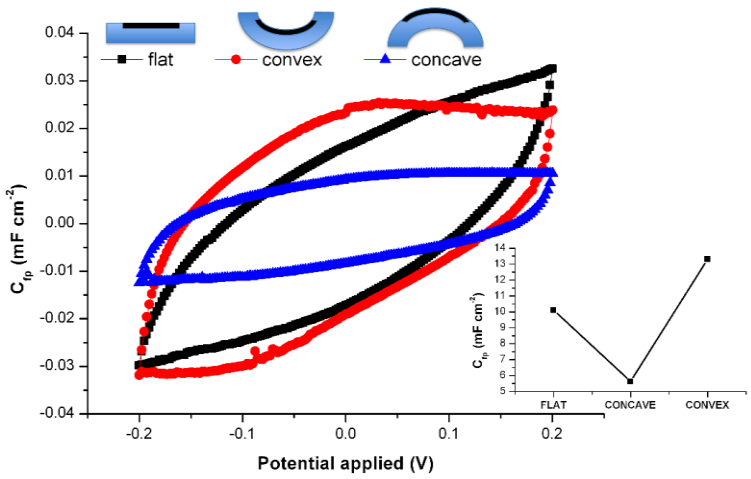

Figure 6. 14. Study of the flexibility of the MSC in three configurations. Cyclic voltammetry curves for all the configurations. In the top inset, a schematic representation of the spatial configuration. The bottom inset shows the areal specific capacitance in function of the configuration.

rGO) and pseudocapacitive (from MoO_2) behaviours. This hybrid was dispersed in a PEDOT [poly(3,4-ethylenedioxythiophene] solution used as conductive binder.

The filling of micro-supercapacitors was performed by capillarity. Only a partial filling was possible which limits the deliverable performance. However, the stability of the material is high even without a packaging reducing the electrolyte evaporation.

More interestingly, the composite formed by rGO flakes decorated by MoO_2 micrometric structures wrapped by PEDOT polymer demonstrates a good flexibility.

Finally, electrochemical performances measured for the uncompleted filled PDMS-based micro-supercapacitor are consistent with the most relevant papers in literature.

Further improvements can be envisaged such as: improving the filling percentage, reducing electrolyte evaporation, increasing the flexibility. Nevertheless, results showed in this chapter are encouraging for micro-supercapacitor applications.

REFERENCES

(1) Miller, J. R.; Simon, P. Electrochemical Capacitors for Energy Management. *Science.* **2008**, *321*, 651–652.

(2) Beidaghi, M.; Gogotsi, Y. Capacitive Energy Storage in Micro-Scale Devices: Recent Advances in Design and Fabrication of Micro-Supercapacitors. *Energy Environ. Sci.* **2014**, *7* (3), 867.

(3) Xiong, G.; Meng, C.; Reifenberger, R. G.; Irazoqui, P. P.; Fisher, T. S. A Review of Graphene-Based Electrochemical Microsupercapacitors. *Electroanalysis* **2014**, *26*, 30–51.

(4) El-Kady, M. F.; Kaner, R. B. Scalable Fabrication of High-Power Graphene Micro-Supercapacitors for Flexible and on-Chip Energy Storage. *Nat. Commun.* **2013**, *4*, 1475.

(5) Li, S.; Wang, X.; Xing, H.; Shen, C. Micro Supercapacitors Based on a 3D Structure with Symmetric Graphene or Activated Carbon Electrodes. *J. Micromechanics Microengineering* **2013**, *23*, 114013.

(6) Wu, Z.-S.; Parvez, K.; Feng, X.; Müllen, K. Graphene-Based in-Plane Micro-Supercapacitors with High Power and Energy Densities. *Nat. Commun.* **2013**, *4*, 2487.

(7) Hsia, B.; Marschewski, J.; Wang, S.; In, J. Bin; Carraro, C.; Poulikakos, D.; Grigoropoulos, C. P.; Maboudian, R. Highly Flexible, All Solid-State Micro-Supercapacitors from Vertically Aligned Carbon Nanotubes. *Nanotechnology* **2014**, *25* (5), 55401.

(8) Krishnamoorthy, K.; Kim, S. J. Mechanochemical Preparation of Graphene Nanosheets and Their Supercapacitor Applications. *J. Ind. Eng. Chem.* **2015**, *32*, 39–43.

(9) Krishnamoorthy, K.; Thangavel, S.; Chelora Veetil, J.; Raju, N.; Venugopal, G.; Kim, S. J. Graphdiyne Nanostructures as a New Electrode Material for Electrochemical Supercapacitors. *Int. J. Hydrogen Energy* **2016**, *41*, 1672–1678.

(10) Shen, C.; Wang, X.; Li, S.; Zhang, W.; Kang, F. A High-Energy-Density Micro Supercapacitor of Asymmetric MnO_2-Carbon Configuration by Using Micro-Fabrication Technologies. *J. Power Sources* **2013**, *234*, 302–309.

(11) Pech, D.; Brunet, M.; Mai, T.; Armstrong, K.; Gaudet, J.; Guay, D. In Fl Uence of the Con Fi Guration in Planar Interdigitated Electrochemical. **2013**, *230*, 230–235.

(12) Kurra, N.; Jiang, Q.; Alshareef, H. N. A General Strategy for the Fabrication of High Performance Microsupercapacitors. *Nano Energy* **2015**, *16*, 1–9.

(13) Aradilla, D.; Bidan, G.; Gentile, P.; Weathers, P.; Thissandier, F.; Ruiz, V.; Gomez-Romero, P.; Schubert, T. J. S.; Sahin, H.; Sadki, S. Novel Hybrid Micro-Supercapacitor Based on Conducting Polymer Coated Silicon Nanowires for Electrochemical Energy Storage. *RSC Adv.* **2014**, *4* (50), 26462–26467.

(14) Kurra, N.; Hota, M. K.; Alshareef, H. N. Conducting Polymer Micro-Supercapacitors for Flexible Energy Storage and Ac Line-Filtering. *Nano Energy* **2015**, *13*, 500–508.

(15) Ehrfeld, W.; Hessel, V.; Schulz, C.; Weber, L. Materials of LIGA Technology. *Microsyst. Technol.* **1999**, *5* (3), 105–112.

(16) Lötters, J. C.; Olthuis, W.; Veltink, P. H.; Bergveld, P. The Mechanical Properties of the Rubber Elastic Polymer Polydimethylsiloxane for Sensor Applications. *J. Micromechanics Microengineering* **1999**, *7* (3), 145–147.

(17) Pech, D.; Brunet, M.; Durou, H.; Huang, P.; Mochalin, V.; Gogotsi, Y.; Taberna, P.-L.; Simon, P. Ultrahigh-Power Micrometre-Sized Supercapacitors Based on Onion-like Carbon. *Nat. Nanotechnol.* **2010**, *5* (August), 651–654.

(18) Pech, D.; Brunet, M.; Taberna, P. L.; Simon, P.; Fabre, N.; Mesnilgrente, F.; Conédéra, V.; Durou, H. Elaboration of a Microstructured Inkjet-Printed Carbon Electrochemical Capacitor. *J. Power Sources* **2010**, *195* (4), 1266–1269.

(19) Giardi, R.; Porro, S.; Topuria, T.; Thompson, L.; Pirri, C. F.; Kim, H. C. One-Pot Synthesis of Graphene-Molybdenum Oxide Hybrids and Their Application to Supercapacitor Electrodes. *Appl. Mater. Today* **2015**, *1* (1), 27–32.

(20) Hu, X.; Zhang, W.; Liu, X.; Mei, Y.; Huang, Y. Nanostructured Mo-Based Electrode Materials for Electrochemical Energy Storage. *Chem. Soc. Rev.* **2015**, *44* (8), 2376–2404.

(21) Kim, H.-S. H.; Cook, J. B.; Tolbert, S. H.; Dunn, B. The Development of Pseudocapacitive Properties in Nanosized-MoO_2. *J. Electrochem. Soc.* **2015**, *162* (5), A5083–A5090.

(22) Zhao, X.; Chu, B. T. T.; Ballesteros, B.; Wang, W.; Johnston, C.; Sykes, J. M.; Grant, P. S.; S. Spray Deposition of Steam Treated and Functionalized Single-Walled and Multi-Walled Carbon Nanotube Films for Supercapacitors. *Nanotechnology* **2009**, *20* (6), 65605.

(23) Chen, K.; Ayón, A. A.; Member, S.; Zhang, X.; Spearing, S. M. Effect of Process Parameters on the Surface Morphology and Mechanical Performance of Silicon Structures After Deep Reactive Ion Etching (DRIE). **2002**, *11* (3), 264–275.

(24) Stoller, M. D.; Ruoff, R. S. Best Practice Methods for Determining an Electrode Material's Performance for Ultracapacitors. *Energy Environ. Sci.* **2010**, *3* (9), 1294–1301.

(25) Rajeswari, J.; Kishore, P. S.; Viswanathan, B.; Varadarajan, T. K. One-Dimensional MoO_2 Nanorods for Supercapacitor Applications. *Electrochem. commun.* **2009**, *11* (3), 572–575.

(26) Li, X.; Shao, J.; Li, J.; Zhang, L.; Qu, Q.; Zheng, H. Ordered Mesoporous MoO_2 as a High-Performance Anode Material for Aqueous Supercapacitors. *J. Power Sources* **2013**, *237*, 80–83.

(27) Mendoza-Sanchez, B.; Brousse, T.; Ramirez-Castro, C.; Nicolosi, V.; S. Grant, P. An Investigation of Nanostructured Thin Film Alfa-MoO_3 Based Supercapacitor Electrodes in an Aqueous Electrolyte. *Electrochim. Acta* **2013**, *91*, 253–260.

(28) Stankova, N. E.; Atanasov, P. A.; Nedyalkov, N. N.; Stoyanchov, T. R.; Kolev, K. N.; Valova, E. I.; Georgieva, J. S.; Armyanov, S. A.; Amoruso, S.; Wang, X.; Bruzzese, R.; Grochowska, K.; Sliwinski, G.; Baert, K.; Hubin, A.; Delplancke, M. P.; Dille, J. Fs- and Ns-Laser Processing of Polydimethylsiloxane (PDMS) Elastomer: Comparative Study. In *Applied Surface Science*; 2015; Vol. 336, pp 321–328.

Chapter 7

Graphene-based Supercapacitors for Wearable Applications

Among the devices used as supercapacitors, the ones based on a standard planar configuration can be limited for some recently proposed applications such as wearable electronics.[1] In the past decade, wearable technologies, also called “e-textiles” or “smart textiles”, have attracted much attention. Indeed, these technologies could be used almost continuously because, during all our lives, everyone is in contact with textiles for up to 90% of the time. Consequently, the market is predicted to reach $5bn in product revenue at the end of the next decade.[2] However, the integration of energy storage devices into textiles remains the main issue.[3]

In the last 5 years, flexible and fabrics-integrated supercapacitors have emerged as valuable alternative to standard bulky batteries.[4,5] The first works used the traditional planar configuration of supercapacitors substituting the traditional foil current collectors by metal grids or conductive fabrics.[6–8] The manufacturing of viable devices for wearable applications is nevertheless still problematic. To overcome this issue, considerable efforts are devoted to build wire-shaped/fibre-shaped electrodes[9–12] to achieve fully-integrated wearables supercapacitors.[8]

This chapter is divided in two parts that focused on the fibre-shaped supercapacitors and the scalable production of e-textiles by mimicking an industrial process, respectively.

Part A: Wired-shaped Supercapacitors

Recently, wearable technologies have attracted much attention. An in-situ hydrothermal synthesis of reduced graphene oxide aerogels onto a copper wire is investigated. The as-synthesized sample shows a peculiar morphology of the aerogel wadded around the current collector. The fabricated device demonstrates outstanding electrochemical properties in comparison with state-of-the-art works. Moreover, flexibility tests are performed, and results are promising to move forward wearable applications.

Part of the work described in this chapter has been previously published in Carbon, 2016 (105), 649-654.

7.1. Motivations

Wire-shaped supercapacitors have attracted much attention in the last couple of years due to their flexibility and integrability to textile fabrics. They can be divided in two categories according to their configuration (Figure 7.1): coaxial fibre-like[9] supercapacitors and two-ply fibre-like supercapacitors.[11,13] Both use gel electrolyte to act both as ion conductor and separator to avoid physical contact between the electrodes.

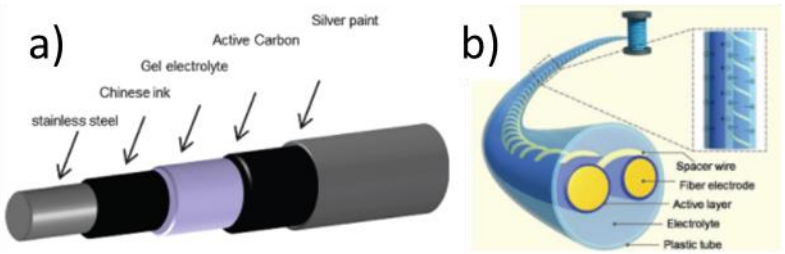

Figure 7. 1. Schematic representation of (a) coaxial fibre-like[9] and (b) two-ply fibre-like supercapacitors[13]

Several carbon-based materials were investigated to increase the energy density without deteriorate the power density of the devices. Indeed, carbon-based materials such as carbon black, glassy carbon, and carbon nanotubes display high specific surface area, stability over wide electrochemical window alongside their earth abundance and low production cost.[9,12,14,15] These materials were nevertheless progressively abandoned for graphene or graphene-like materials. Indeed, graphene has high electrical conductivity, high flexibility and outstanding chemical and mechanical properties.[16–18]

Graphene is also really attractive thanks to its strong C-C bond which allows to be flexible and mechanically robust enough to allow integration into textile.[19] Graphene has been already studied for wire-shaped supercapacitor applications. However, production procedures used up to now are very complex, such as: a graphene core fibre coated using electrochemical deposition of graphene layer or using graphene cylindrical electrodes deposited on Cu mesh around a fibre decorated by radially grown ZnO nanowires.[13,20,21]

Nowadays, 3D-graphene-based structure with porous framework is preferred in supercapacitor application to monolayer graphene due to its higher specific surface area. Moreover, the synthesis procedure is easier, clean and sustainable, and, more importantly, a scalability can be envisaged in the next future. Notwithstanding the outstanding properties of the material, the deposition of the porous structure around the wire to obtain a suitable interface remains a key challenge.

To face this challenge, a concomitant *in-situ* reduction of graphene oxide[22] with a self-assembly procedure of rGO flakes around a copper wire was here reported. The resulting electrodes can be assembled in a two-wire configuration achieving high performance flexible supercapacitors. The resulting deposition of active materials on current collector

during the hydrothermal synthesis permits to avoid the use of binder, resulting in better electrochemical performance.

7.2. Experimental Section

7.2.1. Graphene aerogel synthesis

A 200 µm-diameter copper wire was used as support for the aerogel synthesis. The wire was cleaned in acidic solution for 2 minutes, 1M HCl, to remove the native oxide layer on surface. The cleaned wire was then washed repeatedly in deionized water. The pure rGO aerogel synthesis was the same as used previously (see Chapter 4). Briefly, 2 mg/mL of Graphene Oxide powder (Cheap Tubes Inc.) were dispersed in 19 ml. After a 30 min of sonication, the homogeneous GO dispersion was transferred in the hydrothermal Teflon reactor. Synthesis occurs in a stainless-steel autoclave during 12 hours at a temperature of 180°C. Finally, the aerogel on Copper wire (rGO@Cu) was freeze-dried overnight.

7.2.2. Wire-shaped Supercapacitor assembly

For supercapacitor measurements, a gel electrolyte was used. The gel was prepared by heating the Polyvinylpyrrolidone (PVP, Sigma Aldrich) containing 1M NaI in water (Sigma Aldrich). The as-prepared rGO@Cu wires were dip-coated into the gel solution and aligned onto a glass slide after a partial gelification during 5 minutes at 80°C. Then, wires were carefully assembled in a two-electrode configuration. Finally, the gelification was completed with a heating at 80°C for 5 minutes.

7.2.3. Characterization

The morphology of rGO self-assembled aerogel on copper wire was investigated. The homogeneity of the rGO-based coating was carefully monitored as well as the assembled device by means of Field Emission Scanning Electron Microscopy (FESEM) with a Zeiss Supra 40 microscope.

Cross-sectional preparation of the samples by Focused Ion Beam (FIB) milling allows the investigation of the interface between the rGO aerogel and the Cu-wire. The milling occurred with a 30 kV acceleration voltage and 2 nA current of Ga^+ ions. A current of 600 pA for used for the cleaning. Both sample preparation and imaging process were performed on a Zeiss Auriga dual-beam FIB-FESEM workstation.

Raman spectroscopy at a wavelength of 514.5 nm (Ar-Kr laser source) was carried on with a Renishaw inVia Reflex micro-Raman spectrophotometer, equipped with a cooled CCD camera.

The surface chemical composition was investigated by means of X-ray Photoelectron Spectroscopy (XPS). The apparatus used was a PHI 5000 Versaprobe scanning X-ray photoelectron spectrometer (monochromatic Al K-alpha X-ray source with 1486.6 eV energy, 15 kV voltage and 1 mA anode current). The energy for survey spectra and HR peaks were 187.85 eV and 23.5 eV, respectively. The spot for the acquisition was 100 µm. All samples were analysed using a combined electron and argon ion gun neutralizer system to reduce the charging effect during the measurements. The analysis was carried out using the Multipak 9.6 software. The core-level peak energies were referenced to C1s peak at 284.5 eV (C-C/C-H sp^2 bonds) and the background contribution in HR scans has been subtracted by means of a Shirley function.[23] A 1-minute sputter cleaning was performed using the Ar^+ source with a 2 kV ions accelerating voltage (10 µA ion current).

BET (Brunauer-Emmett-Teller) Specific Surface Area was measured using a Quadrasorb SI (Quantachrome). The N_2 adsorption/desorption isotherms were performed between 0.1 and 0.3 of relative pressure (P/P_0). The pore size distribution was estimated using the Density Functional Theory (DFT) model.

Electrochemical measurements were performed in a two-electrode configuration. Cyclic Voltammetry measurements were performed with a Metrohm Autolab PGSTAT128 potentiostat/galvanostat. Galvanostatic charge/discharge measurements were obtained with an Arbin Instrument Testing System model BT-2000.

7.3. Results and Discussions

A schematic representation of the hydrothermal synthesis, starting from GO dispersion in water, and the supercapacitor assembling are reported in Figure 7.2.a and 7.2.b, respectively. Pristine GO sheets undergo a reduction during the hydrothermal synthesis. The rGO flakes tend to wind around the copper wire by a self-assembling process forming a uniform coating. The resulting rGO@Cu wire was then dip-coated into a PVP-based NaI electrolytic solution. Finally, two rGO@Cu wires were manually assembled to form a two-electrode symmetric configuration separated by the gel electrolyte.

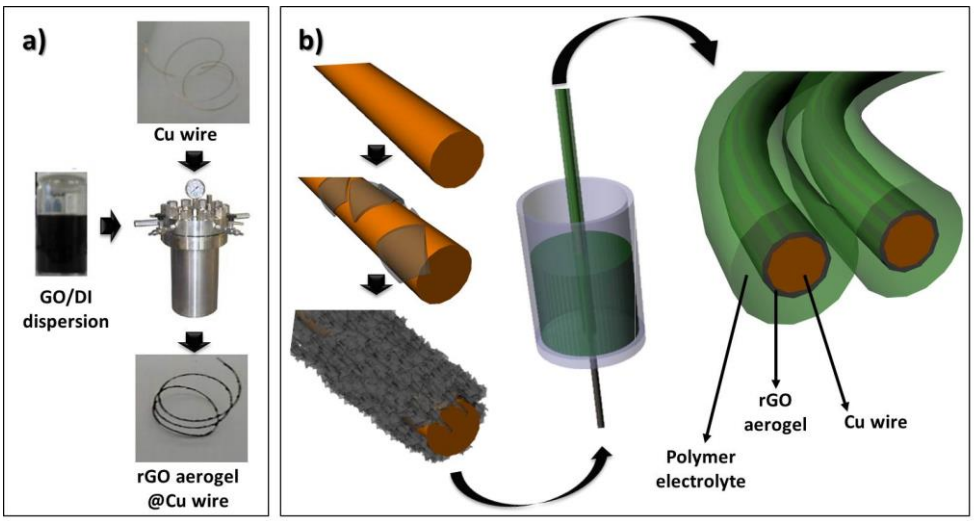

Figure 7. 2. Schematic representation of the (a) hydrothermal synthesis and the (b) self-assembling of rGO flakes around the copper wire followed by the supercapacitor assembling procedure.

7.3.1. Morphological investigation

The as-synthesized rGO@Cu wire was investigated by FESEM before and after the dip-coated step into the electrolytic solution. Low-magnification images are shown in Figure 7.3.a and 7.3.b. The self-assembling of rGO flakes results in a homogeneous coating of the Cu wire.

For sake of investigation, the same hydrothermal process was carried on Ti and Ni wires to study the effect of the support. FESEM images are shown in Figure 7.4 for both samples. The morphology for both samples are completely different. Indeed, the coating is not homogeneous and, more importantly, only partial.

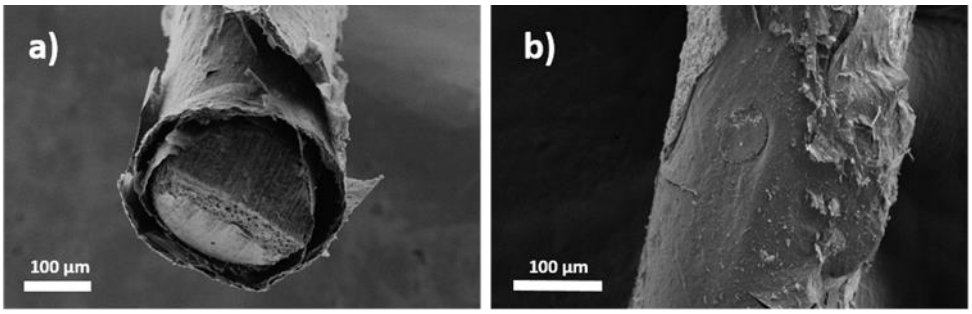

Figure 7. 3. Low magnification FESEM images of the rGO@Cu sample in (a) 45°-tilted and top (b) view.

The structuration of the rGO around the wire is more like a sponge. Moreover, the porous structure is significantly different than the rGO@Cu sample. These observations suggest a non-negligible effect of the metallic support on the self-assembling of rGO flakes. The copper seems to allow a good organization of the flakes around it in addition with its catalytic action during the hydrothermal process as discussed by Huang and co-workers.[24]

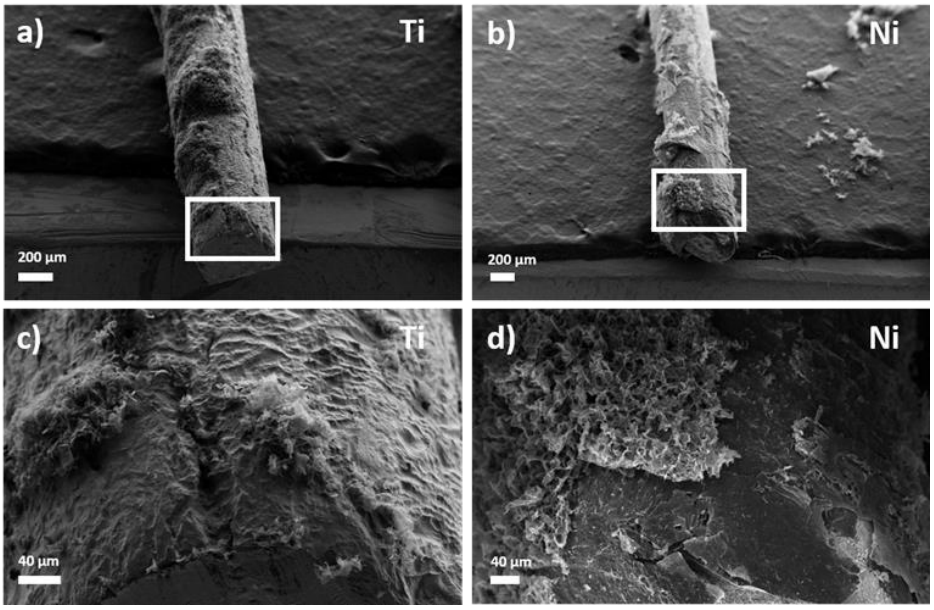

Figure 7. 4. 45°-tilt FESEM images of (a,c) Ti and (b,d) Ni wires after the hydrothermal process.

7.3.2. Cross-sectional study

The self-assembling of rGO flakes around the copper wire was investigated using cross-section images. As reported in Figure 7.5, the structural organization of rGO flakes creates an interconnected porous framework. A higher magnification is shown in the inset. This image displays a 3D-structure constituted by wrinkled and curled-up rGO flakes. The self-assembling mechanism occurs due to new interactions created during the hydrothermal synthesis as reported by Xu *et al*.[25] Indeed, the pristine GO is hydrophilic due to its the oxygen moieties implying a good dispersion in water. During the hydrothermal process, a reduction of the oxygen functionalities occurs in addition to the restoring of the π-π* interaction. These concomitant phenomena allow the self-assembling of rGO flakes in a 3D aerogel structure. This hydrothermal synthesis was used for the first time to grow such porous 3D structure wrapped around a copper wire. The mass loading was measured to be about 200 µg/cm of active material.

The interface between the Cu wire and the rGO-based porous structure is a critical aspect. For sake of understanding, several cross-sections were prepared by FIB milling.

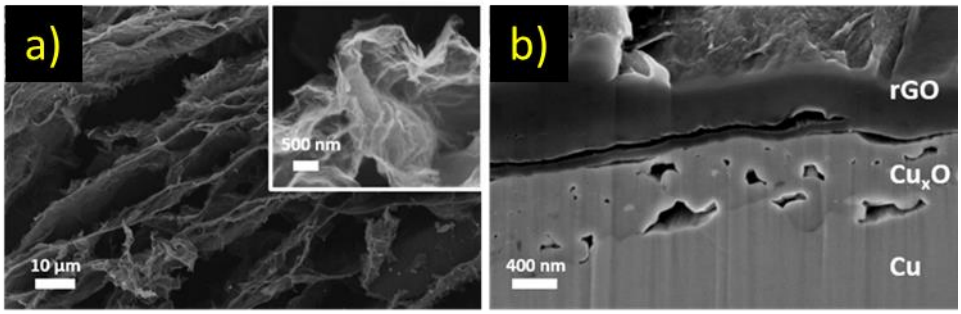

Figure 7. 5. Cross-section image of the interconnected 3D architecture of the rGO aerogel at (a) low and (inset) high magnification. (b) Cross-section image of a FIB-milled region.

The FIB-milled technique allows to obtain cross-section samples without applying mechanical stress. This aspect is critical because the presence of a mechanical stress could affect the adhesion between the active material (rGO-based aerogel) and the substrate (Cu wire). A FIB-milled region showing the interface is shown in Figure 7.5. The image demonstrates clearly the good adhesion of the rGO aerogel onto the copper wire. Interestingly, an oxidized layer of copper, with a thickness in the range of 400 – 700 nm, was formed during the hydrothermal synthesis. This layer may facilitate the adhesion of the rGO@Cu. The composition of the oxidized copper layer and the proof of GO reduction will be discussed in the XPS section.

7.3.3. Study of the chemical composition by XPS

XPS analyses were performed on the same segment used for the FESEM characterization. This sample is clearly the most interesting for the study of the chemical composition. Indeed, it contains the rGO aerogel, which allows to study the reduction process, and an exposed surface of Cu, where rGO has been peeled off, allowing the study of the oxidized layer. The high-resolution XPS spectra of the C1s region for both pristine GO and the rGO aerogel are shown in Figure

7.6.a and 7.6.b, respectively. During the hydrothermal synthesis, a reduction of the oxygen moieties should occur together with the establishment of the π-π* interaction. The comparison of the pristine GO and rGO spectra confirm the expected phenomena. Indeed, the contributions of the carbon-oxygen bonds were dramatically reduced after the hydrothermal synthesis. A semi-quantitative study of the HR C1s peak further confirms these observations. In fact, the (C-O + C=O %)/(C-C sp^2 %) ratio decreases significantly from (65.6/34.4)% to (34.1/59.1)% confirming a higher sp^2 contribution. This change in the chemical composition is important for supercapacitor applications because the conductivity of the carbon-based matrix is directly linked to the level of sp^2 contribution. The π–π* transition is an important feature because it is the fingerprint of extended delocalized electrons. This HOMO-LUMO transition is recognisable in the rGO spectrum while it is absent in the pristine GO one.[26] This transition is observable through its satellite peak that is located at ~6 eV from main C1s peak for aromatic compounds.[27]

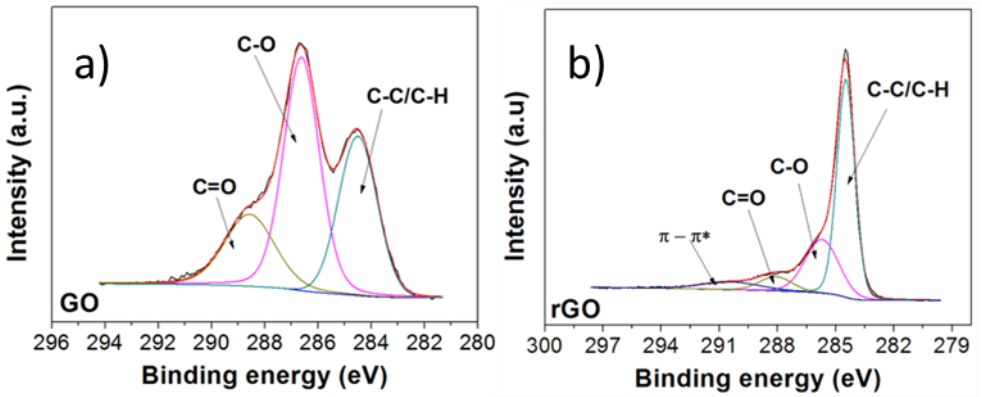

Figure 7. 6. XPS spectra of (a) GO powder and (b) rGO@Cu wire.

The hydrothermal reaction induces the formation of an oxidized Cu layer at the surface of the wire as showed previously with the FESEM analysis. The HR spectrum in the Cu2p peaks region is reported in Figure 7.7.a. The un-

sputtered sample displays a doublet for the Cu2p which is characteristic of the presence of Cu^{2+} species. The $Cu2p_{3/2}$ peak shows contribution of both Cu^{+} and Cu^{2+} with energy values of 932.5 eV and 934.2 eV, respectively. The same interpretation can be made for the $Cu2p_{1/2}$ peak, which is separated by 19.8 eV from the main peak. Nevertheless, the contribution of metallic copper is not observable because the oxide layer is thicker than 10nm that corresponds to the penetration depth of the XPS beam. This observation is in perfect agreement with the FESEM analysis.

For sake of investigation, a surface cleaning by Ar^{+} sputtering was performed for 1 minute. Interestingly, all the contributions of the Cu^{2+} were completely removed. Then, the $Cu2p_{3/2}$ contains only one peak ascribable to the Cu^{+}. To further confirm the previous allegations, XPS analysis was also performed in the Cu LMM Auger region. The spectra before and after the cleaning process are shown in Figure 7.7. The difference between the two spectra is more significant. Indeed, the as-prepared sample shows a characteristic satellite peak at higher binding energy before the main peak around 570 eV and a shoulder at lower binding energy. These three features are the fingerprint of the CuO. The sputtered sample displays only the main peak located at 570.6 eV, which corresponds to the Cu_2O.

To summarize, the surface of the copper wire is covered by a thick layer of Cu_2O and then a thin layer of CuO (<10 nm). This partial oxidation of the Cu wire can be ascribed to the hydrothermal reaction conditions and interfacial redox reactions between the GO sheets and the active Cu surface. Indeed, this chemical reaction was already reported for the *in-situ* formation of highly ordered films starting from GO using planar metallic substrates.[28,29]

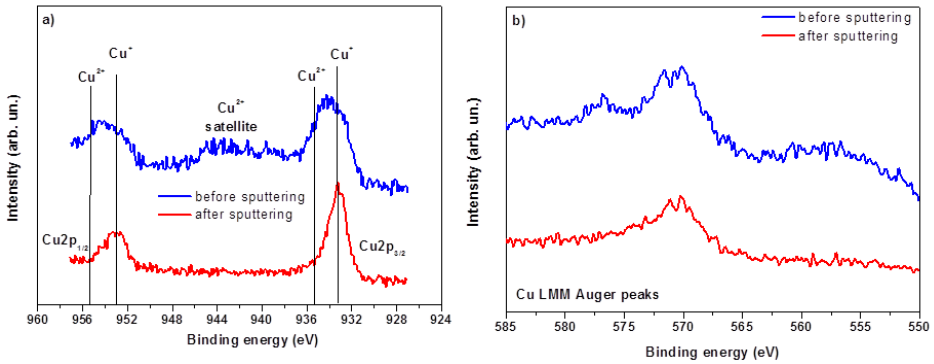

Figure 7. 7. XPS HR peaks of Cu2p (a) and Cu LMM Auger peaks (b) of hydrothermally reduced rGO@Cu sample before (blue line) and after Ar^+ ion sputtering (red line).

7.3.4. Chemical composition analysis by Raman

Raman spectroscopy was used to confirm the XPS results. Pristine GO and rGO@Cu spectra are reported in Figure 7.8. Spectra were centred in the characteristic region of carbonaceous material. Indeed, the first order D and G peaks are located at 1359 cm^{-1} and 1598 cm^{-1}, respectively. The 1D peak is ascribable to the defects in the in plane-sp^2 domains in graphene material. These defects, which can be distortion or vacancies, are induced from the oxidation treatment. The G peak is sharp for pure graphene material. However, it is broader for reduced Graphene oxide due to a first-order inelastic scattering process involving the degenerate iTO and iLO phonons at the G point (E_{2g} mode). The ratio $1_D/1_G$ is close for samples before and after hydrothermal synthesis. A significant decrease was expected after the hydrothermal synthesis due to a reduction of the oxygenated moieties. Nevertheless, the self-assembling of rGO flakes induces a wrinkle of the flakes causing the increase of the defects. The suitable reduction can be confirmed by the disappearance of the photoluminescence background after the hydrothermal synthesis. Indeed. This large band, present in the pristine GO spectrum, is devoted to band-gap emission from electron-confined sp^2 islands and to oxygen-related defect states.

These observations are in line with the XPS previously described.

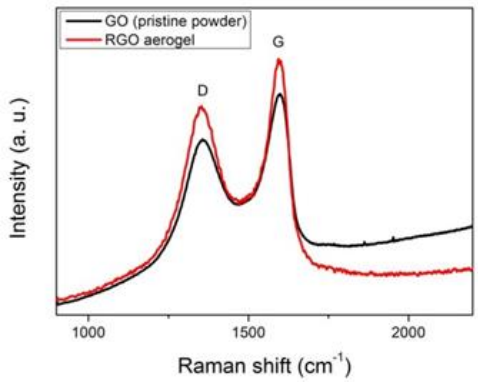

Figure 7. 8. Raman spectra of pristine GO (black curve) and rGO@Cu (red curve).

7.3.5. Specific Surface Area

The BET specific surface area was measured directly on the rGO@Cu wire sample to avoid possible misleading results. Indeed, the rGO coating on top of the covered wire has a particular 3D porous framework. This configuration could be deteriorated during the peeled off step necessary for removing the material from the substrate. The N_2-adsorption/desorption isotherms are shown in Figure 7.9 with the pore size distribution plot calculated with the DFT model in the inset. The BET specific surface area was measured to 185 $m^2 g^{-1}$, which is significantly lower than the pure rGO (460 $m^2 g^{-1}$). This decrease is ascribable to the presence of the copper wire and, as observed from FESEM images, the more packed structure of the rGO aerogel. The average pore diameter is in the meso/macroporous region with a monomodal pore size distribution centred between 1 and 5 nm. This distribution of porosity is beneficial for supercapacitor applications. Indeed, mesopores provide more active sites for interactions between electrode and electrolyte.

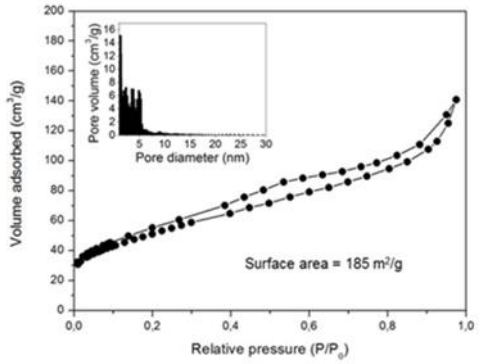

Figure 7. 9. N_2-adsorption/desorption isotherms. The inset displays the corresponding DFT pore size distribution plot

7.3.6. Electrochemical Characterization

The two wires-electrodes were assembled manually using PVP-NaI as gel electrolyte. A cross-section of the device is shown in Figure 7.10.a. The sample was cut using scissors because the interested area was too large (≈ 400 x 100 μm^2) to be prepared using the FIB-milling technique. Consequently, a mechanical stress was induced in the sample. Notwithstanding this stress, the interface between the rGO and the Cu wire is maintained. Figure 7.10.b shows the interface between the active material and the gel electrolyte. Even with an important mechanical stress caused by the cut of the sample, the interface is perfectly preserved. These results are promising. However, the integration of the supercapacitors to textiles fabrics is the key challenge for wearable supercapacitors. To demonstrate the integrability of the rGO@Cu sample, a prototype was fabricated. It was 5 cm long and was inserted to cotton threads. The prototype is shown in Figure 7.10.c with an inset showing an optical microscope image, which confirms the suitable insertion.

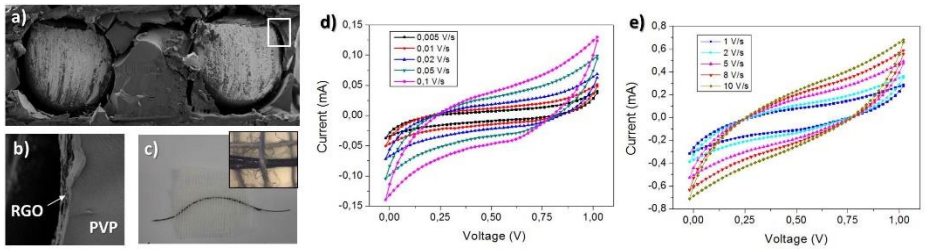

Figure 7. 10. (a) FESEM image of the cross-section of the assembled device, (b) higher magnification of the rGO/PVP interface (indicated by the white square in (a)). (c) Picture of the prototype showing the rGO@Cu wire integrated to cotton threads.

Electrochemical performance of the wire-shaped supercapacitors was evaluated by cyclic voltammetry in a two-electrode configuration. The potential window used was 1 V and the scan rates tested were 5 to 100 mV/s and 1 to 10 V/s as shown in Figure 7.10.d and 7.10.e, respectively. The shape of the curves does not display any contribution of oxygen moieties indicating the suitable reduction of the graphene oxide during the hydrothermal synthesis. The consistent response of rGO@Cu even at scan rates up to 10 V/s shows the fast charging/discharging dynamic of the system. Nevertheless, for the higher scan rates, an important slope is observable. This deviation from the box-like shape characteristic of EDLC is ascribable to the oxidized layer on the top of the copper wire, used as current collector.

Galvanostatic charge/discharge measurements were performed to investigate the electrochemical behaviour of the devices. The wire-shaped supercapacitors were subjected to different current densities between 0.5 and 2 A/g (Figure 7.11.a), to different voltage windows between 0.5 and 1 V at a current density of 0.5 A/g (Figure 7.11.b). The cycling stability was also studied up to 10.000 cycles as shown in Figure 7.11.c.

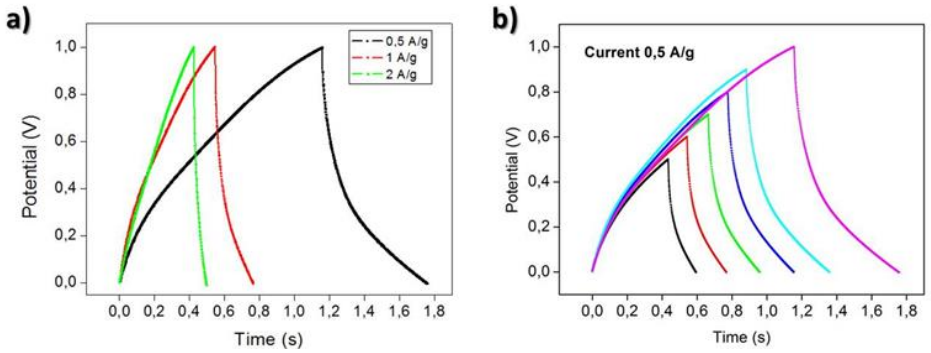

Figure 7. 11. Galvanostatic charge/discharge measurements performed at (a) different current densities and (b) in different voltage window.

The profile of the charge/discharge curves in Figure 7.11 indicates a resistive behaviour. Indeed, the typical triangular shape of EDLC was not observed due to a voltage drop at the beginning of the discharge. The performance of the rGO@Cu sample is appreciable looking at its stability over high current densities. The potential window was tested at a current density of 0.5 A/g. No distortion of the curves was observed, which confirms the good charging/discharging process of the wearable supercapacitors.

The energy storage capabilities were calculated from the cyclic voltammetry curves, according to the procedure reported by Yu *et al*..[4] The linear specific capacitance was measured to be 12.5 mF/cm. The mass loading of the rGO aerogel on copper wire was 200 µg/cm. Then, the gravimetric specific capacitance was 62.5 F/g at a scan rate of 5 mV/s. The evolution of the gravimetric specific capacitance in function of the scan rate is shown in Figure 7.12.

The decrease of the performance with the increase of the scan rate is well-known. This effect is ascribable to a limitation of the ions diffusion in the porous framework when the analysis is fast.[30] A comparison with the most relevant paper in literature is shown in Figure 7.13 for both gravimetric and linear specific capacitance. Obtained value for the gravimetric specific capacitance is in the average of the literature. However, the linear specific capacitance

displayed by rGO@Cu sample is significantly higher than the reported works in literature.

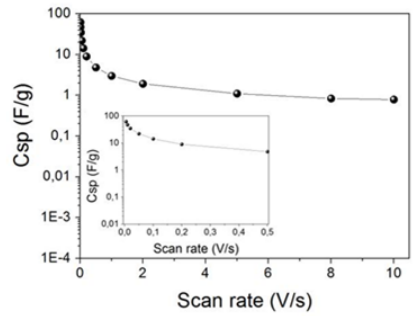

Figure 7. 12. Evolution of the gravimetric specific capacitance in function of the scan rates. The inset shows a zoom for the lower scan rates.

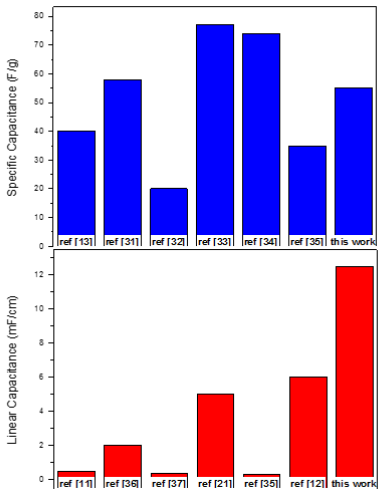

Figure 7. 13.comparison of the (top) gravimetric and (bottom) linear specific capacitance of rGO@Cu with the most relevant papers in literature.[31–37]

The stability of wearable supercapacitors is often limitative for future applications. The Figure 7.14 reports the capacity retention of rGO@Cu up to 10.000 cycles. The stability is outstanding with only 5% of the initial capacitance loss after 10.000 cycles.

The bending of the sample generates mechanical stress that can deteriorate the performance. Therefore, bending tests were performed with an angle of 70°, 120°, and 160°. Results

are remarkable with almost 99% of capacitance retention after 1000 cycles in comparison with the un-bended sample. For sake of completeness, capacitance was measured during folding/unfolding cycles.

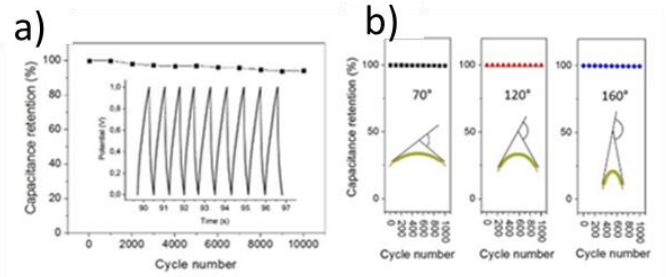

Figure 7. 14. (a) Cyclic stability at a current density of 1 A/g (inset displays the charge/discharge curves). (b) Capacitance retention after 1000 cycles at 70°, 120°, and 160°.

These cycles were performed between the un-bended sample (0°) and a bending of 120°. This test can be discriminant for real market applications. The figure 7.15 reports the capacity retention up to 100 folding-unfolding cycles. A decrease of the performance around 27% is observed. This value seems to be elevated but, comparing to the literature, the result is promising. Indeed, similar devices display 35% loss after only 11 cycles (Gogotsi and co-workers[38]) or 30% after only 50 cycles (Xu and co-workers[39]).

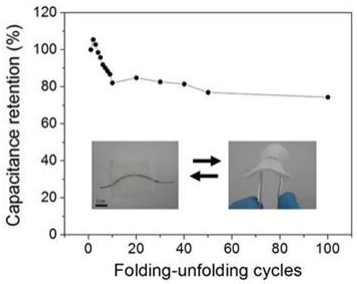

Figure 7. 15. capacitance measurements during 100 folding/unfolding cycles from 0° to 120° of the textile-integrated fibre-supercapacitor. Insets show digital photographs of the flat/bended devices.

7.4. Conclusions

This first part of the chapter demonstrated the easy fabrication of wearable supercapacitors using a green and sustainable hydrothermal synthesis. The self-assembly of rGO flakes around the copper wire created a homogeneous coating. The interface between the active material (rGO) and the current collector (Cu wire) was suitable for integration to cotton threads. Good specific capacitance and stability up to 10.000 cycles were obtained for rGO@Cu. Indeed, obtained values for linear specific capacitance overcome the most relevant works published in literature. Moreover, the flexibility with different bending angles and, more importantly, the capacitance retention over folding/unfolding conditions were demonstrated. To conclude, integrability and flexibility of rGO@Cu wire electrodes drive them to be good candidates for energy storage systems for smart textiles applications.

Part B: Scalable and cost-effective integration of Exfoliated Graphene-based Supercapacitors in Textile

Another approach dealing with a scalable fabrication of electrochemically exfoliated graphene-based wearable supercapacitors is investigated. The deposition method is mimicking an industrial procedure with a deposition rate of 100 m/min on both nylon and cotton fabrics. The graphene-based wearable supercapacitors demonstrate high electrochemical performance. Obtained results are promising but, more importantly, the explored approach is scalable and cost-effective.

7.5. Motivations

As described above, the key challenge for energy storage devices is the integration to textiles keeping their outstanding performances.[3] However, the deposition technique is a non-negligible factor because it influences both the adhesion and the interface between the active materials and the current collectors, the porous framework and, consequently, the final electrochemical performances. The deposition technique used should be tailored according to the physicochemical properties of the active material and the substrate employed.

Graphene and its derivatives graphene oxide and reduced graphene oxide have attracted attention with their remarkable intrinsic properties such as high conductivity, flexibility, high tensile strength, optical transparency, and low density.[40,41] Numerous techniques have been already investigated to coat textiles with graphene or its derivatives materials such as dip coating[42–44], vacuum filtration[45,46],

brush coating[47–49], direct electrochemical deposition[35], electrophoresis[50,51], interfacial trapping method[52], wet transfer of monolayer[53], screen printing[54,55], or self-assembling method[56,57]. However, these are time consuming and/or multi-stage manufacturing processes; not suitable for large scale production. Therefore, there is a need for a simple, low-cost, and scalable process for the fabrication of next generation wearable e-textiles.

Moreover, despite the plethora of research regarding graphene-based textiles supercapacitors, works reported in literature have focused mainly on reduced graphene oxide as active material. Nevertheless, development on electrochemical exfoliation allows to obtain cheap graphene with a good quality. Furthermore, these synthesis procedures have attracted attention due to the environmental-friendly condition and possible scalability in addition to the rapidity of the process.[58,59]

The aim of the second part of this chapter is to study graphene-based wearable supercapacitors produced by means of a padding method. This technique is mimicking an industrial process and allows to produce 100 m of e-textiles in only one minute. In addition to the simple, large scale and cost-effective production used, the active material used is the anodic exfoliated graphene which represents an innovation in this growing research field.

7.6. Materials and Methods

7.6.1. Materials

Graphite flakes and Ammonium Sulphate used for the anodic exfoliation were purchased from Sigma Aldrich. Two textiles fabrics were tested: 100% cotton [“Cotton”] and nylon (1% Elastane) [“Nylon”]. Both were manufactured internally in the University of Manchester textile laboratory. Poly(vinyl alcohol) [Mw: ~130,000] and Lithium Chloride (purity ≥ 99.0%) were purchased from Sigma Aldrich.

7.6.2. Exfoliation of Graphene and Graphene dispersion preparation

The exfoliated graphene was prepared by anodic exfoliation of graphite in $(NH_4)_2SO_4$ using the method already reported by Parvez.[59] Briefly, the exfoliation was performed in a two-electrode system using Platinum as the counter electrode and a graphite flake as the working electrode. A direct current (DC) voltage of +10 V for 3 minutes was applied to dissociate and disperse the graphite flakes into the electrolyte solution. The exfoliated product was collected by vacuum filtration and washed repeatedly with deionised water.

The obtained powder was then dispersed in Isopropanol/water (50:50 V.) by sonication for 16 hours. Thus, a dispersion of 1 mg/mL of Exfoliated Graphene was obtained.

7.6.3. Continuous pad-drying of textiles with graphene-based Ink

Textile fabrics were padded by means of "one dip-one nip" process through exfoliated graphene dispersions to a wet pick-up of ~80% on the weight of the fabric. The pressure between two nip rollers was maintained constant at 1 bar to achieve ~80% pick up. The pick-up% was calculated using following formula:

$$Pick\ up\% = \frac{(The\ weight\ of\ graphene\ coated\ fabric - the\ dry\ weight\ of\ untreated\ fabric)}{The\ dry\ weight\ of\ untreated\ fabric} \times 100$$

The exfoliated graphene padded fabrics were subsequently dried at 100°C for 10 minutes and used without further treatments for e-textile applications. This procedure was repeated up to 5 times to assure a suitable deposition of graphene inside the textile fabrics.

7.6.4. Physicochemical characterization

A Kratos Axis Ultra system spectrophotometer was used to perform the XPS analysis on the surface of the exfoliated graphene to assess its quality.

Philips XL 30 Field Emission Gun Scanning Electron Microscope (SEM) was used to analyse the surface topography of the Exfoliated Graphene coated fabrics.

A topological analysis was performed using Atomic Force Microscopy. The apparatus used was Digital Instruments Nanoscope IIIA. The nanosheets were deposited on a SiO_2/Si substrate. High Resolution – Transmission Electron Microscopy was used to investigate the exfoliated graphene. The instrument used was a Tecnai F30 operating a 300kV fitted with a highly coherent Schottky field emission gun.

Raman analysis was applied to study both the exfoliated graphene powder and the exfoliated graphene coated textiles by means of a Renishaw InVia Reflex micro-Raman spectrometer (Renishaw plc. Wottonunder-Edge, UK) equipped with a cooled CCD camera. The Raman source was a diode laser (λ_{ex} = 514.5 nm), and samples inspection occurred through a microscope objective (100X), in backscattering light collection. The parameters used for the spectra acquisition were 5 mW laser power, 10 s of exposure time and 3 accumulations. The sample of exfoliated graphene powder was carefully pressed on a glass microscope slide while the e-textiles was attached in order to be as flat as possible.

The sheet resistance of conductive e-textiles was measured with four-point probe measurements using a Keithley 2440 source-measure unit. Sheet resistance was calculated from the average of ten measurements.

Cyclic Voltammetry (CV) and Galvanostatic charge/discharge (GCD) measurements were performed using a PGSTAT302N potentiostat (Metrohm Autolab, The Netherlands). All electrochemical measurements were performed using PVA-LiCl as neutral gel electrolyte in a two-electrode cell and symmetrical configuration. Specific Capacitance was calculated using the best practice methods established by Stoller and Ruoff.[60]

7.7. Results and Discussions

7.7.1. Characterization of Exfoliated Graphene

To assess the surface chemical composition of the exfoliated graphene, XPS analysis was carried on the sample. The HR spectrum of the C1s region centred at 284.5 eV is reported in Figure 7.16. The curve can be deconvoluted in 4 different bands. The most intense feature corresponds to the C sp^2 which can be relied to the conductivity of the carbon-based material. A satellite peak was observable at ~6 eV from the C1s main peak and corresponds to the $\pi \rightarrow \pi^*$ interaction. This interaction is a fingerprint of carbon aromatic rings and is ascribable to the delocalized electrons in the material.[26,56] The two other figures are assigned to oxidized carbon such as C-O and C=O. The presence of these groups is devoted to the oxidation process allowing the exfoliation of graphite in exfoliated graphene.

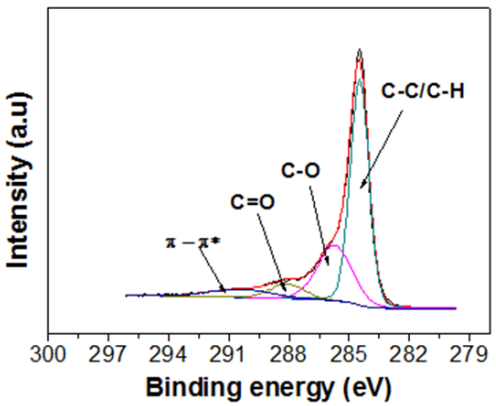

Figure 7. 16. XPS spectrum of the as-exfoliated graphene in the C1s region

In addition to the XPS analysis assessing the surface composition, AFM analysis was performed to determine the flakes thickness. The image is reported in Figure 7.17. Flakes thickness was 2 nm, which corresponds to few-layers graphene.

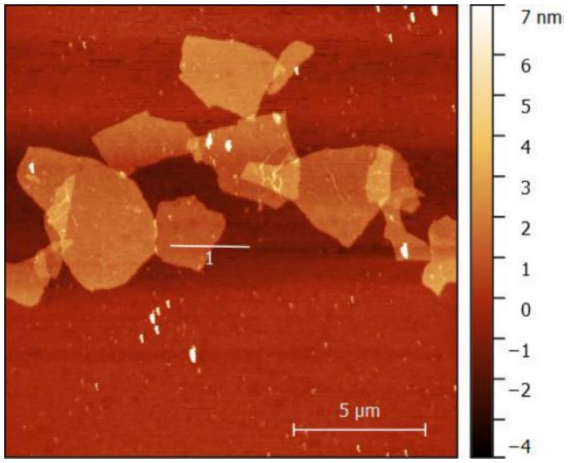

Figure 7. 17. AFM image of solution-exfoliated graphene nanosheets

Then, the flake size was determined by means of SEM analysis. The average lateral size measured was 7.9 µm. The SEM image and the relative size distribution are reported in Figure 7.18.

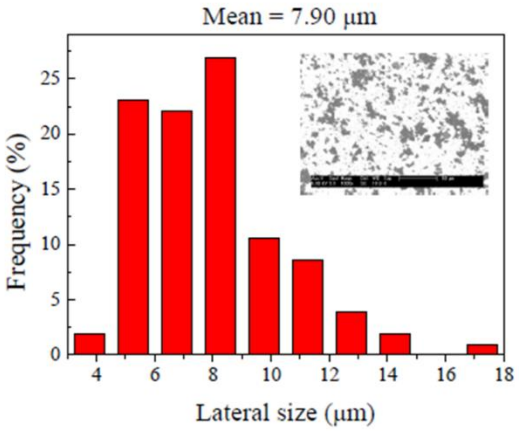

Figure 7. 18. distribution of the flake size by SEM analysis.

High Resolution Transmission Electron Microscopy (HRTEM) image is shown in Figure 7.19, with the Selected Area Electron Diffraction (SAED) pattern. Typical 6-fold symmetric diffraction can be observed from the SAED pattern. The {1-210} plan is stronger than the {0-110} indicating the high crystallinity of a bilayer graphene sheet.[59,61]

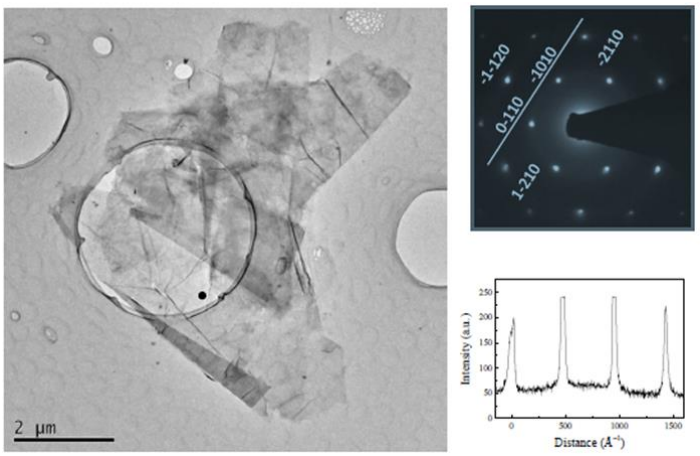

Figure 7. 19. HR-TEM image of the as-prepared exfoliated graphene deposited on Si wafer (left), SAED spectrum focused on the exfoliated graphene (right-top) and direct measurement of the interplanar distance through a line profile (right-bottom).

7.7.2. Exfoliated Graphene coated on Textiles

7.7.2.1. Morphological characterization by SEM

Figure 7.20 displays the Scanning Electron Microscopy image of the morphology of the Exfoliated Graphene coated on Cotton (Figure A and B) and Nylon (Figure C and D) using the Padding method. Exfoliated Graphene flakes tend to wind around the fibre of Cotton with a good homogeneity and make a continuous conductive shell (Figure 7.20.A). Figure 7.20.B displays some defects present on the fibre surface. Figure 7.20.C and 7.20.D, panel C and D show the Nylon based e-textile with the same magnification than panel A and panel B, respectively. A different morphology is observable for the Nylon fabrics in comparison with the Cotton fabrics. Indeed, in the case of Nylon fabrics, Exfoliated Graphene flakes seems to be more packed around the fabrics and to form a homogeneous conductive layer on the surface of the textile while the active material was dispersed around each fibre for the Cotton sample.

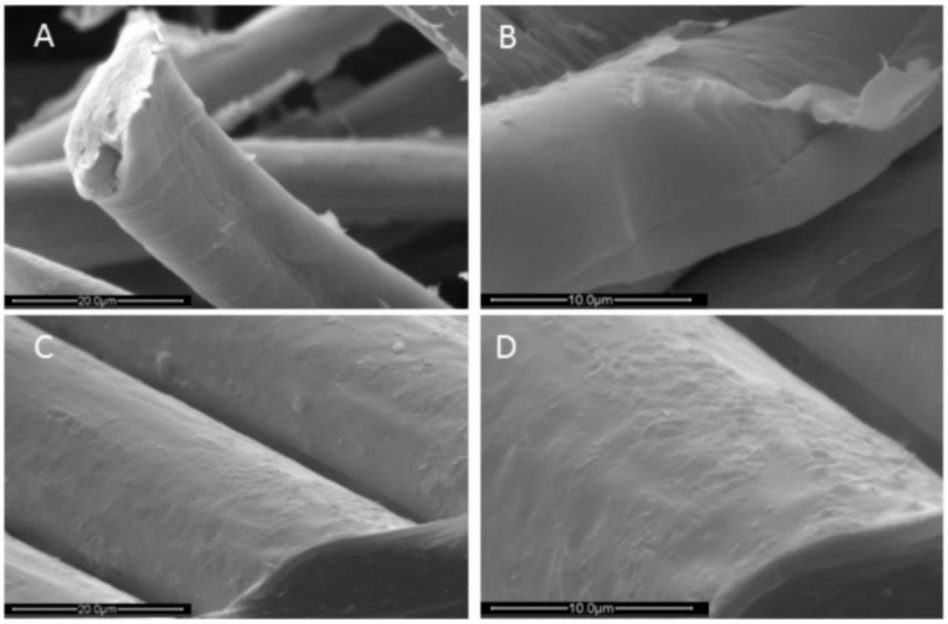

Figure 7. 20. SEM images of exfoliated graphene deposited on (A,B) Cotton and (C,D) Nylon fabrics.

7.7.2.2. Structural characterization by Raman

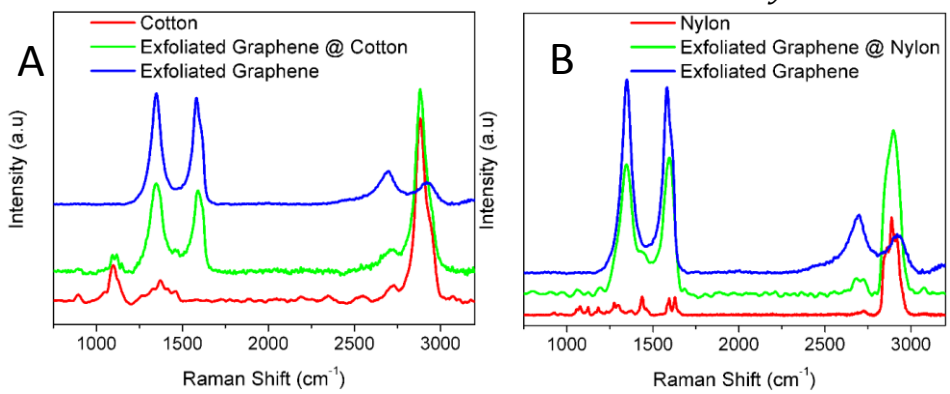

Figure 7. 21. Raman spectra for (A) cotton- and (B) Nylon-based electrodes.

Figure 7.21.A shows the Raman spectra, related to the exfoliated graphene deposited by means of the Padding method (Exfoliated Graphene @ Cotton, green curve), plotted in comparison with the bare cotton alone (red curve) and the exfoliated graphene powder used as active material for the preparation of the e-textiles samples (blue curve). Typical peaks of cotton (red curve) are observable in the fingerprint region 1000 – 1500 cm^{-1} and centred at 2728 cm^{-1} and 2890 cm^{-1}. In the fingerprint region, bands are

ascribable to the C-C bond stretching while peaks at ~2728 cm^{-1} and ~2890 cm^{-1} can be assigned to the C-H stretching modes in CH_2 groups. These assignments are in complete accordance with the study reported previously by Uddin *et al*..[62] The exfoliated graphene spectrum (blue curve) shows four bands centred at 1350 cm^{-1}, 1580 cm^{-1}, 2685 cm^{-1}, and 2930 cm^{-1}. The first two features (1350 cm^{-1}, 1580 cm^{-1}) are the most intense and correspond to the first order D peak and G peak respectively. The intensity of the D peak is due to the size reduction of in plane-sp^2 domains and can be induced by the creation of defects, vacancies, and distortion of the sp^2 domains after oxidation.[63,64] The oxidation occurred during the anodic exfoliation of graphite. The G peak, which is due to the doubly degenerate zone centre E_{2g} mode is normally sharp and intense for pure graphene.[65] Conversely, the blue curve of Figure 7.21.A shows a broad band resulting from the superposition of the G peak and the D' mode (1625 cm^{-1}) due to defect scattering.[63,66] The band at 2685 cm^{-1} corresponds to the 2D peak (historically G') and confirms the quality of the anodic exfoliated material. The last feature at 2930 cm^{-1} is ascribable to the D + D' peak typical of oxidized graphene which is induced by the anodic exfoliation of graphite as described above. The green curve, corresponding to the spectrum of cotton coated by the exfoliated graphene by means of the Padding technique, shows the typical peaks of graphene materials (1350 cm^{-1}, 1580 cm^{-1}, 2685 cm^{-1}, and 2930 cm^{-1}) in addition to the bands assigned to the cotton matrix (1000 – 1160 cm^{-1} region, 1460 cm^{-1}, 2700 – 3000 cm^{-1} region). Those are the more intense bands for a cotton matrix and it is assumed that the less intense features are hidden by the scattering modes of exfoliated graphene. The Raman characterization allows to confirm that the exfoliated graphene was suitably deposited on the cotton fabrics. The Figure 7.21.B shows the Raman spectrum of the exfoliated graphene (blue curve), which is already discussed above, the spectrum of bare nylon fabric (red curve) and the composite 'Exfoliated Graphene @ Nylon'

(green curve). The Raman spectrum of nylon depicts weak features at 800 – 1300 cm^{-1} range which are ascribable to the C-C skeletal backbone structure. The intense feature at 1440 cm^{-1} corresponds to the CH_2 bending while the doublet at 1635 cm^{-1} is characteristic of C=O stretching mode in nylon. The broad peak centred at 2920 cm^{-1} is ascribable to the C-H stretching in CH_2.[67–69] The spectrum of the nylon-based e-textile (green curve) shows the representative features of graphene overlapping the more intense peaks related to the bending of CH_2 groups and the C-H stretching of the Nylon matrix (1440 cm^{-1} and 2918 cm^{-1}). As reported before for the cotton fabrics, the Raman analysis confirms that the exfoliated graphene was suitably deposited on the nylon fabrics by means of the padding technique.

7.7.2.3. Electrical properties of exfoliated graphene coated on textiles

The electrical properties of Exfoliated Graphene coated e-textiles by means of Padding method have been tested. Figure 7.22 reports the sheet resistance values for Cotton (blue curve) and Nylon (red curve) fabrics. Three samples were tested for each fabric: reference sample (no padded), sample padded 1 time, and sample padded 5 times.

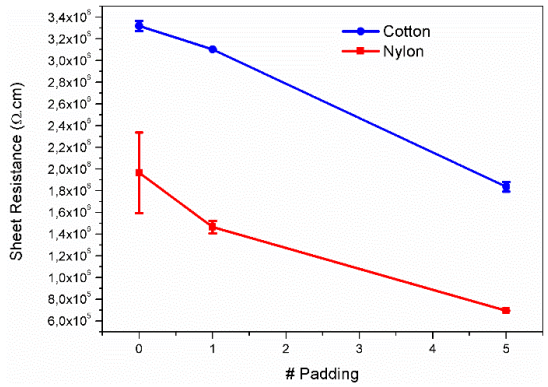

Figure 7. 22. Sheet resistance in function of the padding repetition

The sheet resistance of cotton fabric is significantly higher than nylon one for all the samples. As expected, the sheet resistance decreases with the increase of the padding

repetition. The measured values after 5 repetitions were 700 kΩ.cm and 1.9 MΩ.cm for Nylon and Cotton, respectively. No further decrease was observed after 5 repetitions (data not reported).

7.7.3. Electrochemistry

After careful characterization of the Exfoliated Graphene obtained by anodic exfoliation of Graphite and the resulting e-textiles, electrochemical testing was carried out in a symmetrical two electrode configuration. Individual electrodes were prepared by means of the Padding method without any additional polymeric binders or conductive additives. The padded fabric has a dimension of 10 cm x 10 cm approximatively and was cut in small rectangular pieces with an area of 1 cm^2. The mass loading was 0.8 and 1.7 mg/cm^2 for Cotton and Nylon, respectively. In this work, a gel electrolyte was used to avoid complex packaging manufacturing and the possibility of electrolyte leakage which is one of the main concern for e-textile applications. For an evident reason of user's safety, only pH neutral electrolyte could be used for Supercapacitors in contact with the user's body even if the Specific Capacitance is lower than for strong acidic or basic electrolytes.[70] Lithium Chloride was used because both cations and anions are small and allow to obtain more concentrated electrolyte without phase separation and diffusion limitation.

Cyclic Voltammograms (CV) are reported in Figure 7.23.A and 7.23.B for Cotton and Nylon respectively. The response of the cell shows an almost rectangular shape for the Exfoliated Graphene coated on Cotton and Nylon fabrics which is typical for EDLC. The Nylon based e-textiles seems to be more resistive at high scan rates. However, the obtained current density for the Nylon fabrics are three or four times bigger than for Cotton at the same scan rates. The main concern about the deposition by means of padding directly on textile is the inherent resistivity of the fabrics when compared to

metallic current collectors typically used for Supercapacitors applications. Figure 7.23.C and 7.23.D show the galvanostatic charge / discharge measurements for Cotton and Nylon based e-textiles respectively. The shape of both chrono-potentiograms is almost linear which reveal the good capacitive behaviour at different discharge current densities. However, chrono-potentiograms are slightly asymmetrical with a slower charge than discharge and it is even more noticeable for the Nylon-based e-textiles. At low current density, the supercapacitor seems to charge itself slowly probably due to a limitation of diffusion phenomena through the packed layers of Exfoliated Graphene on the surface of Nylon fabrics as it was discussed above with the SEM analysis (Figure 7.20).

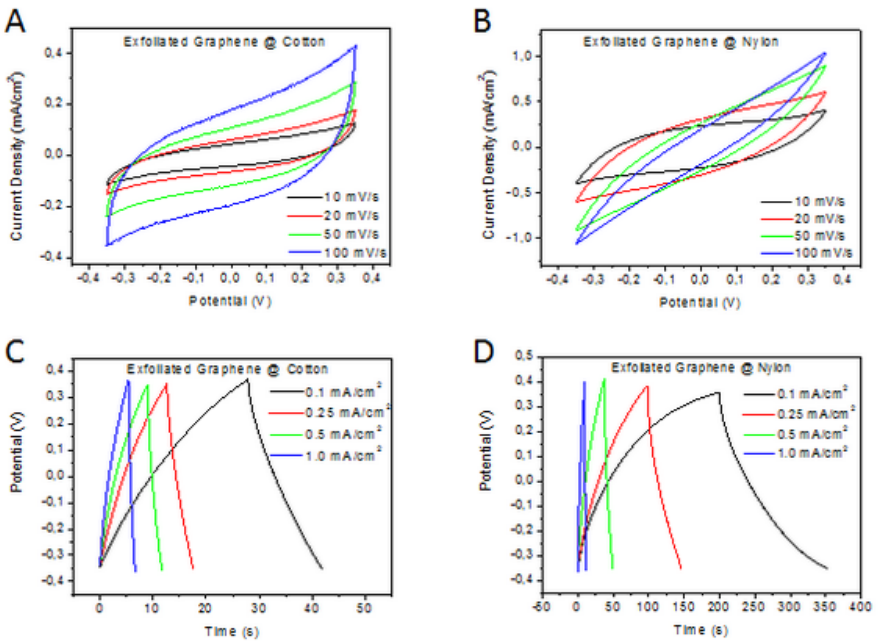

Figure 7. 23. electrochemical characterization using Cyclic Voltammetry and Galvanostatic Charge/Discharge measurements: (A,C) Cotton and (B,D) Nylon.

The Specific Capacitance was calculated using the best practice method established in literature from both cyclic voltammograms and chrono-potentiograms.[60] Results are reported in Figure 7.24.

The Specific Capacitance calculated using both techniques (CV and GCD) correspond almost perfectly. Nylon-based e-textile exhibits higher areal Specific Capacitance than Cotton-based sample. The difference is much important with a factor slightly above 5 at 10 mV/s (90 mF/cm² for Nylon versus 17 mF/cm² for Cotton) or even with an order of magnitude larger for galvanostatic charge / discharge measurement at 0.1 mA/cm² (85 mF/cm² versus 8 mF/cm²).

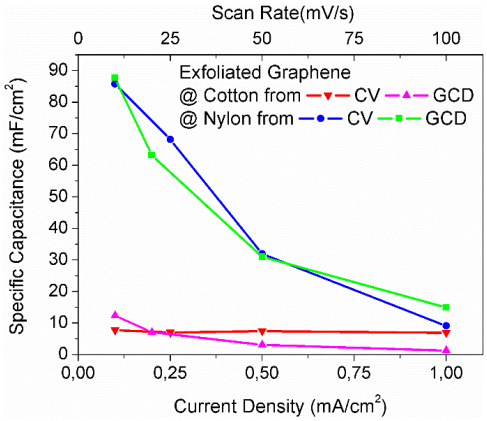

Figure 7. 24. Evolution of the areal specific capacitance calculated from CV and GCD for both Cotton and Nylon textiles.

However, this difference decreases dramatically to almost no significant difference between the samples for Specific Capacitance calculated both from chrono-potentiograms (9 mF/cm² for Nylon versus 7 mF/cm² for Cotton). Interestingly, the Specific Capacitance for the Cotton sample is almost constant at the tested scan rates and current densities. These differences of behaviour could be accredited to a difference of morphology of the sample. Indeed, exfoliated graphene flakes tend to wind around each fibre of the Cotton fabric while they tend to form a layered structure on Nylon surface. By consequences, the accessibility of the active material by the ions from the electrolyte is easier in the case of Cotton and the capacitive behaviour is slightly dependant of the scan rate or the current density used for the measurement. In the other way, ions need more time to form the double layer in the case of Nylon-based e-textile because of the minor accessibility of active material by ions from the

electrolyte. Then, the Specific Capacitance decreases dramatically when the scan rate or the current density is increased due to a diffusion limitation of electrolyte through the active materials.

7.7.4. Cycling Stability

The cycling stability is one of the main concern for comparing Supercapacitors between each other regarding forward to practical applications. It is well known that ideal Electrical Double Layers Capacitors should demonstrate extremely high Capacity retention after repeated charge / discharge cycles. To evaluate our devices, cyclic stability tests were performed at a current density of 1 mA/cm² up to 15.000 cycles. The capacity retention for Cotton and Nylon-based textiles are reported in Figure 7.25 with a blue and a red curve respectively.

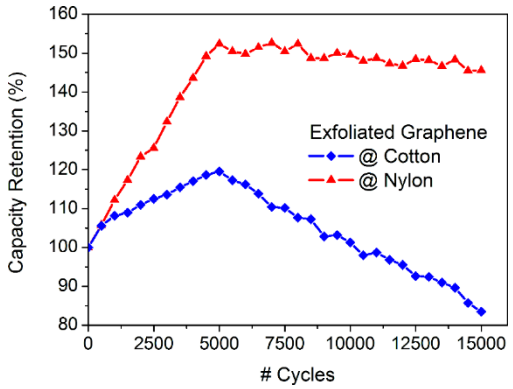

Figure 7. 25. Cyclic stability performed at 1 mA/cm² up to 15.000 cycles for Cotton and Nylon-based e-textiles

The Cotton-based e-textile displays an important increase of the Capacity during the first 500 cycles This phenomenon can be described as the conditioning of the assembled cell due to the permeation of the electrolyte throughout the porous active material.[60] The capacity continues to increase but with a slighter slope until reach the maximum around 5000 cycles. After this point, the device shows a failure and the Capacity Retention decreases gradually until a value of 85 % at 15.000 cycles. This failure could be due to the delamination of

Exfoliated Graphene flakes that where not perfectly deposited around the fibre as described previously as defects in SEM analysis (See Figure 7.20). Indeed, this failure was not observed for the Nylon-based e-textiles which contains more packed flakes of Exfoliated Graphene. Due to this organization, the flakes are less sensitive to the delamination process. Starting from the first cycles for this sample, the conditioning of the cell is observable. Notwithstanding, the Capacity continues to increase almost linearly and reach a value around 150 % of Capacity Retention in comparison with the starting value. This increase could be due to the diffusion of ions from electrolyte through the packed layers of Exfoliated Graphene. Then, the device displays an almost constant behaviour. This lack of failure with the aging of the device validates the possible application of this technique to produce large scale nylon-based e-textiles.

7.8. Conclusions

The second part of this chapter illustrated a simple, cost-effective and scalable production process of graphene-based wearable textiles. The exfoliated graphene deposition on both nylon and cotton substrates was suitably realized using a padding method. This method is mimicking an industrial process and allows to produce up to 100 m/min of graphene-based wearable textiles. Exfoliated graphene flakes tend to wind around the textiles fibres which create a good interface. Even if the sheet resistance of both fabrics is non-negligible, integrated textile supercapacitors show good specific capacitance and high stability over 15.000 cycles. For all the electrochemical measurements, nylon-based supercapacitors demonstrate better performance than cotton-based ones. The difference could be due to the intrinsic lower sheet resistance of the fabric. To summarize, the padding method used here can be envisaged for an up-scaling of graphene-based wearable supercapacitors from laboratory to industrial scale in this growing market.

REFERENCES

(1) Jost, K.; Durkin, D. P.; Haverhals, L. M.; Brown, E. K.; Langenstein, M.; De Long, H. C.; Trulove, P. C.; Gogotsi, Y.; Dion, G. Natural Fiber Welded Electrode Yarns for Knittable Textile Supercapacitors. *Adv. Energy Mater.* **2015**, *5* (4), 1–8.

(2) Hayward, J. *E-Textiles 2017-2027: Technologies, Markets, Players*; IDTechEx, 2017.

(3) Liu, L.; Yu, Y.; Yan, C.; Li, K.; Zheng, Z. Wearable Energy-Dense and Power-Dense Supercapacitor Yarns Enabled by Scalable Graphene–metallic Textile Composite Electrodes. *Nat. Commun.* **2015**, *6*, 7260.

(4) Yu, D.; Qian, Q.; Wei, L.; Jiang, W.; Goh, K.; Wei, J.; Zhang, J.; Chen, Y. Emergence of Fiber Supercapacitors. *Chem. Soc. Rev.* **2015**, *44* (3), 647–662.

(5) Lamberti, A.; Fontana, M.; Bianco, S.; Tresso, E. Flexible Solid-State CuxO-Based Pseudo-Supercapacitor by Thermal Oxidation of Copper Foils. *Int. J. Hydrogen Energy* **2016**, *41* (17), 11700–11708.

(6) Bao, L.; Li, X. Towards Textile Energy Storage from Cotton T-Shirts. *Adv. Mater.* **2012**, *24* (24), 3246–3252.

(7) Shi, C.; Zhao, Q.; Li, H.; Liao, Z. M.; Yu, D. Low Cost and Flexible Mesh-Based Supercapacitors for Promising Large-Area Flexible/wearable Energy Storage. *Nano Energy* **2014**, *6*, 82–91.

(8) Xue, J.; Zhao, Y.; Cheng, C.; Hu, C.; Hu, Y.; Meng, Y.; Shao, H.; Zhang, Z.; Qu, L. An All-Cotton-Derived, Arbitrarily Foldable, High-Rate, Electrochemical Supercapacitor. *Phys. Chem. Chem. Phys.* **2013**, *15*, 8042–8045.

(9) Harrison, D.; Qiu, F.; Fyson, J.; Xu, Y.; Evans, P.; Southee, D. A Coaxial Single Fibre Supercapacitor for Energy Storage. *Phys. Chem. Chem. Phys.* **2013**, *15*, 12215–12219.

(10) Su, F.; Miao, M. Asymmetric Carbon Nanotube-MnO2 Two-Ply Yarn Supercapacitors for Wearable Electronics. *Nanotechnology* **2014**, *25*, 135401.

(11) Fu, Y.; Cai, X.; Wu, H.; Lv, Z.; Hou, S.; Peng, M.; Yu, X.; Zou, D.; Xiao, Y.; Zou, D. Fiber Supercapacitors Utilizing Pen Ink for Flexible/wearable Energy Storage. *Adv. Mater.* **2012**, *24* (42), 5713–5718.

(12) Le, V. T.; Kim, H.; Ghosh, A.; Kim, J.; Chang, J.; Vu, Q. A.; Pham, D. T.; Lee, J.-H.; Kim, S.-W.; Lee, Y. H. Coaxial Fiber Supercapacitor Using All-Carbon Material Electrodes. *ACS Nano* **2013**, *7*, 5940–5947.

(13) Meng, Y.; Zhao, Y.; Hu, C.; Cheng, H.; Hu, Y.; Zhang, Z.; Shi, G.; Qu, L. All-Graphene Core-Sheath Microfibers for All-Solid-State, Stretchable Fibriform Supercapacitors and Wearable Electronic Textiles. *Adv. Mater.* **2013**, *25* (16), 2326–2331.

(14) Wang, G.; Lei, Z.; Jiujun, Z. A Review of Electrode Materials for Electrochemical Supercapacitors. *ChemsucChem* **2012**, *5*, 797.

(15) Chen, T.; Peng, H.; Durstock, K.; Dai, L. High-Performance Transparent and Stretchable All-Solid Supercapacitors Based on Highly Aligned Carbon Nanotube Sheets. *Sci. Rep.* **2014**, *4*, 3612.

(16) Sacco, A.; Porro, S.; Lamberti, A.; Gerosa, M.; Castellino, M.; Chiodoni, A.; Bianco, S. Investigation of Transport and Recombination Properties in Graphene/titanium Dioxide Nanocomposite for Dye-Sensitized Solar Cell Photoanodes. *Electrochim. Acta* **2014**, *131*, 154–159.

(17) Brownson, D. A. C.; Kampouris, D. K.; Banks, C. E. An Overview of Graphene in Energy Production and Storage Applications. *J. Power Sources* **2011**, *196* (11), 4873–4885.

(18) Lamberti, A.; Clerici, F.; Fontana, M.; Scaltrito, L. A Highly Stretchable Supercapacitor Using Laser-Induced Graphene Electrodes onto Elastomeric Substrate. *Adv. Energy Mater.* **2016**, *6* (10), 1–6.

(19) Shao, Y.; El-Kady, M. F.; Wang, L. J.; Zhang, Q.; Li, Y.; Wang, H.; Mousavi, M. F.; Kaner, R. B. Graphene-Based Materials for Flexible Supercapacitors. *Chem. Soc. Rev.* **2015**, *44* (11), 3639–3665.

(20) Bae, J.; Park, Y. J.; Lee, M.; Cha, S. N.; Choi, Y. J.; Lee, C. S.; Kim, J. M.; Wang, Z. L. Single-Fiber-Based Hybridization of Energy Converters and Storage Units Using Graphene as Electrodes. *Adv. Mater.* **2011**, *23*, 3446–3449.

(21) Kou, L.; Huang, T.; Zheng, B.; Han, Y.; Zhao, X.; Gopalsamy, K.; Sun, H.; Gao, C. Coaxial Wet-Spun Yarn Supercapacitors for High-Energy Density and Safe Wearable Electronics. *Nat. Commun.* **2014**, *5* (May), 3754.

(22) Giardi, R.; Porro, S.; Topuria, T.; Thompson, L.; Pirri, C. F.; Kim, H. C. One-Pot Synthesis of Graphene-Molybdenum Oxide Hybrids and Their Application to Supercapacitor Electrodes. *Appl. Mater. Today* **2015**, *1* (1), 27–32.

(23) Shirley, D. A. High-Resolution X-Ray Photoemission Spectrum of the Valence Bands of Gold. *Phys. Rev. B* **1972**, *5* (12), 4709–4714.

(24) Huang, S. Y.; Zhao, B.; Zhang, K.; Yuen, M. M.; Xu, J. B.; Fu, X. Z.; Sun, R.; Wong, C.-P. Enhanced Reduction of Graphene Oxide on Recyclable Cu Foils to Fabricate Graphene Films with Superior Thermal Conductivity. *Sci. Rep.* **2015**, *5*, 14260.

(25) Yuxi Xu, Kaixuan Sheng, C. L.; Shi, G. Self-Assembled Graphene Hydrogel via a One-Step Hydrothermal Process. *ACS Nano* **2010**, *4* (7), 4324–4330.

(26) Fan, X.; Peng, W.; Li, Y.; Li, X.; Wang, S.; Zhang, G.; Zhang, F. Deoxygenation of Exfoliated Graphite Oxide under Alkaline Conditions: A Green Route to Graphene Preparation. *Adv. Mater.* **2008**, *20*, 4490–4493.

(27) Onoe, J.; Nakao, A.; Takeuchi, K. XPS Study of a Photopolymerized C 60 Film. *Phys. Rev. B* **1997**, *55*, 10051.

(28) Cao, X.; Qi, D.; Yin, S.; Bu, J.; Li, F.; Goh, C. F.; Zhang, S.; Chen, X. Ambient Fabrication of Large-Area Graphene Films via a Synchronous Reduction and Assembly Strategy. *Adv. Mater.* **2013**, *25*, 2957–2962.

(29) Fan, Z. J.; Kai, W.; Yan, J.; Wei, T.; Zhi, L. J.; Feng, J.; Ren, Y. M.; Song, L. P.; Wei, F. Facile Synthesis of Graphene Nanosheets via Fe Reduction of Exfoliated Graphite Oxide. *ACS Nano* **2011**, *5*, 191–198.

(30) Wang, Q.; Wang, X.; Xu, J.; Ouyang, X.; Hou, X.; Chen, D.; Wang, R.; Shen, G. Flexible Coaxial-Type Fiber Supercapacitor Based on $NiCo_2O_4$ Nanosheets Electrodes. *Nano Energy* **2014**, *8*, 44–51.

(31) Chen, X.; Qiu, L.; Ren, J.; Guan, G.; Lin, H.; Zhang, Z.; Chen, P.; Wang, Y.; Peng, H. Novel Electric Double-Layer Capacitor with a Coaxial Fiber Structure. *Adv. Mater.* **2013**, *25* (44), 6436–6441.

(32) Yang, Z.; Deng, J.; Chen, X.; Ren, J.; Peng, H. A Highly Stretchable, Fiber-Shaped Supercapacitor. *Angew. Chemie - Int. Ed.* **2013**, *52* (50), 13453–13457.

(33) Meng, Q.; Wu, H.; Meng, Y.; Xie, K.; Wei, Z.; Guo, Z. High-Performance All-Carbon Yarn Micro-Supercapacitor for an Integrated Energy System. *Adv. Mater.* **2014**, *26* (24), 4100–4106.

(34) Ding, X.; Zhao, Y.; Hu, C.; Hu, Y.; Dong, Z.; Chen, N.; Zhang, Z.; Qu, L. Spinning Fabrication of Graphene/polypyrrole Composite Fibers for All-Solid-State, Flexible Fibriform Supercapacitors. *J. Mater. Chem. A* **2014**, *2* (31), 12355–12360.

(35) Chen, Q.; Meng, Y.; Hu, C.; Zhao, Y.; Shao, H.; Chen, N.; Qu, L. MnO_2-Modified Hierarchical Graphene Fiber Electrochemical Supercapacitor. *J. Power Sources* **2014**, *247*, 32–39.

(36) Ren, J.; Bai, W.; Guan, G.; Zhang, Y.; Peng, H. Flexible and Weaveable Capacitor Wire Based on a Carbon Nanocomposite Fiber. *Adv. Mater.* **2013**, *25* (41), 5965–5970.

(37) Kou, L.; Huang, T.; Zheng, B.; Han, Y.; Zhao, X.; Gopalsamy, K.; Sun, H.; Gao, C. Coaxial Wet-Spun Yarn Supercapacitors for High-Energy Density and Safe Wearable Electronics. *Nat. Commun.* **2014**, *5*, 3754.

(38) Jost, K.; Stenger, D.; Perez, C. R.; McDonough, J. K.; Lian, K.; Gogotsi, Y.; Dion, G. Knitted and Screen Printed Carbon-Fiber Supercapacitors for Applications in Wearable Electronics. *Energy Environ. Sci.* **2013**, *6*, 2698–2705.

(39) Xu, H.; Hu, X.; Sun, Y.; Yang, H.; Liu, X.; Huang, Y. Flexible Fiber-Shaped Supercapacitors Based on Hierarchically Nanostructured Composite Electrodes. *Nano Res.* **2015**, *8*, 1148–1158.

(40) Novoselov, K. S.; Geim, A. K.; Morozov, S. V.; Jiang, D.; Zhang, Y.; Dubonos, S. V.; Grigorieva, I. V.; Firsov, A. A. Electric Field Effect in Atomically Thin Carbon Films. *Science.* **2004**, *306*, 666–669.

(41) Novoselov, K. S.; Fal'ko, V. I.; Colombo, L.; Gellert, P. R.; Schwab, M. G.; Kim, K. A Roadmap for Graphene. *Nature* **2012**, *490* (7419), 192–200.

(42) Zhang, Z.; Xiao, F.; Xiao, J.; Wang, S. Functionalized Carbonaceous Fibers for High Performance Flexible All-Solid-State Asymmetric Supercapacitors. *J. Mater. Chem. A* **2015**, *3* (22), 11817–11823.

(43) Ye, X.; Zhou, Q.; Jia, C.; Tang, Z.; Wan, Z.; Wu, X. A Knittable Fibriform Supercapacitor Based on Natural Cotton Thread Coated with Graphene and Carbon Nanoparticles. *Electrochim. Acta* **2016**, *206*, 155–164.

(44) Yu, N.; Yin, H.; Zhang, W.; Liu, Y.; Tang, Z.; Zhu, M. Q. High-Performance Fiber-Shaped All-Solid-State Asymmetric Supercapacitors Based on Ultrathin MnO_2 Nanosheet/carbon Fiber Cathodes for Wearable Electronics. *Adv. Energy Mater.* **2016**, *6* (2), 1–9.

(45) Du, P.; Hu, X.; Yi, C.; Liu, H. C.; Liu, P.; Zhang, H. L.; Gong, X. Self-Powered Electronics by Integration of Flexible Solid-State Graphene-Based Supercapacitors with High Performance Perovskite Hybrid Solar Cells. *Adv. Funct. Mater.* **2015**, *25* (16), 2420–2427.

(46) Sevilla, M.; Ferrero, G. A.; Fuertes, A. B. Graphene-Cellulose Tissue Composites for High Power Supercapacitors. *Energy Storage Mater.* **2016**, *5*, 33–42.

(47) Liu, W.; Yan, X.; Lang, J.; Peng, C.; Xue, Q. Flexible and Conductive Nanocomposite Electrode Based on Graphene Sheets and Cotton Cloth for Supercapacitor. *J. Mater. Chem.* **2012**, *22* (33), 17245.

(48) Liu, L.; Shen, B.; Jiang, D.; Guo, R.; Kong, L.; Yan, X. Watchband-Like Supercapacitors with Body Temperature Inducible Shape Memory Ability. *Adv. Energy Mater.* **2016**, *6* (16).

(49) Guo, M.-X.; Bian, S.-W.; Shao, F.; Liu, S.; Peng, Y.-H. Hydrothermal Synthesis and Electrochemical Performance of MnO2/graphene/polyester Composite Electrode Materials for Flexible Supercapacitors. *Electrochim. Acta* **2016**, *209*, 486–497.

(50) Zhang, X.; Ge, M.; Zheng, Y.; Zhang, K.-Q.; Lin, Z. Fibrous and Flexible Supercapacitors Comprising Hierarchical Nanostructures with Carbon Spheres and Graphene Oxide Nanosheets. *J. Mater. Chem. A* **2015**, *3*, 12761–12768.

(51) Li, P.; Li, J.; Zhao, Z.; Fang, Z.; Yang, M.; Yuan, Z.; Zhang, Y.; Zhang, Q.; Hong, W.; Chen, X.; Yu, D. A General Electrode Design Strategy for Flexible Fiber Micro-Pseudocapacitors Combining Ultrahigh Energy and Power Delivery. *Adv. Sci.* **2017**, *4* (8), 1700003.

(52) Woltornist, S. J.; Alamer, F. A.; McDannald, A.; Jain, M.; Sotzing, G. A.; Adamson, D. H. Preparation of Conductive Graphene/graphite Infused Fabrics Using an Interface Trapping Method. *Carbon N. Y.* **2015**, *81* (1), 38–42.

(53) Neves, a I. S.; Bointon, T. H.; Melo, L. V; Russo, S.; de Schrijver, I.; Craciun, M. F.; Alves, H. Transparent Conductive Graphene Textile Fibers. *Sci. Rep.* **2015**, *5*, 9866.

(54) Zopf, S. F.; Manser, M. Screen-Printed Military Textiles for Wearable Energy Storage. *J. Eng. Fiber. Fabr.* **2016**, *11* (3), 1–8.

(55) Jost, K.; Perez, C. R.; McDonough, J. K.; Presser, V.; Heon, M.; Dion, G.; Gogotsi, Y. Carbon Coated Textiles for Flexible Energy Storage. *Energy Environ. Sci.* **2011**, *4* (12), 5060–5067.

(56) Lamberti, A.; Gigot, A.; Bianco, S.; Fontana, M.; Castellino, M.; Tresso, E.; Pirri, C. F. Self-Assembly of Graphene Aerogel on Copper Wire for Wearable Fiber-Shaped Supercapacitors. *Carbon N. Y.* **2016**, *105*, 649–654.

(57) Li, M.; Pan, F.; Choo, E. S. G.; Lv, Y.; Chen, Y.; Xue, J. Designed Construction of a Graphene and Iron Oxide Freestanding Electrode with Enhanced Flexible Energy-Storage Performance. *ACS Appl. Mater. Interfaces* **2016**, *8* (11), 6972–6981.

(58) Parvez, K.; Li, R.; Puniredd, S. R.; Hernandez, Y.; Hinkel, F.; Wang, S.; Feng, X.; Mullen, K. Electrochemically Exfoliated Graphene as Solution-Processable, Highly Conductive Electrodes for Organic Electronics. *ACS Nano* **2013**, *7* (4), 3598–3606.

(59) Parvez, K.; Wu, Z.; Li, R.; Liu, X.; Graf, R.; Feng, X.; Mullen, K. Exfoliation of Graphite into Graphene in Aqueous Solutions. *J. Am. Chem. Soc* **2014**, *136*, 6083–6091.

(60) Stoller, M. D.; Ruoff, R. S. Best Practice Methods for Determining an Electrode Material's Performance for Ultracapacitors. *Energy Environ. Sci.* **2010**, *3* (9), 1294–1301.

(61) Wang, J.; Manga, K. K.; Bao, Q.; Loh, K. P. High-Yield Synthesis of Few-Layer Graphene Flakes through Electrolyte Expansion of Graphite in Propylene Carbonate Electrolyte. *J. Am. Chem. Soc.* **2011**, *133*, 8888–8891.

(62) Uddin, M. J.; Cesano, F.; Scarano, D.; Bonino, F.; Agostini, G.; Spoto, G.; Bordiga, S.; Zecchina, A. Cotton Textile Fibres Coated by Au/TiO_2 Films: Synthesis, Characterization and Self Cleaning Properties. *J. Photochem. Photobiol. A Chem.* **2008**, *199* (1), 64–72.

(63) Roppolo, I.; Chiappone, A.; Bejtka, K.; Celasco, E.; Chiodoni, A.; Giorgis, F.; Sangermano, M.; Porro, S. A Powerful Tool for Graphene Functionalization: Benzophenone Mediated UV-Grafting. *Carbon N. Y.* **2014**, *77*, 226–235.

(64) Baraket, M.; Walton, S. G.; Wei, Z.; Lock, E. H.; Robinson, J. T.; Sheehan, P. Reduction of Graphene Oxide by Electron Beam Generated Plasmas Produced in Methane/argon Mixtures. *Carbon N. Y.* **2010**, *48* (12), 3382–3390.

(65) Ferrari, A. C.; Meyer, J. C.; Scardaci, V.; Casiraghi, C.; Lazzeri, M.; Mauri, F.; Piscanec, S.; Jiang, D.; Novoselov, K. S.; Roth, S.; Geim, A. K. Raman Spectrum of Graphene and Graphene Layers. *Phys. Rev. Lett.* **2006**, *97* (18), 1–4.

(66) Gigot, A.; Fontana, M.; Serrapede, M.; Castellino, M.; Bianco, S.; Armandi, M.; Bonelli, B.; Pirri, C. F.; Tresso, E.; Rivolo, P. Mixed 1T-2H Phase MoS_2/reduced Graphene Oxide as Active Electrode for Enhanced Supercapacitive Performance. *ACS Appl. Mater. Interfaces* **2016**, *8*, 32842–32852.

(67) Perkas, N.; Shuster, M.; Amirian, G.; Koltypin, Y.; Gedanken, A. Sonochemical Immobilization of Silver Nanoparticles on Porous Polypropylene. *J. Polym. Sci. Part A Polym. Chem.* **2008**, *46* (5), 1719–1729.

(68) Katagiri, G. Raman Spectroscopy of Graphite and Carbon Materials and Its Recent Application. *Tanso* **1996**, *175*, 304–313.

(69) Cho, L. L. Identification of Textile Fiber by Raman Microspectroscopy. *Forensic Sci. J.* **2007**, *6* (1), 55–62.

(70) Bissett, M. A.; Kinloch, I. A.; Dryfe, R. A. W. Characterization of MoS_2–Graphene Composites for High-Performance Coin Cell Supercapacitors. *ACS Appl. Mater. Interfaces* **2015**, *7* (31), 17388–17398.

Concluding Remarks

Graphene has attracted attention of the scientific community since its first isolation by Geim and Novoselov in 2004. Its outstanding properties are appealing for many applications and, in particular, for energy storage technologies.

The development of more efficient energy storage technologies is crucial regarding the current worldwide energy scenario and the use of renewable technologies to produce electricity. Supercapacitors are electrochemical energy storage devices with appealing characteristics such as fast charge-discharge and long cycling life. However, they struggle about the energy density that can be stored into the devices. To overcome this issue, the research activities of this Ph.D. thesis were focused on the increase of the energy density of graphene-based supercapacitors without affecting their power density.

In the first experimental section, different hybrid supercapacitors based on hydrothermally reduced graphene oxide decorated with transition metal oxide (Molybdenum Oxide – MoO_2) or transition metal dichalcogenide (Molybdenum Disulfide – MoS_2) were compared. Both pseudocapacitive materials were synthesized starting from phosphomolybdic acid, as Mo precursor, and in the case of MoS_2, L-cysteine was used as S precursor. The concomitant synthesis of MoS_2 and reduction of GO induce the formation of an aerogel structure containing indistinguishable two-dimensional materials. Interestingly, the MoS_2 structure is composed of both 1T (metallic) and 2H (semiconductor) phases. The 1T phase is metastable, but nanodomains are stabilized by the rGO flakes interconnected through the 3D aerogel network. The electrochemical properties of this polymorph active material are promising due to the increase of one order of magnitude in the specific capacitance resulted

from the comparison with the bare rGO. Moreover, the cycling stability of this material was demonstrated up to 50.000 cycles.

In the second experimental section, the effect of L-ascorbic acid (Vitamin C) as reducing agent for the concomitant reduction of graphene oxide and the synthesis of molybdenum oxide starting from phosphomolybdic acid was investigated. A significant improvement of reproducibility of the GO reduction grade was demonstrated. In addition, an enhancement of the electrochemical performance and a higher stability of the hybrid supercapacitors were demonstrated. Then, this material was used to fabricate PDMS-based micro-supercapacitors. Indeed, miniaturized supercapacitors are attractive to address the crucial need of portable electronic devices. The followed photolithography procedure permits to obtain PDMS-based devices with high flexibility. The active slurry was composed by reduced graphene aerogels decorated by molybdenum oxide microparticles produced by one-pot hydrothermal synthesis using L-ascorbic acid as reducing agent. In this slurry, PEDOT:PSS was used as conductive binder. The filling of the micro-supercapacitors occurred by capillarity. The so fabricated devices show interesting performance consistent with most relevant works in literature.

In the last experimental section, wearable supercapacitors were investigated with the aim to transfer supercapacitors from conventional configurations to textiles applications. First, a flexible supercapacitor was produced using one-pot hydrothermally synthesised reduced graphene oxide aerogel self-assembled on a copper wire. The integration in cotton fabrics was demonstrated. Moreover, the electrochemical performance of the flexible supercapacitors was superior to the relevant works published in this field. A second approach was investigated with the scalable and cost-effective production of wearable supercapacitors. The active material was electrochemically exfoliated graphene produced from graphite. The deposition technique is mimicking a textile industrial plant with a deposition speed of 100 m/min and

works on both nylon and cotton fabrics. The areal specific capacitance was significantly better for nylon fabrics in comparison with cotton fabrics at low current density. Moreover, the cycling stability of both wearable supercapacitors was demonstrated up to 15.000 cycles.

Despite the focus of the scientific community and the interesting results obtained worldwide, graphene-based supercapacitors are still struggling to be integrated in real applications. The major issue is the price of the graphene that cannot compete with activated carbon which is currently used in industry. Hopefully, due to the “rush gold” for large-scale synthesis of high quality graphene, the price will become rapidly competitive. Hybrid supercapacitors showed specific capacitance better than the pure Electrical Double-Layers Capacitors, thus demonstrating that the former are more versatile than the latter for the improvement of the energy density as desired. However, graphene-based EDLCs provided outstanding electrochemical performance at high current density or high scan rate, where hybrid supercapacitors displayed decrease of performance. This observation should be taken in consideration to develop supercapacitors with enhanced energy density without affecting the power density characteristic of this technology.

Supercapacitors technologies have outstanding cycle life allowing them to be used for “fit-and-forget” applications. Nevertheless, current supercapacitors demonstrate high electrochemical performance in a limited range of temperature, pressure, and deformability. The game-changer development will be the scalable and cost-effective production of graphene-based supercapacitors with almost unlimited properties of flexibility, tolerance to elongation/compression cycles and operation in harsh environments (e.g. in a range of temperature from – 200°C up to 300°C), thus allowing the exploitation of these electrochemical energy storage devices wherever it is necessary.